

Springer Proceedings in Physics 267

Ramis Örlü

Alessandro Talamelli

Joachim Peinke

Martin Oberlack *Editors*

Progress in Turbulence IX

Proceedings of the iTi Conference in
Turbulence 2021

 Springer

Springer Proceedings in Physics

Volume 267

Indexed by Scopus

The series Springer Proceedings in Physics, founded in 1984, is devoted to timely reports of state-of-the-art developments in physics and related sciences. Typically based on material presented at conferences, workshops and similar scientific meetings, volumes published in this series will constitute a comprehensive up-to-date source of reference on a field or subfield of relevance in contemporary physics. Proposals must include the following:

- name, place and date of the scientific meeting
- a link to the committees (local organization, international advisors etc.)
- scientific description of the meeting
- list of invited/plenary speakers
- an estimate of the planned proceedings book parameters (number of pages/articles, requested number of bulk copies, submission deadline).

Please contact:

For Americas and Europe: Dr. Zachary Evenson; zachary.evenson@springer.com

For Asia, Australia and New Zealand: Dr. Loyola DSilva; loyola.dsilva@springer.com

More information about this series at <http://www.springer.com/series/361>

Ramis Örlü · Alessandro Talamelli ·
Joachim Peinke · Martin Oberlack
Editors

Progress in Turbulence IX

Proceedings of the iTi Conference
in Turbulence 2021

 Springer

Editors

Ramis Örlü
Linné FLOW Centre
KTH Engineering Mechanics
Stockholm, Sweden

Alessandro Talamelli
Department of Industrial Engineering
Università di Bologna
Forlì, Italy

Joachim Peinke
Institute of Physics
University of Oldenburg
Oldenburg, Niedersachsen, Germany

Martin Oberlack
Department of Mechanical Engineering
TU Darmstadt
Darmstadt, Germany

ISSN 0930-8989

ISSN 1867-4941 (electronic)

Springer Proceedings in Physics

ISBN 978-3-030-80715-3

ISBN 978-3-030-80716-0 (eBook)

<https://doi.org/10.1007/978-3-030-80716-0>

© The Editor(s) (if applicable) and The Author(s), under exclusive license to Springer Nature Switzerland AG 2021

This work is subject to copyright. All rights are solely and exclusively licensed by the Publisher, whether the whole or part of the material is concerned, specifically the rights of translation, reprinting, reuse of illustrations, recitation, broadcasting, reproduction on microfilms or in any other physical way, and transmission or information storage and retrieval, electronic adaptation, computer software, or by similar or dissimilar methodology now known or hereafter developed.

The use of general descriptive names, registered names, trademarks, service marks, etc. in this publication does not imply, even in the absence of a specific statement, that such names are exempt from the relevant protective laws and regulations and therefore free for general use.

The publisher, the authors and the editors are safe to assume that the advice and information in this book are believed to be true and accurate at the date of publication. Neither the publisher nor the authors or the editors give a warranty, expressed or implied, with respect to the material contained herein or for any errors or omissions that may have been made. The publisher remains neutral with regard to jurisdictional claims in published maps and institutional affiliations.

This Springer imprint is published by the registered company Springer Nature Switzerland AG
The registered company address is: Gewerbestrasse 11, 6330 Cham, Switzerland

Preface

iTi has become an established biannual conference on turbulence research taking place in the years between the ETC—European Turbulence Conference and TSFP—Turbulence and Shear Flow Phenomena conferences. With 80–100 participants, the iTi conference places value on the discussions and personal contacts in the location of the beautiful town of Bertinoro in Northern Italy close to Bologna. It continues a tradition that has been started in Bad Zwischenahn/Germany with the first edition of the conference in 2003. In contrast to many conferences, where highly specialized parallel sessions take place, the size of the iTi was purposely designed to host one single session from the very beginning, so that experimentalists, theoreticians and simulation experts can listen simultaneously and enter into a direct dialog with each other. The content-related focus areas of the conference are the interdisciplinary aspects of turbulence, defining the abbreviation iTi—interdisciplinary Turbulence initiative. iTi attracts scientists from the engineering, physics and mathematics communities.

The 9th iTi was planned to be held in the autumn of 2020, but the Covid-19 pandemic has forced us to change our plans. We intentionally did not want to cancel iTi. The feeling was that, in the turbulence community, even in these difficult times, the interest and the need for an intensive scientific exchange was very strong. Against this background, the iTi conference took place as a pure online event, during February 25–26, 2021.

Due to the virtual nature of the conference, 192 scientists from 17 countries with a regular attendance of 60–100 participants throughout all talks participated. In total, there were 69 contributions, of which 4 were invited live talks, 35 were regular live talks and the remainder were on-demand video contributions, covering a wide range of aspects of current turbulence research. Advances in the understanding of turbulence and theory, turbulence modeling and simulation, turbulence experiments, data processing and turbulent scaling laws and a variety of related topics were addressed.

At this point, we would like to thank Dario Klingenberg, Alparslan Yalcin, Jie Liu, Yi Zhang and Tim Gebler from TU Darmstadt without whose help the virtual event would not have been possible.

The content of the 9th iTi conference is documented in this volume comprising 41 contributions. All contributions were thoroughly reviewed by external reviewers, to whom we want to express our thanks for their valuable and important contributions.

Based on the successful previous conferences, we will continue with this initiative for subsequent years with the 10th iTi Conference September 2023.



Finally, it is a distinct desire for us, to pay a special tribute to Charles Rogers Doering, who passed away a few weeks after the iTi on May 15, 2021, shortly before the completion of these proceedings. Charles had given a wonderful and stimulating talk at iTi in his inimitable style on the subject of *Heat transport in steady and turbulent Rayleigh-Bénard convection*. He had been intensely involved with this topic in recent years, and through it he was particularly closely associated with the turbulence community. Charles was not only a brilliant scientist but also an inspiring speaker who could captivate his audience even on highly complex topics. Of the very large number of awards and honors he received during his career, it is worth mentioning that he received the NSF Presidential Young Investigator Award early on—many more followed. In addition to his scientific work, Charles' personality is particularly remembered. He had many facets, of course, but we experienced him above all as a humorous, emphatic, clear, honest, inclusive and always respectful person with whom it was always particularly entertaining to spend an evening.



Stockholm, Sweden
Forlì, Italy
Oldenburg, Germany
Darmstadt, Germany

Ramis Örlü
Alessandro Talamelli
Joachim Peinke
Martin Oberlack

Contents

Part I Experiments

Dynamic Triad Interactions and Non-equilibrium Turbulence	3
Clara M. Velte and Preben Buchhave	
Turbulent/Turbulent Entrainment	13
Krishna S. Kankanwadi and Oliver R. H. Buxton	
Active Control of Turbulent Convective Heat Transfer with Plasma Actuators	21
Rodrigo Castellanos, Theodoros Michelis, Stefano Discetti, Andrea Ianiro, and Marios Kotsonis	
Mean Parameters of Incompressible Turbulent Boundary Layer with Zero Pressure Gradient on the Wall of the TsAGI T-128 Wind Tunnel at Very High Reynolds Numbers	29
Anton Gorbushin, Svetlana Osipova, and Vladimir Zametaev	
Investigation of Self-Similarity of the Temperature Stratified Turbulent Boundary Layer Over the Wavy Surface in Laboratory Conditions	35
D. A. Sergeev, Yu I. Troitskaya, A. A. Kandaurov, and M. I. Vdovin	
On Similarity of Turbulence Statistics of a Turbulent Planar Jet Taking the Static Pressure into Account	43
Tatsuya Ito, Takuya Ito, P. Henrik Alfredsson, Antonio Segalini, and Masaharu Matsubara	
Mean Velocity Profiles over Streamwise-Aligned Permeable Ridges	51
Yuki Okazaki, Yumeto Takase, Yusuke Kuwata, and Kazuhiko Suga	

Energy Dissipation and Total Entropy Production in SHREK Experiment	57
Swapnil Kharche, André Fuchs, Michel Bon-Mardion, Jean-Paul Moro, Bernard Rousset, Christophe Baudet, Joachim Peinke, and Alain Girard	
Part II Simulations and Modelling	
The Filtering Approach as a Tool for Modeling and Analyzing Turbulence	67
Massimo Germano, A. Abbà, A. Cimarelli, Andrea Ferrero, Fernando F. Grinstein, M. Klein, Francesco Larocca, Juan A. Saenz, and Guglielmo Scovazzi	
Dynamic Bridging for Coarse Grained Simulations of Turbulent Material Mixing	79
Fernando F. Grinstein, Juan A. Saenz, and Massimo Germano	
Dynamic Tensorial Eddy Viscosity and Turbulent Stresses	85
A. Abbà, A. Cimarelli, and Massimo Germano	
A Numerical Study of the Spanwise Turbulence Past a Cylinder Flow	91
Andrea Ferrero, Francesco Larocca, Guglielmo Scovazzi, and Massimo Germano	
Asymmetry in Wake of Oscillating Foils with Combined Pitching and Heaving Motion	97
Suyash Verma and Arman Hemmati	
Helical Structures in the Wake of Long Wall-Mounted Prisms at High Incident Angles	103
Arash Zargar and Arman Hemmati	
A Spatially Accelerating Turbulent Flow with Longitudinally Moving Walls	109
Matthew Falcone and Shuisheng He	
Dissimilarity Between Heat and Momentum Transfer of Turbulent Heat Transfer over Surfaces with Hemisphere Protrusions	115
Rika Nagura, Yusuke Kuwata, and Kazuhiko Suga	
Part III Data Processing and Scaling	
The Diagnostic Plot—A Tutorial with a Ten Year Perspective	125
P. Henrik Alfredsson, Antonio Segalini, and Ramis Örlü	

Bayesian Optimisation with Gaussian Process Regression Applied to Fluid Problems 137
 Saleh Rezaeiravesh, Yuki Morita, Narges Tabatabaei, Ricardo Vinuesa, Koji Fukagata, and Philipp Schlatter

Data-Driven Dynamics Description of a Transitional Boundary Layer 145
 F. Foroozan, V. Guerrero, Andrea Ianiro, and Stefano Discetti

Identification of a Stochastic Hopf Bifurcation from Stationary Measurement Data of a Turbulent Flow 153
 Moritz Sieber, Christian Oliver Paschereit, and Kilian Oberleithner

Data-Driven Identification of Robust Low-Order Models for Dominant Dynamics in Turbulent Flows 159
 Y. Schubert, Moritz Sieber, Kilian Oberleithner, and Robert J. Martinuzzi

Experimental Assessment of Symmetry Induced Higher-Moment Scaling Laws in Turbulent Pipe Flow 167
 Spencer Zimmerman, Joseph Klewicki, and Martin Oberlack

Characteristics of Reynolds Shear Stress in Adverse Pressure Gradient Turbulent Boundary Layers 173
 Sylvia Romero, Spencer Zimmerman, Jimmy Philip, and Joseph Klewicki

Energy Transfer in Turbulent Boundary Layers with Adverse Pressure Gradient 181
 Taygun R. Gungor, Ayse G. Gungor, and Yvan Maciel

Influence of Rough Surface Morphology on Boundary Layer Flow 187
 K. Jurčáková, P. Procházka, R. Kellnerová, P. Antoš, and V. Skála

Part IV Theory

Similarity Scaling of a Free, Round Jet in Air 197
 Preben Buchhave, Chunyue Zhu, and Clara M. Velte

Topological Differences in Mean Wakes of Circular and Square Cantilevered Cylinders 203
 Matthew G. Kindree, Dekun Yan, and Robert J. Martinuzzi

Large-Scale-Motions and Self-excited Clustering of Coherent Structures in Wall Turbulence 209
 Sedat Tardu

The Conservative Pressure Hessian and the Free Fluid Particle Model 215
 Maurizio Carbone, Andrew Bragg, Josin Tom, Michael Wilczek, and Michele Iovieno

Modelling The Pressure Hessian in Turbulence Through Tensor Function Representation Theory 223
Maurizio Carbone and Michael Wilczek

Stretched Amplitude Decaying Fourier Modes in the Jet Far-Field 231
Azur Hodžić, K. E. Meyer, W. K. George, and Clara M. Velte

Generalizable Theory of Reynolds Stress 237
T.-W. Lee

Spectral Energetics of a Quasilinear Approximation in Uniform Shear Turbulence 245
Carlos G. Hernández and Yongyun Hwang

Part V Miscellaneous Topics

Turbulence and Uncertainty for Future Renewable Energy Reliability 255
P. Tavner and D. Zappalá

Instability on Rotating Sharp Cones—Revisited 259
K. Kato, P. Henrik Alfredsson, and R. J. Lingwood

Rotational Effects on Layered Structures in Inhomogeneous Stratified Turbulence 267
Oaki Iida

Magnetoclinicity Instability 273
Nobumitsu Yokoi and Steven M. Tobias

Beginning of Taylor’s and Wavy Vortices at the Loss of Stability of a Conducting Liquid Flow Produced by the Rotating Magnetic Field 281
Alexander Zibold

Investigation of the Flow Generated by the Surface Discharge on the Cylinder Body in the Quiescent Air 289
A. V. Ivchenko and V. G. Shakhov

Numerical and Physical Aspects of Large-Eddy Simulation of Turbulent Mixing in a Helium-Air Supersonic Co-flowing Jet 297
Alexey Troshin, Sergey Bakhne, and Vladimir Sabelnikov

Turbulent Energy Production in the Boundary Layer of a Gas Flow Near the Free Surface of a Liquid 303
A. Goltsman and I. Saushin

Phase Distribution of the Developed Three-Component Pipe Flows 309
I. Saushin and A. Goltsman

Contributors

A. Abbà Dipartimento di Scienze e Tecnologie Aerospaziali, Politecnico di Milano, Milano, Italy

P. Henrik Alfredsson Department of Engineering Mechanics, KTH Royal Institute of Technology, Stockholm, Sweden

P. Antoš The Czech Academy of Sciences, Institute of Thermomechanics, Prague, Czech Republic

Sergey Bakhne Central Aerohydrodynamic Institute (TsAGI), Zhukovsky, Russia; Moscow Institute of Physics and Technology, Dolgoprudny, Russia

Christophe Baudet University Grenoble Alpes, LEGI, Grenoble, France

Michel Bon-Mardion CEA IRIG-DSBT, 17 Avenue des Martyrs, Grenoble, France

Andrew Bragg Department of Civil and Environmental Engineering, Duke University, Durham, NC, USA

Preben Buchhave Intarsia Optics, Birkerød, Denmark

Oliver R. H. Buxton Imperial College London, London, UK

Maurizio Carbone Max Planck Institute for Dynamics and Self-Organization, Göttingen, Germany

Rodrigo Castellanos Aerospace Research Group, Universidad Carlos III de Madrid, Leganés, Spain

A. Cimarelli DIEF, University of Modena and Reggio Emilia, Modena, Italy; Università di Modena e Reggio Emilia, Modena, Italy

Stefano Discetti Aerospace Research Group, Universidad Carlos III de Madrid, Leganés, Spain

Matthew Falcone Department of Mechanical Engineering, University of Sheffield, Sheffield, UK

Andrea Ferrero Politecnico di Torino, Torino, Italy

F. Foroosan Aerospace Engineering Research Group, Universidad Carlos III de Madrid, Leganés, Spain

André Fuchs Institute of Physics and ForWind, University of Oldenburg, Oldenburg, Germany

Koji Fukagata Department of Mechanical Engineering, Keio University, Yokohama, Japan

W. K. George Department of Aeronautics, Imperial College London, London, UK

Massimo Germano Department Civil and Environmental Engineering, Duke University, Durham, NC, USA

Alain Girard CEA IRIG-DSBT, 17 Avenue des Martyrs, Grenoble, France

A. Goltsman Institute of Power Engineering and Advanced Technologies, FRC Kazan Scientific Center, Russian Academy of Sciences, Kazan, Tatarstan, Russian Federation

Anton Gorbushin Central Aerohydrodynamic Institute (TsAGI), Zhukovsky, Russia;

Moscow Institute of Physics and Technology, Dolgoprudny, Russia

Fernando F. Grinstein Los Alamos National Laboratory, Los Alamos, NM, USA

V. Guerrero Department of Statistics, Universidad Carlos III de Madrid, Getafe, Spain

Ayşe G. Gungor Faculty of Aeronautics and Astronautics, Istanbul Technical University, Istanbul, Turkey

Taygun R. Gungor Department of Mechanical Engineering, Laval University, Quebec City, QC, Canada;

Faculty of Aeronautics and Astronautics, Istanbul Technical University, Istanbul, Turkey

Shuisheng He Department of Mechanical Engineering, University of Sheffield, Sheffield, UK

Arman Hemmati Department of Mechanical Engineering, University of Alberta, Edmonton, AB, Canada

Carlos G. Hernández Department of Aeronautics, Imperial College London, London, UK

Azur Hodžić Department of Mechanical Engineering, Technical University of Denmark, Lyngby, Denmark

Yongyun Hwang Department of Aeronautics, Imperial College London, London, UK

Andrea Ianiro Aerospace Engineering Research Group, Universidad Carlos III de Madrid, Leganés, Spain

Oaki Iida Department of Mechanical Engineering, Nagoya Institute of Technology, Nagoya, Japan

Michele Iovieno Dipartimento di Ingegneria Meccanica e Aerospaziale, Politecnico di Torino, Torino, Italy

Takuya Ito Department of Mechanical Systems Engineering, Shinshu University, Nagano, Japan

Tatsuya Ito Department of Mechanical Systems Engineering, Shinshu University, Nagano, Japan

A. V. Ivchenko Samara National Research University, Russia Samara,

K. Jurčáková The Czech Academy of Sciences, Institute of Thermomechanics, Prague, Czech Republic

A. A. Kandaurov Institute of Applied Physics Russian Academy Science, 46 Ul'yanov St., Nizhny Novgorod, Russia

Krishna S. Kankanwadi Imperial College London, London, UK

K. Kato Department of Engineering Mechanics, KTH, Stockholm, Sweden

R. Kellnerová The Czech Academy of Sciences, Institute of Thermomechanics, Prague, Czech Republic

Swapnil Kharche CEA IRIG-DSBT, 17 Avenue des Martyrs, Grenoble, France

Matthew G. Kindree University of Calgary, Alberta, Canada

M. Klein Universität der Bundeswehr München, Neubiberg, Germany

Joseph Klewicki Department of Mechanical Engineering, University of Melbourne, Parkville, VIC, Australia

Marios Kotsonis Department of Aerodynamics, Delft University of Technology, Delft, The Netherlands

Yusuke Kuwata Department of Mechanical Engineering, Osaka Prefecture University, Sakai, Osaka, Japan

Francesco Larocca Politecnico di Torino, Torino, Italy

T.-W. Lee Arizona State University, Tempe, AZ, USA

R. J. Lingwood Department of Engineering Mechanics, KTH, Stockholm, Sweden; Department of Mechanical and Aerospace Engineering, Brunel University London, London, UK

Yvan Maciel Department of Mechanical Engineering, Laval University, Quebec City, QC, Canada

Robert J. Martinuzzi Department of Mechanical and Manufacturing Engineering, University of Calgary, Alberta, Canada

Masaharu Matsubara Department of Mechanical Systems Engineering, Shinshu University, Nagano, Japan

K. E. Meyer Department of Mechanical Engineering, Technical University of Denmark, Lyngby, Denmark

Theodoros Michelis Department of Aerodynamics, Delft University of Technology, Delft, The Netherlands

Yuki Morita Department of Mechanical Engineering, Keio University, Yokohama, Japan

Jean-Paul Moro CEA IRIG-DSBT, 17 Avenue des Martyrs, Grenoble, France

Rika Nagura Department of Mechanical Engineering, Osaka Prefecture University, Sakai, Japan

Martin Oberlack Chair of Fluid Dynamics, Technische Universität Darmstadt, Darmstadt, Germany

Kilian Oberleithner Laboratory for Flow Instabilities and Dynamics, Technische Universität Berlin, Berlin, Germany

Yuki Okazaki Department of Mechanical Engineering, Osaka Prefecture University, 1-1, Gakuen-cho, Naka-ku, Sakai, Osaka, Japan

Ramis Örlü FLOW, Engineering Mechanics, KTH Royal Institute of Technology, Stockholm, Sweden

Svetlana Osipova Central Aerohydrodynamic Institute (TsAGI), Zhukovsky, Russia;
Moscow Institute of Physics and Technology, Dolgoprudny, Russia

Christian Oliver Paschereit Chair of Fluid Dynamics, Technische Universität Berlin, Berlin, Germany

Joachim Peinke Institute of Physics and ForWind, University of Oldenburg, Oldenburg, Germany

Jimmy Philip Department of Mechanical Engineering, University of Melbourne, Parkville, VIC, Australia

P. Procházka The Czech Academy of Sciences, Institute of Thermomechanics, Prague, Czech Republic

Saleh Rezaeiravesh SimEx/FLOW, Engineering Mechanics, KTH Royal Institute of Technology, Stockholm, Sweden

Sylvia Romero Department of Mechanical Engineering, University of Melbourne, Parkville, VIC, Australia

Bernard Rousset CEA IRIG-DSBT, 17 Avenue des Martyrs, Grenoble, France

Vladimir Sabelnikov Central Aerohydrodynamic Institute (TsAGI), Zhukovsky, Russia

Juan A. Saenz Los Alamos National Laboratory, Los Alamos, NM, USA

I. Saushin Institute of Power Engineering and Advanced Technologies, FRC Kazan Scientific Center, Russian Academy of Sciences, Kazan, Tatarstan, Russian Federation

Philipp Schlatter SimEx/FLOW, Engineering Mechanics, KTH Royal Institute of Technology, Stockholm, Sweden

Y. Schubert Laboratory for Flow Instabilities and Dynamics, Technische Universität Berlin, Berlin, Germany

Guglielmo Scovazzi Duke University, Durham, USA

Antonio Segalini Department of Engineering Mechanics, KTH Royal Institute of Technology, Stockholm, Sweden

D. A. Sergeev Institute of Applied Physics Russian Academy Science, 46 Ul'yanov St., Nizhny Novgorod, Russia

V. G. Shakhov Samara National Research University, RussiaSamara,

Moritz Sieber Laboratory for Flow Instabilities and Dynamics, Technische Universität Berlin, Berlin, Germany;
Chair of Fluid Dynamics, Technische Universität Berlin, Berlin, Germany

V. Skála The Czech Academy of Sciences, Institute of Thermomechanics, Prague, Czech Republic

Kazuhiko Suga Department of Mechanical Engineering, Osaka Prefecture University, Sakai, Osaka, Japan

Narges Tabatabaei SimEx/FLOW, Engineering Mechanics, KTH Royal Institute of Technology, Stockholm, Sweden

Yumeto Takase Department of Mechanical Engineering, Osaka Prefecture University, 1-1, Gakuen-cho, Naka-ku, Sakai, Osaka, Japan

Sedat Tardu Université Grenoble Alpes, LEGI, Grenoble, France

P. Tavner Department of Engineering, Durham University, Durham, UK

Steven M. Tobias Department of Applied Mathematics, University of Leeds, Leeds, UK

Josin Tom Department of Civil and Environmental Engineering, Duke University, Durham, NC, USA

Yu I. Troitskaya Institute of Applied Physics Russian Academy Science, 46 Ul'yanov St., Nizhny Novgorod, Russia

Alexey Troshin Central Aerohydrodynamic Institute (TsAGI), Zhukovsky, Russia; Moscow Institute of Physics and Technology, Dolgoprudny, Russia

M. I. Vdovin Institute of Applied Physics Russian Academy Science, 46 Ul'yanov St., Nizhny Novgorod, Russia

Clara M. Velte Department of Mechanical Engineering, Technical University of Denmark, Lyngby, Denmark

Suyash Verma University of Alberta, Edmonton, AB, Canada

Ricardo Vinuesa SimEx/FLOW, Engineering Mechanics, KTH Royal Institute of Technology, Stockholm, Sweden

Michael Wilczek Max Planck Institute for Dynamics and Self-Organization, Göttingen, Germany

Dekun Yan University of Calgary, Alberta, Canada

Nobumitsu Yokoi Institute of Industrial Science, University of Tokyo, Tokyo, Japan;
Visiting researcher at the Nordic Institute for Theoretical Physics (NORDITA), Stockholm, Sweden

Vladimir Zametaev Central Aerohydrodynamic Institute (TsAGI), Zhukovsky, Russia;
Moscow Institute of Physics and Technology, Dolgoprudny, Russia

D. Zappalá Faculty of Aerospace Engineering, TU Delft, Delft, Netherlands

Arash Zargar Department of Mechanical Engineering, University of Alberta, Edmonton, AB, Canada

Chunyue Zhu Department of Mechanical Engineering, Technical University of Denmark, Kgs. Lyngby, Denmark

Alexander Zibold Donetsk, Ukraine

Spencer Zimmerman Department of Mechanical Engineering, University of Melbourne, Parkville, VIC, Australia

Part I

Experiments

Dynamic Triad Interactions and Non-equilibrium Turbulence



Clara M. Velte and Preben Buchhave

Abstract The classical K41 theory, based on the ideas of Kolmogorov, Richardson and Batchelor, has in recent years with accumulating evidence become subject to increased scrutiny. We elaborate on the idea that the deficiencies of the theory originate in the fundamental assumption of universal equilibrium, which in turn is the result of the basic assumption of locality of nonlinear interactions. These very fundamental assumptions are argued to have no anchoring in the governing Navier-Stokes equation. The possibility for other kinds of solutions are discussed from a historical perspective. K41 is also identified to represent an equilibrium solution that cannot predict non-equilibrium turbulence.

1 Why the Need for New Perspectives on the Established Theory?

The theoretical framework developed by Kolmogorov (including the contributing ideas of Richardson and Batchelor, often collectively referred to as the ‘K41’ theory [1–3]), has comprised the cornerstone of our understanding of turbulence for more than half a century. It has up until recently not been so frequently acknowledged that Kolmogorov’s ideas were initially heavily questioned. In fact, it took two decades before K41 was convincingly supported by experiments; first in a turbulent round jet by Gibson [4] and secondly (and more widely acknowledged) by Grant, Stewart and Moilliet [5]. Once these empirical studies supporting K41 finally appeared, the theory has been amply supported by further experiments and simulations in some flows, while other theories have been more successful in predicting non-K41 types of flows (c.f. [6–12]), including arguments by Kolmogorov himself [13]. In fact, even after K41 had become commonly accepted, Kolmogorov would still refer to K41

C. M. Velte (✉)

Department of Mechanical Engineering, Technical University of Denmark, Kgs.,
Lyngby, Denmark
e-mail: cmve@dtu.dk

P. Buchhave

Intarsia Optics, Birkerød, Denmark

as “purely phenomenological” [14]. This is further emphasized by the fact that the famous $k^{-5/3}$ spectral power law can be obtained from pure dimensional analysis (and was in fact found independently by others around the same time [15, 16]).

G.K. Batchelor was an early adopter and a strong proponent of Kolmogorov’s ideas. He even contributed with a mathematical framework on homogeneous turbulence [17]. Unfortunately, homogeneous flows are not well representative of actual flow, not least in that practical flows are of finite extent in time and space. Another critique would be that few (if any) flows display even approximate homogeneity in all directions across the domain of the flow. Furthermore, a homogeneous flow cannot remain stationary, as can be seen directly from the energy equation, c.f. [18].

In fact, the classical experiments in decaying grid turbulence (van Kármán, Howarth, Batchelor, Townsend, Corrsin and Comte-Bellot), designed to mimic the ideal case of homogeneous flow, played a key role in the early acceptance and controversy of K41. As grid turbulence decays rather slowly, at least in the initial period of decay (approximately $u^2 \propto t^{-1}$, as expected from the van Kármán-Howarth solution), one was faced with the practical problem that the test sections of the wind tunnels would be too short compared to the initial turbulence decay to reach definitive conclusions regarding independence upon initial conditions (or universality). By making the mesh dimension smaller, this decay length could be shortened, but at the expense of increased measurement errors with the hotwires used [17]. With the introduction of exponentially decaying turbulence [19] and subsequently experimental support in fractal grid turbulence, which certainly did not obey K41, a broader acceptance began to emerge that there may indeed be more to the story.

As early as in 1992, the late John L. Lumley asked [20]: “What part of modeling is in serious need of work? Foremost, I would say, is the mechanism that sets the level of dissipation in a turbulent flow, particularly in changing circumstances”. We know today, from careful studies, that K41 can with great success describe turbulence in simple statistically stationary free shear flows [9], but unfortunately appears to have limited predictive capabilities in flows that accelerate, decay or separate—all common features of important engineering flows. These are also flows for which the (K41 based) turbulence models struggle.

In the following, we will argue that K41 is indeed an equilibrium solution that in general predicts (nearly) stationary turbulence satisfactorily. However, it is becoming increasingly accepted in the community that we must develop a more accurate understanding of turbulence that is valid also for the scientifically and technologically important class of non-stationary flows.

1.1 *Why Experiments Cannot Prove a Theory*

Although K41 was a great intellectual achievement given the resources available at the time of development, from the author’s own experience (including repeated comments from proposal reviewer comments and the ERC review and interview process) [21], there seems to exist a widespread misconception that K41 has been

proven by experiments. This is a logical fallacy, since experiments can—at best—support or increase our confidence in a theory, but they can never prove the generality of a theory. On the other hand, one experiment is, in principle, sufficient to *disprove* the generality of a theory. And, in fact, there exist several experiments that do and the field is slowly opening up to this possibility, see e.g. [22].

A simple example could be used to illustrate the point; One could carry out a vast range of experiments indicating that the Earth is flat. This does however not ‘prove’ the idea. If carried out in a different manner, an experiment could indicate that the Earth is curved, or even round (or even more complex geometries, if the experiments are continually refined). The same principle of course applies to other theories, including the K41 theory. To disprove a theory by a carefully designed experiment, it all comes down to targeting its weak points—usually its assumptions (if otherwise correctly deduced). George [9] and the authors argue that it is, in particular, the central assumption of universal local (small scale) equilibrium that constitutes the core weakness of the K41 theory.

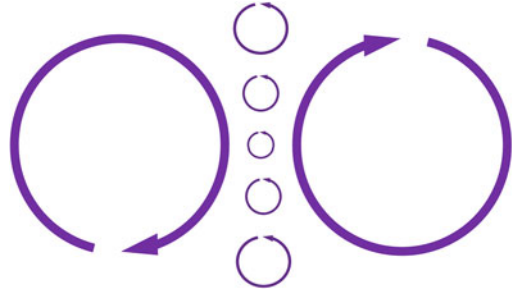
2 The Assumption of Universal Equilibrium

When presenting repeated arguments against the universal equilibrium assumption (e.g. during an ERC Starting Grant interview [21]), it also became apparent to the first author that it is a common misconception that the universal equilibrium assumption would not be postulated to hold under ‘changing circumstances’. However, even current theoretical, experimental and numerical work repeatedly make use of this assumption also in highly non-equilibrium flows (e.g. gas/wind turbines, separation, stagnation etc.). Furthermore, Batchelor makes it quite clear that the theory applies also under ‘changing circumstances’, as he writes himself in his book “Homogeneous Turbulence” [17] (Chap. 6: “The Universal Equilibrium Theory”): “In particular, the statistical quantities determined by the equilibrium range are independent of the properties of the large-scale components of the turbulence...” and “If the spectrum shape can be determined, then, according to the foregoing theory, it will apply to all kinds of turbulent motion, whatever their large-scale properties, the only condition being that the Reynolds number should be sufficiently large.”

2.1 Local Equilibrium and the Locality of Scale Interactions

Being a statistician, it does not seem surprising that Kolmogorov based his fundamental view of small-scale turbulence [1–3] on a gas dynamics (statistical physics) analogy to the small and intermediate turbulent scales. In this analogy between the fluid and the flow, the small and intermediate scales would behave relative to the large scales similarly to how molecules in a thermal equilibrium relate to a corresponding thermodynamic macroscopic system. Just like individual molecules in thermody-

Fig. 1 Thought experiment illustrating non-local interactions under high shear conditions



dynamic equilibrium, the wide range of small and intermediate turbulent flow scales were, through local interactions, *assumed* to be effectively decoupled from the large energy containing scales ([17, 23], Sect. 21.3) *and* at a state of statistical local (or small scale) equilibrium—no matter what the dynamics of the large scales. However, even molecules can be pushed out of a thermodynamic equilibrium. And the small and intermediate turbulent scales are *much* larger than molecules.

Thus, a consequence of assuming local interactions and decoupling between the large versus the intermediate and small scales was Kolmogorov’s Zeroth Hypothesis¹: that the smallest and intermediate scales could be considered to be in local equilibrium. *But*, this very fundamental assumptions has no anchoring in the equations that govern fluid flow.

Furthermore, the K41 theory was developed for the scales where the energy was the smallest. But in fact the inertial and dissipative range (or universal equilibrium range) together contain the majority of the energy in high Reynolds number turbulence. Batchelor also recognized this, see Chapter VII of [17], where the presented grid turbulence experiments evidenced that the energetic scales constituted only roughly 20% of the turbulent kinetic energy.

The breakdown of these ideas can be illustrated by a simple thought experiment: Suppose that two large counter-rotating vortices are located next to one another. Their motion can set the fluid in between into rotation and directly generate significantly smaller scales in between, if spaced sufficiently close together (see Fig. 1). In such a system, energy can be directly transferred through non-local interactions from energetic to inertial or even dissipative scales. Furthermore, the dynamics (non-equilibrium) in the large energetic scales can translate directly into the small and intermediate scales.

This thought experiment strongly indicates that the central assumption of local interactions and decoupling between the energetic scales from the small and intermediate scales (and hence the derived consequence of local equilibrium) cannot hold true. And this leaves the theory with only a single hope of remaining valid: the *requirement that all scales are in equilibrium*. One could thus argue that K41 is in fact an equilibrium solution.

¹ In fact, Kolmogorov only implied this. Batchelor [17] codified it into the form we now take for granted.

2.2 The Crucial Constancy of Spectral Energy Flux

If the Reynolds number is sufficiently large, the energy containing and dissipative scales were hypothesized to separate leaving a buffer-like region in between in wavenumber space where only transfer between scales of similar size occurs. This intermediate region can, under the stated assumptions, only depend on the (constant) spectral flux of energy, ε_k , passing down along the cascade. As the energy is fed into the dissipation range at this rate, the dissipation of energy, ε , must in this setting take place at the same rate, requiring consequently ε_k (inertial range) = ε . Because of this equality, the dissipation, concentrated in the small scales, can be directly estimated from the large energy containing scales. The small and intermediate scales are thus believed to behave in a universal manner as long as the Reynolds number is ‘large enough’. Almost all turbulence theories and turbulence models are based on some form of this basic idea. A vivid illustration of this is the so-called “zeroth-law of turbulence”, $\varepsilon \propto u'^3/\ell$. This is really just a definition of ℓ , which can in turn, thanks to the arguments above, be assumed to be proportional to the integral scale.

It is, based on these arguments, simply a task of dimensional analysis to derive one of the most famous results in turbulence, $E(k) \propto \varepsilon_k^{2/3} k^{-5/3}$, the $-5/3$ law, where k is the wavenumber and $E(k)$ is the wavenumber dependent turbulent kinetic energy. Although Kolmogorov developed his theory using velocity differences in physical space, this $-5/3$ slope in wavenumber space has over the decades become the ‘hallmark’ of the established K41 picture and hence also of turbulence. As a consequence, all of the energy being generated at the large scales has to pass through this $-5/3$ -range through (non-linear) local interactions in an (approximately) monotonic fashion until being eventually dissipated as the scales become too small to counter friction forces. These hypotheses were later refined [13], but the main ideas of local equilibrium and local interactions remain intact. Thus, models and hypotheses frequently only allowed for interactions between scales of similar size.

It is important to note that this picture relies crucially upon the assumption that *nothing* modifies the constancy of the spectral flux in the inertial subrange (or $k^{-5/3}$ range). Any process adding or removing energy at wavenumbers (such as deviations from equilibrium in time or non-local interactions in space) in this range will make the assumed constant spectral flux ε_k vary, and hence also the dissipation, ε .

In such a flow setting, the K41 description cannot be used.

3 Nonlinear Triadic Energy Transfer

From the Fourier transform of the non-linear term, $(\mathbf{u} \cdot \nabla)\mathbf{u}$, in the governing Navier-Stokes equation, formulated in wavenumber space, the transfer of energy can be seen to be restricted between triads of wavenumbers (say, \mathbf{k}_1 , \mathbf{k}_2 and $\mathbf{k} = \mathbf{k}_1 + \mathbf{k}_2$) in so-called triadic interactions. This energy transfer could in principle happen between any triadic combination of wavenumber vectors, since the equations do not favor any

particular combination. However, adding the assumption of only local interactions being allowed (or at least being strongly favored), energy exchange is limited to triads of similar size. The vast majority of cascade models (c.f. [17, 18, 23], e.g. by Kovasnay, Heisenberg, Onsager) indeed assume only local interactions are important (and [constant] spectral flux only depends on ε and k). But none of these have so far been able to accurately describe how turbulent kinetic energy transfers from lower to higher wavenumbers in non-stationary or transient experiments. In fact, direct coupling seems to be possible even between scales of very different sizes, with energy being able to flow towards both higher and lower energies (although, clearly, the net effect is energy transport towards higher wavenumbers).

3.1 *The Navier-Stokes Machine and New Theory Developments*

The inspiration to include the time component in the description came from Professor William K. George, in particular from the paper he wrote for the “Whither Turbulence and Big Data in the 21st Century” meeting in 2015 [24]. There, he pointed out that time should be included in the nonlinear triadic energy exchange and he speculated whether one should expand the concept of triadic interactions to ‘quadratics’.

Our interpretation [25] of the role of time in the decomposition is somewhat different, as we find that time only has a direct effect in the case of finite resolution and high intensity turbulence. The Navier-Stokes equation describes the momentum balance in a point in time and space. And through the definition of velocity, $\mathbf{u}(\mathbf{r}, t) = d\mathbf{r}/dt$, temporal and spatial fluctuations are coupled *at a mathematical point*. However, in real experimental and numerical observations, flow fields are described with finite temporal and spatial domains and resolution. The finite resolution thus results in a decoupling of the spatial and temporal fluctuations of the velocity. Consequently, the velocity instead becomes a stochastic function of four independent parameters—three spatial coordinates and time.

The Fourier-decomposition of the nonlinear term in the Navier-Stokes equation thus becomes [25]:

$$F.T. \{(\mathbf{u} \cdot \nabla) \mathbf{u}\} = \frac{1}{(2\pi)^4} \iiint \int d\mathbf{k}_1 d\omega_1 \frac{1}{(2\pi)^4} \iiint \int d\mathbf{k}_2 d\omega_2 \times$$

$$\iiint \int \mathbf{W}(\mathbf{r}) W(t) e^{-i[(\mathbf{k}-\mathbf{k}_1-\mathbf{k}_2)\cdot\mathbf{r}-(\omega-\omega_1-\omega_2)t]} d\mathbf{r} dt \left\{ [i\mathbf{k}_2 \cdot \hat{\mathbf{u}}(\mathbf{k}_1, \omega_1)] \hat{\mathbf{u}}(\mathbf{k}_2, \omega_2) \right\}$$

where $\mathbf{W}(\mathbf{r}, t)$ and $W(t)$ are top-hat windows delimiting the finite measurement or simulation domains in the infinite integrals. These windows can also be generalized to describe *flows* that are finite in space and time, however with more complex profiles in time and space in general (and for free shear flows in particular). ‘*F.T.*’ and $\hat{\cdot}$ denote Fourier transform. Note that the choice of Fourier transform as a basis

function for decomposition is in fact an arbitrary choice, but we follow convention and use Fourier transforms although local homogeneity is not assumed.

In a second order nonlinear term, such as the one in the Navier-Stokes equation, $(\mathbf{u} \cdot \nabla)\mathbf{u}$, two waves can interact to generate or interact with a third wave. If we include time, as done in the expression above, temporal frequencies will be added that will broaden the phase match condition.

If Taylor's hypothesis applies, there is no temporal development except for constant advection, \mathbf{u}_0 , of the frozen field. In this case, the temporal frequencies can be directly related to the spatial frequencies (wavenumbers) and the classical phase match condition applies: $[\omega - (\omega_1 + \omega_2)] \Rightarrow [\mathbf{k} - (\mathbf{k}_1 + \mathbf{k}_2)] \cdot \mathbf{u}_0$.

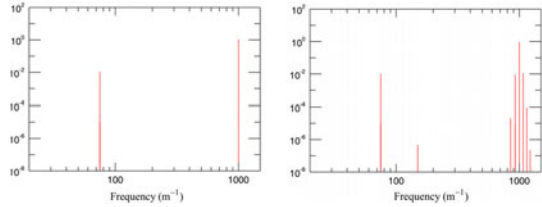
Much more interesting is then the case of high intensity turbulence, where Taylor's hypothesis cannot be invoked. If we consider the total phase match exponent in the integral, we observe that a mismatch in the spatial phase can be compensated by a corresponding mismatch in the temporal phase. Since the integral covers all space and time, at least of the limited flow or measurement domain, the modal interactions can be generated from velocities both prior to and after the point in time where the Navier-Stokes equation is currently operating. These dynamic interactions [25] can, respectively, be denoted 'advanced' and 'delayed'.

This is merely one of the ways in which real measured or simulated velocity fields behave differently from homogeneous Batchelor-turbulence [17]. The finite nature of real flows (as well as that of simulation or measurement domains), here expressed in terms of the windows $\mathbf{W}(\mathbf{r})$ and $W(t)$, impacts the observed interactions as well [25]. This can in fact be immediately observed from the above expression, where the two windows could be defined e.g. as a top-hat. When evaluating the integral, the product of the integrand with the added windows will lead to a convolution between them. The top-hats would transform into sinc-functions with a finite width, as opposed to delta-functions which would be the case for an infinite domain as the velocity field is defined by Batchelor. The broadening of the interaction peaks would allow for interactions to happen not just between strict delta function overlaps, but between peaks of finite width that can overlap to varying degrees. Furthermore, the peaks may in fact interfere either constructively or destructively, depending on the overlap as the sign of the interaction peak may vary with distance from its peak value.

A detailed discussion on these matters can be found in [25] including a discussion on the patterns of interaction efficiency between two waves, the time duration of interactions (what is commonly referred to as 'coherent structures') and the dynamic spectral development of turbulence.

A good spatial overlap between the waves (i.e. with constructive interference) will lead to higher interaction efficiency, which explains why local interactions are often favored. However, as we all know, there exist many so-called non-equilibrium flows in which non-local interactions can be quite efficient as well. These are typically flows where large and small scales are allowed to interact over a long period of time. Then even flows where the waves do not overlap efficiently spatially can exchange significant amounts of energy in non-local interactions. This can happen e.g. in thin shear layers or near large vortices, although fractal turbulence may be one of the most illustrative examples.

Fig. 2 Non-local interactions resulting from the Navier-Stokes equation. (left) Input signal and (right) result after several iterations through the Navier-Stokes equation



In fractal grid turbulence, waves of certain wavelengths are injected by shedding from grid bars of variable thickness into an approximately constant advection velocity. The injected waves are travelling at the same speed and traveling in the same direction along the stream. This type of turbulence is known for developing rapidly, which is very much enhanced by the extended temporal overlap between waves of different wavelengths. Depending on the spatial overlap of the introduced components, some grids are more efficient in interactions and therefore develop faster than other grid configurations.

We will briefly illustrate these ideas with a very simple simulation tool, which we have dubbed the ‘NS-machine’ [26]. It is basically a one-cell Direct Numerical Simulation tool, with which we have been able to predict the downstream development even of high intensity turbulent flows. The simulations have been validated by several experiments [27]. The only input into these simulations is the Navier-Stokes Equation. While the main drawback with simulating at a single point is that it does not explicitly include and treat the pressure term (although it can be included using pressure models), the results are still quite convincing in comparison with several experimental data sets—even in high intensity flows.

Figure 2 shows an example of one low and one high wavenumber component as an input signal (left) to the Navier-Stokes equation that is allowed to interact over time (right). From the example, it is clear that the two components can indeed interact non-locally. The generated components can be understood by simply substituting the sum of two waves into the non-linear term of the Navier-Stokes equation, which can be seen to result in sums, differences and doubling of the input wavenumbers [26].

4 Establishing a New Laboratory and Developing a Theoretical Framework

In previous work [25, 26], we have with quite simple means been able to advance and better understand the dynamics of turbulence interactions, including the implications for real flows under practical experimental conditions. This understanding can be used to describe the underlying processes for how turbulence evolves. The next natural step is to expand to a full-field description, encompassing all four dimensions. Properly capturing the ‘full’ dynamics will, of course, require more advanced tools. Since the statistics has to be extensive to obtain sufficient statistical convergence,

Direct Numerical Simulations is not a viable tool in our investigations. Luckily, technological developments are at a level of maturity that allows us to carry out the measurements with the generous support from the European Research Council (Starting Grant 803419) and the Poul Due Jensen (Grundfos) Foundation.

To be able to target the Universal Equilibrium assumption and the classical view of turbulence, our group is therefore in the process of establishing a cutting edge laboratory at the Technical University of Denmark, the Department of Mechanical Engineering. The laboratory consists of two main setups; one to quantify the degree of non-equilibrium and one to measure and analyze the true underlying processes, to be described in coming work e.g. [28–31]. This will allow us to directly test e.g. the assumptions of locality of interactions and whether it results in universal equilibrium under circumstances that directly challenge these two central assumptions—regardless of the dynamics at the large scales.

In parallel to the establishment of the laboratory, our group is also developing a rigorous theoretical framework that allows us to properly analyze the various scale interactions. This has not been a trivial endeavour, but these developments have finally reached a level of maturity that allows us to analyze measurement results and test the fundamental assumptions.

A key component is including time in the description and to be open to the fact that turbulent cascade processes may exhibit dynamic behavior. Including realistic experimental or numerical conditions, such as finite resolution and flow domain sizes in both space and time, affect significantly the observed interactions, their efficiency and what components are available to interact [25, 26].

The interested reader can follow our developments on the DTU Turbulence Research Laboratory webpage: <https://www.trl.mek.dtu.dk/>.

Acknowledgements Professor William K. George is acknowledged for many helpful discussions. Financial support from the Poul Due Jensen Foundation (Grundfos Foundation) for this research is gratefully acknowledged.

References

1. A.N. Kolmogorov, The local structure in incompressible viscous fluid for very large Reynolds numbers. *Dok. Akad. Nauk. S. S. S. R.* **30**, 299–303 (1941)
2. A.N. Kolmogorov, Decay of isotropic turbulence in incompressible viscous fluids. *Dok. Akad. Nauk. S. S. S. R.* **31**, 538–541 (1941)
3. A.N. Kolmogorov, Dissipation of energy in the locally isotropic turbulence. *Dok. Akad. Nauk. S. S. S. R.* **32**, 19–21 (1941)
4. M.M. Gibson, Spectra of Turbulence at High Reynolds Number. *Nature* **195**, 1281–1283 (1962)
5. H.L. Grant, R.W. Stewart, A. Moilliet, Turbulence spectra from a tidal channel. *J. Fluid Mech.* **12**, 241–268 (1962)
6. H.S. Ribner, M. Tucker, Structure of turbulence in a contracting stream. *NACA Report 1113* (1953)
7. G.K. Batchelor, I. Proudman, The effect of rapid distortion of a fluid in turbulent motion. *Q. J. Mech. Appl. Math.* **7**(1), 121–152 (1954)

8. G.I. Barenblatt, A.A. Gavrillov, On the theory of self-similar degeneracy of homogeneous isotropic turbulence. *J. Exp. Theor. Phys.* **38**(2), 399 (1974); (Russian original - *ZhETF*, Vol. 65, No. 2, p. 806, February 1974)
9. W.K. George, Reconsidering the local equilibrium hypothesis and implications for 'K41'-based theories of turbulence, in *Proceedings of the 2nd ERCOFTAC SIG 44 Workshop, Turbulent Flows: Fundamentals and Applications* (2013)
10. W.K. George, The decay of homogeneous isotropic turbulence. *Phys. Fluids A: Fluid Dyn.* **4**, 1492 (1992)
11. W.K. George, M.M. Gibson, The self-preservation of homogeneous shear flow turbulence. *Exp. Fluids* **13**, 229–238 (1992)
12. U. Frisch, *Turbulence: The Legacy of A. N. Kolmogorov* (Cambridge University Press, Cambridge, 1995). <https://doi.org/10.1017/CBO9781139170666>
13. A.N. Kolmogorov, A refinement of previous hypotheses concerning the local structure of turbulence in a viscous fluid at high Reynolds number. *J. Fluid Mech.* **13**, 82–85 (1962)
14. R. Livi, A. Vulpiani (eds.), *The Kolmogorov Legacy in Physics* (Springer, Berlin, 2003). <https://doi.org/10.1007/b93809>
15. L. Onsager, The distribution of energy in turbulence. *Phys. Rev.* **68**, 286 (1945)
16. C.F.V. Weizsäcker, Das Spektrum der Turbulenz bei groSSen Reynoldsschen Zahlen. *Zeitschrift für Physik* **124**(7–12), 614–627 (1948)
17. G.K. Batchelor, *Homogeneous Turbulence*, 2nd ed. (Cambridge University Press, Cambridge, UK, 1953)
18. J.O. Hinze, *Turbulence*. McGraw-Hill Series In Mechanical Engineering (1975). ISBN 9780070290372
19. W.K. George, H. Wang, The exponential decay of homogeneous turbulence. *Phys. Fluids* **21**, 025108 (2009). <https://doi.org/10.1063/1.3081557>
20. J.L. Lumley, Some comments on turbulence. *Phys. Fluids* **4**, 201–211 (1992)
21. C.M. Velte, Universal Equilibrium and Beyond - Challenging the Richardson-Kolmogorov Paradigm. Proposal for the European Research Council Starting Grant calls in 2017 and 2018. Starting Grant (StG) UniEqTURB, PE8, ERC-2018-STG (2017–2018)
22. Turbulent Cascades II, EUROMECH-ERCOFTAC Colloquium 589, 5-7 December 2017, École Centrale de Lyon, Écully, France
23. A. Monin, A. Yaglom, *Statistical Fluid Mechanics*, vol. 2 (MIT Press, Cambridge, MA, 1972)
24. W.K. George (2017) A 50-Year Retrospective and the Future, in *Whither Turbulence and Big Data in the 21st Century?* ed. by A. Pollard, L. Castillo, L. Danaila, M. Glauser (2017), pp. 13–43. ISBN 978-3-319-41217-7
25. P. Buchhave, C.M. Velte, Dynamic triad interactions and evolving turbulence spectra. Submitted for review (2019), [arXiv:1906.04756](https://arxiv.org/abs/1906.04756) [physics.flu-dyn]
26. P. Buchhave, C.M. Velte, A 1D Navier-Stokes Machine and its application to turbulence studies. Submitted for review (2020), [arXiv:2002.10184](https://arxiv.org/abs/2002.10184) [physics.flu-dyn]
27. M. Dotti, R.K. Schlander, P. Buchhave, C.M. Velte, Experimental investigation of the turbulent cascade development in time by injection of single large-scale Fourier modes. *Exp. Fluids* **61** (2020). <https://doi.org/10.1007/s00348-020-03041-2>, [arXiv:1908.05613](https://arxiv.org/abs/1908.05613) [physics.flu-dyn]
28. S.L. Ribergård, Y. Zhang, H. Abitan, J.S. Nielsen, N.S. Jensen, C.M. Velte, A novel laboratory pushing the limits for optics-based basic turbulence investigations, in *Proceedings ISPIV* (2021)
29. Y. Zhang, H. Abitan, S.L. Ribergård, C.M. Velte, A novel volumetric velocity measurement method for small seeding tracers in large volumes, in *Proceedings ISPIV* (2021)
30. H. Abitan, Y. Zhang, S.L. Ribergård, J.S. Nielsen, C.M. Velte, Development of an optical set-up for 3D PIV with a large volume, in *Proceedings ISPIV* (2021)
31. S.L. Ribergård, N.S. Jensen, J.S. Nielsen, C.M. Velte, Mounting and support for 2-axis scheinpflug focusing for unity-magnification, high-speed particle velocimetry, in *Proceedings ISPIV* (2021)

Turbulent/Turbulent Entrainment



Krishna S. Kankanwadi and Oliver R. H. Buxton

Abstract The interfacial region between two bodies of turbulent fluid was investigated through simultaneous particle image velocimetry (PIV) and planar laser induced fluorescence (PLIF) experiments in the far wake of a circular cylinder. Interface conditioned plots of enstrophy revealed the existence of a turbulent/turbulent interface (TTI) where the enstrophy adjusts itself between the two regions. An enstrophy jump was present even in the most extreme cases of subjected free-stream turbulence. Further analysis of the TTI through the lens of the enstrophy budget equation highlighted the altered roles of inertia and viscosity in the vicinity of the TTI. Unlike the turbulent/non-turbulent interface (TNTI), the inertial term is largely responsible for enstrophy production in the outer regions of the interface, whilst viscosity plays a much more subdued role. The global effects of free-stream turbulence on entrainment behaviour was investigated through the measurement of the mean entrainment flux. It was shown that an increase in intensity of the free-stream turbulence acted to reduce the mean entrainment flux into the wake. Length scale of the background turbulence on the other hand did not greatly influence entrainment behaviour in the far wake of a circular cylinder.

1 Introduction

The growth of a turbulent body of fluid is strictly governed by the flow physics at the outer boundary of the fluid region. These dynamics control the process of entrainment, which describes the process by which mass is transferred from the surroundings into the body of fluid. Hence, it is instrumental in the growth of a turbulent region of fluid. The understanding of this process is critical, since the industrial and environmental applications that are governed by it, are vast. Examples range from the growth of a turbulent boundary layer to the spreading of wind turbine

K. S. Kankanwadi (✉) · O. R. H. Buxton
Imperial College London, London, UK
e-mail: krishna.kankanwadi12@imperial.ac.uk; ksk112@ic.ac.uk

O. R. H. Buxton
e-mail: o.buxton@imperial.ac.uk

© The Author(s), under exclusive license to Springer Nature Switzerland AG 2021
R. Örlü et al. (eds.), *Progress in Turbulence IX*, Springer Proceedings in Physics 267,
https://doi.org/10.1007/978-3-030-80716-0_2

wakes in a wind farm. As a result of the importance of this process, entrainment from a non-turbulent background has been extensively studied [1, 2]. However, even though most industrial and environmental applications exist in the presence of background turbulence, an understanding of turbulent/turbulent entrainment is lacking. The few studies that have examined it have highlighted the importance of both the background turbulence intensity, TI , as well as the integral length scale, L_{12} , of the background turbulence to be important in influencing the entrainment behaviour [3–5]. This chapter aims to summarise and build up on the work presented in reference [6].

The behaviour of a region of turbulent fluid inside a turbulent environment was investigated using two separate experimental campaigns. These included a planar particle image velocimetry (PIV) experiment as well as a cinematographic stereoscopic PIV experiment. Both of which were accompanied by simultaneous planar laser induced fluorescence (PLIF) experiments that were conducted alongside the PIV measurements. These measurements were conducted in the far wake of a circular cylinder approximately 40 cylinder diameters downstream of the rear face. Conducting simultaneous PLIF experiments that run alongside the PIV experiments is imperative to demarcate the wake fluid from the turbulent background. An illustration of the experimental setup used for both campaigns is depicted in Fig. 1. During the experimental campaign, both, regular square grids as well as fractal square grids were utilised to generate user specified background turbulence conditions. Figure 2 represents the experimental envelope of both campaigns indicating the background turbulence parameters present for each conducted run. It should be noted that run 1a is the control case as it represents a run conducted with no grid being placed upstream of the circular cylinder. All of the runs conducted have been classified into three groups based largely on the intensity of the subjected background turbulence.

2 Turbulent/Turbulent Interface

Simultaneously captured PLIF data was used to identify the location of the wake boundary for each snapshot. The wake boundary was identified by placing a threshold, on the modulus of the gradient of the light intensity ($|\nabla\phi|$). Further details regarding this methodology can be found in reference [6]. Upon establishing the location of the wake boundary, it is possible to extract statistics conditioned on the location of the boundary, within the interface. For the remainder of this chapter, the interface normal coordinate is referred to as γ . Note that $\gamma > 0$ represents the free-stream whereas $\gamma < 0$ lies inside the wake. Interface conditioned statistics presented in the following sections are derived as a spatial average over the length of the field of view as well as being temporally averaged across all collected snapshots. This process is represented by the following symbology, $\langle \rangle_I$.

Figure 3 depicts the behaviour of interface conditioned enstrophy, $\langle \omega^2 \rangle_I$ as a function of the normal distance away from the interface for all conducted runs. Run 1a, which represents the no-grid case reproduces the characteristic enstrophy jump that

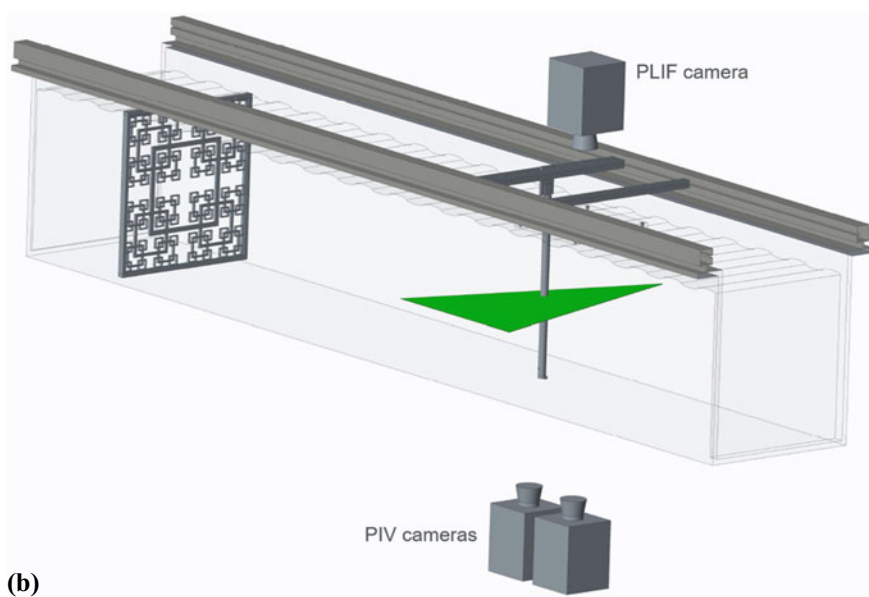
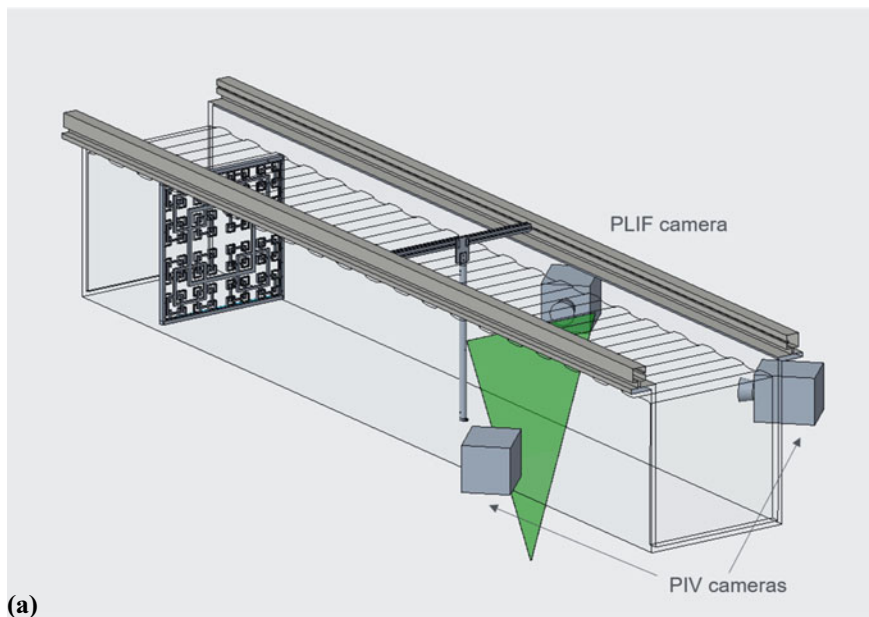


Fig. 1 Illustration of the experimental setup. **a** Campaign 1: Planar PIV and PLIF experiment. **b** Campaign 2: Cinematographic stereoscopic PIV and PLIF experiment

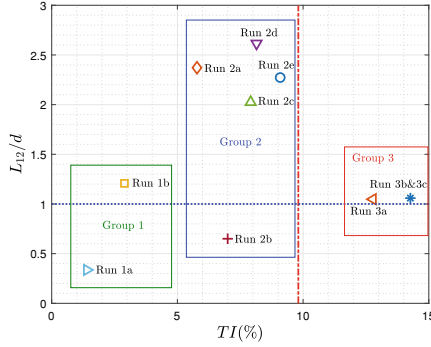
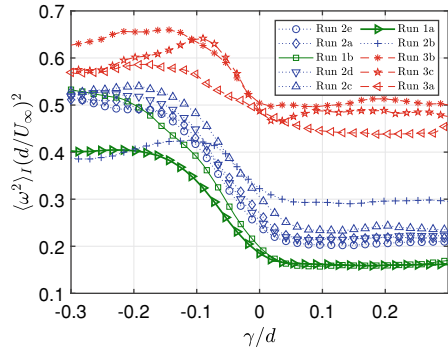


Fig. 2 Experimental envelope highlighting the background turbulence parameters for runs conducted in both experimental campaigns. Note that the red dot-dashed line represents the background turbulence intensity present at the location of the field of view for the no grid case. The blue dotted line indicates a length scale equal to the cylinder diameter [6]. Reproduced with permission

Fig. 3 Interface conditioned jump of enstrophy as a function of normal distance away from the interface [6]. Reproduced with permission



is present in a turbulent non-turbulent interface [7]. Furthermore, it is clear to see that regardless of the level of background turbulence that is available, an enstrophy jump is always observed. This holds true even for cases that lie in group 3 where the intensity of the background turbulence is greater than the intensity found inside the wake itself. This is a crucial result as it goes to show that similar to the turbulent/non-turbulent interface, there exists a turbulent/turbulent interface where the turbulence adjusts itself between the two regions.

In order to investigate the turbulent/turbulent interface in greater detail, the behaviour of each term of the enstrophy budget equation (see (1)) was investigated in the vicinity of the interface. Analysis similar to this is fairly common for the turbulent/non-turbulent interface (TNTI) [8, 9]. The TNTI may be sub-divided into two regions where different flow physics dominate. Van Reeuwijk and Holzner [8] have described the innermost region as the buffer layer, where inertial production of enstrophy dominates ($\omega_i \omega_j s_{ij}$ term). By definition, the free-stream side of the TNTI consists of irrotational fluid, where vorticity is non-existent. Therefore, in the outer-

most part of the interface, also known as the viscous superlayer, the inertial term is unable to produce any enstrophy. Accordingly, the viscous diffusion term, $\nu \frac{\partial(\omega^2/2)}{\partial x_j \partial x_j}$, takes over all responsibility for enstrophy production in the superlayer, since the dissipation term is strictly negative. Rather than being a sink of enstrophy as it is in the rest of the interface, the viscous diffusion term is the only method by which enstrophy may be produced in the outermost region of the interface and thereby is the only process by which enstrophy is imparted to the surrounding fluid.

$$\frac{D}{Dt} \frac{\omega^2}{2} = \omega_i \omega_j s_{ij} + \nu \frac{\partial(\omega^2/2)}{\partial x_j \partial x_j} - \nu \left(\frac{\partial \omega_i}{\partial x_j} \right)^2 \quad (1)$$

However, this restriction on the inertial term is lifted when rotational fluid is available in the background, via free-stream turbulence. The following section now investigates the role of viscosity and strain in enstrophy production in a turbulent/turbulent interface. Figures 4 and 5 depict the interface conditioned behaviour of the inertial and viscous diffusion term. Firstly, it should be noted that the behaviour observed by the no-grid case is identical to literature published on the TNTI [7–9]. The characteristic peak in enstrophy production through the viscous diffusion term at the outer edge of the interface is clearly replicated. Additionally, further into the turbulent core this term quickly turns into a sink of enstrophy, as per the literature. Furthermore, the lack of any enstrophy production through both the inertial and viscous terms on the free-stream side of the interface is also evident. However, this no longer holds true when free-stream turbulence is applied. With the newly available vorticity on the free-stream side of the turbulent/turbulent interface, the inertial term is able to contribute to enstrophy production in the outer regions of the interface. Figure 5 highlights behaviour similar to the no-grid case for the viscous diffusion term in groups 1 and 2, whereas, in the case of group 3 turbulence, this similarity is slightly lost as the level of noise is greatly increased. However, looking at the magnitude of both terms it is possible to say that any contribution of the viscous diffusion term is greatly overshadowed by the inertial term. When background turbulence is available, the inertial term takes over much of the responsibility for enstrophy production in the vicinity of the interface, leading to the conclusion that viscosity plays a negligible role in a turbulent/turbulent interface.

3 Turbulent/Turbulent Entrainment

Upon establishing the physics by which entrainment occurs in a turbulent environment, the effect of background turbulence on entrainment into the wake is examined in this section. A methodology similar to that of Mistry et al. [1] is utilised to calculate the entrainment mass flux for all conducted runs. Temporal averaging over the entire set of snapshots and normalising by the cylinder diameter as well as the free-stream velocity, gives the normalised mean entrainment mass flux as can be seen

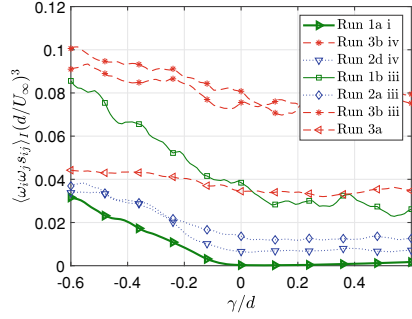


Fig. 4 Interface conditioned plot of the inertial term as a function of normal distance away from the interface

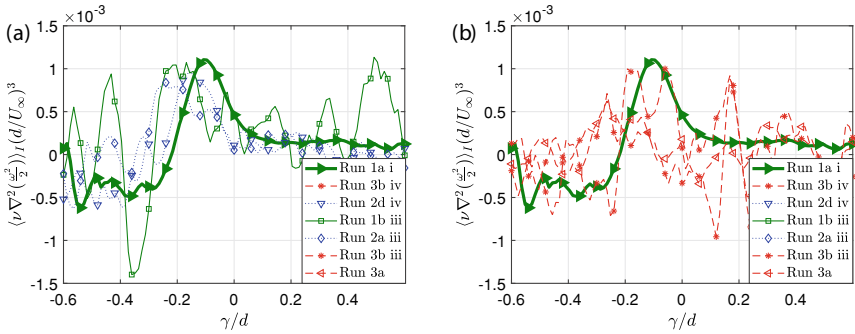


Fig. 5 Interface conditioned plot of the viscous diffusion term for **a** groups 1 and 2 and **b** group 3

in Fig. 6. This figure depicts the behaviour of the mean entrainment mass flux as a function of the subjected background turbulence intensity. It is clear to see that a net reduction in mean flux is observed as the turbulence intensity in the background is increased. Cases in groups 1 and 2 experience a slight reduction in mean entrainment flux whereas group 3 is subjected to a severe reduction. The behaviour in group 3 cases can be so extreme, such that one of the cases even displays net detrainment.

This behaviour can be explained by further analysing each data set. The numerical values displayed alongside each data point in Fig. 6 reflects the skewness value of the data set. Group 2 behaviour may be explained through a slight reduction in skewness values. This is further exaggerated for cases that reside in group 3. Examining the probability density functions of normalised flux (not shown here for brevity) for cases in group 3, makes it clear that the severe reduction in entrainment flux comes as a result of extreme detrainment events [6]. These events create an imbalance as they are not compensated by similar extreme entrainment events. Thereby, tipping the balance towards the detrainment side.

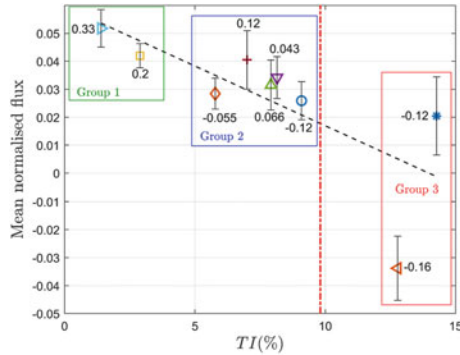


Fig. 6 Entrainment mass flux as a function of background turbulence intensity. Note that the values next to each data-point represent the skewness value of the data set and the error bars represent a 95% confidence interval. The black dashed line denotes a linear regression, whereas, the red dot-dashed line indicates the turbulence intensity found inside the wake at the location of the field of view for the no-grid case [6]. Reproduced with permission

Length scale on the other hand, has a negligible effect on the mean flux (not shown). We thereby establish turbulence intensity as the dominant parameter in influencing entrainment in a turbulent environment.

References

1. D. Mistry, J. Philip, J.R. Dawson, I. Marusic, Entrainment at multi-scales across the turbulent/non-turbulent interface in an axisymmetric jet. *J. Fluid Mech.* **802**, 690–725 (2016)
2. J. Westerweel, C. Fukushima, J.M. Pedersen, J.C.R. Hunt, Momentum and scalar transport at the turbulent/non-turbulent interface of a jet. *J. Fluid Mech.* **631**, 199–230 (2009)
3. S.J. Gaskin, M. McKernan, F. Xue, The effect of background turbulence on jet entrainment: an experimental study of a plane jet in a shallow coflow. *J. Hydraul. Res.* **42**(5), 533–542 (2004)
4. I. Eames, C. Jonsson, P.B. Johnson, The growth of a cylinder wake in turbulent flow. *J. Turbul.* **N39**(12) (2011)
5. C.Y. Ching, H.J.S. Fernando, A. Robles. Breakdown of line plumes in turbulent environments. *J. Geophys. Res.: Oceans* **100**(C3), 4707–4713 (1995)
6. K.S. Kankanwadi, O.R.H. Buxton, Turbulent entrainment into a cylinder wake from a turbulent background. *J. Fluid Mech.* **905**, A35 (2020)
7. C.B. da Silva, J.C.R. Hunt, I. Eames, J. Westerweel, Interfacial Layers between regions of different turbulence intensity. *Annu. Rev. Fluid Mech.* **46**(1), 567–590 (2014)
8. M. Van Reeuwijk, M. Holzner, The turbulence boundary of a temporal jet. *J. Fluid Mech.* **739**, 254–275 (2013)
9. T.S. Silva, M. Zecchetto, C.B. Da Silva, The scaling of the turbulent/non-turbulent interface at high Reynolds numbers. *J. Fluid Mech.* **843**, 156–179 (2018)

Active Control of Turbulent Convective Heat Transfer with Plasma Actuators



Rodrigo Castellanos, Theodoros Michelis, Stefano Discetti, Andrea Ianiro,
and Marios Kotsonis

Abstract We study an array of streamwise-oriented Dielectric Barrier Discharge (DBD) plasma actuators as an active control technique in turbulent flows. The analysis aims at elucidating the mechanism of interaction between the structures induced by the DBD-plasma actuators and the convective heat transfer process in a fully developed turbulent boundary layer. The employed flush-mounted DBD-plasma actuator array generates pairs of counter-rotating, stationary, streamwise vortices. The full three-dimensional, velocity field is measured with stereoscopic PIV and convective heat transfer at the wall is assessed by infrared thermography. The plasma actuator forcing diverts the main flow, yielding a low-momentum region that grows in the streamwise direction. The suction effect promoted on top of the exposed electrodes confines the vortices in the spanwise direction. Eventually, the pair of streamwise vortices locally reduces the convective heat transfer with a persistence of several outer lengthscales downstream of the actuation.

R. Castellanos (✉) · S. Discetti · A. Ianiro
Aerospace Engineering Research Group, Universidad Carlos III de Madrid, 28911 Leganés, Spain
e-mail: rcastell@ing.uc3m.es

S. Discetti
e-mail: sdiscett@ing.uc3m.es

A. Ianiro
e-mail: aianiro@ing.uc3m.es

T. Michelis · M. Kotsonis
Department of Aerodynamics, Delft University of Technology,
2629HS Delft, The Netherlands
e-mail: T.Michelis@tudelft.nl

M. Kotsonis
e-mail: M.Kotsonis@tudelft.nl

1 Introduction

The irruption of computational tools and novel control strategies is opening new research opportunities in the field of turbulent flows and their application to the industrial field. The need for efficient control devices in compact spaces is fostering the development of advanced heat-transfer control strategies. Heat-transfer control applications are found in several fields such as cooling of electronics or film-cooling in turbomachinery [5].

A common solution for convective heat transfer enhancement in turbulent flows consists of using passive vortex generators. Some designs induce pairs of counter-rotating streamwise vortices, whereas others produce co-rotating vortices. The production of near-wall streamwise vortices that persist over a significant downstream distance promotes cross-stream momentum transfer within the boundary layer. This serves to transport high-momentum fluid from the outer region towards the wall which make this kind of devices ideally suitable for heat-transfer or mixing enhancement. Conversely, if the objective is to reduce heat transfer, it is known that a sufficiently powerful, stationary vortex embedded in a turbulent boundary layer and aligned to the streamwise direction, may substantially reduce turbulent wall fluxes according to the persistence theory of turbulence [2].

Even though passive methods do not require neither external power source nor complex devices, there are many applications in which the control is required at very specific or off-design conditions, making active techniques the most suitable option for overall efficiency. This study proposes the usage of Dielectric Barrier Discharge (DBD) plasma actuators to actively control convective heat transfer in turbulent flows. The DBD-plasma actuators are flush, surface-mounted active flow control devices used to promote a body force near the surface. Indeed, past studies have successfully employed DBD-plasma actuators [3, 4] to introduce streamwise vortices in order to control turbulent boundary layers. Wicks et al. [6] investigated the vorticity generation mechanism of a streamwise-oriented array of plasma actuators in an operational manner analogous to vortex generators. The authors conclude that both the wall-normal vorticity introduced by the array as well as the boundary layer vorticity are re-oriented towards the streamwise direction.

By combining the ideas brought forward by persistence theory and the observations of the various investigations mentioned above, the present work aims to generate stationary streamwise vortices within a fully-developed turbulent boundary layer, with the final goal of reducing convective heat transfer downstream of the control location. The boundary layer hereby considered develops on a zero pressure gradient (ZPG) flat plate. A series of streamwise-oriented DBD plasma actuators with opposing actuation directions are utilised to produce the required streamwise vortices on the wall surface (similarly to [6]). The assessment of the effect of the stationary vortices on the surface convective heat transfer process is carried out by means of infrared (IR) thermography over a Joule-heated printed circuit board (PCB). This combination is used as a heat-flux sensor, located downstream with respect to

the plasma-actuator array. Stereoscopic Particle Image Velocimetry (PIV) measurements aim to capture the three-dimensional features of the introduced stationary vortices and the interactions that lead to the observed patterns in the convective heat transfer distribution.

2 Experimental Setup and Methodology

The experimental campaign was carried out in the anechoic vertical wind tunnel (A-Tunnel) at Delft University of Technology. A turbulent boundary layer develops on a smooth aluminum flat plate of 1 m length and 20 mm thickness, spanning the entire width of the squared (50×50 cm) test section. The flat plate is installed between two parallel, side-walls to ensure two-dimensional flow. Two main inserts are flush-mounted into the flat plate, namely the plasma actuator and the heat-flux sensor (see Fig. 1). A movable trailing-edge flap is used to modify the position of the stagnation point. The boundary layer is tripped close to the leading edge with zig-zag turbulators in combination with a strip of silicon carbide grit downstream. The experiments are carried out for a single inflow velocity, $U_\infty = 11.8$ m/s.

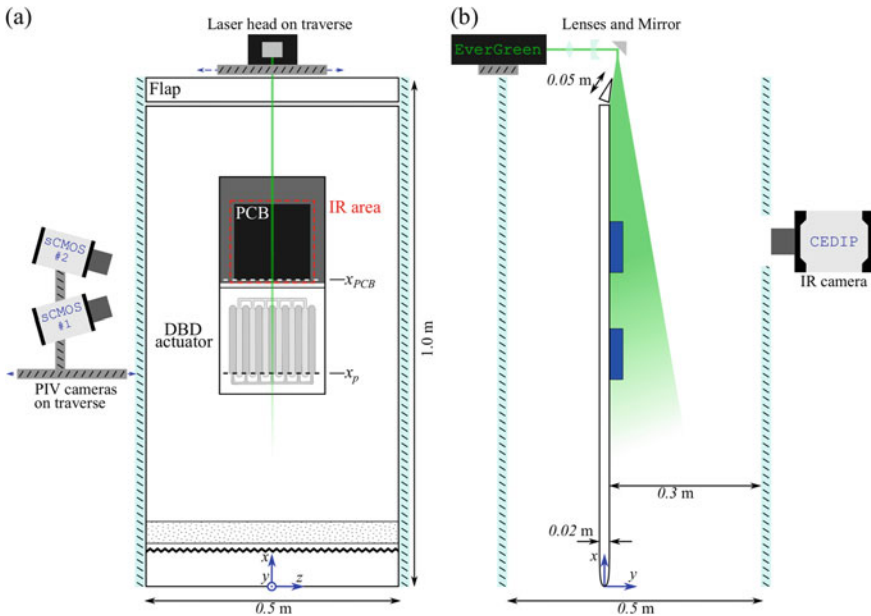


Fig. 1 Schematic of the experimental setup. **a** Front view; the measurement area of infrared thermography is indicated (---). **b** Side view; the field of views of the stereo-PIV measurements are highlighted (■)

The DBD-plasma actuator array is constructed as a repeated pattern of 6 double actuators with a spanwise wavelength $\lambda = 26$ mm and streamwise length $L = 128$ mm. The electrodes are manufactured by silver particle deposition on a polymethacrylate plate of 3 mm thickness. The discharge is initiated by a continuous sinusoidal signal at a frequency of 2 kHz and a peak-to-peak discharge voltage fixed at 20 kV.

Stereo-PIV velocity-field measurements are performed in two regions of interest: the plasma actuator and the heat-flux sensor. Seeding particles are produced using a glycol-water solution with mean droplet diameter of 1 μm . Illumination is provided by a dual cavity Nd:Yag Quantel Evergreen laser (200 mJ/pulse at 10 Hz). Two LaVision Imager sCMOS CLHS cameras equipped with Nikon NIKKOR 60mm focal distance lenses are used. The cameras and the laser head are mounted on an automated traverse system to scan 3D effects in the spanwise direction.

Infrared thermography is used to measure the convective heat flux at the wall. A thermally-thin PCB is used as heated-thin-foil sensor. A constant heat-flux by Joule effect q_j'' is provided to the PCB by a stabilized power supply. The convective heat transfer distribution is expressed in non-dimensional form in terms of Nusselt number ($Nu = h\delta_p/k_{air}$) where k_{air} is the air thermal conductivity, h is the convective heat-transfer coefficient, and δ_p is the boundary layer thickness at the plasma onset x_p . The computation of h is performed through a steady-state energy balance, modeling the PCB as a heated-thin-foil sensor [1]. The temperature measurements are performed with a CEDIP-SC7300 Titanium IR camera (320 \times 256 pixel MCT sensor and Noise Equivalent Temperature Difference (NETD) < 25 mK).

3 Plasma Actuation Effects on Flow Fields and Heat Transfer

The 3D flow field is reconstructed in a region covering two opposing actuators. Figure 2 depicts the average streamwise velocity \bar{U} on the $y - z$ plane at $\hat{x} = \delta_p$, $3\delta_p$, and $5\delta_p$ along with a superimposed vector plot of the corresponding \bar{V} and \bar{W} velocity components (being $\hat{x} = x - x_p$). On the most upstream location of actuation ($\hat{x} = 0$), the fluid ejected laterally by the discharge is replenished by entrainment from above the exposed electrodes. This generates a circulation leading to a vortical motion. At $\hat{x} = \delta_p$, the streamwise vortices are already developed and begin to depart from the wall; their core is located at approximately $y \approx \delta_p/10$. The location of the vortex core is identified by the roll-up in the vector field and by λ_2 isolines. The counter-rotating, streamwise vortices mutually interact at $z/\lambda = 1$ pushing the fluid away from the wall while the suction effect on top of the exposed electrodes sustains the entrainment towards the wall at $z/\lambda = 1/2$ and $3/2$. The vortices are then progressively displaced away from the wall and grow in size, an indication of vortex strength reduction, in agreement with [6]. It must be noted, however, that the pair of counter-rotating, streamwise vortices is confined for several outer scales in the

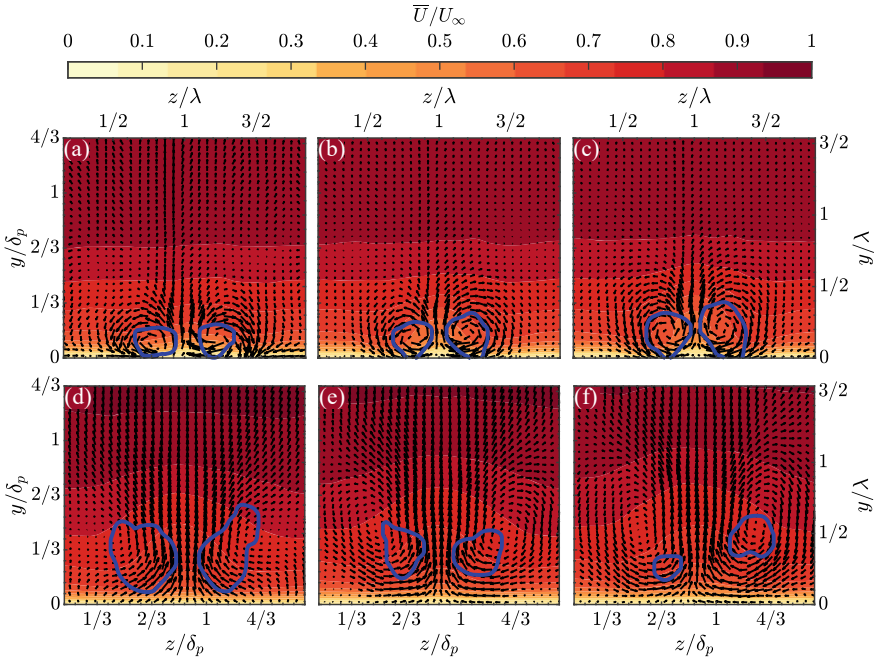


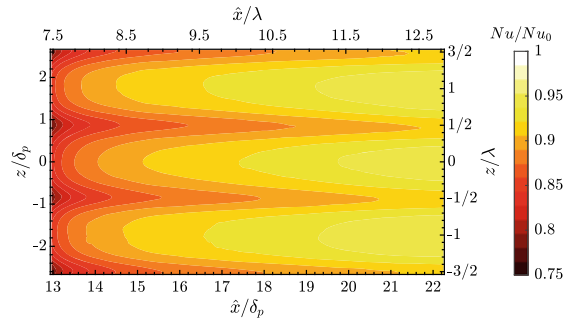
Fig. 2 Evolution of plasma actuation in the $y-z$ plane at $\hat{x} = \delta_p$ (a), $3\delta_p$ (b), $5\delta_p$ (c), $14\delta_p$ (d), $16\delta_p$ (e), $18\delta_p$ (f). The contour depicts the streamwise velocity distribution at each plane. The quiver represents the flow motion based on \bar{V} and \bar{W} velocity components. Negative λ_2 isolines (—) illustrate the locations of vortical flow structures

space between two consecutive, opposing, exposed electrodes, i.e. $1/2 < z/\lambda < 3/2$ according to Fig. 2, suggesting vortex persistence.

Moving further downstream, the effect of the plasma actuation is still persisting (Fig. 2d–f). Note that the upstream edge of the heat-flux sensor is located at x_{PCB} , i.e. $\hat{x} = 13\delta_p$. The induced structures are strong enough to divert the flow, affecting also the outer region of the boundary layer. The pairs of counter-rotating vortices generated upstream by the plasma actuation are less evident due to dissipation. The vortices progressively expand in the spanwise direction and lose strength. Nonetheless, the mutual interaction between the pair of vortices yields a significant wall-normal velocity that clearly persists and which is progressively expanded over a wider area in the spanwise direction. The ejected fluid out of the wall is then replenished by fluid from the outer region of the boundary layer.

The induced action of the vortices has evident effects on the convective heat transfer distribution. The time-averaged Nusselt number map is shown in Fig. 3, computed from IR measurements over a region covering two pairs of opposing plasma actuators to show its uniformity. The results are normalized with the Nusselt number at reference flow conditions Nu_0 (i.e. without plasma forcing). The plasma forcing is composed of two main effects on the heat-transfer distribution: a uniform reduction

Fig. 3 Nu/Nu_0 contour map for plasma actuated flow



over the whole region where the actuator array is deployed, and a localized, predominant decrease at the location where the plasma plumes lift-off to promote out-of-the-wall motion. Eventually, the plasma forcing provides a reduction of 9% in convective heat transfer within the region covered by the heat-flux sensor, far downstream the DBD-plasma actuator.

4 Conclusions

The usage of DBD plasma actuators for heat-transfer control in a well-developed TBL has been studied experimentally. The plasma actuator array was designed to induce pairs of counter-rotating, streamwise vortices. The results from stereo-PIV confirm the formation of such vortices which are locally confined by the suction effect promoted by the plasma discharge along the electrodes. The local confinement prevents the vortices to expand in the spanwise direction, making them stationary and hence persistent along the DBD actuator array. Downstream of the actuation, the vortices reduce their intensity but a strong up-wash motion at the plasma-jet impingement location ($z/\lambda = 1$) persists. At this spanwise location, a wide ribbon of heat-transfer deficit is observed from IR thermography measurements. The local velocity deficit at this location as a consequence of the flow blockage promotes the reduction of Nusselt number even several δ_p downstream the actuation. An average reduction of 9% in Nusselt number is achieved over a wide region of interest confirming the effectiveness of the plasma-induced large scales structures to control heat transfer.

Acknowledgements Rodrigo Castellanos, Stefano Discetti and Andrea Ianiro have been supported by the project ARTURO, ref. PID2019-109717RB-I00/AEI/10.13039/501100011033, funded by the Spanish State Research Agency. Theodoros Michelis and Marios Kotsonis are supported by the European Research Council under StG project GloWing (#803082).

References

1. G.M. Carlomagno, G. Cardone, Infrared thermography for convective heat transfer measurements. *Exp. Fluids* **49**(6), 1187–1218 (2010)
2. A.J. Cotel, R.E. Breidenthal, A model of stratified entrainment using vortex persistence. *Appl. Sci. Res.* **57**(3), 349–366 (1996)
3. M. Kotsonis, Diagnostics for characterisation of plasma actuators. *Meas. Sci. Technol.* **26**(9), 092001 (2015)
4. J.J. Wang, K.S. Choi, L.H. Feng, T.N. Jukes, R.D. Whalley, Recent developments in DBD plasma flow control. *Prog. Aerosp. Sci.* **62**, 52–78 (2013)
5. R.L. Webb, N. Kim, *Enhanced Heat Transfer* (Taylor and Francis, NY, 2005)
6. M. Wicks, F.O. Thomas, T.C. Corke, M. Patel, A.B. Cain, Mechanism of vorticity generation in plasma streamwise vortex generators. *AIAA J.* **53**(11), 3404–3413 (2015)

Mean Parameters of Incompressible Turbulent Boundary Layer with Zero Pressure Gradient on the Wall of the TsAGI T-128 Wind Tunnel at Very High Reynolds Numbers



Anton Gorbushin, Svetlana Osipova, and Vladimir Zametaev

Abstract The mean parameters of an incompressible equilibrium turbulent boundary layer (TBL) with zero pressure gradient (ZPG) were measured on the nozzle flat wall and on the perforated wall of the TsAGI T-128 transonic wind tunnel in the range $Re_\theta = 5.3 \times 10^4 - 3 \times 10^5$ —velocity profiles, skin friction coefficient, and shape factor. Novel data were obtained for TBL ZPG on perforated wall in the range $Re_\theta \approx 8.2 \times 10^4 - 3 \times 10^5$. This study supplements existing TBL ZPG data on the smooth wall at very high Reynolds numbers and enrich them by presenting novel results in the Reynolds number range $Re_\theta = 2.35 \times 10^5 - 2.9 \times 10^5$.

1 Introduction

Lively interest in studies of turbulent boundary layers (TBLs) on smooth surfaces at high Reynolds numbers is driven by two main reasons:

- practical questions from large aircraft and ships designers;
- fundamental interest: what would happen to the TBL at $Re \rightarrow \infty$?

However, the greatest interest has always attracted canonical case— incompressible ZPG TBL. Most of the papers focused on this issue can be divided into the three main groups:

- studies of TBL on the flat plate in wind or water tunnels;
- measurements of TBL on wind tunnel walls;
- atmospheric boundary layers researches.

A. Gorbushin (✉) · S. Osipova · V. Zametaev
Central Aerohydrodynamic Institute (TsAGI), Zhukovskiy, Russia
e-mail: gorbushin@tsagi.ru; gorbushin.ar@mipt.ru

S. Osipova
e-mail: svetlana.l.osipova@tsagi.ru; osipova.sl@mipt.ru

V. Zametaev
e-mail: zametaev.vb@mipt.ru

Moscow Institute of Physics and Technology, Dolgoprudny, Russia

Smits et al. [1] and Marusic et al. [2] came to the conclusion: even though there are a lot of available results on TBL canonical case, it's quite important to continue researches to identify all the time and length characteristic scales. One of the preferred methods is to conduct experiments at facilities, which could provide thick turbulent boundary layers.

Equally interesting is the turbulent boundary layer on perforated walls. Perforated walls are used in the intakes of jet engines and in the test sections of transonic wind tunnels. The parameters of the boundary layer on the perforated wall of the test section of the wind tunnel are used for:

- setting the boundary condition in the problem of the influence of perforated walls of test section on the aerodynamic characteristics of aircraft models;
- estimating the drag of the test section when designing new facilities;
- optimizing the position of moving elements of the test section of existing facilities in order to improve the quality of the flow and minimize the drag of test section [3].

The goal of this study was to supplement existing TBL ZPG data at very high Reynolds numbers and enrich them by presenting novel results in the Reynolds number range $Re_\theta = 2.35 \times 10^5 - 2.9 \times 10^5$ for smooth wall and $Re_\theta \approx 8.2 \times 10^4 - 3 \times 10^5$ for the perforated wall.

2 Experimental Set-Up

The experiments were held in T-128 facility: continuous variable-density closed-circuit transonic wind tunnel with a four-stage compressor and main drive with a power of 100 MW. T-128 is equipped with 4 changeable test sections with unique walls of variable permeability: perforated and slotted. The facility was described more thoroughly in [3, 4].

TBL mean parameters were measured with two rakes of Pitot tubes: first was mounted on a smooth wall at the nozzle outlet (Fig. 1a), second—at the end of the test section #1 upper perforated wall (Fig. 1b). Pressures were measured using small-sized pressure modules.

The research was carried out at low Mach numbers $M = 0.2 - 0.4$ in the range $Re_\theta = 5.6 \times 10^4 - 3 \times 10^5$. Reynolds number of the flow was regulated by setting total pressure values in the range $P_t \approx 100 - 380$ kPa. The streamwise turbulence intensity on the axis of the test section was estimated as 0.20% at $M = 0.2$ and 0.16% at $M = 0.3$ & 0.4 (D.S. Sboev, private communication).

The geometry of nozzle side walls was adapted to minimize longitudinal pressure gradient. It was $dC_p/dx = -0.006 \text{ m}^{-1}$ at $-3\text{m} < x < 0$, which corresponds to the dimensionless local streamwise pressure gradient parameter [5] $K_p = \nu/U_e^2 \times dU_e \nu/dx \approx 7 \times 10^{-10}$. The pressure coefficient across the nozzle at $x = -0.157 \text{ m}$ is in the range from -0.02 to 0.0046 , which corresponds to the upper estimate of the longitudinal velocity nonuniformity $\pm 0.6\%$.



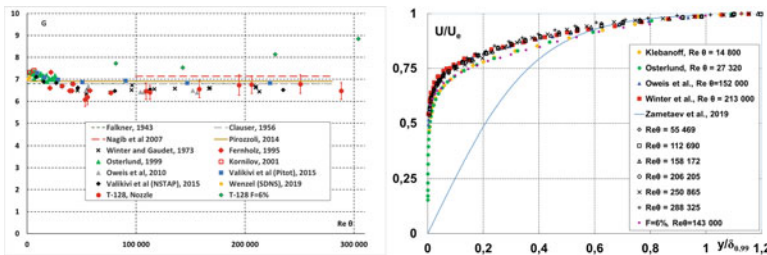
(a) T-128 wind tunnel nozzle and rake installed on its upper wall (b) Rake installed on the perforated upper wall of test section

Fig. 1 Experimental set-up

3 Results

First, the Clauser equilibrium parameter was evaluated to determine whether the boundary layer on the nozzle wall was in equilibrium $G \approx 6.5 - 7$ (Fig. 2a). The coincidence of the experimental data obtained in this study with the results of other researchers (including [6–8]) allows to conclude that the boundary layer at the exit of the T-128 wind tunnel nozzle is in equilibrium. Figure 2a also shows that Clauser’s equilibrium parameter is higher for TBL on the perforated wall ($F = 6\%$) $G \approx 7.5 - 9$.

Comparison of non-dimensional velocity profiles obtained in T-128 with other researchers’ data is displayed on Fig. 2b. For TBL on smooth wall in the nozzle were achieved maximum Reynolds number $Re_\theta = 2.88 \times 10^5$ and the record-high von Kármán number $\delta^+ \sim 1 \times 10^5$. Logarithmic law was maintained up to $y^+ \approx 1.3 \times 10^4$. The results obtained show that even at the very large Re numbers, the outer bound of the logarithmic region $y/\delta \approx 0.15$ is preserved. Collapse of the data in the outer region confirms the self-similarity and equilibrium of the boundary layer.



(a) Clauser equilibrium parameter G as a function of Re_θ (b) Comparison of non-dimensional velocity profiles obtained in T-128 with other researchers’ data

Fig. 2 Results

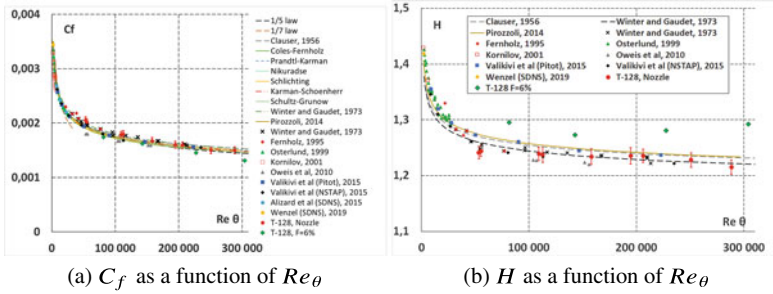


Fig. 3 Results

Stationary streamwise velocity profile $UU_e = e^{-\eta} \int_0^\eta \exp(\eta - e^{-\eta}) d\eta$ [9] agrees well with experimental data beginning with $y/\delta_{0,99} \approx 0.6$. This analytical solution could be a useful complement to the existing wake velocity profile models.

Velocity profile on perforated wall of T-128 test section in its inner region appears to go lower in the comparison with the other researchers’ data and looks similar to Klebanoff [10] and Österlund [11] results on the smooth wall. However in the outer region data obtained on perforated wall tends to agree with the data on smooth wall.

Skin friction coefficient was calculated using the Clauser chart method. Values of constants in the classical logarithmic velocity profile were chosen as recommended by [6]: $k = 0.384$ and $B = 4.17$. The same k and B were used for smooth and perforated wall cases.

For smooth wall agreement of experimental data in the range $Re_\theta = 7 \times 10^4 - 3 \times 10^5$ does not exceed $\Delta c_f = \pm 0.00006 (\pm 3.7\%)$ (Fig. 3a). The empirical and semi-empirical dependencies were described thoroughly in [4].

As for TBL on the perforated wall, local skin friction coefficient on perforated wall is nearly 2 – 10% less than that on the smooth wall when permeability coefficient is $F = 6\%$. The result was predictable, since perforation is an intermediate state between a smooth wall and a mixing layer. A further decrease in the friction coefficient of the turbulent boundary layer on the perforated wall one may expect with an increase of its permeability coefficient.

Data obtained on shape factor as a function of Re_θ is shown in Fig. 3b. For TBL on the smooth wall experimental data agreement at high Reynolds numbers does not exceed $\Delta H = \pm 0.012 (\pm 1\%)$. Experimental results begin noticeably flat at $Re_\theta > 6 \times 10^4$.

As for TBL on perforated wall, its shape factor is higher than that on the smooth wall: $H \approx 1.28 - 1.29$.

4 Conclusions

The results obtained in this study supplement the available data of TBL on smooth wall and present novel data in the range $Re_\theta \approx 2.35 \times 10^5 - 2.9 \times 10^5$ including the data on perforated wall.

The dimensionless velocity profiles obtained in T-128 on smooth wall turned out to be universal in the range $Re_\theta \approx 5.5 \times 10^4 - 2.9 \times 10^5$.

The results of measurements of the boundary layer parameters on the smooth wind tunnel wall presented in this study, as well as those obtained by Winter and Gaudet [12], Fernholz et al. [8], Metzger and Klewicki [13], Castillo et al. [14], and Nickels et al. [15] show good agreement with the data obtained on a flat plate by Klebanoff [10], Österlund [11], Kornilov and Litvinenko [16], Vallikivi et al. [5], Oweis et al. [7]. The test results showed the self-similarity of the velocity profiles in the outer (wake) part of the turbulent boundary layer on smooth and perforated walls at high Reynolds numbers.

An analysis of the experimental results presented in this study confirms the conclusion of [1, 2] that new experimental data including the direct measurement techniques such as floating elements and oil film interferometry are required to refine the asymptotic behaviour of the friction coefficient and the shape factor of the velocity profile parameter as $Re \rightarrow \infty$.

Acknowledgements Experimental investigations were performed at the Central Aerohydrodynamic Institute. Data processing was funded by RFBR, project number 19-38-90296. Analysis of data and preparation of manuscript were carried out with a grant from the Russian Science Foundation (project number 20-11-20006) at MIPT.

References

1. A.J. Smits, B.J. McKeon, I. Marusic, High-Reynolds number wall turbulence. *Annu. Rev. Fluid Mech.* **43**(1), 353–375 (2011). <https://doi.org/10.1146/annurev-fluid-122109-160753>
2. I. Marusic, J. Monty, M. Hultmark, A. Smits, On the logarithmic region in wall turbulence. *J. Fluid Mech.* **716**, R3 (2013). <https://doi.org/10.1017/jfm.2012.511>
3. S.A. Glazkov, A.R. Gorbushin, S.L. Osipova, A.V. Semenov, Interference of test section movable elements on its drag and flow uniformity at transonic speed. In: *AIP Conference Proceedings*, vol. 1770, p. 030008 (2016). <https://doi.org/10.1063/1.4963950>
4. A.R. Gorbushin, S.L. Osipova, V.B. Zametaev, Mean parameters of an incompressible turbulent boundary layer on the wind tunnel wall at very high Reynolds numbers. *Flow Turbul. Combust.* (2020). <https://doi.org/10.1007/s10494-020-00232-z>
5. M. Vallikivi, M. Hultmark, A.J. Smits, Turbulent boundary layer statistics at very high Reynolds number. *J. Fluid Mech.* **779**, 371–389 (2015). <https://doi.org/10.1017/jfm.2015.273>
6. H. Nagib, K. Chauhan, P. Monkewitz, Approach to an asymptotic state for zero pressure gradient turbulent boundary layers. *Philos. Trans. R. Soc. A* **365** (2007). <https://doi.org/10.1098/rsta.2006.1948>
7. G.F. Oweis, E.S. Winkel, J.M. Cutbrith, S.L. Ceccio, M. Perlin, D.R. Dowling, The mean velocity profile of a smooth-flat-plate turbulent boundary layer at high Reynolds number. *J. Fluid Mech.* **665**, 357–381 (2010). <https://doi.org/10.1017/S0022112010003952>

8. H. Fernholz, E. Krause, M. Nockemann, M. Schober, Comparative measurements in the canonical boundary layer at $Re\theta \leq 6 \times 10^4$ on the wall of the DNW. *Phys. Fluids*, **7**, 1275–81 (1995). <https://doi.org/10.1063/1.868516>
9. V. Zametaev, A. Gorbushin, I. Lipatov, Steady secondary flow in a turbulent mixing layer. *Int. J. Heat Mass Transf.* **132**, 655–661 (2019). <https://doi.org/10.1016/j.ijheatmasstransfer.2018.12.012>
10. P.S. Klebanoff, Z.W. Diehl, Some features of artificially thickened fully developed turbulent boundary layers with zero pressure gradient. NACA Report, vol. 1110 (1952)
11. J.M. Österlund, Experimental studies of zero pressure-gradient turbulent boundary-layer flow. Dissertation, Royal Institute of Technology (1999)
12. K.G. Winter, L. Gaudet, *Turbulent Boundary-Layer Studies at High Reynolds Numbers at Mach Numbers between 0.2 and 2.8*. ARC R&M 3712 London, pp. 1–57 Her Majesty's Stationery Office (1973)
13. M.M. Metzger, J.C. Klewicki, A comparative study of near-wall turbulence in high and low Reynolds number boundary layers. *Phys. Fluids* **13**, 692–701 (2001). <https://doi.org/10.1063/1.1344894>
14. L. Castillo, J. Seo, H. Hangan et al., Smooth and rough turbulent boundary layers at high Reynolds number. *Exp. Fluids* **36**, 759 (2004). <https://doi.org/10.1007/s00348-003-0758-y>
15. T.B. Nickels, I. Marusic, S. Hafez, N. Hutchins, M.S. Chong, Some predictions of the attached eddy model for a high Reynolds number boundary layer. *Philos. Trans. R. Soc. A* **365**(1852), 807–822 (2007). <https://doi.org/10.1098/rsta.2006.1950>
16. V.I. Kornilov, Yu.A. Litvinenko, Skin friction measurements in an incompressible turbulent boundary layer. Part 1. Adverse pressure gradient. *Thermophys. Aeromech.* **4**, 475–491 (2001)

Investigation of Self-Similarity of the Temperature Stratified Turbulent Boundary Layer Over the Wavy Surface in Laboratory Conditions



D. A. Sergeev, Yu I. Troitskaya, A. A. Kandaurov, and M. I. Vdovin

Abstract This work is devoted to investigation of the self-similarity behavior of the stably thermostratified air turbulent boundary layer above the wavy surface for a wide range of wind speed and wave state parameters. Experiments were carried out on the TSWiWaT facility with special system of wave damping using underwater plastic net which allowed to adjust the wave parameters independently on the wind speed. It was shown that the profiles of the velocity defect and the temperature defect in the turbulent airflow boundary layer near water surface are self-similar. Besides, for both velocity and temperature the form of self-similarity profiles did not depend on parameters of surface roughness, but only depend on the wind speed.

1 Introduction

One of the central and the most important problem in case of applied tasks of marine hydrometeorology and physical oceanography is investigation of exchange processes (fluxes of momentum, heat and moisture) in atmosphere boundary layer. Field observation of a turbulent airflow over a wavy water surface are connected with many difficulties in measuring characteristics of the wind flow and waves under severe wind condition when steep and breaking waves forming. The good alternative is laboratory modelling of wind-wave interaction at the high-speed wind-wave facilities. In such case, different methods can be applied for measuring fluxes in turbulent boundary layer. In [1] the momentum and heat fluxes were obtained from direct eddy correlation flux measurement and the by hot film (wire). But in the case of strong winds and breaking waves spray of droplets fall on the heated film leading to significant measurement errors. In laboratory experiment [2] at strong winds the surface stress was determined from a momentum budget between selected sections of the tank. In [3] the same idea (measurement of the temperature differences between selected sections) was applied for measuring heat fluxes. However, this is not direct method,

D. A. Sergeev (✉) · Y. I. Troitskaya · A. A. Kandaurov · M. I. Vdovin
Institute of Applied Physics Russian Academy Science, 46 Ul'yanov St., 603950 Nizhny
Novgorod, Russia
e-mail: daniil@ipfran.ru

errors are still significant and the data is contrary to the field observations. In [4] surface drag coefficient was directly obtained by so called profiling method on the base of hypothesis of the self-similarity of the mean airflow velocity profiles in the wind-wave flume. Using Pitot gauges less sensitive for falling droplets than hot films (wires) allowed to obtain mean profiles for high winds. But in those experiments the parameters of the waves in the experiment were determined by the wind forcing. This fact narrowed the area of applicability of the self-similar hypothesis. This work is devoted to the generalization of the theory of self-similarity for the case of temperature profiles for a wide range of conditions (wind speeds and surface waves).

2 The Description of the Experimental Setup

The experiments were carried out at the Thermo stratified Wind-Wave Tank (TSWi-WaT) of IAP RAS. The detailed description of this experimental facility, the principles of creating and controlling the parameters of airflow is given in [4]. The general scheme of the experiments is shown in Fig. 1. The airflow velocity at the axis of the wind tunnel is proportional to the fan frequency rotation F (see Fig. 2) and varied in experiment from 8.8 m/s to 19 m/s, which corresponds to the equivalent wind speed U_{10} on the standard height of 10 meters from 10 m/s to 35 m/s. To perform the temperature stratification of the turbulent boundary layer above the water surface, the air entering the tunnel was heated to 30–40 °C (depending on the airflow speed). The temperature on the water surface in all the experiments was maintained constant of about 15 °C.

A special feature of this experiment was the ability to varying surface waves independently on the wind speed in the flume. For this purpose, the plastic net 0.25 mm thick with a cell of 1.6×1.6 mm has been stretched along the entire channel. The net did not affect the heat exchange, but the characteristics of surface waves varied depending on its depth: the waves were absent when the net was located at the level of the undisturbed surface of the water, but at maximum depth (33 cm) it had practically no effect on the parameters of the surface disturbances for all wind speeds implemented on the facility. The wave parameters in the flume were measured by wire gauges with sampling rate 100 Hz.

The temperature and wind speed at the inlet of the flume were controlled with the additional hot film gauge. Also, the temperature gauge was placed under water in the working section to measure the temperature of the surface layer of water. Velocity and temperature profiles in the working section of the flume (at a distance of 6.5 m from the entrance channel) were measured simultaneously with Pitot gauge and hot film correspondingly, mounted on the vertical scanner. The L -shaped Pitot tube with the differential pressure transducer Baratron MKS 226 A provided the resolution of velocity measurement 3 cm/s. The resolution of temperature measurements was 0.1 °C. The scanning method with the consecutive height increment of 3–5 mm and occurring time of 2 min at each point was used. For each fixed wind speed and net depth two profiles of velocity and temperature were measured for subsequent

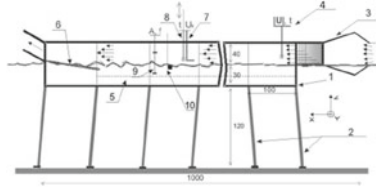


Fig. 1 General scheme of the experiment. (1) wind wave channel body, (2) wind wave bearings, (3) convergent diffusion section with a honeycomb, (4) hot film anemometer at the entrance, (5) a net along the channel installed on the different depths, (6) wave absorber, (7) Pitot tube on a scanning system, (8) hot film anemometer on the same scanning system, (9) wire wave-gauge, (10) a gauge for water temperature measurements. The sizes are in cm

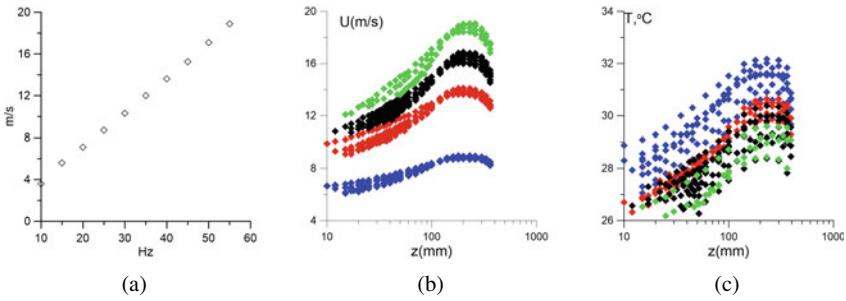


Fig. 2 **a** Axis wind speed via rotation frequency, **b** measured velocity profiles, **c** measured temperature profiles. Fan frequency: blue—20 Hz, red 30 Hz, black 35 Hz, green 40 Hz

averaging. The lower level of scanning was located at a distance of 1 cm from the crests of the waves and depended on the wind speed, while the upper layer was 38 cm (in 2 cm below the upper lid of the wind tunnel). Measured profiles are shown on the Fig. 2.

3 The Self-Similar Behavior of the Velocity and Temperature Defect Profiles

The algorithm suggested in [4], which generalizes the model of the turbulent boundary layer above the flat rigid surface [5], was used to investigate self-similar behavior of the profiles. In this work for the first time the self-similar behavior of the velocity defect profiles in the near-wall turbulent flows was studied, and following expression was proposed:

$$\frac{U_{\max} - U(z)}{u_*} = F\left(\frac{z}{\delta}\right), \tag{1}$$

where U_{\max} is the maximum speed in a turbulent boundary layer, u_* is the wind friction velocity and δ is the boundary layer thickness. According to [5] for non-gradient turbulent boundary layer at a flat rigid plate in the wind tunnel, the following approximation of the self-similar velocity profile:

$$U_{\max} - U(z) = \begin{cases} u_* \left(-\frac{1}{\kappa} \ln(z/\delta) + \alpha \right); & z/\delta < 0.15, \\ \beta u_* (1 - z/\delta)^2; & z/\delta > 0.15, \end{cases} \quad (2)$$

where $\kappa = 0.4$ is the Karman constant.

The constants α and β can be obtained from the best fitting of the experimental data. The results of previous experiments [4] in the wind-wave facility showed that the velocity profile in the airflow above the waved water surface is also self-similar, and the velocity profile can be approximated by the expression (2). Determining the constants α and β included the following data processing. The profiles of air velocity defect measured at a certain frequency of rotation of the fan and set of the net positions controlling waves, were expressed in terms of the self-similar coordinate $y = z/\delta$ and normalized by the scale of velocity βu_* . Obtained dimensionless velocity defect profiles are shown in Fig. 3 for a number of fan rotation frequencies. It can be seen that the experimental points for a fixed speed and set of net positions (different surface waves) collapse on certain curves, confirming the self-similarity of the profile of the flow velocity defect in the flume above the water surface.

With this normalization the logarithmic part of the self-similar profile of the velocity defect has the form:

$$\frac{U_{\max} - U(z)}{\beta u_*} = \frac{1}{\beta} \left(-\frac{1}{\kappa} \ln(y) + \alpha \right). \quad (3)$$

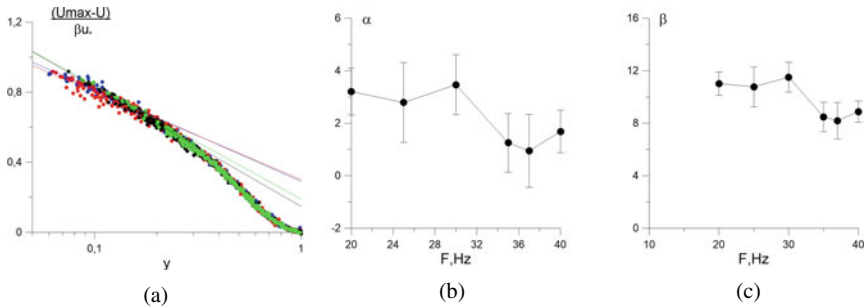


Fig. 3 **a** Dimensionless velocity defect profiles for all wind speeds and net positions, colour of symbols corresponds the same conditions as on Fig. 2, **b** dependence of the constant α on the fan frequency rate, **c**) the same for β

Taking into account (1)–(3), it is easy to determine the constants α and β from the logarithmic best fitting of the experimental points. A certain difference between the fitting curves near the water surface can be seen from Fig. 2.

The dependencies of the constants α and β on the fan speed are shown in Fig. 3. A spread of the constants is statistically significant within the 95% confidence intervals shown on the figure. And we see, that behavior of the α and β with increasing wind speed (fan frequency) is close to each other.

Similar processing was carried out with the temperature profiles. Allows determining the Stanton number and temperature roughness from the temperature profiles in the flume. We used in this case the self-similarity of the profile of the temperature defect, which was defined similarly to the expression (1) for the velocity defect:

$$\frac{T_{\max} - T(z)}{T_*} = G\left(\frac{z}{\delta_T}\right), \quad (4)$$

where

$$T_* = \frac{\langle T'w' \rangle}{u_*}. \quad (5)$$

For the approximation of the self-similar dependence for the profile of the temperature defect the expression similar to (2) was used:

$$T_{\max} - T(z) = \begin{cases} T_* \left(-\frac{1}{\kappa} \text{Pr}_t \ln(z/\delta_T) + \alpha_T \right); & z/\delta_T < 0.15, \\ \beta_T T_* (1 - z/\delta_T)^2; & z/\delta_T > 0.15, \end{cases} \quad (6)$$

For implementation the profiling method for measuring turbulent heat flux in atmosphere boundary layer we need to set the turbulent Prandtl number Pr_t . According to [6] Pr_t was assumed to be 0.85. This value was also obtained by direct numerical simulation of turbulent boundary layer above waved water surface. To determine the constants α_T and β_T data similar processing was carried out as described above for the velocity profile. The profiles of the temperature defect of the airflow were expressed in terms of the self-similar coordinate $y = z/\delta_T$ and normalized by the curvature of the temperature factor $\beta_T T_*$. Obtained dimensionless profiles of the temperature defect are shown in Fig. 4 for various fan rotation frequencies and net positions.

The dependencies of the constants α_T and β_T on the fan frequency rate are shown on Fig. 4, where no statistically significant spread in the constants within 95% confidence intervals, with $\alpha_T = 2.8$, $\beta_T = 9.5$. It differs from the case of a velocity profiles, when the constants showed a significant dependence on wind speed.

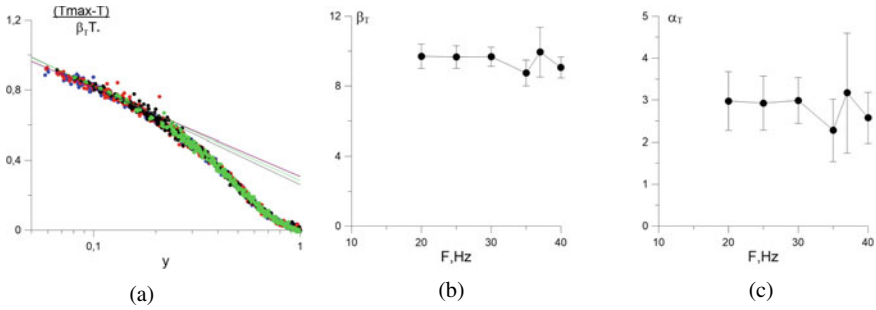


Fig. 4 **a** Dimensionless temperature defect profiles for all wind speeds and net positions, colour of symbols corresponds the same conditions as on Fig. 2, **b** dependence of the constants α_T on the fan frequency rate, **c** the same for β_T

4 Conclusion

A series of experiments to study the self-similarity of the temperature and velocity profiles in a stably stratified temperature turbulent boundary layer over the wavy water surface was carried out at the TSWiWaT IAP RAS. Simultaneous measurements of the airflow velocity and temperature were obtained for a wide range of wind speed and characteristics of the surface waves. It was shown that the profiles of the velocity defect and the temperature defect of the turbulent airflow boundary layer near water surface are self-similar. Besides, for both velocity and temperature the form of self-similarity profiles, i.e. constants α , β , α_T , β_T did not depend on parameters of surface roughness. These constants were obtained from the best fitting of the experimental data. A significant dependence of α , β and the absence of a dependence of α_T , β_T (within 95% confidence intervals) on the wind speed were demonstrated.

Obtained results are useful for further applying method of retrieving parameters of the wind flow including momentum and heat fluxes, drag and heat exchange coefficients.

Acknowledgements This work was supported by the Russian Foundation of Basic Research projects 21-55-52005, 20-05-00322 (carrying out experiments) and in its turn was supported by the Russian Science Foundation project 19-17-00209 (data processing), A. Kandaurov and M. Vdovin are personally grateful to the President grant for young scientists MK-5503.2021.1.5.

References

1. Y.-H.L. Hsu, Turbulent transfers in the atmospheric surface layer under varied stability conditions - a laboratory study. Ph.D. dissertation. University of Delaware (1981)
2. M.A. Donelan, B.K. Haus, N. Reul, W.J. Plant, M. Stiassne, H.C. Graber, O.B. Brown, E.S. Saltzman, On the limiting aerodynamic roughness in very strong winds. *Geophys. Res. Lett.* **31**, L18306 (2005)

3. D. Jeong, B.K. Haus, M.A. Donelan, Enthalpy transfer across the air-water interface in high winds including spray. *J. Atmos. Sci.* **69**(9), 2733–2748 (2012)
4. Y.I. Troitskaya, D.A. Sergeev, A.A. Kandaurov, G.A. Baidakov, M.A. Vdovin, V.I. Kazakov, Laboratory and theoretical modeling of air-sea momentum transfer under severe wind conditions. *J. Geophys. Res.* **117**, C00J21 (2012)
5. J.O. Hinze, *Turbulence: An Introduction to Its Mechanism and Theory* (McGraw-Hill, New York, 1959)
6. O.A. Druzhinin, Y.I. Troitskaya, S.S. Zilitinkevich, Stably stratified airflow over a wavy water surface. Part 1: Stationary turbulence regime. *Q. J. R. Meteorol. Soc.* **142**, 759–772 (2016)

On Similarity of Turbulence Statistics of a Turbulent Planar Jet Taking the Static Pressure into Account



Tatsuya Ito, Takuya Ito, P. Henrik Alfredsson, Antonio Segalini,
and Masaharu Matsubara

Abstract The pressure gradient in a jet is usually regarded as negligibly small when deriving the streamwise velocity profile from the momentum equations. In addition one assumes that the bulk streamwise momentum is conserved in the streamwise direction. On the other hand, it is known that the pressure distribution in the jet is well balanced with the square of the lateral velocity fluctuation, indicating that pressure is not negligible in the lateral momentum equation. The purpose of this study is to determine the importance of the pressure in the jet by evaluating balances in the streamwise and lateral momentum equations from experimental data measured by a static pressure tube and an X-probe. The turbulence fluctuations and the static pressure indicate similarities in their lateral distributions and are well balanced in the streamwise and lateral momentum equations. Although the contribution of the static pressure to the streamwise momentum is small, it is of the same order as that of the turbulent statistics in the lateral momentum equation.

T. Ito · T. Ito · M. Matsubara (✉)

Department of Mechanical Systems Engineering, Shinshu University, Nagano, Japan

e-mail: mmatsu@shinshu-u.ac.jp

T. Ito

e-mail: 18w4801j@shinshu-u.ac.jp

T. Ito

e-mail: 19w4008j@shinshu-u.ac.jp

P. H. Alfredsson · A. Segalini

Department of Engineering Mechanics, KTH Royal Institute of Technology,
Stockholm, Sweden

e-mail: phal@mech.kth.se

A. Segalini

e-mail: segalini@mech.kth.se

1 Introduction

For a planar turbulent jet, Townsend [4] derived similarity solutions for the mean streamwise and lateral velocity distributions by introducing an eddy viscosity. Since then, many experiments have supported Townsend's theory, and the planar turbulent jet, as well as that of a round jet, is considered to be a successful application of the eddy viscosity hypothesis. The fact that a similarity velocity distribution is consistent with experiments indicates not only that the eddy viscosity approximation in the streamwise momentum equation is appropriate, but also that the turbulence statistics also follow the similarity law, which has been experimentally examined and verified. Miller and Comings [3] derived the streamwise and lateral momentum equations for the planar jet and showed that the lateral distribution of the mean pressure is in good agreement with that of the square of the lateral velocity fluctuations. Because of their limited measurement range, the similarity was not fully clarified. Bradbury [1] found similarity of the pressure distributions, suggesting that they are well balanced in the lateral mean momentum equation. The purpose of this study is to determine the importance of the pressure in the jet by studying the balances in the streamwise and lateral momentum equations using experimental data.

2 Experimental Setup

The experimental apparatus was the same as that of Matsubara et al. [2], where a two-dimensional jet issued into a soundproof chamber from a fully developed turbulent channel flow. The channel width is 10 mm, its length is 1000 mm and its spanwise width 300 mm. The coordinate system is defined such that x is the streamwise direction, and y is the position in the lateral flow direction, with the origin at the centre of the channel exit. The time averaged and fluctuation components of the streamwise velocity are U and u , those of the lateral velocity are V and v , and the mean pressure is given as P . The centre velocity U_0 at the outlet is 24 m/s, and the Reynolds number based on U_0 and the duct width d is around 15000.

A hot-wire X-probe was used for the measurements of the streamwise and lateral velocity components. The hot-wire sensors of 1 mm length and 2.5 μm diameter are spaced 1 mm apart with 90° intersection angle. Calibrations for the flow velocity and angle are carried out in a 2–25 m/s velocity range and a $\pm 36^\circ$ angle range.

The mean pressure distribution was measured using a pitot-static pressure tube and a high-precision differential pressure gauge with a ± 100 Pa range. The pitot tube has a diameter of 3 mm and a static pressure measurement hole on the side 18 mm downstream from the tip. The reference static pressure is measured inside the soundproof chamber far away from the jet. The traversing device that moves the pitot tube in the x and y directions is computer controlled and the same computer also samples the signal from the differential pressure gauge.

3 Results

The jet width δ is defined as $\delta = \frac{1}{U_c} \int_0^\infty U dy$ where U_c is the velocity at the jet centre. For the integration, the lateral distributions of U are fitted to a polynomial. The jet width δ and U_c^{-2} from the curve fitting are shown in Fig. 1. For $x > 0.150$ m, both values vary linearly with x . This linearity and the good agreement of the U distribution with a $\text{sech}^2(y/\delta)$ distribution, are consistent with Townsend's theory. The straight lines intercept the x axis at 0.0306 m and 0.0320 m, respectively and the slope, $\beta = d\delta/dx$, is 0.135.

Figure 2 shows the y -distributions of the turbulence statistics scaled with δ and U_c , where, $\eta = y/\delta$. Not only the mean velocity components U and V , but also the turbulence statistics of the velocity fluctuations and the pressure P show similarity for the lateral distributions for $x \geq 0.220$ m. The similarity in the turbulence statistics of the fluctuating velocity indicates that the turbulence statistic equations are in balance with the chosen length and velocity scales. In addition, the similarity is maintained even though the local Reynolds number $Re_{\text{local}} = U_c \delta / \nu$ increases downstream. This suggests that the effect of viscosity on the jet development is negligible. To investigate the balance of turbulence statistics, the Reynolds decomposition is introduced into the two-dimensional Navier-Stokes equations. After averaging for the mean and Reynolds stresses, the following conservative form of the equations is obtained:

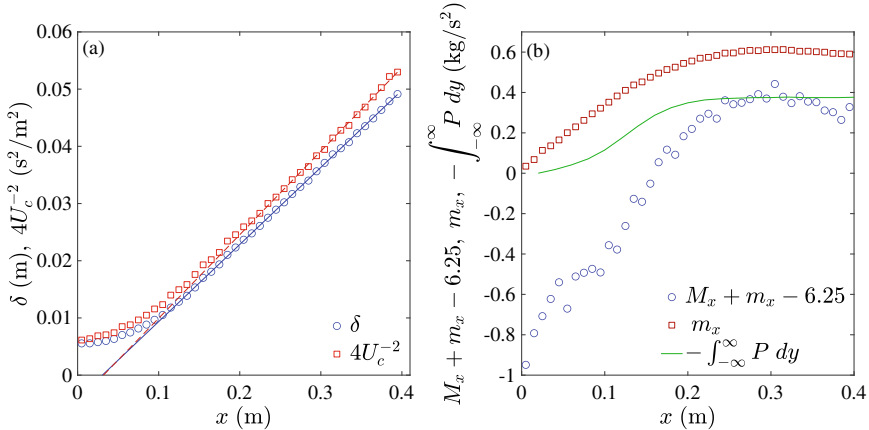


Fig. 1 Streamwise variations of jet properties as function of downstream distance x . **a** Jet width δ and U_c^{-2} , **b** Various contributions to the streamwise momentum equation: the streamwise momentum M_x , the longitudinal Reynolds stress m_x and pressure contributions

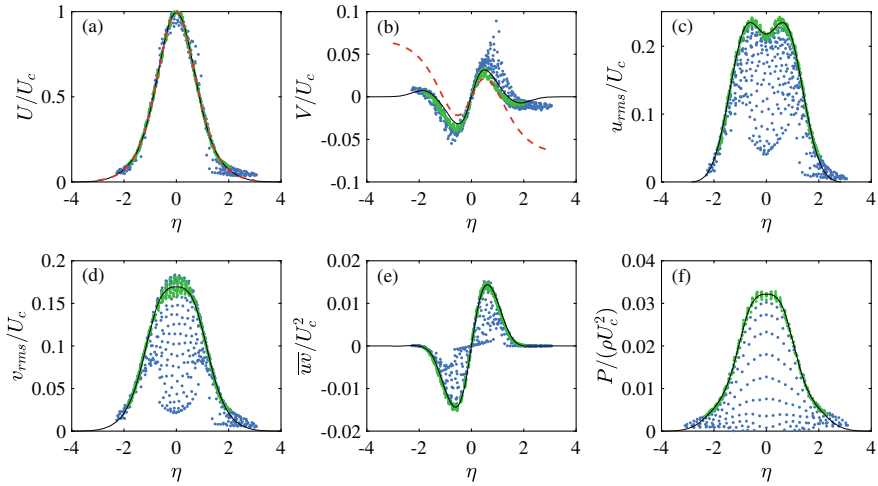


Fig. 2 Lateral distributions of various flow quantities. The blue symbols show data for $x < 220$ mm where similarity has not yet been reached, whereas green symbols are obtained in the similarity region, $x \geq 220$ mm. The dashed lines in (a) and (b) are $\text{sech}^2\eta$ and $\beta(\eta \text{sech}^2\eta - \frac{1}{2} \tanh \eta)$, respectively, whereas the solid black lines are fitted using (5)a, c, d, and f and (6)b, e

$$\frac{\partial U^2}{\partial x} + \frac{\partial UV}{\partial y} = -\frac{1}{\rho} \frac{\partial P}{\partial x} - \frac{\partial \overline{u^2}}{\partial x} - \frac{\partial \overline{uv}}{\partial y} \quad (1)$$

$$\frac{\partial UV}{\partial x} + \frac{\partial V^2}{\partial y} = -\frac{1}{\rho} \frac{\partial P}{\partial y} - \frac{\partial \overline{uv}}{\partial x} - \frac{\partial \overline{v^2}}{\partial y}, \quad (2)$$

where ρ is the density of the fluid and the overline denotes the time average. By integrating (1) and (2) with respect to y from $-\infty$ to y_m , where y_m denotes the measurement y position, the following equations are obtained

$$U(y_m)V(y_m) = -\int_{-\infty}^{y_m} \frac{\partial U^2}{\partial x} dy - \frac{1}{\rho} \int_{-\infty}^{y_m} \frac{\partial P}{\partial x} dy - \int_{-\infty}^{y_m} \frac{\partial \overline{u^2}}{\partial x} dy - \overline{uv}(y_m) \quad (3)$$

$$-\frac{P(y_m)}{\rho} = \int_{-\infty}^{y_m} \frac{\partial UV}{\partial x} dy + V^2(y_m) + \overline{v^2}(y_m) + \int_{-\infty}^{y_m} \frac{\partial \overline{uv}}{\partial x} dy + \text{const.} \quad (4)$$

Miller and Comings [3] derived these equations and attempted a comparison for each term. Since spatial differentiation and integration are required for evaluating each of these terms, the similarity distributions of the dimensionless turbulence statistics are expressed by the following functions with fitted constants σ and a_i ,

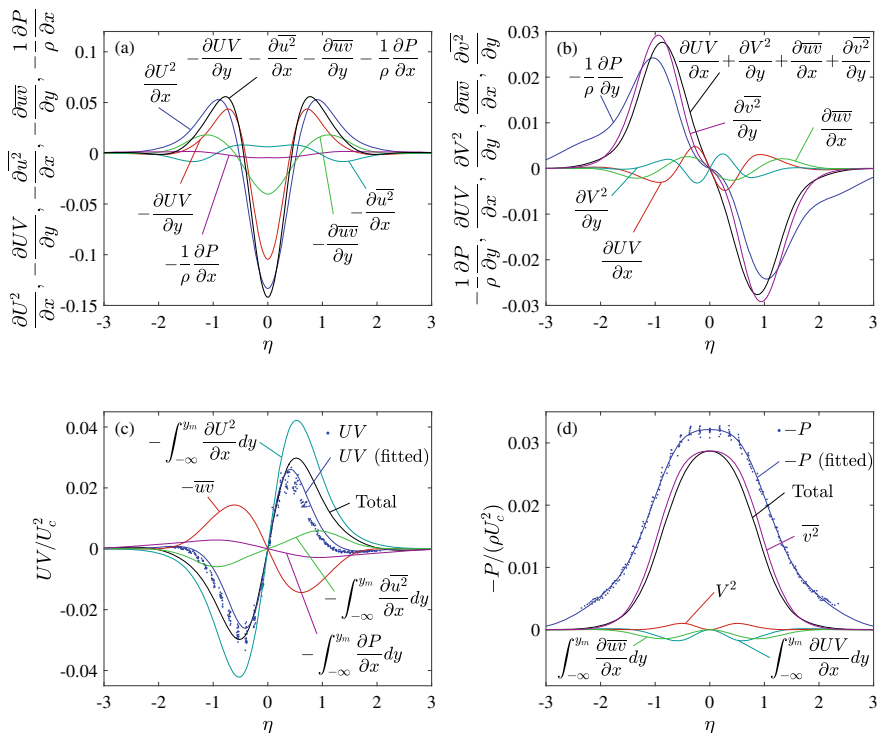


Fig. 3 Comparisons among the terms in 1–4

$$f_s = e^{-\sigma\eta^2} (a_6\eta^6 + a_4\eta^4 + a_2\eta^2 + a_0) \tag{5}$$

$$f_a = e^{-\sigma\eta^2} (a_7\eta^7 + a_5\eta^5 + a_3\eta^3 + a_1\eta), \tag{6}$$

f_s is applied to the symmetric similarity distributions, and f_a is for the antisymmetric similarity distributions. The fitted functions shown as solid lines in Fig. 2 are good approximations to the data within the similarity region.

The distribution of each term in (1)–(4) obtained by numerical differentiation and integration is shown in Fig. 3. As seen in Fig. 3a, the leading term in (1) is $\frac{\partial U^2}{\partial x}$ and it well balances with the total of the other terms. Figure 3b also shows a good balance of the terms in (2) with the leading terms $\frac{1}{\rho} \frac{\partial P}{\partial y}$ and $\frac{\partial \bar{v}^2}{\partial y}$. The other terms of (2) only marginally influence the balance.

Figure 3c shows the terms of (3). The measured UV and the total (all terms) of the right-hand side of (3) are in good agreement around the jet centre, although the peak of the total is slightly shifted outside. This indicates that the conservation law of the streamwise momentum is well kept in the measurement results around the jet centre. The dominant terms are the mean velocity terms and $\bar{u}\bar{v}$, demonstrating that the average velocity distribution is well-predicted even if the terms including

P and $\overline{u^2}$ are ignored as done by Townsend. Although the pressure term is small, it is still about 10% of the total, and is not negligible when considering the balance of turbulence statistics. It is also expected that the pressure affects the streamwise momentum conservation in the jet.

The measured dimensionless static pressure is compared with the total of the right-hand side of (4) in Fig. 3d. The shapes of the distributions are similar though the distribution of P is wider and the value at the centre is slightly higher than the total. The distribution of the total is close to the distribution of v^2 since the other three terms are small and also that the distribution of V^2 is similar but with opposite sign to the other two terms thereby decreasing the overall contribution of these terms.

By substituting ∞ for y_m in (4) and integrating in x , the following conservation equation is obtained

$$\rho \int_{-\infty}^{\infty} U^2 dy + \rho \int_{-\infty}^{\infty} \overline{u^2} dy + \int_{-\infty}^{\infty} P dy = \text{const.} \quad (7)$$

The first term on the left-hand side represents the streamwise momentum, so it is denoted as M_x . The second term, denoted as m_x , is not momentum, but the longitudinal Reynolds stress acting on the cross section perpendicular to the x -axis. The last term is the contribution of pressure to the momentum balance. Figure 1b shows the streamwise changes of these terms. The momentum M_x increases downstream, and reaches a constant for $x > 0.25$ m. Though the magnitude of m_x is about 10% of M_x , its change is about the same order as that of M_x . m_x at first increases downstream, but slightly decreases downstream of $x = 0.30$ m. The pressure integration rapidly changes around $x = 0.12$ m and becomes constant for $x > 0.25$ m. The rapid momentum increase downstream of the duct exit is about three times larger than the pressure decrease, so this increase cannot be explained by the pressure gradient alone. In the similarity region ($x > 0.25$ m) the integration of the pressure is constant because the pressure is proportional to the inverse of x whereas the lateral scale δ is proportional to x these variation cancel each other. However, the favorable pressure gradient before the similarity region contributes to the momentum increase.

4 Summary

The turbulence statistics and the static pressure indicate similarities in their lateral distributions and are well balanced in the streamwise and lateral momentum equations. Although the contribution of the static pressure to the streamwise momentum is small, it is of the same order as the turbulent fluctuations in the lateral momentum equation. It is clear that the static pressure distribution cannot be ignored when considering the balance of the turbulence statistics.

References

1. L.J.S. Bradbury, The structure of a self-preserving turbulent plane jet. *J. Fluid Mech.* **23**, 31–64 (1965)
2. M. Matsubara, P.H. Alfredsson, A. Segalini, Linear modes in a planar turbulent jet. *J. Fluid Mech.* **888**, A26 (2020)
3. D.R. Miller, E.W. Comings, Static pressure distribution in the free turbulent jet. *J. Fluid Mech.* **3**, 1–16 (1957)
4. A.A. Townsend, *The Structure of Turbulent Shear Flow* (Cambridge University Press, Cambridge, 1956)

Mean Velocity Profiles over Streamwise-Aligned Permeable Ridges



Yuki Okazaki, Yumeto Takase, Yusuke Kuwata, and Kazuhiko Suga

Abstract To understand the effects of permeable roughness on logarithmic velocity profiles, discussions of the PIV measurement data of turbulent channel flows over rib-roughened porous media are carried out. By fitting the measured mean velocity profiles to the logarithmic law, parameters: the zero-plane displacement d , the equivalent roughness scale h and the von Kármán constant κ are obtained. It is found that the parameters normalized by the mean pore diameter d/D_p , h/D_p become almost constant regardless of the roughness geometry and the permeability. Moreover the zero-plane displacement has a linear relationship with the roughness scale as $d/h \simeq 2.5$. The von Kármán constant κ for permeable roughness case is smaller than that for impermeable case. The equivalent sand grain roughness height k_s^+ has an almost linear relationship with h^+ as $k_s^+ = 8h^+$. This implies that the von Kármán constant for the present cases is $\kappa \simeq 0.25$. Although it was reported that h^+ for flat porous wall cases correlated to the permeability Reynolds number Re_κ regardless of the wall permeability, that for permeable roughness cases does not show the same tendency.

1 Introduction

Since porous media have large specific surface areas, they are used in many industrial devices such as heat exchangers. In such devices, flows over porous media often become typically turbulent. Hence it is important for engineers to understand the turbulent flows over porous media. Accordingly, many studies [2–5, 7] were performed for turbulent flows over porous media. Those studies reported that turbulence over porous media became stronger as the wall permeability increased. Moreover, the parameters of the logarithmic mean velocity profiles correlated to the wall permeability.

Y. Okazaki (✉) · Y. Takase · Y. Kuwata · K. Suga
Department of Mechanical Engineering, Osaka Prefecture University,
1-1, Gakuen-cho, Naka-ku, Sakai, Osaka, Japan
e-mail: okazaki@htlab.me.osakafu-u.ac.jp

© The Author(s), under exclusive license to Springer Nature Switzerland AG 2021
R. Örlü et al. (eds.), *Progress in Turbulence IX*, Springer Proceedings in Physics 267,
https://doi.org/10.1007/978-3-030-80716-0_7

However, the surface structure of the porous media is not always flat but it is often uneven. For example, the river beds and the vegetation canopies, which are considered as porous media, have surface irregularity. For industrial devices, porous media often have structural roughness for higher performance. In such a situation, turbulent flows are affected by the combined effect of the surface roughness and permeability. Accordingly, such combined effects on turbulence should be discussed.

Raupach et al. [8], Jiménez [9] and Flack and Schultz [10] summarized a number of experimental and numerical investigations for rough wall turbulent boundary layers. By those studies, it is known that the roughness function ΔU^+ , which is the downward shift of the logarithmic velocity profile, have a good correlation to the equivalent sand grain roughness height k_s . Although surface roughness geometry is not limited to two-dimensional, the basic two-dimensional roughness geometries are classified by the ratio of the roughness intervals w to roughness height k into two types: d-type roughness for $w/k < 3 - 4$ and k-type roughness for $w/k > 3 - 4$. These two types of roughness show different tendency of the roughness function.

Although many studies focused on the effects of roughness and permeability on turbulence separately, combined effects of permeability and roughness had never been systematically discussed, to the best of the authors' knowledge. Hence we performed PIV measurements for turbulent flows over porous media with k-type roughness, $w/k = 9$ [1]. It was confirmed that the recirculation behind the rib became weak due to the flow through the rib. Accordingly, turbulence over k-type permeable roughness became weak as the permeability increased. In this study, to further understand the effects of the permeability on d-type rough-walled turbulence, PIV measurements for turbulent channel flows over rib-roughened porous media of $w/k = 1$ are conducted.

2 Experimental Setup

PIV measurements are performed for turbulent channel flows over permeable rough walls. As shown in Fig. 1a, porous media are filled in the bottom half of the flow facility so that the clear channel height is $H = 30\text{mm}$. Since the width of the test section is $300\text{mm}(10H)$, the aspect ratio of the test section is 1:10. Measurements are performed at the symmetry plane of the channel where the two-dimensionality is confirmed in our previous study [3]. Square porous ribs, whose height k is 10% of the channel height H , are mounted on the porous surface with constant spacing $w = k$ as illustrated in Fig. 1b. Three kinds of porous media: #30, #20 and #13 are used in this study. Their porosities are almost the same as $\varphi = 0.8$ but their permeabilities are different $K = 0.004, 0.020$ and 0.033 mm^2 , respectively, for #30, #20 and #13. Their mean pore diameters D_p are about 30%, 60% and 90% of the rib height. The impermeable case (case solid) is also measured for comparison. The measured Reynolds numbers are listed in Table 1.

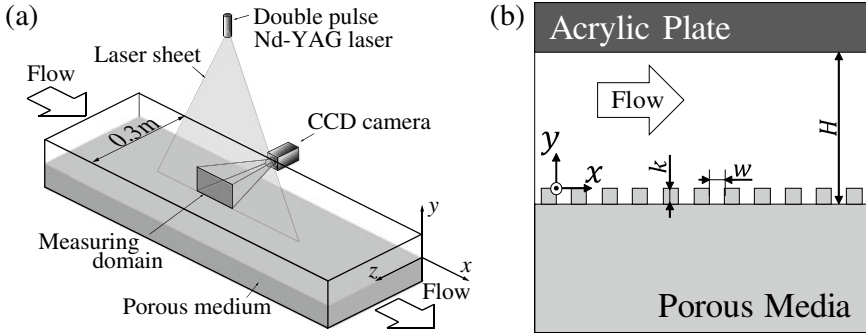


Fig. 1 Flow facility: **a** schematic view of the test section, **b** side view of the test section

Table 1 Turbulence conditions: Re_b , $Re_\tau = \frac{u_\tau \delta}{\nu}$ and Re_K are the bulk Reynolds number, the friction Reynolds number and the permeability Reynolds number; κ , d , h and k_s are the best fitted values of the von Kármán constant, the zero-plane displacement, the roughness scale, the equivalent sand grain roughness, respectively

Case	Re_b	Re_τ	Re_K	k^+	κ	d^+	h^+	k_s^+
Solid	5000	220	0	42	0.38	0	0.64	–
	10200	430	0	79	0.40	0	0.8	–
	15300	620	0	113	0.38	0	1.2	–
	19700	790	0	143	0.40	0	1.05	–
#30	4600	240	1.0	50	0.32	15	2.45	38
	9900	540	2.3	107	0.31	32	6.2	88
	15300	860	3.4	164	0.29	49	13	155
	19000	1080	4.4	208	0.29	62.5	16.2	197
#20	4800	380	3.0	64	0.31	36	13	185
	9900	780	6.0	128	0.31	73	28.5	390
	14900	1170	8.9	189	0.31	107	41	584
	19100	1670	12.3	262	0.31	150	68	969
#13	4900	410	4.0	67	0.27	60	25.8	249
	10000	830	8.0	133	0.26	125	56	524
	15200	1320	12.4	205	0.27	200	90	895
	19600	1780	16.5	272	0.28	260	120	1272

3 Results

Figure 2a shows the mean velocity profiles at $Re_b \simeq 15000$ in a semi-log chart. Here, the superscript ‘+’ denotes a normalized value based on the friction velocity u_τ at the rib-top position. As described in Breugem et al. [7] and Suga et al. [2], the logarithmic velocity profiles are fitted to the log-law form of Best [6]:

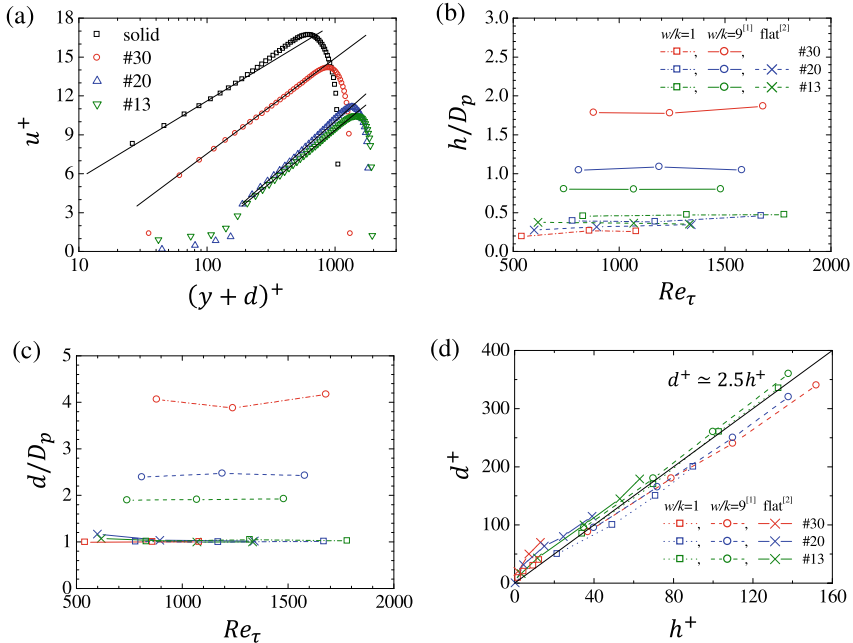


Fig. 2 Logarithmic velocity profiles and log-law parameters: **a** mean velocity profiles with fitting lines of (1), **b**, **c** equivalent roughness height and zero-plane displacement against the bulk Reynolds number with flat porous wall cases [2, 4] and permeable roughness cases of $w/k = 9$ [1], respectively, **d** correlation between the zero-plane displacement and the equivalent roughness scale

$$u^+ = \frac{1}{\kappa} \ln \frac{y+d}{h}, \quad (1)$$

where the parameters κ , d , h are the von Kármán constant, the zero-plane displacement from the rib-top and the roughness scale, respectively. It is observed that the logarithmic distributions shift downward as the permeability increases and the downward shift almost saturates at case #20. In addition, the logarithmic slopes of permeable roughness cases are steeper than that of the impermeable case. This corresponds to that κ becomes smaller for the permeable cases although the $\kappa \approx 0.4$ for the impermeable case. The same tendency was confirmed in the results for flat porous walled turbulence [2, 4]. Figure 2b, c shows d and h normalized by the mean pore diameter D_p against the bulk Reynolds number. Each parameter is almost constant regardless of Re_τ . The constants: h/D_p and d/D_p for the flat porous wall cases and permeable roughness cases of $w/k = 1$ are almost the same regardless of the wall permeability as $h/D_p \approx 0.35$, $d/D_p \approx 1$. This general tendency suggests that these parameters are independent of the Reynolds number and are determined by the surface geometry. Figure 2d shows the correlation between d^+ and h^+ together with the data of

the k-type ($w/k=9$ [1]) and flat [4] porous surfaces. It is found that similar linear relationships are seen regardless of the roughness geometry. All shown cases collapse to $d^+ \simeq 2.5h^+$.

For the mean velocity over impermeable roughness, the roughness function ΔU^+ , which relates to the pressure loss, correlates with the equivalent sand grain roughness height k_s^+ in the fully rough regime:

$$\Delta U^+ = \kappa^{-1} \ln k_s^+ - 3.5. \tag{2}$$

with ΔU^+ , the log-law form:

$$u^+ = \kappa^{-1} \ln \hat{y}^+ + 5.0 - \Delta U^+ \tag{3}$$

is usually applied for rough-wall turbulence. Here, \hat{y} is the wall normal distance from an appropriate origin. With (2) and (3), $\kappa^{-1} \ln k_s^+ = \kappa^{-1} \ln h^+ - 8.5$. This relationship rewritten as:

$$k_s^+ = h^+ e^{8.5\kappa}. \tag{4}$$

Figure 3 shows k_s^+ for the permeable roughness cases against the equivalent roughness h^+ . The distributions of k_s^+ for permeable roughness cases seem to be almost collapsed to $k_s^+ \simeq 8h^+$ regardless of the roughness geometry and permeability. With (4), this suggests that $\kappa \simeq 0.25$ in the permeable roughness wall turbulence and that k_s^+ can be predicted by h . For the flat porous surfaces [4, 5] discussed that the parameters, d and h had linear relationships to the permeability Reynolds number $Re_K = u_\tau \sqrt{K}/\nu$. The same tendency can be seen for the cases with permeable roughness while the proportional coefficient changes depending on the permeability and the roughness geometry. Although the above findings are very suggestive, further discussions to characterize the roughness scale are required to find a universal law of the mean velocity over permeable rough walls.

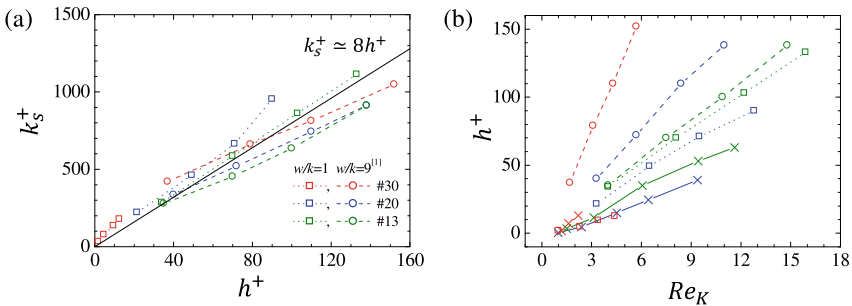


Fig. 3 **a** Correlation of equivalent sand roughness with equivalent roughness scale, **b** equivalent sand roughness against permeability Reynolds number

4 Concluding Remarks

To understand the effects of permeable roughness on logarithmic velocity profiles, PIV measurements of turbulent channel flows over rib-roughened porous media are carried out. The presently measured roughness geometry is the so-called d-type roughness whose rib interval w to the rib height h is $w/k = 1$. After fitting the mean velocity profiles to the logarithmic law, parameters: the zero-plane displacement d , the equivalent roughness scale h and the von Kármán constant κ are obtained. By the discussion of these log-law parameters obtained by the present study and our previous study of k-type roughness: $w/k = 9$, the following remarks are concluded.

(1) The parameters normalized by the mean pore diameters d/D_p , h/D_p become constant regardless of the roughness geometry and the permeability. Moreover d^+ and h^+ have a linear relationship with $d/h \simeq 2.5$.

(2) The equivalent sand grain roughness height and the roughness scale show a linear relation: $k_s^+ = 8h^+$. This leads to the von Kármán constant of $\kappa \simeq 0.25$.

(3) Although h^+ correlates to the permeability Reynolds number Re_κ , the proportional coefficient changes with the permeability and roughness geometry.

Further discussions to characterize the roughness scale are required to find a universal law of the mean velocity over permeable rough walls.

Acknowledgements This study was financially supported by research grants KAKENHI no. 19H02069 and no. 20J14351 of the Japan Society for the Promotion of Science.

References

1. Y. Okazaki, A. Shimizu, Y. Kuwata, K. Suga, Turbulence characteristics over k-type rib roughened porous walls. *Int J Heat Fluid Flow* **82**, 108541 (2020)
2. K. Suga, Y. Matsumura, Y. Ashitaka, M. Kaneda, Effects of wall permeability on turbulence. *Int J Heat Fluid Flow* **31**(6), 974–984 (2010)
3. K. Suga, S. Tominaga, M. Mori, M. Kaneda, Turbulence characteristics in flows over solid and porous square ribs mounted on porous walls. *Flow Turb Combust* **91**, 19–40 (2013)
4. K. Suga, Y. Nakagawa, M. Kaneda, Spanwise turbulence structure over permeable walls. *J Fluid Mech* **822**, 186–201 (2017)
5. C. Manes, D. Poggi, L. Ridol, Turbulent boundary layers over permeable walls: scaling and near-wall structure. *J Fluid Mech* **687**, 141–170 (2011)
6. AC Best (1935) Transfer of heat and momentum in lowes layers of the atmosphere, Tech Rep 65 Geophys Mem, Met Off Lond
7. W.P. Breugem, B.J. Boersma, R.E. Uittenbogaard, The influence of wall permeability on turbulent channel flow. *J Fluid Mech* **562**, 35–72 (2006)
8. M.R. Raupach, R.A. Antonia, S. Rajagopalan, Rough-wall turbulent boundary layers. *Appl Mech Rev* **44**, 1–25 (1991)
9. J. Jiménez, Turbulent flows over rough walls. *Annu Rev Fluid Mech* **36**, 173–196 (2004)
10. K.A. Flack, M.P. Schultz, Review of hydraulic roughness scales in the fully rough regime. *J Fluid Eng* **132**, 041203-1-041203–10 (2010)

Energy Dissipation and Total Entropy Production in SHREK Experiment



Swapnil Kharche, André Fuchs, Michel Bon-Mardion, Jean-Paul Moro, Bernard Rousset, Christophe Baudet, Joachim Peinke, and Alain Girard

Abstract The Superfluid High REynolds von Kármán experiment (SHREK) has been designed to study the fundamental characteristics of turbulence at very high Reynolds number flows using a medium of normal helium (HeI) or superfluid helium (HeII). The velocity fluctuations were measured by the technique of hot-wire anemometry in classical liquid helium at $T = 2.2\text{K}$ and $P = 3\text{bar}$. The dimensionless dissipated power per unit mass estimated from the hot-wire measurements has found to reach an asymptotic value with respect to Reynolds number for each of the configuration of von Kármán flow. The turbulence cascade is one of the non-equilibrium thermodynamic process, which can be expressed by solving the Fokker-Planck equation (FPE) using the experimental hot-wire data. Using the solution of FPE in terms of drift and diffusion coefficient, the total entropy change ΔS_{tot} is estimated from the system entropy change ΔS_{sys} and the medium entropy change ΔS_{med} for each of the turbulence cascade trajectory starting from integral length scale L down to Taylor microscale λ . The validity of the integral fluctuation theorem is proved. Experimentally, the validity of the increase of entropy principle is addressed for the SHREK experimental data with respect to Re_λ up to $O(10^4)$.

1 Introduction

The fundamental understanding of the complexity of turbulence is becoming clearer with the advancement of numerical simulations and the extent of experimental observations. As of today, our laboratory scale turbulence experiments are limited in size which makes it difficult to reach very high Reynolds number flows. The well known turbulence theories such as K41 [1] and K62 [2] are based on the assumption of very

S. Kharche (✉) · M. Bon-Mardion · J.-P. Moro · B. Rousset · A. Girard
CEA IRIG-DSBT, 17 Avenue des Martyrs, 38000 Grenoble, France
e-mail: alain.girard@cea.fr

C. Baudet
University Grenoble Alpes, LEGI, Grenoble, France

A. Fuchs · J. Peinke
Institute of Physics and ForWind, University of Oldenburg, Oldenburg, Germany

© The Author(s), under exclusive license to Springer Nature Switzerland AG 2021
R. Örlü et al. (eds.), *Progress in Turbulence IX*, Springer Proceedings in Physics 267,
https://doi.org/10.1007/978-3-030-80716-0_8

Table 1 Details of the configurations of VK flow: f_1 & f_2 is the frequency of top and bottom propeller/turbine respectively in Hz [For example: for data set D, $-f_1$ is the frequency of top turbine whereas $f_2 = 1.2f_1$ is the frequency of bottom turbine; for data set A and G, $f_1 = f_2$]

Data set	Flow Type	f_1 & f_2	Min Re_λ	Max Re_λ	Max λ (mm)	Min λ (mm)
A	Co-Rotation	$+f_1 + f_2$	720	3690	1.04	0.45
B	Contra	$-0 + f_2$	2340	6180	0.65	0.25
C	Contra	$-f_1 + 3f_1$	3360	7820	0.50	0.35
D	Contra	$-f_1 + 1.2f_1$	3360	9460	0.89	0.41
E	Contra	$-f_1 + 1.5f_1$	1380	9260	1.6	0.40
F	Anti-Contra	$+f_1 - 0$	1390	8450	1.4	0.32
G	Anti-Contra	$+f_1 - f_2$	5510	13600	0.61	0.31

high Reynolds number flows. To address the validity of such theories, it is necessary to study very high Reynolds number turbulent flows on the laboratory scale. For this reason, we have constructed a von Kármán (VK) flow facility which can be operated using liquid helium (HeI) or superfluid (HeII). Very low kinematic viscosity (ν) of helium at low temperature allows to generate very high Reynolds number flows. It has been argued that the dimensionless dissipated power per unit mass reaches a constant value for sufficiently high Reynolds number flows [3, 4]. The first aim of the present work is to address the validity of that statement up to the Reynolds number of $O(10^7)$. In addition, the approach of Fokker-Planck equation (FPE) has been used to describe the turbulence cascade using the SHREK experimental data. Using the estimated drift and diffusion coefficients of the FPE, the change in the total entropy of production is calculated for each of the cascade trajectory [5]. The second aim of this work is to show the dependence of the mean of total entropy change with respect to very high Reynolds number flows. This paper is organized as follows. Firstly, the basis of experimental data sets is explained. Secondly, the results are presented with the discussion. Finally, the conclusions are made based on our experimental findings.

2 Experimental Data Sets

The experimental data used in the present analysis belongs to the **Superfluid High REynolds von Kármán** experiment with a working fluid of classical liquid helium at $T=2.2K$ and $P=3bar$. Detailed explanation of the experimental set-up, its dimensions and its operation are described in B. Rousset et al. [6]. The velocity fluctuations in the VK flow are measured using the well known technique of hot-wire anemometry. A home-made hot-wire made of Platinum-Rhodium Wollaston wire is used. The hot-wire of length $300\mu m$ and diameter $1.27\mu m$ is installed slightly above the equatorial plane in order to avoid the shear layer effects. The experimental data sets are categorized based on the flow configuration as shown in Table 1.

Using this facility, different types of VK flows can be generated such as co-rotation, contra and anti-contra flow configuration. For more details of the experimental data and the convention of rotation of turbines, one is referred to Kharche et al. [7].

3 Results and Discussion

The energy injected in the flow transfers from large to small scales in the inertial range. Eventually, this transferred energy dissipates into heat at the smallest scales within the dissipation range. It follows that in the steady state the injected, transferred and the dissipated power are equal. The energy transfer rate ϵ ($\frac{m^2}{s^3}$ or $\frac{W}{kg}$) is estimated from the third order structure function (S_3) using the relation $\epsilon = -\frac{5}{4} \frac{S_3}{r}$, where $r(m)$ is the spatial scale [7]. This gives $\epsilon = 2.6 W/kg$ for the data set G with $f_1 = f_2 = 0.6Hz$. In the VK flow, the energy is dissipated in the control volume between the top and bottom turbine. The volume of the VK cell in the SHREK experiment contributes to about $V_{He} = 0.31m^3$ which contains around $M_{He} = 47kg$ of liquid helium at $T = 2.2K$ and at an absolute $P = 3$ bar. Assuming homogeneous dissipation rate in the VK cell, $\epsilon = 2.6 W/kg$ corresponds to the dissipated power $P_d=122W$.

In an ideal case, the injected power (P_i) must be equal to the dissipated power in order to maintain the steady temperature inside the VK cell ($T=2.2K \pm 0.1mK$). In the VK cell, $P_i = 2\pi f_1 C_1 + 2\pi f_2 C_2$, where C_1 and C_2 are the measured torques (N-m) on the top and bottom propellers respectively [6]. For the above example of data set G with $f_1 = f_2 = 0.6Hz$ the measured injected power adds up to $P_i = 108W$. This value is close to the estimated dissipated power which shows the consistency of P_i and P_d within the same order of magnitude (for data set G with $f_1 = f_2 = 0.45Hz$, $P_d=44W$ and $P_i = 51W$). P_d and P_i are also found to be in good agreement with the cooling capacity of the refrigerator used in the SHREK facility.

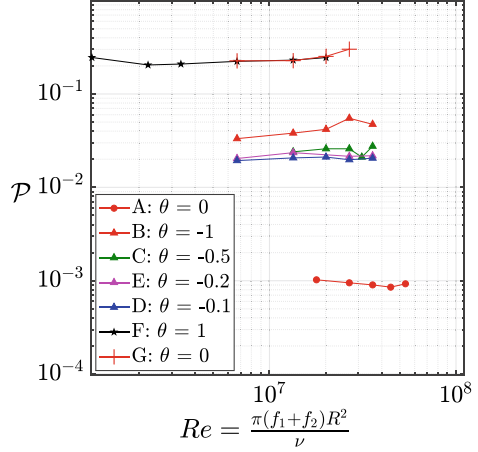
In order to discuss the dimensionless dissipated power per unit mass, following nomenclature is used. R is the radius of the VK cell and H is the height of the turbulent flow region between two turbines. The angular velocity $\Omega = \frac{2\pi(f_1+f_2)}{2}$. The Reynolds number $Re = \frac{\pi(f_1+f_2)R^2}{\nu}$. The rotation number $\theta = \frac{(f_1-f_2)}{(f_1+f_2)}$. And finally, the dimensionless dissipated power per unit mass is then given by, $\mathcal{P} = \frac{\epsilon M_{He}}{\rho R^4 \Omega^3 \pi H}$, where ρ is the density of HeI. Figure 1 shows \mathcal{P} with respect to Re for different VK flow configurations for which θ varies from -1 to 1. From this figure, we can see that \mathcal{P} reaches a fixed asymptotic value based on the flow configuration, which shows that, we have attained a regime where \mathcal{P} is independent of the Re . Based on the relatively higher shear and rotation rate induced by the turbine frequency from $\theta = 0$ to $\theta = \pm 1$, \mathcal{P} increases from the co-rotation to contra and maximum for the anti-contra VK flow configuration as shown in Fig. 1.

To estimate the change in total production of entropy (ΔS_{tot}) during each of the turbulence cascade process the approach of FPE has been used. The FPE for the evolution of velocity increment $u_r = u(x+r) - u(x)$ with respect to scale r in

Fig. 1 Dimensionless dissipated power per unit mass as a function of Re for the data sets A to G. The minimum and maximum Taylor microscale

$$\lambda = \sqrt{\frac{15\nu u_{rms}^2}{\epsilon}} \text{ and}$$

$Re_\lambda = \frac{u_{rms}\lambda}{\nu}$ are also mentioned in Table 1, where u_{rms} is the root mean square velocity of the fluctuating velocity component



terms of the conditional probability density function (CPDF) of u_r is written as [5]

$$-\frac{\partial}{\partial r} p(u_r|u_{r'}) = -\frac{\partial}{\partial u_r} [D^{(1)}(u_r) p(u_r|u_{r'})] + \frac{\partial^2}{\partial u_r^2} [D^{(2)}(u_r) p(u_r|u_{r'})] \quad (1)$$

where $r < r'$ and $p(u_r|u_{r'})$ is the CPDF of u_r conditioned on $u_{r'}$. $D^{(1)}$ is the drift and $D^{(2)}$ is the diffusion coefficient which are estimated for each of the experimental data sets mentioned in Table 1 [8]. For each independent turbulent cascade trajectory from L down to λ , ΔS_{tot} can be calculated using the drift and diffusion coefficients from the Fokker-Planck equation. ΔS_{tot} can be expressed as the sum of the medium entropy change ΔS_{med} and the system entropy change ΔS_{sys} which is estimated using the following relations [9].

$$\Delta S_{tot} = \Delta S_{med} + \Delta S_{sys} \quad (2)$$

$$\Delta S_{med} = \int_L^\lambda \partial_r u_r \frac{D^{(1)}(u_r, r) - \partial_u D^{(2)}(u_r, r)}{D^{(2)}(u_r, r)} dr \quad (3)$$

$$\Delta S_{sys} = -\ln \frac{p(u_\lambda, \lambda)}{p(u_L, L)} \quad (4)$$

where ΔS_{med} takes into account the evolution of the trajectory of velocity increment from scale L down to λ . And ΔS_{sys} allows measurement of the change in entropy based on the initial and final states of the system, $p(u_L, L)$ is the probability of velocity increment u_L on scale L and $p(u_\lambda, \lambda)$ is the probability of velocity increment u_λ on scale λ . The second law of thermodynamics states that $\langle \Delta S_{tot} \rangle \geq 0$, where $\langle \cdot \rangle$ denotes the mean value. Figure 2 shows the PDF of ΔS_{tot} , ΔS_{med} and ΔS_{sys} for data set E. This figure shows the presence of fewer entropy consuming trajec-

Fig. 2 Probability density function of ΔS_{tot} , ΔS_{med} and ΔS_{sys} for the data set E

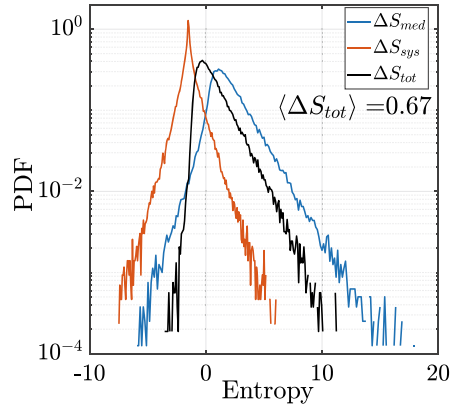
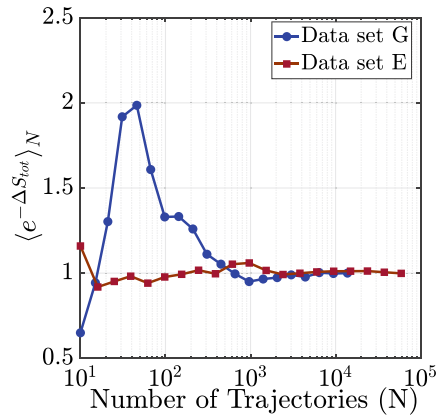


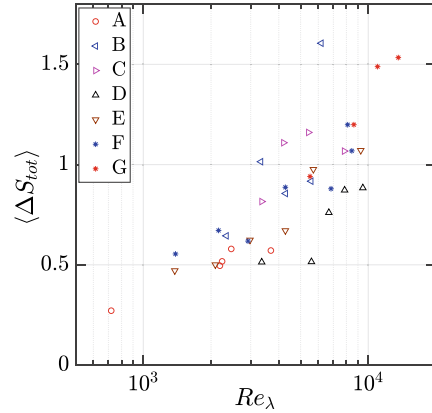
Fig. 3 Evolution of $\langle e^{-\Delta S_{tot}} \rangle_N$ for two different flow configurations with respect to N



ories ($\Delta S_{tot} < 0$) as compared to larger number of entropy producing trajectories ($\Delta S_{tot} > 0$), which results into $\langle \Delta S_{tot} \rangle = 0.67$ satisfying the second law of thermodynamics. The corollary of the second law of non-equilibrium thermodynamics is the integral fluctuation theorem (IFT) expressed by $\langle e^{-\Delta S_{tot}} \rangle = 1$ [10]. Following the FPE analysis, it is found that the IFT is satisfied for the SHREK experimental data quite accurately as shown in Fig. 3. Besides $\langle \Delta S_{tot} \rangle > 0$, a direct consequence of the IFT is the adequate presence of entropy consuming trajectories.

Furthermore, the dependence of $\langle \Delta S_{tot} \rangle$ is addressed with respect to Re_λ for all the data sets as shown in Fig. 4. This figure indicates that the increase in Re_λ lead to the build up of disorderliness, irreversibilities and randomness within the turbulence cascade. It also shows the increase in the degrees of freedom with respect to the increase in Re_λ . Therefore, Fig. 4 experimentally suggests the increase of entropy principle subjected to the increase in Re_λ in a turbulent flow.

Fig. 4 The mean of the change in total entropy of production ($\langle \Delta S_{tot} \rangle$) as a function of Re_λ for the data sets A to G as mentioned in Table 1



4 Conclusion

The local hot-wire measurements were carried out in the SHREK facility at $T = 2.2\text{K}$ in order to study the turbulent flows at Re_λ up to $O(10^4)$. The dimensionless dissipated power per unit mass shows a different but constant asymptotic value with respect to increase in global Re for each of the configurations of the VK flow. The FPE has been solved using the experimental data which led to the estimation of total entropy change of production. It has been found that the IFT is valid for the SHREK experiment with a positive mean total entropy of production satisfying the second law of non-equilibrium thermodynamics. Experimentally, the increase of entropy principle has been investigated for the VK turbulent flows, which indicates the increase in disorderliness, irreversibilities and randomness which are linked to the increase in number of degrees of freedom within the turbulence energy cascade with respect to increasing Re_λ .

Acknowledgements We acknowledge the support of the EUHIT program funded in the FP7 program, (Grant Agreement No. 312778). This work could be performed through the program Chair of Excellence of Laboratoire d'Alliances Nanosciences-Energies du Futur (LANEF, ANR funded contract ANR-10-LABX-51-01) and the project of Ecouturb funded by the ANR (contract: ANR-16-CE30-0016).

References

1. A.N. Kolmogoro (1941) Dokl. Akad. Nauk SSSR, vol. 32, pp. 16–18
2. A.N. Kolmogorov, J Fluid Mech **13**(1), 82–85 (1962)
3. D. Kuzzay, D. Faranda, B. Dubrulle, Physics of Fluids **27**(7), 075105 (2015)
4. B. Saint-Michel et al., Physics of Fluids **26**(12), 125109 (2014)
5. Peinke, J., et al. (2019) Annual Review of Condensed Matter Physics, vol. 10, pp. 107–132
6. Rousset, B., et al. (2014) American Institute of Physics, vol. 85, pp. 103908
7. Kharche, S., et al. (2019) iTi 2018, Springer Proceedings in Physics, vol 226

8. Fuchs, A., et al. (2020) https://github.com/andre-fuchs-uni-oldenburg/OPEN_FPE_IPT
9. Reinke, N., Fuchs, A., Nickelsen, D., Peinke, J., (2018) *J Fluid Mech*, vol. 848, pp. 117–153
10. U. Seifert et al., *Phys. Rev. Lett.* **95**(4), 040602 (2005)

Part II

Simulations and Modelling

The Filtering Approach as a Tool for Modeling and Analyzing Turbulence



Massimo Germano, A. Abbà, A. Cimarelli, Andrea Ferrero,
Fernando F. Grinstein, M. Klein, Francesco Larocca, Juan A. Saenz,
and Guglielmo Scovazzi

Abstract The Filtering Approach (FA) is a simple multiscale method of analysis, it extends the statistical formalism to a generic filtering operator and main ingredients are the Generalized Central Moments (GCM) homomorphic to the Statistical Central Moments (SCM). In the past this technique was intensively used to model turbulent flows in the context of the Large Eddy Simulation (LES) and at present is more and more applied to analyze turbulence and extract statistical data from under-resolved databases. In this paper we will briefly summarize the main multiscale characters of the FA, the well known identity relating GCM of the second order at different levels

M. Germano (✉)

Department Civil and Environmental Engineering, Duke University, Durham NC27708, USA
e-mail: mg234@duke.edu

A. Abbà

Politecnico di Milano, 20156 Milano, Italy
e-mail: antonella.abb@polimi.it

A. Cimarelli

Università di Modena e Reggio Emilia, 41125 Modena, Italy
e-mail: andrea.cimarelli@unimore.it

A. Ferrero · F. Larocca

Politecnico di Torino, 10100 Torino, Italy
e-mail: andrea.ferrero@polito.it

F. Larocca

e-mail: francesco.larocca@polito.it

F. F. Grinstein · J. A. Saenz

Los Alamos National Laboratory, Los Alamos, NM 87545, USA
e-mail: fgrinstein@lanl.gov

J. A. Saenz

e-mail: juan.saenz@lanl.gov

M. Klein

Universität der Bundeswehr München, Neubiberg 85577, Germany
e-mail: markus.klein@unibw.de

G. Scovazzi

Duke University, Durham, NC 27708, USA
e-mail: guglielmo.scovazzi@duke.edu

© The Author(s), under exclusive license to Springer Nature Switzerland AG 2021
R. Örlü et al. (eds.), *Progress in Turbulence IX*, Springer Proceedings in Physics 267,
https://doi.org/10.1007/978-3-030-80716-0_9

is discussed in detail, and a new identity relating GCM of the third order at different levels is presented. Finally some recent developments are illustrated. The structure of the subfilter stresses and the decomposition of the Reynolds stresses is examined, hybrid LES modeling procedures are applied and metrics that measure the statistical homogeneity of a turbulent flow are proposed.

1 Introduction

The Navier-Stokes equations, that describe mathematically the motion of a fluid, become chaotic for a sufficiently high Reynolds number characteristic of the particular flow. As such a numerical solution, however much resolved and extended in space and time, is everything and nothing at the same time. As remarked by [1], this trajectory is apparently uncorrelated to the *true* solution of a flowfield if it is allowed to evolve over a long time, and hence is called a pseudo-orbit. Moreover there are profound and unresolved theoretical problems about the *true* solutions of the Navier-Stokes equations, their unicity and so on, see [2] for a detailed exploration of that and the related implications as regards to the numerical simulation of turbulent flows.

Only when we define a statistical operator $\langle \dots \rangle_e$ we can produce averaged quantities $\langle u \rangle_e$, $\langle uv \rangle_e$, \dots , and we can make comparisons. But the translation of theory in practice is not so simple. To carry out something in accordance with our theories or our ideals can be very difficult. If we open a book on turbulence, it starts with a statistical description of a turbulent flow. Usually the objectivity of turbulence relies on theories that consider fluid flow experiments that *can be repeated many times under a specified set of conditions*, as we read in Pope [3], page 34, but practically it is not so easy to have at our disposal an ensemble of realizations, so we have to recur to some surrogate in order to replace it [4]. Moreover a database produced by a numerical code is usually *coarse grained* [5], limited in *resolution* in space and time that we generally indicate with Δ , and in *extent* in time and in the homogeneous directions, that we generally indicate as T and Z respectively. If we have two or more databases of the same turbulent flow, produced by the same code or different codes for different values of resolution Δ and extent T , the basic problem is their *comparison*, in other words the extraction of their *objectivity*. Usually all that is performed face up to the *truth* represented by experimental data or Direct Numerical Simulation (DNS), ideally obtained in the limit $\Delta \rightarrow 0$ and $T \rightarrow \infty$. Long time and long space averages are the usual ingredients of an explicit averaging *statistical* operator, and the values provided by them, $u(\Delta, T)$ have to be compared with the *absolute*, the *true* quantities $u(\Delta \rightarrow 0, T \rightarrow \infty)$. All that is not so simple, and the Filtering Approach provides some help.

The Filtering Approach (FA) is a simple multiscale approach to the analysis of turbulent flows. As usual its origins are deeply rooted in the past, see [6] for some historical notes on that, and a recent important motivation was to understand what the computer was producing in the first numerical simulations of turbulent flows. The Leonard [7] idea of representing the Large Eddy Simulation of a generic turbulent

quantity $a(\mathbf{x}, t)$, computed with a code characterized by a grid length h , with a filtered representation $\langle a \rangle_f$ due to a filtering operator \mathcal{F} characterized by a filtering length $\Delta \approx h$

$$\mathcal{F}[a] \equiv \langle a \rangle_f = \int F(\mathbf{x}, \mathbf{y}; \Delta) a(\mathbf{y}, t) d\mathbf{y} \quad ; \quad \int F(\mathbf{x}, \mathbf{y}; \Delta) d\mathbf{y} = 1 \quad (1)$$

was in our opinion a major step in the turbulence studies. On its wake an operational formulation was proposed based on a hierarchy of filtering operators and on the Generalized Central Moments, (GCM) [8], that extend the Statistical Central Moments (SCM) and the statistical formalism to a generic filtering operator. Fundamentals to the multiscale approach are some simple identities that relate the GCM at different resolution levels, in particular with the statistical one.

In this paper some recent developments are presented. The structure of the sub-filter stress [12] and a new decomposition of the Reynolds stress [14] are examined, a new dynamic modeling procedure is applied to the LES of Shock Driven Turbulent Mixing [20] and indices that measure the statistical homogeneity of a turbulent flow are proposed [23]. Some conclusions are finally provided.

2 Statistical and Generalized Central Moments

Main ingredients of the statistical approach are the Statistical Central Moments associated to the statistical operator \mathcal{E} , defined as

$$\begin{aligned} \tau_e(a, b) &\equiv \langle ab \rangle_e - \langle a \rangle_e \langle b \rangle_e \\ \tau_e(a, b, c) &\equiv \langle abc \rangle_e - \langle a \rangle_e \tau_e(b, c) - \langle b \rangle_e \tau_e(c, a) - \langle c \rangle_e \tau_e(a, b) - \langle a \rangle_e \langle b \rangle_e \langle c \rangle_e \\ \tau_e(a, b, c, d) &\equiv \dots \end{aligned} \quad (2)$$

and it is easy to see that due to the operational rules of the statistical averaging operator, rules that in turbulence are often referred as the Reynolds rules of the mean, $\langle \langle a \rangle_e \rangle_e = \langle a \rangle_e$ and $\langle a \langle b \rangle_e \rangle_e = \langle a \rangle_e \langle b \rangle_e$, we have an equivalent formulation of the SCM given by

$$\tau_e(a, b) = \langle a' b' \rangle_e \quad ; \quad \tau_e(a, b, c) = \langle a' b' c' \rangle_e \quad ; \quad \dots \quad (3)$$

where the brackets indexed e stand for the statistical average $\langle a \rangle_e = \mathcal{E}[a]$ and the apex stands for the statistical fluctuations $a' = a - \langle a \rangle_e$.

In the general case of a linear and constant preserving filtering operator \mathcal{F} the Reynolds rules of the mean are usually not satisfied. We can however associate formally to \mathcal{F} the *Generalized Central Moments*, GCM, algebraically homomorphic to the SCM

$$\begin{aligned}
\tau_f(a, b) &\equiv \langle ab \rangle_f - \langle a \rangle_f \langle b \rangle_f \\
\tau_f(a, b, c) &\equiv \langle abc \rangle_f - \langle a \rangle_f \langle bc \rangle_f - \langle b \rangle_f \langle ca \rangle_f - \langle c \rangle_f \langle ab \rangle_f + 2\langle a \rangle_f \langle b \rangle_f \langle c \rangle_f \\
&\equiv \langle abc \rangle_f - \langle a \rangle_f \tau_f(b, c) - \langle b \rangle_f \tau_f(c, a) - \langle c \rangle_f \tau_f(a, b) - \langle a \rangle_f \langle b \rangle_f \langle c \rangle_f \\
\tau_f(a, b, c, d) &\equiv \dots
\end{aligned} \tag{4}$$

and that is the starting point of the Filtering Approach. The GCM have the same algebraic properties as the SCM, and in a sense they extend the statistical formalism to a generic filtering operator \mathcal{F} . We refer for more detail on that to [6, 8] and we also remark a recent paper where the formal relationships between filtering and averaging are defined using generalized central moments in the more complex case of variable density flows [9].

2.1 Multiscale Identities

Let us now derive some important identities that are the basic ingredients of the Filtering Approach and that characterizes its multiscale nature. Let us consider the GCM associated to the product $\mathcal{P} = \mathcal{GF}$ of two filtering operators. It is easy to derive the following important relations that connect the GCM at different scales of resolution

$$\tau_p(a, b) = \langle \tau_f(a, b) \rangle_g + \tau_g(a_f, b_f) \tag{5}$$

$$\begin{aligned}
\tau_p(a, b, c) &= \langle \tau_f(a, b, c) \rangle_g + \tau_g(a_f, \tau_f(b, c)) + \tau_g(b_f, \tau_f(c, a)) \\
&\quad + \tau_g(c_f, \tau_f(a, b)) + \tau_g(a_f, b_f, c_f)
\end{aligned} \tag{6}$$

where we use the simplified notation $a_f \equiv \langle a \rangle_f$, $b_f \equiv \langle b \rangle_f$, $c_f \equiv \langle c \rangle_f$. We remark that if we also assume that $\mathcal{FG} = \mathcal{GF}$

$$\langle \langle \dots \rangle_g \rangle_f = \langle \langle \dots \rangle_f \rangle_g \tag{7}$$

we can additionally write

$$\begin{aligned}
\tau_{fg}(a, b) &= \langle \tau_g(a, b) \rangle_f + \tau_f(a_g, b_g) \\
&= \langle \tau_f(a, b) \rangle_g + \tau_g(a_f, b_f) = \tau_{gf}(a, b)
\end{aligned} \tag{8}$$

$$\begin{aligned}
\tau_{fg}(a, b, c) &= \langle \tau_g(a, b, c) \rangle_f + \tau_f(a_g, \tau_g(b, c)) + \tau_f(b_g, \tau_g(c, a)) \\
&\quad + \tau_f(c_g, \tau_g(a, b)) + \tau_f(a_g, b_g, c_g) \\
&= \langle \tau_f(a, b, c) \rangle_g + \tau_g(a_f, \tau_f(b, c)) + \tau_g(b_f, \tau_f(c, a)) \\
&\quad + \tau_g(c_f, \tau_f(a, b)) + \tau_g(a_f, b_f, c_f) = \tau_{gf}(a, b, c)
\end{aligned} \tag{9}$$

Moreover when $\mathcal{GF} = \mathcal{G}$ we have more simply

$$\tau_g(a, b) = \langle \tau_f(a, b) \rangle_g + \tau_g(a_f, b_f) \quad (10)$$

$$\begin{aligned} \tau_g(a, b, c) &= \langle \tau_f(a, b, c) \rangle_g + \tau_g(a_f, b_f, c_f) + \tau_g(a_f, \tau_f(b, c)) \\ &+ \tau_g(b_f, \tau_f(c, a)) + \tau_g(c_f, \tau_f(a, b)) \end{aligned} \quad (11)$$

and we remark again that these identities represent very important multiscale properties of the GCM. The first one is well known, it has played an important role in the development of the dynamic modeling approach [10] and we remark here that the flexibility of this approach was recently discussed and demonstrated also in the context of modeling the commutation errors in LES [11]. The second one, the relation (6) connecting GCM of the third order, is new, and it is very important in the case of compressible flows, where $a = \varrho$ represents the density and $b = u_i, c = u_j$ are the velocity components.

3 Recent Contributions

3.1 Structure of the Subfilter Stress

The second order GCM associated to a velocity field $\tau_f(u_i, u_j)$ are better known under the name of *subfilter stresses*. Their intimate structure has been studied [12] based on the following considerations. Due to the additive properties of the GCM we can write

$$\tau_f(u_i, u_j) = [\tau_f(\tilde{u}_i, u_j) + \tau_f(u_i, \tilde{u}_j) + \tau_f(w_i, u_j) + \tau_f(u_i, w_j)] / 2 \quad (12)$$

where

$$u_i = \tilde{u}_i + w_i \quad (13)$$

is a generic additive decomposition of the turbulent velocity field u_i . All that is exact, and a first approximation is

$$\tau_f(u_i, u_j) \approx \frac{\tau_f(\tilde{u}_i, u_j) + \tau_f(u_i, \tilde{u}_j)}{2} \quad (14)$$

that we can formally write in terms of a tensorial eddy viscosity ν_{ki}

$$\tau_f(u_i, u_j) \approx -\nu_{kj} \partial_k \tilde{u}_i - \nu_{ki} \partial_k \tilde{u}_j \quad (15)$$

given explicitly by

$$\nu_{ki} = -\frac{1}{4} \int \int F(\mathbf{x}, \mathbf{y}) F(\mathbf{x}, \mathbf{z}) (y_h - z_h) (u_j(\mathbf{y}) - u_j(\mathbf{z})) dy dz \quad (16)$$

This last relation is due to the fact that we can explicitly write [13]

$$\tau_f(\tilde{u}_i, u_j) = \frac{1}{2} \int \int F(\mathbf{x}, \mathbf{y}) F(\mathbf{x}, \mathbf{z}) (\tilde{u}_i(\mathbf{y}) - \tilde{u}_i(\mathbf{z})) (u_j(\mathbf{y}) - u_j(\mathbf{z})) dy dz \quad (17)$$

and we can approximate at the first order

$$\tilde{u}_i(\mathbf{y}) - \tilde{u}_i(\mathbf{z}) \sim (y_h - z_h) \frac{\partial \tilde{u}_i(\mathbf{x})}{\partial x_h} \quad (18)$$

3.2 Decomposition of the Reynolds Stress

The second order SCM associated to a velocity field $\tau_e(u_i, u_j)$ and to a scalar $\tau_e(u_i, \varphi)$ are better known under the name of *Reynolds stresses* and *Reynolds fluxes*. A fundamental problem in the analysis of turbulence is to extract the Reynolds stresses and the Reynolds fluxes from a database obtained by a numerical simulation or an experimental exploration, and in [14, 15] the previously derived operational relations between SCM and GCM are applied to this particular problem. Let us indicate the Reynolds averaging operator as \mathcal{E} , and the filtered average as \mathcal{F} . Let us first assume that $\mathcal{E}\mathcal{F} = \mathcal{E}$. In terms of SCM and GCM we define the following quantities

$$\begin{aligned} R_{ij} &\equiv \tau_e(u_i, u_j) \\ \tau_{ij} &\equiv \tau_f(u_i, u_j) \\ T_{ij} &\equiv \tau_e(\langle u_i \rangle_f, \langle u_j \rangle_f) \end{aligned} \quad (19)$$

where u_i are the components of the velocity field at a given time and location. We have

$$R_{ij} = \langle \tau_{ij} \rangle_e + T_{ij} \quad (20)$$

Let us now only assume that $\mathcal{E}\mathcal{F} = \mathcal{F}\mathcal{E}$, a much weaker, very general and respected assumption. We define the following additive GCM

$$\vartheta_{ij} \equiv \tau_f(\langle u_i \rangle_e, \langle u_j \rangle_e) \quad (21)$$

and by applying the identity (5) we have

$$\langle R_{ij} \rangle_f + \vartheta_{ij} = \langle \tau_{ij} \rangle_e + T_{ij} \quad (22)$$

This new identity has been recently applied to the study of the decomposition of the Reynolds stress from filtered data [14] when filtering is not applied in homogeneous statistical directions or in time for statistically stationary turbulent fields.

We can extend all that to compressible flows. As in [16, 17] we will not introduce Favre averages. Let us first of all assume that $\mathcal{EF} = \mathcal{E}$, and let us define the following GCM

$$\begin{aligned}
 R_{\rho i} &\equiv \tau_e(\rho, u_i) \ ; \ R_{ij} \equiv \tau_e(u_i, u_j) \\
 R_{\rho ij} &\equiv \tau_e(\rho, u_i, u_j) \\
 \tau_{\rho i} &\equiv \tau_f(\rho, u_i) \ ; \ \tau_{ij} \equiv \tau_f(u_i, u_j) \\
 \tau_{\rho ij} &\equiv \tau_f(\rho, u_i, u_j) \\
 T_{\rho i} &\equiv \tau_e(\langle \rho \rangle_f, \langle u_i \rangle_f) \ ; \ T_{ij} \equiv \tau_e(\langle u_i \rangle_f, \langle u_j \rangle_f) \\
 T_{\rho ij} &\equiv \tau_e(\langle \rho \rangle_f, \langle u_i \rangle_f, \langle u_j \rangle_f)
 \end{aligned} \tag{23}$$

where ρ is the density and u_i are the components of the velocity field at a given time and location. We have

$$R_{\rho i} = \langle \tau_{\rho i} \rangle_e + T_{\rho i} \ ; \ R_{ij} = \langle \tau_{ij} \rangle_e + T_{ij} \tag{24}$$

$$R_{\rho ij} = \langle \tau_{\rho ij} \rangle_e + T_{\rho ij} + \tau_e(\langle \rho \rangle_f, \tau_{ij}) + \tau_e(\langle u_i \rangle_f, \tau_{\rho j}) + \tau_e(\langle u_j \rangle_f, \tau_{\rho i}) \tag{25}$$

We remark finally that this decomposition of the Reynolds stresses for compressible flows is very simple if compared to the usual ones expressed in terms of the statistical or the Favre fluctuations.

3.3 Dynamic Coarse Grained Modeling

Coarse Grained Simulation [5] combines classical large eddy simulations based on explicit sub-grid scale models and implicit LES (ILES) relying on subgrid models provided by physics-capturing numerics. We can apply this method to the Flow Simulation Methodology [18, 19] in a hybrid ILES/RANS approach. All that is motivated by the study of a challenging problem, the turbulent mixing driven by a shock wave [20, 21].

The role here of the Filtering Approach is to suggest dynamic blending procedures based on the following main points. We have remarked that the multiscale identity that connects the turbulent subgrid stress at different levels

$$\tau_{fg}(a, b) = \langle \tau_f(a, b) \rangle_g + \tau_g(a_f, b_f) \tag{26}$$

has played an important role in the development of the dynamic modeling approach [10]. If the test filter \mathcal{G} is the statistical operator \mathcal{E} we could imagine dynamic models [22] constrained by the Reynolds stress. Following Speziale [18] we assume that

$$\tau_{ij}^{LES} \sim f(\Delta/L) \tau_{ij}^{RANS} \quad (27)$$

where f is the so called *contribution function*. Empirically we could write

$$f(\Delta/L) = [1 - \exp(-\beta\Delta^2)]^m \quad (28)$$

where Δ is a grid length and m and β *ad hoc* coefficients, but a dynamic procedure could remove such arbitrariness. We can write

$$\tau_{ij}^{RANS} = \tau_{ij}^{RES} + \langle \tau_{ij}^{LES} \rangle \quad (29)$$

and to exploit this multiscale identity in order to determine dynamically the contribution function f .

3.4 Statistical Homogeneity Indices

Many important benchmark turbulent flows are provided with one or more homogeneous direction. Sustained homogeneous turbulence is provided with homogeneity in time and three space directions, homogeneous decaying turbulence and decaying Taylor Green vortex flow are homogeneous in three directions, plane channel turbulent flow is homogeneous in time and two space directions, turbulent flow past a cylinder is homogeneous in time and the spanwise direction. In all these cases the objective in these chaotic simulations is to extract from the obtained database some statistical quantities, typically the mean values and the Reynolds stresses for the velocity components.

In the case of the turbulent flow past a cylinder we have two homogeneities, the time t and the spanwise spatial direction z , and we can average along one or both of them. Given the turbulent velocity field $u_i(x, y, z, t)$ we will introduce the following space and time *statistical* filtering operators \mathcal{T} and \mathcal{Z}

$$\begin{aligned} \mathcal{Z}\{u_i\} &\equiv \langle u_i \rangle_z \equiv \frac{1}{Z} \int_0^Z u_i(x, y, z', t) dz' \\ \mathcal{T}\{u_i\} &\equiv \langle u_i \rangle_t \equiv \frac{1}{T} \int_0^T u_i(x, y, z, t') dt' \end{aligned} \quad (30)$$

and we define \mathcal{E} as the product of the two, $\mathcal{E} \equiv \mathcal{T}\mathcal{Z}$, where Z and T are the extents of the computational domain in the spanwise direction z and in time t .

Let us first of all examine the differences between space and time averages. Consistently with the filtering approach based on the GCM let us define the following turbulent stresses associated to the filters \mathcal{T} and \mathcal{Z}

$$\begin{aligned}
 \tau_z(u_i, u_j) &\equiv \langle u_i u_j \rangle_z - \langle u_i \rangle_z \langle u_j \rangle_z \\
 \tau_t(u_i, u_j) &\equiv \langle u_i u_j \rangle_t - \langle u_i \rangle_t \langle u_j \rangle_t \\
 \tau_e(u_i, u_j) &\equiv \langle u_i u_j \rangle_{zt} - \langle u_i \rangle_{zt} \langle u_j \rangle_{zt} \\
 \tau_z(\langle u_i \rangle_t, \langle u_j \rangle_t) &\equiv \langle \langle u_i \rangle_t \langle u_j \rangle_t \rangle_z - \langle u_i \rangle_{zt} \langle u_j \rangle_{zt} \\
 \tau_t(\langle u_i \rangle_z, \langle u_j \rangle_z) &\equiv \langle \langle u_i \rangle_z \langle u_j \rangle_z \rangle_t - \langle u_i \rangle_{tz} \langle u_j \rangle_{tz}
 \end{aligned} \tag{31}$$

We note that due to $\mathcal{E} = \mathcal{Z}\mathcal{T} = \mathcal{T}\mathcal{Z}$ we have the two identities

$$\begin{aligned}
 \tau_e(u_i, u_j) &\equiv \tau_z(\langle u_i \rangle_t, \langle u_j \rangle_t) + \langle \tau_t(u_i, u_j) \rangle_z \\
 &\equiv \tau_t(\langle u_i \rangle_z, \langle u_j \rangle_z) + \langle \tau_z(u_i, u_j) \rangle_t
 \end{aligned} \tag{32}$$

and we can define two measures of turbulence resolution, the first related to the time average and the second to the spanwise average, given by

$$M_t(x, y) = \frac{\langle \tau_t(u_i, u_i) \rangle_z}{R_{ii}} \quad ; \quad M_z(x, y) = \frac{\langle \tau_z(u_i, u_i) \rangle_t}{R_{ii}} \tag{33}$$

where $R_{ij} \equiv \tau_e(u_i, u_j)$. We remark that by definition $M = 0$ corresponds to a perfect DNS and $M = 1$ to a perfect RANS. As such $M_t(x, y)$ and $M_z(x, y)$ measure and can be defined as *indices of the statistical homogeneity* in time \mathcal{T} and in the spanwise direction \mathcal{Z} . They are related to the total Reynolds RANS stress produced by the joint average $\mathcal{E} = \mathcal{Z}\mathcal{T} = \mathcal{T}\mathcal{Z}$.

We remark finally that in the general case

$$\mathcal{E} = \mathcal{E}_1 \mathcal{E}_2 = \mathcal{E}_1 \mathcal{E}_2 \mathcal{E}_3 = \dots \tag{34}$$

we can read all that as a multiscale analysis of the variance, where \mathcal{E} is the statistical operator and \mathcal{E}_i are different nested partitions of the probability. In this case the relations

$$\langle u \rangle_e = \langle \langle u \rangle_2 \rangle_1 = \langle \langle \langle u \rangle_3 \rangle_2 \rangle_1 = \dots \tag{35}$$

$$\begin{aligned}
 \tau_e(u, v) &= \tau_1(\langle u \rangle_2, \langle v \rangle_2) + \langle \tau_2(u, v) \rangle_e \\
 &= \tau_1(\langle u \rangle_2, \langle v \rangle_2) + \langle \tau_2(\langle u \rangle_3, \langle v \rangle_3) \rangle_1 + \langle \langle \tau_3(u, v) \rangle_2 \rangle_1 \\
 &= \dots
 \end{aligned} \tag{36}$$

are better known in applied statistics respectively as the Law of Total Expectation and the Law of Total Variance, the *Adam's and Eve's laws* [24–26]. The total statistical mean $\langle u \rangle_e$ is the average of the partial means, and the total statistical covariance $\tau_e(u, v)$ is the average of the partial covariances plus the statistical covariances of the

partial mean values. Our multiscale identities are the generalization of the Adam's and Eve's laws to a hierarchy of generic filtering operators, and we really think that this simple multiscale approach could be usefully applied not only to modelling turbulent flows but also to the analysis of turbulent databases.

4 Conclusions

In the paper the main peculiarities of the Filtering Approach based on the Generalized Central Moments are summarized and some recent applications both in the analysis and modelling of turbulent flows are presented. All that in the spirit of illustrating *a unified theory linking the direct approach to the statistical one by a continuous interval of intermediate steps* [8].

References

1. J. Lee, Chaos and direct numerical simulation in turbulence. *Theoret. Comput. Fluid Dyn.* **7**, 363–395 (1995)
2. J.L. Guermond, J.T. Oden, S. Prudhomme, Mathematical perspectives on large eddy simulation models for turbulent flows. *J. Math. Fluid. Mech.* **6**, 194–248 (2004)
3. S.B. Pope, *Turbulent flows*. Cambridge University Press, pag. 603–604 (2000)
4. N. Aubry, On the hidden beauty of the proper orthogonal decomposition. *Theoret. Comput. Fluid Dyn.* **2**, 339–352 (1991)
5. F.F. Grinstein, *Coarse Grained Simulation and Turbulent Mixing*, Cambridge (2016)
6. M. Germano, Fundamentals of large eddy simulation, Advanced Turbulent Flows Computations, R Peyret and E Krause eds., CISM Courses and Lectures 395:81–130, Springer (2000)
7. A. Leonard, Energy cascade in large-eddy simulations of turbulent fluid flows. *Adv. Geophys.* **18A**, 237–248 (1975)
8. M. Germano, Turbulence: the filtering approach. *J. Fluid Mech.* **238**, 325–336 (1992)
9. J.A. Saenz, D. Aslangil, D. Livescu, Filtering, averaging, and scale dependency in homogeneous variable density turbulence. *Phys. Fluids* **33**, 025115 (2021)
10. M. Germano, U. Piomelli, P. Moin, W.H. Cabot, A dynamic subgrid-scale eddy viscosity model. *Phys. Fluids* **A3**, 1760–1765 (1991)
11. M. Klein, M. Germano, Analysis and modelling of the commutation error. *Fluids* **6**(1), 15 (2021)
12. A. Cimarelli, A. Abbà, M. Germano, General formalism for a reduced description and modelling of momentum and energy transfer in turbulence. *J. Fluid. Mech.* **866**, 865–896 (2019)
13. M. Germano, A direct relation between the filtered subgrid stress and the second order structure function. *Phys. Fluids* **19**, 038102 (2007)
14. M. Klein, M. Germano, Decomposition of the Reynolds stress from filtered data. *Phys. Rev. Fluids* **3**, 114606 (2018)
15. M. Klein, C. Kasten, M. Germano, Decomposition of turbulent fluxes from filtered data and application to turbulent premixed combustion modelling. *Flow Turbul. Combust.* **103**, 503–517 (2019)
16. M. Germano, On the hybrid RANS-LES of compressible flows, *Progress in Hybrid RANS-LES Modelling*, S Girimaji et al. eds., Springer, 253–263 (2014)
17. M. Germano, A. Abbà, R. Arina, L. Bonaventura, On the extension of the eddy viscosity model to compressible flows. *Phys. Fluids* **26**, 041702 (2014)

18. C.G. Speziale, Turbulence modeling for time-dependent RANS and VLES: a review. *AIAA J.* **36**(2), 173–184 (1998)
19. M. Germano, Comment on “Turbulence modeling for time-dependent RANS and VLES: a review”. *AIAA J.* **36**(9), 1766 (1998)
20. F.F. Grinstein, J.A. Saenz, R.M. Rauenzahn, M. Germano, D.M. Israel, Dynamic bridging modeling for coarse grained simulations of shock driven turbulent mixing. *Comput. Fluids* **199**, 104430 (2020)
21. F.F. Grinstein, J.A. Saenz, M. Germano, Coarse grained simulations of shock-driven turbulent material mixing. *Phys. Fluids* **33**, 035131 (2021)
22. M. Germano, A statistical formulation of the dynamic model. *Phys. Fluids* **8**, 565–570 (1996)
23. A. Ferrero, F. Larocca, G. Scovazzi, M. Germano, *A numerical study of the spanwise turbulence past a cylinder flow*, 17th ETC, 3–6 Sept. 2019, Torino, ITALY (2019)
24. R.A. Fisher, *Statistical methods for research workers*, Oliver and Boyd, Edinburgh, Scotland (1925)
25. J.A. Rice, *Mathematical statistics and data analysis*, Third Edition, Thomson (2007)
26. J.K. Blitzstein, J. Hwang, *Introduction to probability*, CRC Press LLC (2014)

Dynamic Bridging for Coarse Grained Simulations of Turbulent Material Mixing



Fernando F. Grinstein, Juan A. Saenz, and Massimo Germano

Abstract We revisit coarse-grained simulation strategies for turbulent material mixing applications involving shock-driven turbulence, based on bridging LANL's Radiation Adaptive Grid Eulerian (xRAGE)—implicit large-eddy simulation (ILES), and Besnard-Harlow-Rauenzahn (BHR)—Reynolds-Averaged Navier-Stokes (RANS), using Low-Mach-Corrected (LMC) hydrodynamics. Tests of a new dynamic LMC-xRAGE/BHR bridging paradigm demonstrate much-improved scale-resolving enabling higher simulated mixing and turbulence levels on coarser grids. Impact assessments are carried out based on simulations of a canonical shock-tube experiment.

1 Background

In shock-driven turbulence applications such as inertial-confinement-fusion capsule-implosion experiments, we are interested in predicting the mixing consequences of material interpenetration and hydro-dynamical instabilities arising from perturbations at shocked/accelerated material interfaces. The 3D variable-density hydrodynamics depend on initial conditions (IC) and involve transition to turbulence, non-equilibrium turbulence development, and late-time relaminarization. Such flow physics can be captured with a coarse grained simulation paradigm [1], presuming the spectral cascade transfer of energy (*the rate limiting step*) is determined by the initial and boundary condition constrained large-scale dynamics, and using mixing transition criteria and effective turbulence Reynolds numbers (Re) for macroscopic convergence metrics [2]. Because shocks and turbulence are involved, resolving

F. F. Grinstein (✉) · J. A. Saenz
Los Alamos National Laboratory, Los Alamos, NM 87545, USA
e-mail: fgrinstein@lanl.gov

J. A. Saenz
e-mail: juan.saenz@lanl.gov

M. Germano
Duke University, Durham, NC 27708, USA
e-mail: mg234@duke.edu

© The Author(s), under exclusive license to Springer Nature Switzerland AG 2021
R. Örlü et al. (eds.), *Progress in Turbulence IX*, Springer Proceedings in Physics 267,
https://doi.org/10.1007/978-3-030-80716-0_10

all relevant physical scales in shock-driven turbulence simulations becomes prohibitively expensive. ILES addresses the seemingly insurmountable issues posed by underresolution [4] by combining shock and turbulence emulation capabilities based on a single numerical model [3].

Strategies bridging large-eddy simulation (LES) and RANS are the aerospace and automobile industry standard for full scale simulations [5]. Blended hybrids such as the Flow Simulation Methodology [6, 7] scale the closure terms on the RANS equations by a contribution function $0 < f(\Delta/L) < 1$, where Δ is the local grid size, and L is a reference bridging length. Balance between modeled and computed dissipation is based on the RANS stress model R_{ij}^m locally morphing into SGS Favre-averaged LES stress SGS model \tilde{R}_{ij}^s ,

$$\tilde{R}_{ij}^s \equiv f(\Delta/L) R_{ij}^m, \quad (1)$$

where the contribution function $f(\Delta/L)$ vanishes in the high fidelity limit ($\Delta \rightarrow 0$) and approaches unity at the low resolution limit (pure RANS). Formal relations such as (1)—involving ensemble-averaged RANS and spatially-filtered LES quantities, are interpreted in a generalized-function (integral) sense. Hybrids exploit the structural similarity of equations for RANS and LES, and use the relationships between filtering and averaging operations—e.g. [8, 9].

FSM was originally intended to locally bridge direct numerical simulation (DNS) and RANS as a function of grid resolution. More generally, FSM can be used to locally blend a high-fidelity simulation strategy (such as ILES) with RANS to generate a sophisticated LES strategy in-between. The issue of interest is the computation of the dissipation which has to be supplemented by the model for underresolved flow conditions. For sufficiently fine resolution the dissipation range is resolved and the RANS contribution should switch itself off—i.e., $f(\Delta/L) \rightarrow 0$ as $\Delta \rightarrow 0$. In the FSM approach first proposed in Speziale [6]—and subsequently pursued in various forms by others, empirical *ad hoc* forms for the contribution function f were prescribed.

Dynamically solving for f based on decomposing the full stress into modeled and resolved components and using a differential filter as secondary filtering operation to define the resolved part was first proposed in Germano [10], and recently extended [11, 12] by additionally requiring the resolved stress to approach the full stress with grid resolution refinement to ensure realizability of the bridging-based LES. In our dynamic FSM paradigm for turbulent material mixing applications, the full stress is decomposed in terms of modeled \tilde{R}_{ij}^s and resolved T_{ij} parts,

$$R_{ij}^{full} = \tilde{R}_{ij}^s + T_{ij}. \quad (2)$$

We use ILES as high-resolution limit strategy in the formalism, so there is no explicit LES SGS model, and the hybrid \tilde{R}_{ij}^s is directly related to the RANS stress R_{ij}^m in terms of f through (1).

For consistency and realizability of the generated LES in approaching the high resolution / fidelity limit, we require that $T_{ij} \rightarrow R_{ij}^{full}$ as $\Delta/L \rightarrow 0$. We enforce this additional modeling constraint, in terms of $\gamma = (\Delta/L)^l$, for $l \geq 1$, by assuming that R_{ij}^{full} can be approximated by a resolution-dependent weighted-average of the RANS and resolved stresses,

$$R_{ij}^{full} \sim \gamma R_{ij}^m + (1 - \gamma)T_{ij}. \quad (3)$$

We substitute equation (1) into (2), use (3), and after contracting with a generic tensor quantity q_{ij} – e.g., $q_{ij} = T_{ij}$, we solve for f – see full derivations in [11, 12],

$$f(\Delta/L) = \gamma \{1 - [q_{ij}T_{ij}] / [q_{ij}R_{ij}^m]\}. \quad (4)$$

For consistency we also require $f \equiv 1$ for $\gamma \geq 1$.

In the FSM bridging DNS and RANS [6, 7], the bridging length L was an estimated Kolmogorov length scale. Choosing L as the Kolmogorov scale amounts to choosing L as the smallest hydrodynamic length scale in the turbulent flow—a small fraction of the Taylor microscale characterizing the smallest vortices of the turbulence. For xRAGE-BHR bridging LES, it is still useful to *compute* a Taylor microscale [13]—typically $\gtrsim 10$ cells for xRAGE ILES [14], to characterize the smallest vortical structures in the simulated turbulence. In what follows, a small fraction of the computed Taylor microscale is chosen, i.e., $L \sim \text{few cells}$.

By design, the contribution function enforces realizability of the bridging-based LES through (1) in the high fidelity limit $\Delta \rightarrow 0$, when LES \rightarrow DNS (if based on the Navier-Stokes equations), or LES \rightarrow ILES based on the Euler equations. The choice of l controls how the numerics-based ILES SGS model is supplemented by the explicit SGS model generated by the bridging strategy for intermediate resolutions. For xRAGE numerics—1st-order near shocks and 2nd-order in smooth flow regions, $l \geq 2$ is a suitable choice.

Present ILES is based on the newly available directionally-unsplit LMC xRAGE numerical hydrodynamics [11, 12, 15]. The default 2nd-order split xRAGE hydrodynamics [16] was used in our previous *sequential* ILES/RANS simulations of the CEA shock-tube laboratory experiments [17] running pure ILES at early times to generate RANS initialization at a selected prescribed start time. In contrast, the present dynamic bridging LES/RANS paradigm acts at all times. Detailed discussion of BHR initialization issues can be found in [11, 12].

2 Simulations of the CEA Planar Shock Tube Experiments

We revisit the CEA shock-tube laboratory experiments [18], involving high (SF₆) and low (air) density gases, Atwood number, $At = 0.67$, presumed geometries of the membranes and the wire mesh initially separating the gases, and reshock off an end-

wall. A shocked SF_6 region is created upstream in terms of a higher-density higher-pressure SF_6 region for a Mach 1.45 shock (strength 0.54). The planar primary shock propagates in the through unshocked SF_6 , and then through the SF_6 /Air contact discontinuity. The shock propagates through the contact discontinuity and reflects at the end of the simulation box where purely reflecting boundary conditions are enforced – to enable reshock simulation.

The early CEA (0.05mm resolution) simulations [19] were based on the 2D Navier-Stokes equations. In the more recent *sequential* xRAGE-ILES/BHR-RANS hybrid simulation studies [17], xRAGE-ILES generated data was used to provide physics-based IC to BHR-RANS just before 1st reshock, and was also used as reference for its assessment. By prescribing ILES generated 3D IC and allowing for 3D convection with just enough resolution in Grinstein [17], the computed dissipation in 3D RANS (vs. 2D RANS) was found to effectively supplement the modeled dissipation following 1st reshock. However, the 3D RANS cannot resolve well the subsequent consequences of a new transitional flow event at 2nd reshock [17]. This limitation is typical of a standalone RANS and motivates our pursuit of suitable *blended* LES/RANS capable of dynamically adapting the simulation model to local flow conditions for applications driven by multiple shocks.

As in Grinstein [11], our 3D dynamic BHR simulations use $q_{ij} = T_{ij}$ in conjunction with $l = 2$. Moreover, as in Grinstein [17] we used between $0.1\text{--}5.5 \times 10^9$ computational cells, based on adaptive mesh refinement with finest resolutions ranging between 0.2mm and 0.05mm.

Spectral content and standard deviation need to be prescribed for the initial material sharp-interface conditions. Following [17] IC are defined as superposition of six equally-weighted wavelengths in the neighborhood of h (characteristic initial *eggcrate* length and mix thickness), in addition to (red-noise) $\sim k^{-2}$ deformations with standard deviation $0.04h$ and shortest wavelength of at least 4 coarsest cells.

Mix width, as well as velocity magnitude and variance data from the experiments [18, 19] are used for benchmarking the ILES predictions—see [12] for detailed discussion of validation results and analysis. In turn, ILES is then used as detailed reference for bridging results for same domain, resolution, and initial conditions.

Mixing measures less sensitive to subgrid contributions may enable accurate prediction of quantities of interest with the bridging-based generated LES with less resolution than typically required with the ILES high-fidelity option. Such potential benefits were noted in Grinstein [11] with regard to having scalar-mixing predictions converged on coarser grids with the more-accurate LMC xRAGE. In what follows, we examine the impact of choices of the bridging length L in this context.

Figure 1 shows centerplane predicted mass-fraction distributions associated with dynamic bridging and LMC-xRAGE ILES for the coarsest 0.2mm resolution (2-level AMR) case. Prediction accuracy is determined by ability to capture the vortical structures responsible for the onset and development of turbulence, and bridging modeling efficiency is directly determined by how much *less* resolution is required to resolve the flow scales not amenable to modeling [20]. Results with bridging length $L \sim 2$, and $L \sim 4$ (smallest) cells are shown at selected times before, after,

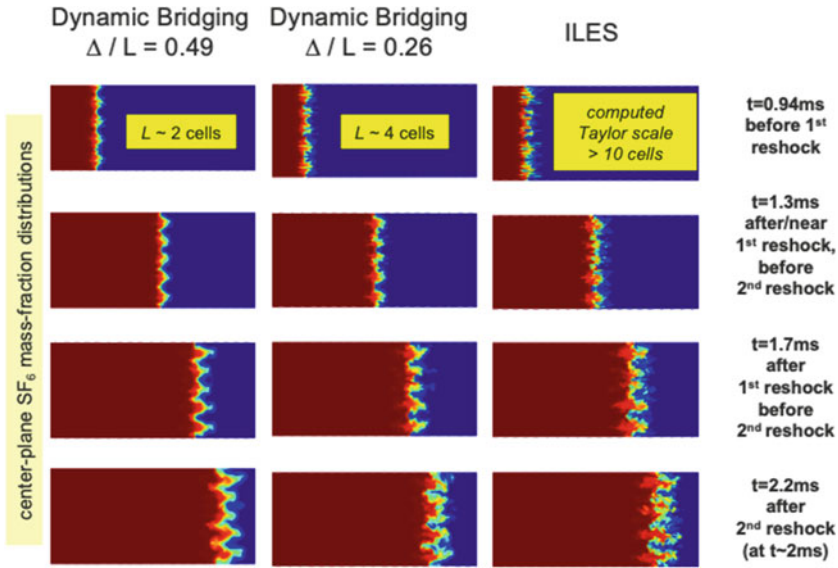


Fig. 1 Dynamic BHR versus ILES for 0.2mm resolution (two-level AMR)

and between the reshock events. Varying the bridging length directly impacts the detailed captured content of space/time fluctuations effects.

For the sake of quantitative mix analysis, we consider here a frequently used integrated mixing measure—e.g. [21], $TMX = 4 \int \bar{\rho}^2 \bar{Y}_{air} \bar{Y}_{SF6} dx$, in terms of the mass density ρ , SF_6 and air mass fractions Y_{SF_6} and $Y_{air} = 1 - Y_{SF_6}$, and using transverse-plane averaging, $\bar{\phi}(x) = \int \phi(x, y, z) dydz / \int dydz$.

Figure 2 compares TMX versus resolution and bridging length L . The ability of the dynamic bridging model to capture the basic mixing features with less resolution is well apparent between first and second reshock, where the 0.2mm and 0.1mm bridging predictions for $\Delta/L = 0.26$ are nearly the same and in very good agreement with the finest (0.05mm) ILES – suggesting preferred bridging/resolution trade-offs and robust mixing capturing with coarser gridding. Beyond second reshock, bridging with 0.1mm resolution and $\Delta/L = 0.26$ still provides very good predictions – albeit RANS corrections to better converged (resolved) ILES appear less necessary there.

For the tested planar shock tube case, we attain the same level of accuracy with significantly less resolution than required with the highest-fidelity turbulence simulation models typically used at scale with default xRAGE hydrodynamics [12]. Two levels of grid-coarsening savings are achieved for the mixing predictions: one associated with the more-accurate LMC xRAGE hydrodynamics, and an additional one from using the dynamic xRAGE-BHR bridging.

Los Alamos National Laboratory is operated by TRIAD LLC for US DOE NNSA. This research was supported by the LANL PEM Mix & Burn Project.

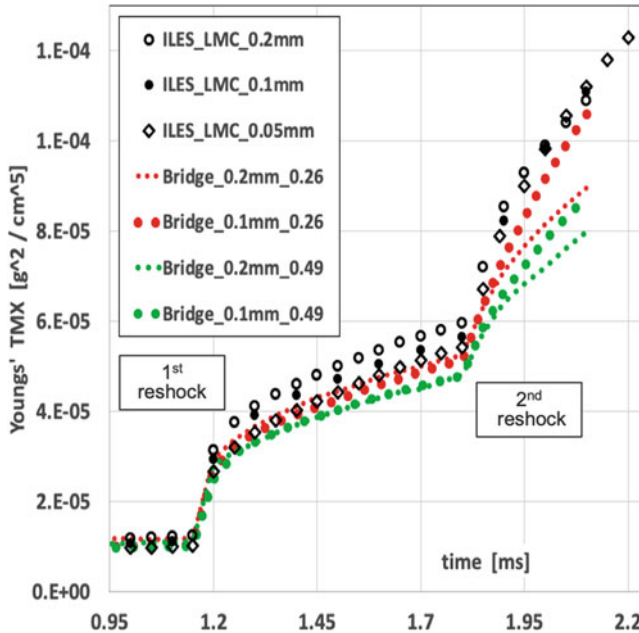


Fig. 2 TMX for LMC-xRAGE ILES and dynamic BHR versus resolution for $\Delta/L = 0.26, 0.49$

References

1. F.F. Grinstein, *Coarse Grained Simulation and Turbulent Mixing*. (Cambridge, NY, 2016)
2. Y. Zhou, F.F. Grinstein, A.J. Wachtor, B.M. Haines, *Phys. Rev. E* **89**, 013303 (2014)
3. F.F. Grinstein, L.G. Margolin, W.J. Rider, *ILES Book*. (Cambridge, NY, 2nd Printing, 2010)
4. S. Ghosal, *J. Comput. Phys.* **125**, 187–206 (1996)
5. J. Frolich, D.A. von Terzi, *Prog. Aerosp. Sci.* **44**, 349–77 (2008)
6. C.G. Speziale, *AIAA J.* **36**(2), 173–184 (1998)
7. H.F. Fasel, D.A. von Terzi, R.D. Sandberg, *J. Appl. Mech.* **73**, 405–412 (2006)
8. M. Germano, *J. Fluid Mech.* **238**, 325–336 (1992)
9. J.A. Saenz, D. Aslangil, D. Livescu, *Phys. Fluids* **33**, 025115 (2021)
10. M. Germano, *AIAA J.* **36**(9), 1766–1767 (1998)
11. F.F. Grinstein, J.A. Saenz, M. Germano et al., *Comput. Fluids* **199**, 104430 (2020)
12. F.F. Grinstein, J.A. Saenz, M. Germano, *Phys. Fluids* **33**, 035131 (2021)
13. A.J. Wachtor, F.F. Grinstein, J.R. Ristorcelli et al., *Phys. Fluids* **25**, 025101 (2013)
14. F.F. Grinstein, *Phys. D Nonlinear Phenom.* **407**, 132419 (2020)
15. F.F. Grinstein, J.A. Saenz, J.C. Dolence, T.O. Masser et al., *CAMWA* **78**, 437–458 (2019)
16. M. Gittings et al., *Comput. Sci. Discov.* **1**, 015005 (2008)
17. F.F. Grinstein, *Comput. Fluids* **151**, 58–72 (2017)
18. F. Poggi, M.-H. Thorembey, G. Rodriguez, *Phys. Fluids* **10**, 2698 (1998)
19. C. Mugler, S. Gauthier, *Phys. Fluids* **12**, 1783 (2000)
20. F.S. Pereira, L. Eca, G. Vaz, S.S. Girimaji, *J. Comput. Phys.* **363**, 98–115 (2018)
21. M. Hahn, D. Drikakis, D.L. Youngs, R.J.R. Williams, *Phys. Fluids* **23**, 046101 (2011)

Dynamic Tensorial Eddy Viscosity and Turbulent Stresses



A. Abbà, A. Cimarelli, and Massimo Germano

Abstract In the theoretical framework provided by an alternative decomposition of the turbulent stresses, a new formalism for their approximation and understanding has been proposed in [1] that spontaneously directs to a tensorial turbulent eddy viscosity. Based on this, new modelling approaches for LES, representing subgrid fluxes for momentum, energy and heat fluxes, based on the second order inertial properties of the grid element are developed. The new model has firstly tested in the case of typical LES benchmark for compressible flow, such as the turbulent channel flow. A numerical simulation of turbulent flows in a more complex geometry using unstructured meshes has been performed, exploiting the properties of the eddy viscosity model based on the inertial tensor of the numerical grid element. The analysis highlights the capability of the model to well reproduce the anisotropic character of the turbulent flows.

1 Theoretical Framework

The old idea of Boussinesq to represent the turbulent stress by means of an eddy viscosity has been developed during the years and applied to the formulation of many different turbulence models. However, its fundamental hypothesis of isotropicity is violated not only by the large turbulent scales but also by the small ones. Hence, tensorial eddy viscosity models have been proposed to overcome the isotropicity assumption and to combine with the disalignment between the strain rate tensor and the subfilter stress. Non-isotropic grids are usually used in numerical simulations with

A. Abbà (✉)

Dipartimento di Scienze e Tecnologie Aerospaziali, Politecnico di Milano, 20156 Milano, Italy
e-mail: antonella.abba@polimi.it

A. Cimarelli

DIEF, University of Modena and Reggio Emilia, 41125 Modena, Italy
e-mail: andrea.cimarelli@unimore.it

M. Germano

Department Civil and Environmental Engineering, Duke University, Durham NC27708, USA
e-mail: mg234@duke.edu

the aim to better represent the large anisotropic turbulent structures. Moreover the size and anisotropic geometry of grid elements directly affect the subgrid turbulence through implicit filtering and such information can be usefully taken into account. First [2, 3] introduced different length scales associated to the face element diagonal with the aim to take into account the resolution anisotropy. Other proposals, based on empirical arguments, has followed [4, 5].

In a previous paper [1] an alternative decomposition of the turbulent stresses has been proposed that naturally directs to a tensorial turbulent eddy viscosity. In the present work, we extend that approach to the modelling of the subgrid terms in the energy equation.

2 The Flow Equations and the Subgrid Model

The following filtered Navier–Stokes equations, in non dimensional form, are used to represent a turbulent compressible flow in a LES context,

$$\partial_t \bar{\rho} + \partial_j (\bar{\rho} \tilde{u}_j) = 0 \quad (1)$$

$$\partial_t (\bar{\rho} \tilde{u}_i) + \partial_j (\bar{\rho} \tilde{u}_i \tilde{u}_j) = -\frac{1}{\gamma Ma^2} \partial_i \bar{p} + \frac{1}{Re} \partial_j \tilde{\sigma}_{ij} - \partial_j \tau_{ij} + \bar{\rho} f_i \quad (2)$$

$$\begin{aligned} \partial_t (\bar{\rho} \tilde{e}) + \partial_j (\bar{\rho} \tilde{h} \tilde{u}_j) &= \frac{\gamma Ma^2}{Re} \partial_j (\tilde{u}_i \tilde{\sigma}_{ij}) - \frac{1}{\kappa Re Pr} \partial_j \tilde{q}_j - \frac{1}{\kappa} \partial_j Q_j \\ &\quad - \frac{\gamma Ma^2}{2} \partial_j (J_j - \tau_{kk} \tilde{u}_j) + \gamma Ma^2 \bar{\rho} f_j \tilde{u}_j. \end{aligned} \quad (3)$$

As usual the Favre filter $\tilde{\cdot}$ is applied to velocity u , specific total energy e , enthalpy h and temperature T while \bar{p} denotes the filtered pressure. $\tilde{\sigma}$ and $\tilde{\mathbf{q}}$ represent the filtered momentum and heat diffusive fluxes, respectively. The equation of state for a perfect gas $\bar{p} = \bar{\rho} \tilde{T}$, and the constitutive equations

$$\tilde{\sigma}_{ij} = 2\mu(\tilde{S}_{ij} - \frac{1}{3}\tilde{S}_{kk}\delta_{ij}), \quad \tilde{q}_i = -\mu\partial_i \tilde{T} \quad (4)$$

complete the system. \tilde{S} is the resolved strain rate tensor and μ the dynamic viscosity, defined according to the Sutherland law. The following terms

$$\tau_{ij} = \bar{\rho} (\widetilde{u_i u_j} - \tilde{u}_i \tilde{u}_j), \quad Q_i = \bar{\rho} (\widetilde{u_i T} - \tilde{u}_i \tilde{T}), \quad J_i = \bar{\rho} (\widetilde{u_i u_k u_k} - \tilde{u}_i \tilde{u}_k \tilde{u}_k),$$

represent the subgrid stress tensor, heat flux and diffusion flux respectively. Considering the generalized central moment definition [6]

$$\tau(u_i, u_j, u_k) = \bar{\rho} \widetilde{u_i u_j u_k} - \tilde{u}_i \tau_{jk} - \tilde{u}_j \tau_{ik} - \tilde{u}_k \tau_{ij} - \bar{\rho} \tilde{u}_i \tilde{u}_j \tilde{u}_k \quad (5)$$

the turbulent diffusion flux can be written as

$$J_i = \tau(u_i, u_k, u_k) + 2\tilde{u}_k \tau_{ik} + \tilde{u}_i \tau_{kk}. \quad (6)$$

Following [1], we model the subgrid stresses as

$$\tau_{ij} = -\bar{\rho} (\nu_{kj} \partial_k \tilde{u}_i + \nu_{ki} \tilde{u}_j) \quad (7)$$

where ν_{ki} are the components of a tensorial subgrid viscosity

$$\nu_{ki} = -\frac{1}{2} \tau(x_h, x_k) \partial_h \tilde{u}_i. \quad (8)$$

An expression similar to (7), where the velocity gradients are substituted by the strain rate components, has been derived by [7] starting from a fourth order eddy viscosity tensor. The moment

$$\tau(x_h, x_k) = \frac{1}{K_f} \int_{K_f} (\xi_k - x_k)(\xi_h - x_h) d\xi \quad (9)$$

is related to the inertial tensor of the filter volume K_f and take into account the anisotropy of computational grid, see [1, 8]. This approach is extended to model also the scalar quantities

$$Q_i = -\frac{1}{2} \bar{\rho} \nu_{ih} \partial_h \tilde{T}, \quad \tau(u_i, u_k, u_k) \simeq \tau(u_i, u_k u_k) = -\frac{1}{2} \bar{\rho} \nu_{ih} \partial_h (\tilde{u}_k \tilde{u}_k) \quad (10)$$

Now a dynamic procedure is applied. Each subgrid term is multiplied by a tensorial coefficient [1]

$$\tau_{ij} = -C_{ij} (\nu_{kj} \partial_k \tilde{u}_i + \nu_{ki} \tilde{u}_j) \quad (11)$$

$$Q_i = -\frac{1}{2} C_i^Q \bar{\rho} \nu_{ih} \partial_h \tilde{T} \quad (12)$$

$$\tau(u_i, u_k u_k) = -\frac{1}{2} C_i^J \bar{\rho} \nu_{ih} \partial_h (\tilde{u}_k \tilde{u}_k). \quad (13)$$

A test filter operator $\widehat{\cdot}$ and a Favre test filter $\check{\cdot} = \widehat{\rho \cdot} / \widehat{\rho}$ are introduced with corresponding subtest fluxes

$$T_{ij} = \widehat{\rho u_i u_j} - \check{\rho u_i} \check{u}_j, \quad Q_i^{st} = \widehat{\rho u_i T} - \check{\rho u_i} \check{T}, \quad T(u_i, u_k u_k) = \widehat{\rho u_i u_k u_k} - \check{\rho u_i} (\check{u}_k \check{u}_k).$$

The Germano identity reads

$$\mathcal{L}_{ij} = T_{ij} - \widehat{\tau}_{ij}, \quad \mathcal{L}_i^Q = Q_i^{st} - \widehat{Q}_i, \quad \mathcal{L}_i^J = T(u_i, u_k u_k) - \widehat{\tau}(u_i, u_k u_k). \quad (14)$$

We apply the tensorial viscosity model to the test filtered terms

$$T_{ij} = -C_{ij} \widehat{\rho} \left(\widehat{\nu}_{kj} \partial_k \check{u}_i + \widehat{\nu}_{ki} \check{u}_j \right) \quad (15)$$

$$Q_i^{st} = -\frac{1}{2} C_i^Q \widehat{\rho} \widehat{\nu}_{ih} \partial_h \check{T} \quad (16)$$

$$T(u_i, u_k u_k) = -\frac{1}{2} C_i^J \widehat{\rho} \widehat{\nu}_{ih} \partial_h (\check{u}_k \check{u}_k). \quad (17)$$

where

$$\widehat{\nu}_{ki} = -\frac{1}{2} \tau \widehat{\tau}(x_h, x_k) \partial_h \check{u}_i. \quad (18)$$

Assuming the scale invariance of the tensorial coefficients we get

$$C_{ij} = \frac{\mathcal{L}_{ij}}{\mathcal{N}_{ij}}, \quad C_i^Q = \frac{\mathcal{L}_i^Q}{\mathcal{N}_i^Q}, \quad C_i^J = \frac{\mathcal{L}_i^J}{\mathcal{N}_i^J}. \quad (19)$$

By this way the tensorial coefficients are dynamically determined since the terms \mathcal{L}_{ij} , \mathcal{L}_i^Q , \mathcal{L}_i^J and

$$\mathcal{N}_{ij} = \widehat{\rho} \widehat{\nu}_{kj} \partial_k \check{u}_i + \widehat{\rho} \widehat{\nu}_{ki} \partial_k \check{u}_j - \widehat{\rho} \widehat{\nu}_{kj} \partial_k \check{u}_i - \widehat{\rho} \widehat{\nu}_{ki} \partial_k \check{u}_j \quad (20)$$

$$\mathcal{N}_i^Q = \widehat{\rho} \widehat{\nu}_{ki} \partial_k \check{T} - \widehat{\rho} \widehat{\nu}_{ki} \partial_k \check{T} \quad (21)$$

$$\mathcal{N}_i^J = \widehat{\rho} \widehat{\nu}_{ki} \partial_k (\check{u}_k \check{u}_k) - \widehat{\rho} \widehat{\nu}_{ki} \partial_k (\check{u}_k \check{u}_k) \quad (22)$$

are known by the resolved velocity and temperature fields. The coefficients are clipped to get non negative total dissipation. This dynamic procedure to determine the coefficients using (19) is independent on the flow geometry and conditions.

2.1 Results

The compressible flow equations and the illustrated subgrid model have been implemented in a numerical code based on the Local Discontinuous Galerkin approach. The code is based on the FEMilaro finite element library [9]. For more details we refer to [10, 11].

In order to evaluate the performances of the described model, the compressible turbulent channel flow at the bulk Reynolds number $Re = 2795$ and Mach $Ma = 0.7$ has been simulated. The computational mesh is obtained by a structured mesh with N_x , N_y , N_z hexahedra, each one split into 6 tetrahedral elements. The 4th order polynomial degree has been used. Three different resolutions have been used which

Table 1 Grid parameters of the present simulations and DNS [12]

$N_x \times N_y \times N_z$	Δ_x^+	Δ_z^+	$\Delta_{ymin}^+ / \Delta_{ymax}^+$
$16 \times 16 \times 12$	24	11	0.67/8.2
$12 \times 16 \times 10$	32	13.5	0.67/8.2
$8 \times 16 \times 8$	48	22	0.67/8.2
DNS	4.89	4.89	0.19/2.89

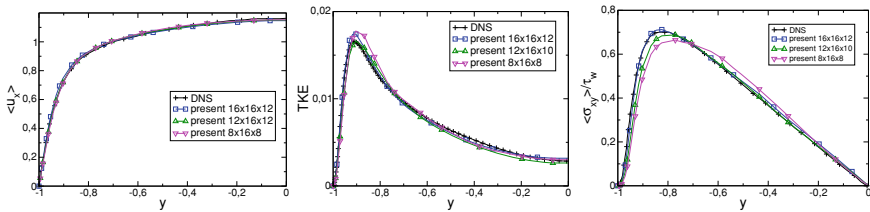
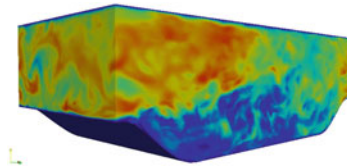


Fig. 1 Mean velocity, turbulent kinetic energy and shear stress in the channel flow

Fig. 2 Streamwise component of the velocity field for the periodic hill flow



grid parameters are summarized in Table 1. Figure 1 shows the streamwise velocity, the turbulent kinetic energy and shear stress profiles. A very good agreement with DNS [12] is observed for high and middle resolutions but also the lower one presents good performances.

Then the flow over periodic hills at $Re = 2800$ and $Ma = 0.2$ [13] has been considered and the use of an unstructured grid highlights the peculiarity of the model. The minimum sizes of the elements close to the lower wall are $\Delta x = 0.023$, $\Delta y = 0.00325$, $\Delta z = 0.062$. The flow separates on the top of each hill, creating a significant turbulent recirculation bubble, and then re-attaches before the next hill, where the flow is accelerated on the forward side. A sketch of the streamwise velocity field is depicted in Fig. 2. The profiles of mean streamwise velocity and of shear stresses are compared with the results of the DNS [13] in Fig. 3. The negative peak in the recirculating region and the following accelerating trend are well reproduced in the streamwise velocity profiles. No relevant differences are evident between the results of LES and the DNS in these plots. In conclusion, the comparison with DNS results highlights how the present model accurately capture the anisotropy of the considered flows also at the lower resolutions.

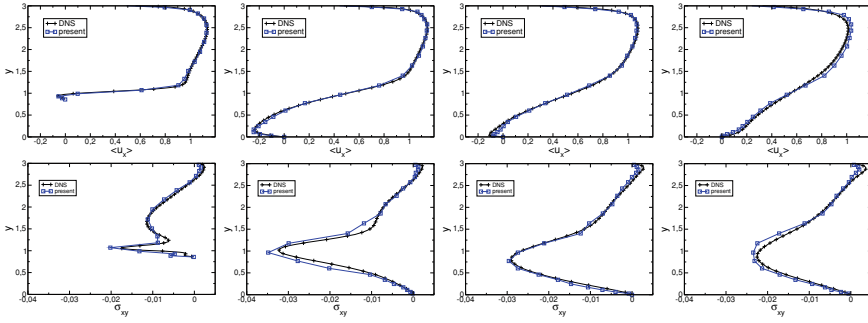


Fig. 3 Mean profiles of longitudinal velocity and turbulent shear stresses in the periodic hill flow at different x positions: $x = 0.5, x = 2, x = 4, x = 6$

Acknowledgements We acknowledge that the results of this research were made possible by the computational resources made available at CINECA (Italy) by the high performance computing projects IS CRA-C HP10CGORK5.

References

1. A. Cimarelli, A. Abbà, M. Germano, General formalism for a reduced description and modelling of momentum and energy transfer in turbulence. *J. Fluid Mech.* **866**, 865–896 (2019)
2. U. Schumann, Subgrid scale model for finite difference simulations of turbulent flows in plane channels and annuli. *J. Comput. Phys.* **18**(4), 376–404 (1975)
3. S. Zahrai, F. Bark, R. Karlsson, On anisotropic subgrid modeling. *Eur. J. Mech. B. Fluids* **14**, 459–486 (1995)
4. J. Bardina, J. Ferziger, W. Reynolds, Improved turbulence models based on large eddy simulation of homogeneous, incompressible, turbulent flows. NASA NCC 2–15 report TF-19 (1983)
5. A. Abbà, D. Campaniello, M. Nini, Filter size definition in anisotropic subgrid models for large eddy simulation on irregular grids. *J. Turbul.* **18**, 589–610 (2017)
6. M. Germano, Turbulence: the filtering approach. *J. Fluid Mech.* **238**, 325–336 (1992)
7. F. Gallerano, E. Napoli, A dynamic subgrid-scale tensorial eddy viscosity model. *Contin. Mech. Thermodyn.* **11**, 1–14 (1999)
8. S.W. Haering, M. Lee, R.D. Moser, Resolution-induced anisotropy in large-eddy simulations. *Phys. Rev. Fluids* **4**(11), (2019)
9. FEMilaro, a finite element toolbox. Available under GNU GPL v3, <https://bitbucket.org/mrestelli/femilaro/wiki/Home>
10. A. Abbà, L. Bonaventura, M. Nini, M. Restelli, Dynamic models for Large eddy simulation of compressible flows with a high order DG method. *Comput. Fluids* **122**, 209–222 (2015)
11. A. Abbà, A. Recanati, M. Tugnoli, L. Bonaventura, Dynamical p-adaptivity for LES of compressible flows in a high order DG framework. *J. Comput. Phys.* **420**, 109720 (2020)
12. L. Wei, A. Pollard, Direct numerical simulation of compressible turbulent channel flows using the discontinuous Galerkin method. *Comput. Fluids* **47**, 85–100 (2011)
13. M. Breuer, N. Peller, C. Rapp, M. Manhart, Flow over periodic hills - Numerical and experimental study in a wide range of Reynolds numbers. *Comput. Fluids* **38**(2), 433–457 (2009)

A Numerical Study of the Spanwise Turbulence Past a Cylinder Flow



Andrea Ferrero, Francesco Larocca, Guglielmo Scovazzi,
and Massimo Germano

Abstract Many flows of industrial interest and many important benchmark turbulent flows are statistically stationary in time and are provided with a spanwise direction of homogeneity. The numerical simulation of such flows is conditioned by the discretization in space and time, and the statistical analysis of the data is biased by the finite extent of the produced dataset. In this work the flow around a circular cylinder at Reynolds 3900 is numerically investigated by an implicit Large Eddy Simulation. The computations are performed by a modal Discontinuous Galerkin finite element solver and the produced database is analysed in order to quantify the temporal and spanwise contribution to the estimation of the statistics. The goal of the work is to investigate a procedure which allows to quantify the statistical efficiency of the operators which are used to perform the average in time and in the spanwise direction. Finally, the hierarchical nature of the modal basis used in each element is exploited to perform a local element-wise filtering operation which allows to quantify the contributions given by the smallest resolved scales to the statistics.

1 Introduction

Many flows of industrial interest and many important benchmark turbulent flows are statistically stationary in time and are provided with a spanwise direction of homogeneity. Typical examples are the flow in blade cascades and more simply the

A. Ferrero (✉) · F. Larocca
Politecnico di Torino, Corso Duca degli Abruzzi 24, Torino, Italy
e-mail: andrea_ferrero@polito.it

F. Larocca
e-mail: francesco.larocca@polito.it

G. Scovazzi · M. Germano
Duke University, 2080 Duke University Road, Durham, USA
e-mail: guglielmo.scovazzi@duke.edu

M. Germano
e-mail: mg234@duke.edu

flow around a cylinder. The numerical simulation of such flows is conditioned by the discretization in space and time, and the statistical analysis of the data is biased by the finite extent of the produced dataset. In a previous paper the authors have examined in detail the statistical error in the time averages [1], but we remark that, due to the spanwise homogeneity, statistics can be also computed with a combined average in time and in the spanwise direction. As remarked in [2], an insufficient spanwise extent can produce a overprediction of the streamwise and normal turbulent intensities and correspondingly artificial suppression of the spanwise turbulent intensity. These considerations can be used to define a minimum spanwise extension required to correctly describe the evolution of the largest structures. However, this provides only a lower bound to the spanwise extension: in a general flow it is not clear a-priori whether it is more convenient to collect the statistics by performing a simulation with a relatively large spanwise extension and a small time window or the contrary. In order to find a numerical criterion which allows to quantify the efficiency of computing statistics in time and in the spanwise direction, the potential of some indices of statistical resolution is investigated.

In particular a database of the turbulent flow past a circular cylinder at Reynolds 3900 is produce by means of an implicit Large Eddy Simulation (LES). The computations are carried out by means of a modal Discontinuous Galerkin (DG) finite element solver based on the use of a modal orthonormal basis implemented following the guidelines of [3]. The solver is compressible but in this study a low far field Mach number ($M_\infty = 0.2$) is assumed in order to make comparisons with available experimental results in almost incompressible conditions [4].

Finally, the hierarchical nature of the modal orthonormal basis used inside each element allows to perform a local element-wise filtering operation: in this way it is possible to quantify the contributions given by the smallest resolved scales.

2 Indices of Statistical Resolution

The turbulent flow past a cylinder is characterised by two homogeneities, the time t and the spanwise spatial direction z , and we can average along one or both of them in order to estimate average fields and Reynolds stresses. Given the turbulent velocity field $u_i(x, y, z, t)$ we will introduce the following space and time *statistical* filtering operators \mathcal{T} and \mathcal{Z}

$$\begin{aligned}\mathcal{Z}\{u_i\} &\equiv \langle u_i \rangle_z \equiv \frac{1}{Z} \int_0^Z u_i(x, y, z', t) dz' \\ \mathcal{T}\{u_i\} &\equiv \langle u_i \rangle_t \equiv \frac{1}{T} \int_0^T u_i(x, y, z, t') dt'\end{aligned}\tag{1}$$

and we define as \mathcal{E} the product of the two

$$\mathcal{E}\{u_i\} \equiv \mathcal{T}\mathcal{Z} \equiv \mathcal{Z}\mathcal{T} \equiv \langle u_i \rangle_e \equiv \frac{1}{ZT} \int_0^Z \int_0^T u_i(x, y, z', t') dz' dt' \quad (2)$$

where Z and T are the extents of the domain in the spanwise direction z and in time t . The turbulent stresses can be defined by means of the operators \mathcal{T} and \mathcal{Z}

$$\begin{aligned} \tau_z(u_i, u_j) &\equiv \langle u_i u_j \rangle_z - \langle u_i \rangle_z \langle u_j \rangle_z \\ \tau_t(u_i, u_j) &\equiv \langle u_i u_j \rangle_t - \langle u_i \rangle_t \langle u_j \rangle_t \\ \tau_e(u_i, u_j) &\equiv \langle u_i u_j \rangle_{zt} - \langle u_i \rangle_{zt} \langle u_j \rangle_{zt} \\ \tau_z(\langle u_i \rangle_t, \langle u_j \rangle_t) &\equiv \langle \langle u_i \rangle_t \langle u_j \rangle_t \rangle_z - \langle u_i \rangle_{zt} \langle u_j \rangle_{zt} \\ \tau_t(\langle u_i \rangle_z, \langle u_j \rangle_z) &\equiv \langle \langle u_i \rangle_z \langle u_j \rangle_z \rangle_t - \langle u_i \rangle_{tz} \langle u_j \rangle_{tz} \end{aligned} \quad (3)$$

We note that due to $\mathcal{E} = \mathcal{Z}\mathcal{T} = \mathcal{T}\mathcal{Z}$ we have the two identities

$$\begin{aligned} \tau_e(u_i, u_j) &\equiv \tau_z(\langle u_i \rangle_t, \langle u_j \rangle_t) + \langle \tau_t(u_i, u_j) \rangle_z \\ &\equiv \tau_t(\langle u_i \rangle_z, \langle u_j \rangle_z) + \langle \tau_z(u_i, u_j) \rangle_t \end{aligned} \quad (4)$$

and we can define two measures of turbulence resolution, the first related to the time average and the second to the spanwise average, given by

$$\begin{aligned} M_t(x, y) &= \frac{\langle \tau_t(u_i, u_i) \rangle_z}{R_{ii}} = 1 - \frac{\tau_z(\langle u_i \rangle_t, \langle u_i \rangle_t)}{R_{ii}} \\ M_z(x, y) &= \frac{\langle \tau_z(u_i, u_i) \rangle_t}{R_{ii}} = 1 - \frac{\tau_t(\langle u_i \rangle_z, \langle u_i \rangle_z)}{R_{ii}} \end{aligned} \quad (5)$$

where $R_{ij} \equiv \tau_e(u_i, u_j)$. The indices $M_t(x, y)$ and $M_z(x, y)$ allow to quantify the relative contribution given by time and spanwise direction to the evaluation of the statistics. For example, where $M_t \rightarrow 0$ the statistics are mainly captured by sampling in the spanwise direction while where $M_t \rightarrow 1$ the statistics are mainly captured by sampling in time. The index M_z shows an opposite behaviour.

3 Numerical Results

The simulations are performed on an unstructured mesh with approximately $3 \cdot 10^5$ elements by a third order accurate DG scheme ($p = 2$): $3 \cdot 10^6$ degrees of freedom are employed for each equation. Time integration is performed by means of an explicit RK3 method. The spanwise extension of the domain along the direction z is set equal to three diameters D . The simulation is carried out for several hundreds of convective times CT , as shown in Fig. 1a which reports the time evolution of the drag coefficient C_d . A snapshot of the vorticity magnitude field is reported in Fig. 1b which puts in evidence the development of turbulence structures in the wake.

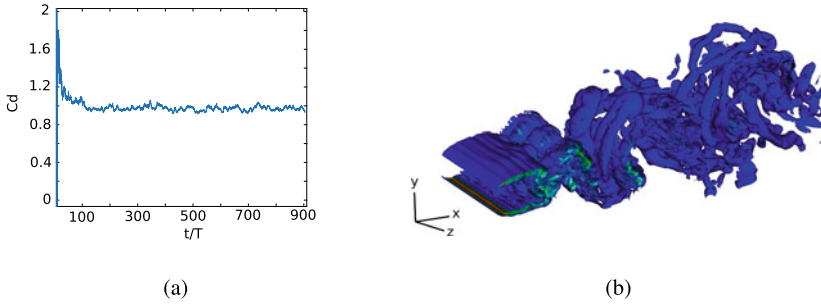


Fig. 1 Drag coefficient history (a) and instantaneous vorticity magnitude field (b)

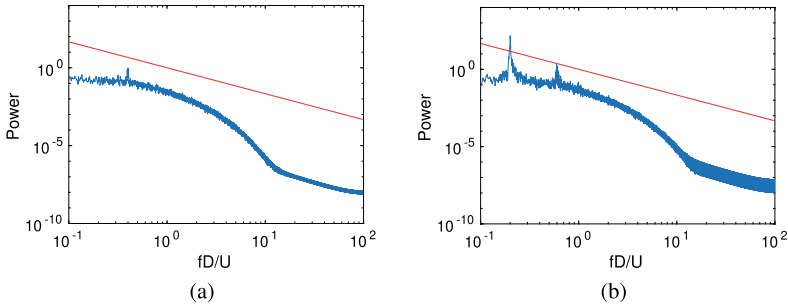


Fig. 2 Spectrum for the streamwise (a) and normal (b) velocity at $x/D = 4$ and $y/D = 0$

The spectrum of the streamwise and normal velocity in a station located at $x/D = 4$ and $y/D = 0$ is reported in Fig. 2. The spectrum is computed from a time window with $400CT$ and it is averaged along the spanwise direction z . The plots show a peak at $fD/U = 0.4$ for the streamwise velocity and two peaks at $fD/U = 0.2$ and $fD/U = 0.6$ for the normal velocity: this is in line with the results reported by [4].

The R_{11} component of the Reynolds stress tensor is evaluated in the station at $x/D = 2.02$ according to (4). The results are reported in Fig. 3a for two different choices of the average windows T and Z and they are compared with the experimental results from [4]. The numerical simulation is performed for $T = 400CT$ with a spanwise extension $Z = 3D$ and it is used to generate a global database. Two subsets are extracted from this database by selecting different extensions in time and spanwise direction: ($T = 100CT, Z = 3D/20$) and ($T = 5CT, Z = 3D$). In this problem the computational cost is directly proportional to both the spanwise extension and the duration of the simulated time window. This means that the same computational cost could be associated to the two subsets. However, the results reported in Fig. 3a show that the estimation of the Reynolds stresses performed from the dataset with ($T = 100CT, Z = 3D/20$) is significantly closer to the experimental results. In contrast, the results obtained from the dataset with ($T = 5CT, Z = 3D$) appear to be far from statistical convergence since they are characterised by a strongly asymmetric

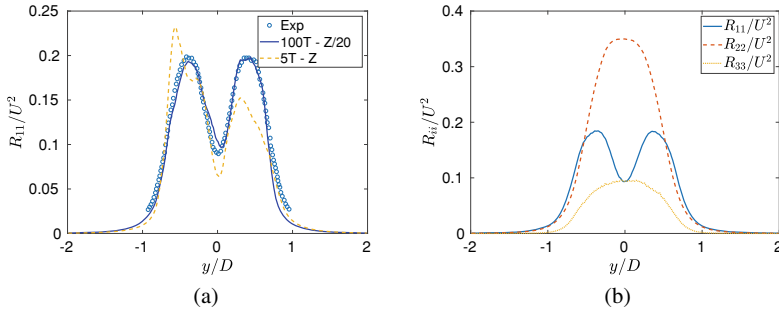


Fig. 3 Effects of the choice on the spanwise extension and time window size on R_{11} (a) and comparison of the Reynolds stresses in the three directions (b) for the control station at $x/L = 2.02$

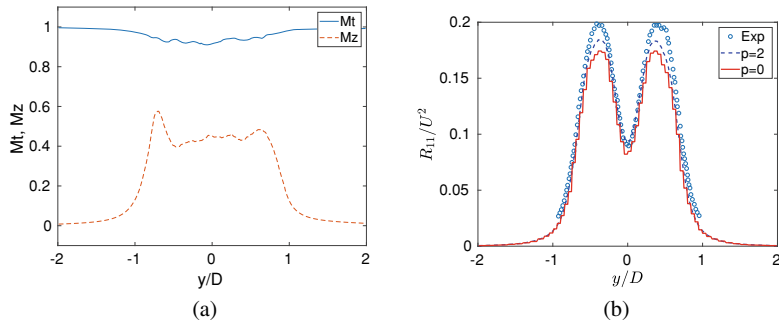


Fig. 4 Indices of statistical resolution (a) and element-wise modal filtering (b) for the control station at $x/L = 2.02$

distribution. This first test suggests that in the considered test case time averaging is more efficient with respect to averaging in the spanwise direction. This can be explained by the fact that in this problem the flow field is dominated by the streamwise velocity and so the transport of turbulent structures in the streamwise direction determines strong temporal fluctuations for a fixed control station. Furthermore, the streamwise fluctuations are significantly stronger with respect to the spanwise fluctuations, as confirmed by the distribution reported in Fig. 3b.

In order to verify the possibility to link the statistical efficiency of time and spanwise directions to a measurable quantity the indices M_t and M_z are evaluated and reported in Fig. 4a: the plot shows clearly that the index M_t is systematically higher than the index M_z for all the values of y . This result suggests a general strategy which can be applied for statistically steady flows with a direction of spatial homogeneity. First of all, a preliminary simulation can be done by choosing the minimum spanwise extension which is necessary to allow the correct evolution of the largest structures and running the simulation for a few convective times. Then the results of this preliminary simulation can be used to estimate the indices M_t and M_z which provide insight in the statistical efficiency of time and spanwise direction:

finally, a full simulation can be set up by increasing the runtime or the spanwise extension, according to the indications provided by M_t and M_z .

Finally, the plot in Fig. 4b shows a comparison between the experimental values of R_{11} and the numerical predictions evaluated according to (4) for the full order results ($p = 2$) and for a filtered solution ($p = 0$) obtained by truncating the results of the $p = 2$ simulation to the first term in each element. This makes it possible to quantify the contributions given by the turbulent structures whose size is comparable to the size of the element. The results show that this contribution is small in the present simulation and so it is possible to assume that the contribution of the subgrid scales is even smaller. This explains why the implicit LES approach provides reasonable results. However, for problems characterised by higher values of Reynolds number, the contributions associated to the subgrid scales can be more important and so an explicit LES with a subgrid model would be more suitable. In that case, the modal nature of the DG solution can be exploited to develop dynamic approaches for the subgrid scale model, following for example the guidelines provided by [5]. As a final remark, in this work the extensions of the spanwise and temporal windows are normalised with respect to the diameter and the convective time: it would be possible to get more physical insight by normalising with respect to the spatial and temporal turbulence scales. However, the use of diameter and convective time simplifies the investigation since these values are known a-priori.

Acknowledgements We acknowledge the CINECA award under the ISCRA initiative for the availability of high performance computing resources and support.

References

1. A. Ferrero, F. Larocca, M. Germano, G. Scovazzi, A study on the statistical convergence of turbulence simulations around a cylinder, in *AIP Conference Proceedings*, vol. 2293(1) (2020)
2. M.R. Mankbadi, N.J. Georgiadis, Examination of parameters affecting large-eddy simulations of flow past a square cylinder. *AIAA J.* **53**, 1706–1712 (2015)
3. F. Bassi, L. Botti, A. Colombo, D.A. Di Pietro, P. Tesini, On the flexibility of agglomeration based physical space discontinuous Galerkin discretizations. *J. Comput. Phys.* **231**(1), 45–65 (2012)
4. P. Parnaudeau, J. Carlier, D. Heitz, E. Lamballais, Experimental and numerical studies of the flow over a circular cylinder at Reynolds number 3900. *Phys. Fluids* **20**, (2008)
5. A. Abbà, L. Bonaventura, M. Nini, M. Restelli, Dynamic models for large eddy simulation of compressible flows with a high order DG method. *Comput. Fluids* **122**, 209–222 (2015)

Asymmetry in Wake of Oscillating Foils with Combined Pitching and Heaving Motion



Suyash Verma and Arman Hemmati

Abstract This is a numerical study of the dynamics of primary and secondary vortex structures in high performance wakes of oscillating foils with combined heaving and pitching motion at Reynolds number of 8000. The peak performance is associated with either high efficiency or large thrust production, which are achieved at specific motion settings. Using three-dimensional direct numerical simulations, we characterized and compared the dominant instability features for two peak propulsive wakes of a teardrop foil. Spanwise vortex dislocations on paired rollers for high efficiency setting revealed qualitative features of elliptic instability of primary vortex that led to tongue-like, and crescent shaped valley and bulge formations. However, asymmetric shedding of vortex dipoles in large thrust production setting depicted large scale dislocations in the form of conjoint hairpin-horseshoe formations that emerged out of vortex cores. These hinted at the dominance of both core and centrifugal instability. Here, we propose a hypothesis that large scale dislocations have greater influence on the spatial topology of secondary vortex structures compared to their temporal topology, which were observed to be similar in both wakes.

1 Introduction

Dynamics of coherent structures (e.g., *rollers*) in turbulent wakes of oscillating hydrofoils have been observed to play a dominant role in propulsive mechanisms of various marine biological species, such as fish [1]. These studies have contributed to the development of efficient underwater propulsors and energy harvesting technologies. The fluid mechanics of these systems, however, still require further analysis to optimize their design. Mainly, instability mechanisms in wakes of oscillating hydrofoils that could promote vortex dislocations on rollers and subsequent formation of secondary vortex pairs (or *ribs*), remains not fully explored at this time. This will also enrich our

S. Verma · A. Hemmati (✉)
University of Alberta, 116 St & 85 Ave, Edmonton, AB, Canada
e-mail: arman.hemmati@ualberta.ca

S. Verma
e-mail: suyash@ualberta.ca

© The Author(s), under exclusive license to Springer Nature Switzerland AG 2021
R. Örlü et al. (eds.), *Progress in Turbulence IX*, Springer Proceedings in Physics 267,
https://doi.org/10.1007/978-3-030-80716-0_13

understanding of dominant and complex interactions between the large scale vortex structures (*rollers* and *ribs*) that directly impact flow properties, such as pressure and shear distribution with implications on flow entrainment and turbulence.

Numerical [2] and experimental [3] studies on three-dimensional wakes of stationary bluff bodies (e.g., cylinders) have revealed the presence of dominant instability modes (Mode-A and Mode-B) that governed the wake transition at low Reynolds numbers (Re). The characteristic features of the instability further detailed the mechanism of secondary vortex formation, which originated either on account of deforming primary vortex core (Mode-A) or streamwise stretching of the braid shear layer between the primary vortex rollers [3]. Direct numerical simulations (DNS) have also provided capabilities and insights into modeling of prominent instability modes in wakes of rigid bodies (e.g., hydrofoils) that execute an oscillatory motion, either pitching [4] or heaving [5]. For both motions, instability modes were characterized with respect to the spanwise wavelength of the counter-rotating rib pair as well as their temporal periodicity in each full and half shedding cycle, respectively. Although mechanism of centrifugal instability was hinted as being responsible for the formation of rib pairs, an elaborate discussion is still lacking [4]. Evaluation of instability and secondary vortex characteristics for an oscillatory hydrofoil in combined heaving and pitching motion is not fully explored.

This study focused on the quantitative and qualitative analyses of three-dimensional spatio-temporal characteristics of both primary and secondary vortex formations in the wake of an infinite span oscillating foil with a combined pitching and heaving motion. Specifically, the study focused on wakes corresponding to peak propulsive performance regimes for high propulsive efficiency and large thrust generation. Identification and comparative assessments of vortex dislocations on the primary vortex rollers are discussed along with their association to previously identified elliptic and centrifugal instability of the vortex core, and braid shear layer, respectively. The paper is setup such that numerical method is described first, followed by discussion of the results and major conclusions.

2 Problem Description

The wake of an infinite span teardrop hydrofoil was numerically simulated using DNS with motion parameters corresponding to peak propulsive performance based on a recent experimental study [6]. We utilized the Overset Grid Assembly (OGA) method in OpenFOAM to perform the combined pitching and heaving motions. OGA is based on a finite volume solver, which has been well validated for study of wake and vortex dynamics [7]. The three-dimensional Navier–Stokes equations were solved directly at a chord based Reynolds number of $Re = U_\infty c / \nu = 8000$. Second-order accurate temporal (backward Euler) and spatial (central-difference) schemes were employed for discretization of equations.

The computational domain included a stationary background grid and another overlapping grid that modeled the hydrofoil motion. The background grid extended

$20c$, $16c$ and $2\pi c$ in the streamwise, cross-stream and spanwise directions, respectively. A combined heaving and pitching motions were prescribed for the foil, which followed sinusoidal formulations:

$$h = h_0 \sin(2\pi ft) \quad \text{and} \quad \theta = \theta_0 \sin(2\pi ft + \phi).$$

Here, h , θ , f and ϕ denote the heave and pitch amplitude, oscillation frequency and phase offset, respectively. A uniform velocity along with a zero pressure gradient was assigned at the inlet boundary, while a Neumann outflow condition was prescribed at the outlet boundary. The domain sides were assigned a periodic boundary condition. All remaining edges were assigned a zero gradient condition for both velocity and pressure whereas a no-slip wall condition was ensured for the moving foil. More details on the validation for the numerical solver can be found in [7].

Performance results from [6] indicated that a high efficiency (and small thrust) was achieved when $h_0 = 0.125$, $\theta_0 = 10^\circ$, $f^* = 0.48$ and $\phi = 270^\circ$. Similarly, a large thrust generation (and low efficiency) was observed at $h_0 = 0.375$, $\theta_0 = 15^\circ$, $f^* = 0.64$ and $\phi = 330^\circ$. Thus, the prominent instability features were evaluated in the wake of foils within this parameter space.

3 Results and Discussion

Using isosurfaces of normalized Q -criterion ($Q^* = Qc^2/U_\infty^2$), we first describe the primary vortex mode corresponding to the wake of high efficiency (η) motion setting along with the prominent vortex dislocations on the spanwise rollers (Fig. 1a). Paired counter-rotating vortices ($2P^T$ mode) were observed near the foil, which merged to form reverse Von Kármán wake downstream. Fine scale corrugations were evident on the upstream leading edge roller (LEV_{ac}), which hints at development of a spanwise instability. Besides, the merger of a weaker leading edge vortex structure (LEV_c) with the stronger trailing edge vortex (TEV_c) formed a structure with larger circulation that led to a stronger strain field intensity. This further promoted formations of dislocations (identified as valleys and bulges) with larger depth to width ratios compared to upstream corrugations. Qualitatively, these dislocation features seem comparable to the tongue-like formations, and crescent shaped features, that were previously identified in the wake of stationary bluff bodies [2, 8]. Such tongue-like formations were attributed to a characteristic instability of primary vortex core [8], whose mechanism was also described later in terms of elliptic instability of a vortex pair [3, 9]. We made a quantitative assessment for the ratio of spanwise wavelength (λ_i) for dislocations to the diameter of invariant vortex core (d_{inv}). The estimated ratio was close to 2, similar to the observations of [9]. Thus, both quantitative and qualitative evidence suggested that an elliptic instability of vortex core should be prominent in the high η wake. Investigation of the asymmetric wake (dominated by vortex dipoles or couples) for large thrust settings revealed large scale dislocations in the form of conjoint hairpin-horseshoe vortex structures (Fig. 1b). This resembled

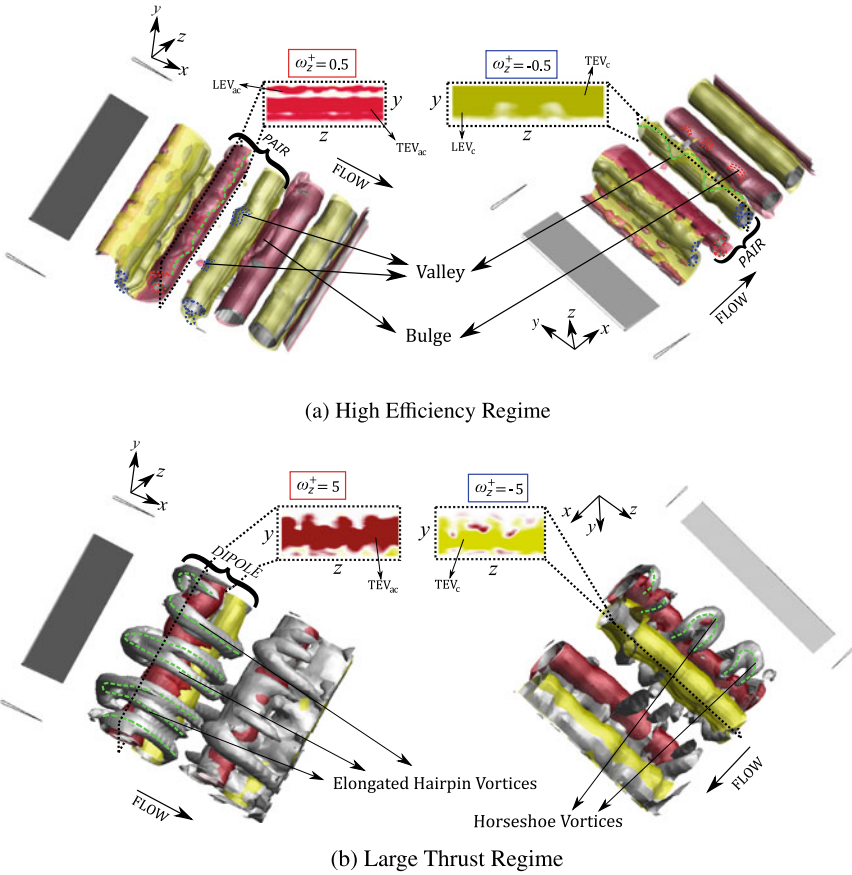


Fig. 1 Vortex dislocations identified on primary vortex structures in the wake (**a** $Q^* = 0.01$ and **b** $Q^* = 0.09$). Figures on *left* and *right* depict the *top* and *bottom* view, respectively

qualitative characteristics of core instability. A mechanism for emergence of hairpin vortices out of vortex cores had been proposed [2]. However, conjoint large scale structures observed for our asymmetric wake was unique in terms of spatial topology for hairpin legs that wrapped around coupled spanwise rollers. Interaction of these hairpin legs with the braid vorticity region, i.e. small scale vorticity between two subsequent dipoles, could indicate a centrifugal instability mechanism, which can further lead to formations of secondary vortex pairs. Ratio of λ_i/d_{inv} revealed a value equal to 1.813, which was similar to that of high efficiency wake. Detailed Floquet stability analyses could provide more insight into the dominant instability modes in both wakes.

The analyses of instability characteristics hint at their apparent contribution to the formation of secondary streamwise vortices or *ribs* [3, 9]. We therefore assessed the spatio-temporal characteristics of counter-rotating *rib* pairs in the wake. Figure 2

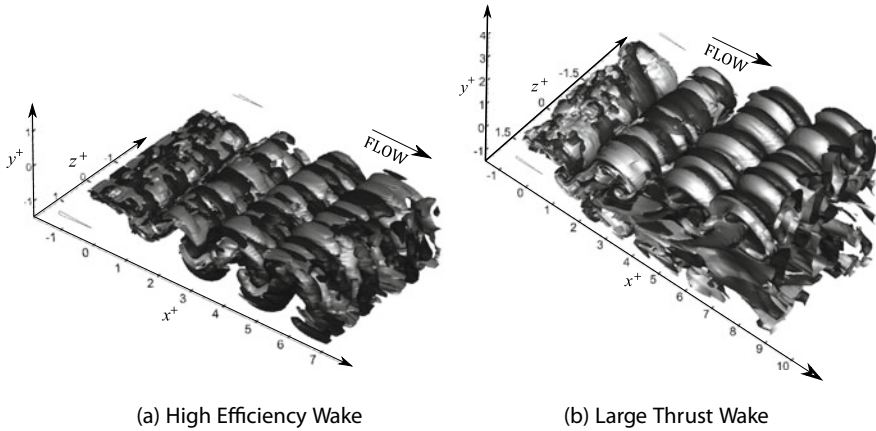


Fig. 2 Secondary vortex structures in the wake of an oscillating foil for two performance regimes, identified using iso-surfaces of ω_x

depicts *ribs* structures for the high efficiency and large thrust cases. In case of the former, continuous and alternating tubes (in spanwise direction) appeared to pass over one side of the spanwise rollers. It revealed a qualitative similarity to Mode-B arrangement in the wake of stationary cylinders [8]. In contrast, the large thrust generation wake depicted an asymmetric spatial topology. Paired ribs wrapped around each dipole while being connected in the braid vorticity region. This topology appeared qualitatively similar to Long wavelength mode [4] and Mode-A [5] for purely pitching and heaving foils, respectively. The looped *rib* pairs further reflected a qualitative similarity to elongated hairpin legs in Fig. 1b, which wrapped around the coupled *rollers*. This similarity supports the argument of a centrifugal instability mechanism [2] for interaction of developed hairpin-horseshoe structures with the braid vorticity. It also explains the interconnected nature of *rib* pairs between two subsequent dipoles. The spanwise wavelength ($\lambda_z = \lambda/c$) and temporal periodicity (with respect to shedding cycles) of the *rib* configurations were also evaluated using statistical correlations of streamwise vorticity (ω_x) on specific spanwise planes that passed through individual primary vortex cores. The estimated λ_z for both wakes was in the range of 0.7–0.8, thereby supporting our qualitative observations that their characteristics were similar to the purely pitching [4] or heaving foils [5]. The *rib* pairs further maintained their direction of rotation with each full shedding cycle. It is therefore apparent that large-scale vortex dislocations have greater influence on spatial topology of secondary structures, rather than causing changes in spanwise wavelength or streamwise periodicity for the two wakes.

4 Conclusions

The wakes corresponding to peak propulsive performance regimes of an oscillating foil with combined heaving and pitching motion were investigated numerically at $Re = 8000$. The high efficiency wake depicted fine scale spanwise corrugations on paired rollers ($2P$ mode) near the foil, whereas deeper valleys and bulges were observed for individual rollers downstream. These resembled tongue-like and crescent shaped formations, whose spanwise wavelength was approximately twice the diameter of invariant stream-tube within the core vortex. Such qualitative and quantitative evidence suggested that elliptic instability of the primary vortex core dominates the high efficiency wake. Contrarily, the wake of large thrust generating configuration depicted conjoint hairpin-horseshoe vortex formations that emerged out of the core, and led to an intense spanwise deformation of rollers. The core instability mechanism was prominent based on the quantitative estimation of the wavelength for these dislocations. Moreover, interaction of developed hairpin legs with the braid vorticity further revealed the possible association with formation of secondary vortex pairs, and hence a prominence of centrifugal instability. Evaluation of secondary vortex characteristics in the wakes further indicated resemblance to long wavelength mode and Mode-A observed previously for purely pitching and heaving foils, respectively. However, the asymmetric topology of the wrapped *rib* pairs around dipoles indicated an influence of the large scale dislocations observed for the wake in large thrust generation configuration. However, these dislocations did not affect the spanwise wavelength or temporal periodicity of *rib* pairs in both propulsive wakes.

Acknowledgements This research has received support from the Canada First Research Excellence Grant. The computational analysis was completed using Compute Canada clusters.

References

1. A.J. Smits, Undulatory and oscillatory swimming. *J. Fluid Mech.* (2019)
2. R. Mittal, S. Balachandar, Generation of streamwise vortical structures in bluff body wakes. *Phys. Rev. Lett.* (1995)
3. C.H.K. Williamson, Three-dimensional wake transition. *J. Fluid Mech.* (1996)
4. J. Deng, C.P. Caulfield, Three-dimensional transition after wake deflection behind a flapping foil. *Phys. Rev. E - Stat. Nonlinear Soft Matter Phys.* (2015)
5. L. Sun, J. Deng, X. Shao, Three-dimensional instabilities for the flow around a heaving foil. *Phys. Rev. E* (2018)
6. T. Van Buren, D. Floryan, A.J. Smits, Scaling and performance of simultaneously heaving and pitching foils. *AIAA J.* (2019)
7. S. Verma, A. Hemmati, Performance of overset mesh in modeling the wake of sharp-edge bodies. *Computation* (2020)
8. M. Brede, H. Eckelmann, D. Rockwell, On secondary vortices in the cylinder wake. *Phys. Fluids* (1996)
9. T. Leweke, C. Williamson, Cooperative elliptic instability of a vortex pair. *J. Fluid Mech.* **360**, 85–119 (1998)

Helical Structures in the Wake of Long Wall-Mounted Prisms at High Incident Angles



Arash Zargar and Arman Hemmati

Abstract The coherent wake structures behind a rectangular prism at different incidence angles are numerically studied at $Re = 250$. The results indicated that changing the incidence angle altered the critical Reynolds number at which the wake transitions to unsteady flow. The variation in wake dynamics and evolution of vortex structures are evaluated and characterized at high incidence angles. The change in the wake size and surface pressure distribution due to variations in the incidence angle are also related to the change in wake topology.

1 Introduction

The flow structures around a wall-mounted rectangular prism have various engineering applications at low Reynolds numbers, for example, in designing the cooling system of electronic chips, developing biomedical devices, and optimizing the performance of small heat exchangers. This has motivated extensive research on the characteristics of the wake of prisms at all ranges of Reynolds number. However, these studies focused only on small depth-to-height ratio prisms.

Rastan et al. [1] numerically studied the onset of vortex shedding for a wall-mounted prism with an aspect ratio of $AR = 7$ and reported that it starts at the Reynolds number of $75 < Re < 85$. They identified that the flow field of the prism remains steady at lower Reynolds numbers. Saha [2] investigated the effect of aspect ratio on the wake dynamics of a square prism at the Reynolds number of 250. They reported that the intensity of unsteadiness in the wake of a prism decreases by decreasing the aspect ratio. Thus, the wake of a square prism with an aspect ratio of 2 was classified as weakly unsteady, while the wake of a prism with $AR = 5$ appeared to be fully unsteady. Sakamoto et al. [3] mentioned that decreasing aspect ratio leads

A. Zargar · A. Hemmati (✉)

Department of Mechanical Engineering, University of Alberta, 10-203 Donadeo Innovation Centre for Engineering, 9211-116 Street NW, Edmonton, AB T6G 1H9, Canada
e-mail: arman.hemmati@ualberta.ca

A. Zargar
e-mail: zargar@ualberta.ca

to changing the vortex shedding characteristics from a Karman-like to an arc-type vortex shedding. Therefore, it can be inferred that changing the geometrical shape of the body would alter the onset of wake unsteadiness.

Characterizing the shape and orientation of structures in the wake of square prisms or circular cylinders can be categorized as a classical problem in fluid mechanics. Models of the wake of a square prism can be divided into two classes. The first class hypothesizes that there are different vortex structures, specifically tip, base, Karman type, and horseshoe vortices, in the wake. The origin and characteristics of these structures are different, and they can exist simultaneously in the wake [4, 6]. However, another hypothesis ponders the occurrence of a single arc-type structure in the wake, which connects tip, base, and Karman-type structures [5]. The most rigorous argument supporting the latter hypothesis is the fact that most studies captured a single dominant frequency in the wake of a wall-mounted square prim. This strongly hints at the presence of a single structure.

Most recently, Zargar et al. [7] numerically analyzed the flow dynamics behind a wall-mounted rectangular prism with a large depth-ratio at different incidence angles using Direct Numerical Simulations (DNS). They reported that there exists a critical incidence angle at which the flow behavior changes from steady to unsteady, while the flow is utterly steady at zero incident angle. Their results demonstrated that changing the incidence angle leads to the formation of evolving helical structures in the wake. They captured different peak frequencies above the critical incidence angle and demonstrated the characteristic length and origin of the peak frequencies. Furthermore, they established a skeleton model for the unsteady wake. This paper expands on their observations by highlighting particular changes to the surface parameters and wake dynamics after the onset of unsteadiness.

2 Problem Description

This study examined the effect of incidence angle on the unsteady wake dynamics and vortex interactions behind a long wall-mounted rectangular prism at $Re = 250$ by directly solving the three-dimensional Navier–Stokes and continuity equations in OpenFOAM. The prism had a height of h , and a width and length of $w = 0.83h$ and $l = 4.15h$, respectively. The long prism was placed at 10 different incidence angles from $i = 0^\circ$ to $i = 45^\circ$ at 5° increments with respect to the incoming flow. The computational domain extended $L \approx 35h$ in the x -direction, $12h \leq W \leq 15h$ in the y -direction and $H = 5h$ in the z -direction. The boundary conditions were set as uniform normal velocity (U_∞) at the inlet, Neumann condition for all flow parameters at all other boundaries, and no-slip wall condition for the ground and prism faces. The spatial grid consisted 3.9×10^6 – 5.2×10^6 hexahedral elements, while the temporal grid was uniform and set such that the Courant number remained below 0.8. Validation and verification of the simulations are described comprehensively in Zargar et al. [7].

3 Results

The effect of changing incidence angle on formation and evolution of coherent wake structures was examined by looking at the isosurfaces of normalized Q -criterion. Figure 1a shows that increasing the incidence angle leads to the formation of a vortex tube in the wake region. Furthermore, there was a critical range of incidence angle between $40^\circ \leq i \leq 45^\circ$, at which the wake behavior changed from steady to unsteady. This coincided with the formation of helical structures in the wake, which are identified in Fig. 1b.

Vorticity distribution is another important parameter in characterizing the shape of coherent structures in the wake. The flow behind a long-wall-mounted rectangular prism remained steady for the incidence angle of $i < 40^\circ$ at $Re = 250$, whereas it was unsteady at $i > 40^\circ$. To identify the wake features that led to the formation of unsteady flow, time-averaged streamwise vorticity distributions are compared for different incident angles in the wake of the long prism in Fig. 2. A single vortex pair with a large vorticity (V_t) can be recognized at all incident angles, which is associated with the vortex tube in the wake (similar to Fig. 1a). Increasing the incidence angle to $i = 45^\circ$ leads to the formation of an extra focal point in the wake that is identified as V_s in Fig. 2c. Zargar et al. [7] captured the formation of a vortical structure in the near wake of the long prism, which originated from the leading edge of the prism, inducing unsteady fluctuations in the wake. Figure 2 shows that the induced unsteady flow created an extra streamwise vortical structure that has not been captured in

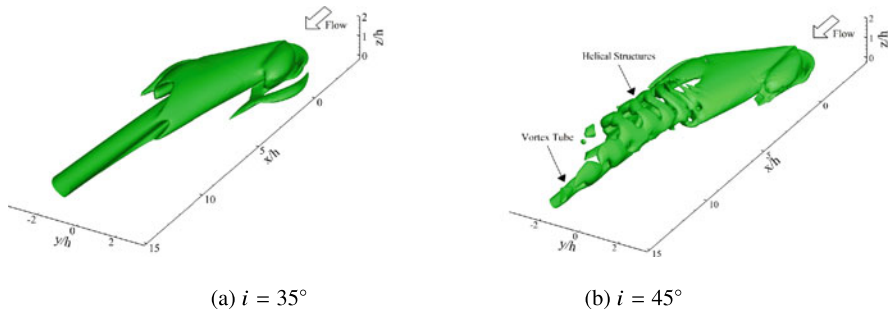


Fig. 1 Isosurface of $Q^* = 4.42 \times 10^{-2}$ at different incident angles at $Re = 250$. ($Q^* = \frac{Q \times h^2}{U_\infty^2}$)

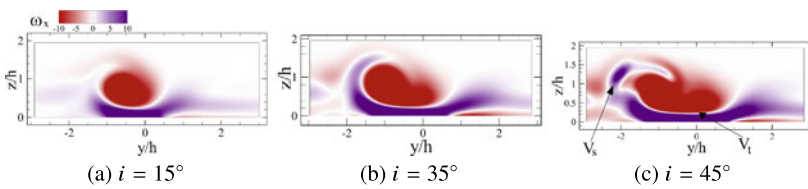


Fig. 2 Time-averaged vorticity distribution at $x/h = 7.5$ for different incidence angles

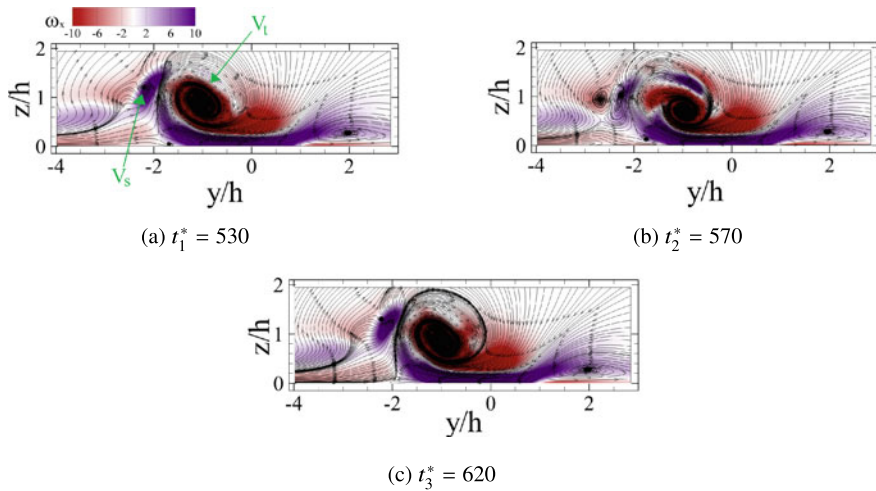


Fig. 3 Snapshot of vorticity contours overlaid by flow streamlines for $i = 45^\circ$ at $x/h = 7.5$

previous studies of square prisms. Following the terminology of Zargar et al. [7], this structure span out of the “Frontal-Tip-Vortex”.

Figure 3 shows snapshots of vorticity distribution in the wake at $t^* = 530, 570$ and 620 for the case of $i = 45^\circ$. These plots are overlaid by instantaneous flow streamlines. These results reveal that the position and size of vortical structures associated with the vortex tube (V_t) are approximately steady. However, the extra streamwise wake structure (V_s) is strongly unsteady, which leads to the formation of complex vortex interactions in the wake. The vortex dynamics observed here is enormously different from the previously proposed wake models for short depth-ratio rectangular prisms. Zargar et al. [7] showed that helical structures in the wake at $i = 45^\circ$ evolve at a low frequency, which leads to periods of strong and weaker flow fluctuations. Figure 3 shows that variations in the vorticity distribution coincided with the evolution of helical structures in the wake.

The change in wake dynamics at high incidence angles results in alterations in the wake size, and hence the aerodynamics forces and moments. Figure 4 shows the time-averaged streamlines calculated at the first cell from the ground plane. Comparing the position of highlighted saddle points in the wake for the cases of $i = 0^\circ$ and 25° revealed that wake loses its symmetry in the y -direction at higher incidence angle. It is also notable that the distribution of critical points for the case of $i = 45^\circ$ altered in comparison to the lower incidence angles. This indicates that there has been a change in wake dynamics at this incident angle. If position of the last saddle point (L_s) in the wake is considered as the flow reattachment point to the ground plane, the distance of this saddle point from the body is an appropriate measure for the wake size. As shown in Fig. 5a, distance of the flow reattachment point is approximately constant for $i \leq 30^\circ$. However, the last saddle point distance (L_s), and thus the wake size, increased significantly for $i \geq 35^\circ$.

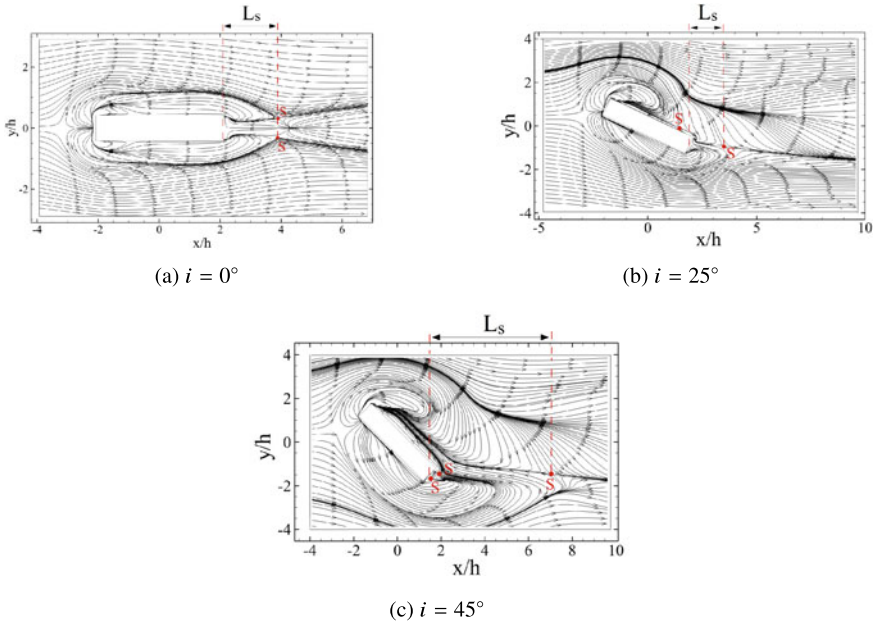


Fig. 4 Time-averaged streamlines based on velocity vectors at the first cell from the ground

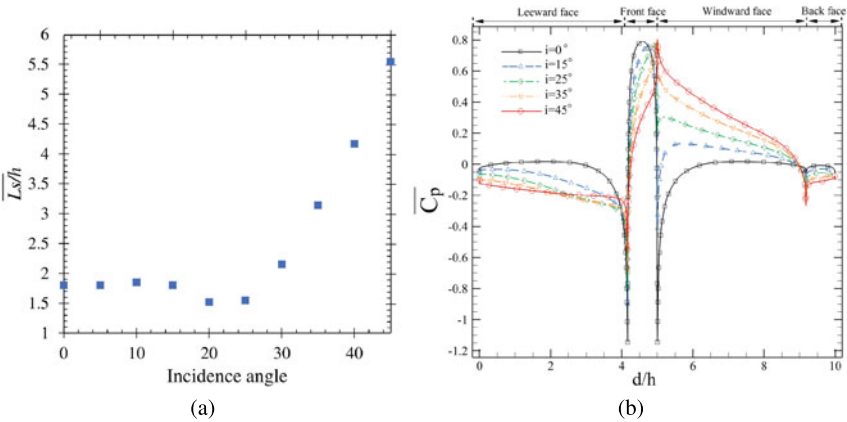


Fig. 5 The distance between the last saddle point and the prism's back-face and the surface pressure coefficient on the mid-height of the prism at different incidence angles

Figure 5b shows that changing the incidence angle altered the surface pressure distribution on the faces of the prism, which led to alteration of the force and moment coefficients. Increasing the incidence angle disrupted the surface pressure distribution symmetry and moved location of the stagnation point on the prism. At $i = 0^\circ$, the pressure coefficient was negative on the frontal part of the side faces due to the

formation of small separation bubbles. At $i = 45^\circ$, the stagnation point moved on the edge of the windward and front faces. This modification increased the pressure coefficient and altered the pressure distribution on surfaces of the prism. This is a sufficient measure to identify onset of the formation of vortical structures, which is important in development of mechanisms to control the wake.

4 Conclusion

This study numerically examined the wake of a wall-mounted rectangular prism with an aspect ratio of 1.2 and depth ratio of 4.15 at different incidence angles. The Reynolds number based on the height of the prism was $Re = 250$, which constituted a steady wake at zero incident angle. The results demonstrated that increasing the incidence angle leads to the formation of a vortex tube in the wake. At a critical incidence angle of $40^\circ \leq i \leq 45^\circ$, the flow behavior changed to unsteady, which coincided with the formation of helical structures. The time-averaged vorticity distribution revealed an extra focal point in the wake due to the formation of a new unsteady vortical structure. The results demonstrated that changing the incidence angle altered position of the stagnation point and changed the surface pressure distribution as a means to identify the onset of wake unsteadiness, and thus formation of helical structures.

Acknowledgements This work received support from Future Energy Systems Institute and Alberta Innovates. Simulations were completed using Compute Canada resources.

References

1. M.R. Rastan, A. Sohankar, M.M. Alam, Low-Reynolds-number flow around a wall-mounted square cylinder: flow structures onset of vortex shedding. *Phys. Fluids* **29**(10), (2017)
2. A.K. Saha, Unsteady flow past a finite square cylinder mounted on a wall at low Reynolds number. *Comput. Fluids* **88**, 599–615 (2013)
3. H. Sakamoto, M. Arie, Vortex shedding from a rectangular prism and a circular cylinder placed vertically in a turbulent boundary layer. *J. Fluid Mech.* **126** (1983)
4. H.F. Wang, Y. Zhou, C.K. Chan, W.O. Wong, K.S. Lam, Flow structure around a finite-length square prism, in *15th Australasian Fluid Mechanics Conference* (2004)
5. H.F. Wang, Y. Zhou, The finite-length square cylinder near wake. *J. Fluid Mech.* (2009)
6. B.L. da Silva, R. Chakravarty, D. Sumner, D.J. Bergstrom, Aerodynamic forces and three-dimensional flow structures in the mean wake of a surface-mounted finite-height square prism. *Int. J. Heat Fluid Flow* **83**, (2020)
7. A. Zargar, A. Gungor, A. Tarokh, A. Hemmati, Coherent structures in the wake of a long wall-mounted rectangular prism at large incident angles. *Phys. Rev. Fluids* **6**(3), (2021)

A Spatially Accelerating Turbulent Flow with Longitudinally Moving Walls



Matthew Falcone and Shuisheng He

Abstract A new theory is proposed to explain the development of spatially accelerating flows with the aim of helping to resolve some of the long-standing issues related to the understanding of their development. This new theory postulates that on the onset of the acceleration a new laminar boundary layer forms superimposed on the existing turbulent flow with the development of the accelerating flow characterised by the development and subsequent transition of the new boundary layer. The theory has been tested using Direct Numerical Simulations of an innovative idealised acceleration using an accelerating moving wall which results in a relative acceleration between the wall and the fluid. The results indicated that the flow in general behaves similarly to previous studies and is found to support the new theory. $\overline{u'u'}$ is found to exhibit downstream growth from the onset of the acceleration consistent with the amplification of the near-wall structures by the new boundary layer. Increases in the wall-normal and spanwise stresses does not occur until the onset of transition where turbulent spots begin to develop. The theory is also supported by the lack of response from the eddy viscosity prior to the new boundary layer's transition.

1 Introduction

Spatial acceleration is encountered in a wide range of engineering applications such as turbomachinery and airfoils in addition to natural flows. However, despite its prevalence, spatial acceleration contains interesting and not well-understood phenomena including laminarisation which can have a significant effect of flow physics. Laminarisation occurs when a turbulent flow reverts to a more laminar-like state and has been found to occur in flows undergoing severe spatial acceleration. The process

M. Falcone (✉) · S. He

Department of Mechanical Engineering, University of Sheffield, Sheffield, UK

e-mail: mfalcone1@sheffield.ac.uk

S. He

e-mail: s.he@sheffield.ac.uk

by which this reversion occurs has become known as the island of ignorance. For subsonic flows, spatial acceleration is typically imposed by reducing the effective flow area which results in an increasing velocity due to mass conservation. The resulting flow physics is thus complicated by the effect of streamline contraction which results from the reduction in flow area.

Much of the current understanding of spatial acceleration derives from the seminal work of Narasimha and Sreenivasan [4], who split the process of laminarisation into four regions: Fully turbulent (I), the region after the onset of the acceleration where the flow remains turbulent; reverse transitional (II), the region where the flow begins to become more laminar-like corresponding to the location of the island of ignorance; quasi-laminar (III), where the statistics that describe the flow tend towards values more consistent with a laminar flow; and retransition (IV), where the flow begins to return to the turbulent state after the removal of the acceleration. The cause of the laminarisation was not found to be due to a significant reduction in the magnitude of the turbulent stresses, which were in fact found to be near-frozen, but due to their relative domination by the increasing pressure gradient which results from the acceleration. This phenomenon has since been referred to as ‘soft’ laminarisation [3]. This also raises important questions as to why the Reynolds stresses freeze with the onset of acceleration.

The new theory proposed here is that on the onset of the acceleration a new laminar boundary layer forms superimposed on the existing turbulent flow with the phenomena of the accelerating flow characterised by the development, growth and subsequent breakdown to turbulence of this new boundary layer in a process akin to bypass transition. As will be shown, this theory has the potential to explain aspects of spatial acceleration not well explained by the current theory including the cause of the frozen Reynolds stresses. It should also be noted that there are some key differences between the new theory and the current understanding of spatial acceleration. Firstly, previous studies have alluded to the development of a laminar sub-boundary layer as a result of the laminarisation [4]. Here, we propose that the new boundary layer develops from the onset of the acceleration and hence would develop irrespective of the presence of laminarisation. Secondly, a key aspect of the new theory is that the onset of transition/retransition is, like bypass transition, linked to the development of instabilities in the new laminar boundary layer and is not inherently linked to the end of the acceleration.

This paper presents Direct Numerical Simulations (DNS) of an idealised spatially accelerating flow which has utilised longitudinally non-uniform moving walls to provide a relative spatial acceleration. The purpose of this is to understand the effect of flow acceleration on a simpler flow setup to test the potential of this new theory without some of the complex physics associated with typical spatially accelerating flows including streamline contraction.

2 Methodology

The DNS was performed using an ‘in-house’ channel flow solver, CHAPSim [1]. The solver uses a temporal discretisation comprising a third-order, low-storage Runge-Kutta scheme for the convective terms and the implicit second-order Crank-Nicolson scheme for the diffusive terms. The idealised acceleration was implemented by modifying the streamwise velocity boundary condition of a channel flow so that the velocity opposed the direction of the flow, with the magnitude of the wall velocity becoming larger with downstream distance resulting in a relative acceleration. This is shown in Fig. 1 where the arrows represent the wall velocity and the yellow highlighted region is where acceleration occurs. In this paper, a linear acceleration is presented such that the wall velocity is defined as $U_w = -Cx$, where C is a positive constant. Given the absolute bulk fluid velocity, U_0 is constant, the result is an increasing relative velocity between the wall and the fluid: $U_{rel} = U_0 + Cx$.

A single case is shown in this paper with an inlet Reynolds number based on the half-channel height $Re_0 = U_{rel}\delta/\nu = 2800$ ($Re_{\tau,0} = 176$). The flow is linearly accelerated over 15 half-channel heights to $Re_1 = 5600$ ($Re_{\tau,1} = 324$). The domain size ($X \times Y \times Z$) was $30\delta \times 2\delta \times 4\delta$ with a mesh of $1620 \times 288 \times 360$. The changes in wall, absolute and relative velocity for the case are shown in the line plot in Fig. 1.

3 Results and Discussion

The instantaneous results highlight the key features of the development of the relative spatial acceleration. Figure 2 shows the contour plots of the instantaneous streamwise (Fig. 2a) and wall-normal (Fig. 2b) velocity fluctuations at $y^{+0} = 4.9$. The red line

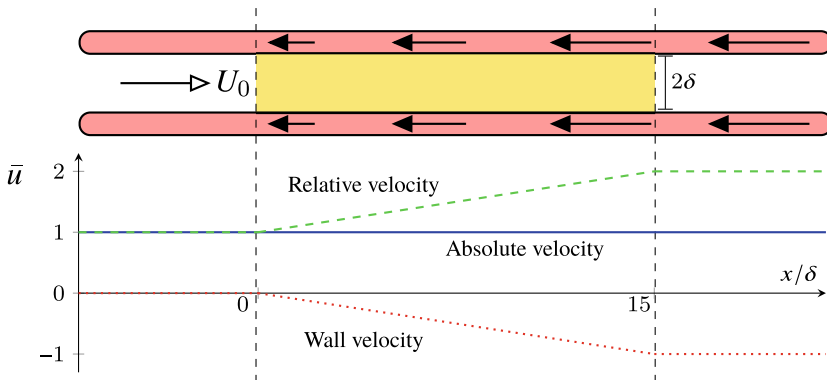


Fig. 1 Schematic of the methodology used to create the relative acceleration. Top: the walls of a channel flow with the arrows representing the wall velocity. Bottom: The absolute, wall, and relative flow velocities for the case. The dashed lines represent the start and the end of the acceleration

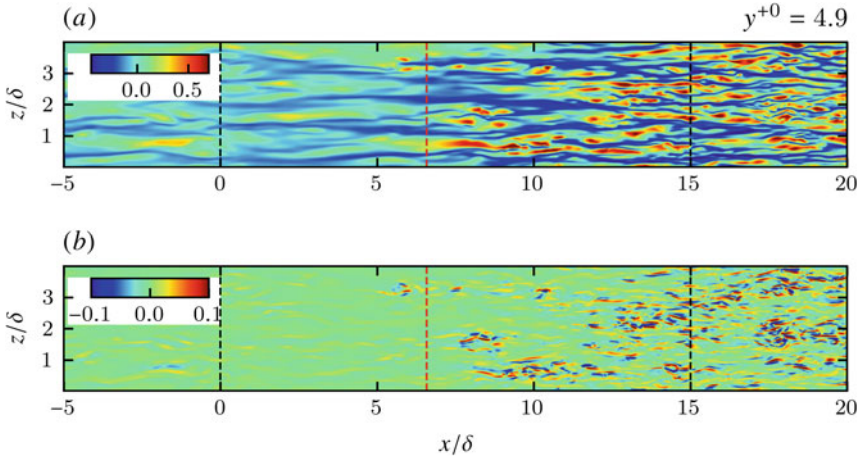


Fig. 2 $x - z$ contours of u' (a), and v' (b). Black lines at $x/\delta = 0$ and $x/\delta = 15$ represents the start and end of the acceleration. The red line indicates the onset of transition as indicated by $C_{f,min}$

indicates the approximate location of the onset of transition. Prior to the start of the acceleration, u' exhibits the ubiquitous near-wall streaky structures present in wall shear flows. After the start of the acceleration at $x/\delta = 0$, the near-wall streaks strengthen mildly. At $x/\delta \approx 6$, localised spots begin to appear in the contour plot indicated by the patches of larger magnitude fluctuations of shorter spatial scale. These spots, which initially coexist with the strengthened streaks, grow as they are convected downstream as indicated by the spots at different stages of development (at $x/\delta \approx 6$, $x/\delta \approx 8$, $x/\delta \approx 10$). By the end of the acceleration at $x/\delta = 15$, new turbulence is found to extend across the spanwise extent of the wall. In contrast, v' remains unaffected by the acceleration until the onset of transition, where spots appear coincident with the spots in u' .

This development can be explained by the new theory. The new boundary layer, forming on the onset of the acceleration, modulates the pre-existing turbulent structures resulting in the stretching of the near-wall streaks by the mean shear associated with the developing boundary layer and extracting energy from the mean flow as indicated in Fig. 2a. Eventually, similar to bypass transition, secondary instabilities develop on these strengthened streaks resulting in their breakdown forming turbulent spots. Given the streaks are streamwise turbulent structures, their strengthening primarily affects u' and thus v' does not increase until the streaks breakdown with the onset of transition. The development of the fluctuations exhibits similarities to contour plots found in studies of bypass transition [2]. Consequently, the stages of transition in this flow can be described similarly to Jacobs and Durbin [2] with pre-transition ($0 < x/\delta \lesssim 6$), transition ($6 \lesssim x/\delta \lesssim 15$), and fully turbulent ($x/\delta \gtrsim 15$).

The flows can be further characterised through statistics. Figure 3a shows the development of the maximum normal Reynolds stresses to illustrate the disturbance energy growth. $\overline{u'u'}$ exhibits downstream growth from the start of the acceleration

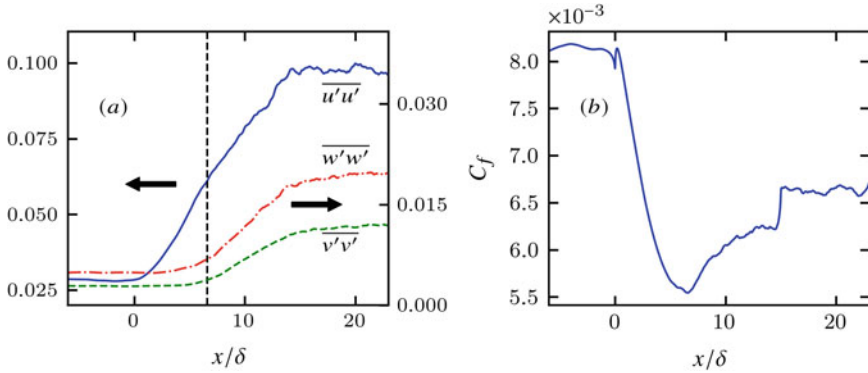


Fig. 3 **a** The maximum normal Reynolds stresses against x/δ . Each component is annotated in figure. The vertical line represents the location of $C_{f,min}$. **b** Skin friction coefficient, C_f

similarly to studies of spatial acceleration [5], associated with rises in production, while $\overline{v'v'}$ and $\overline{w'w'}$ shows a clear delay until the onset of transition which is consistent with Fig. 2 and is indicative of the freezing of wall-normal and spanwise stresses observed in spatial acceleration. This delay is also associated with the response of pressure strain (not presented) which until the onset of transition remains subdued. Figure 3b shows the development of the skin friction coefficient, C_f . After the start of the acceleration, C_f rises briefly before falling rapidly due to the increasing velocity and reaches a minimum before increasing rapidly following the onset of transition. $C_{f,min}$, similar to bypass transition appears to be an indicator of the location of the onset of transition. These results show that in this case the onset of transition occurs well before the end of the acceleration. This indicates that, as suggested by the new theory, transition is not inherently linked to the end of the acceleration.

Figure 4a shows that the Reynolds shear stress, $\overline{u'v'}$ increases by $\sim 60\%$ during pre-transition which is limited to the near-wall region ($y^+ \sim < 60$). With the onset of transition, $\overline{u'v'}$ increases over a broad wall-normal region, the extent of which increases with downstream distance. These changes are again consistent with previous investigations of spatial acceleration [5]. The eddy viscosity, μ_t is presented in Fig. 4b which shows that during pre-transition it remains constant. This is significant as it implies that the increasing $\overline{u'v'}$ during pre-transition is entirely related to the increase in mean shear consistent with a laminar-like response of the flow to the acceleration during pre-transition. After the onset of transition, the eddy viscosity begins increasing progressively from wall to the centre of the channel.

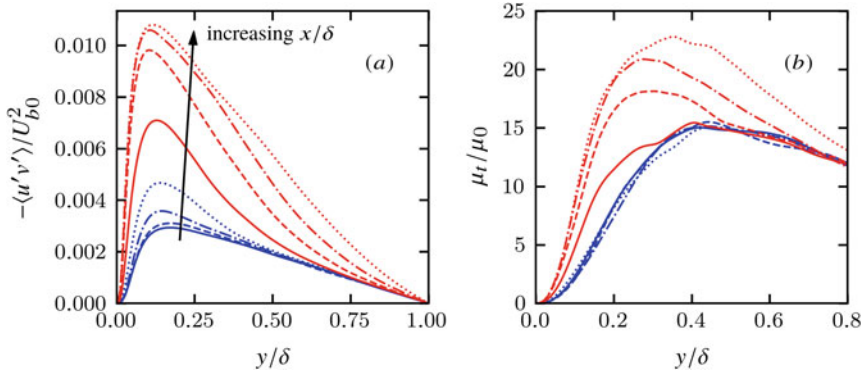


Fig. 4 **a** Reynolds shear stress, $\overline{u'v'}$ and **b** eddy viscosity, μ_t against y/δ . $x/\delta \in \{0, 2, 4, 6, 9, 13, 17, 21\}$. Blue lines indicate locations before transition; red lines those after

4 Conclusion

An innovative methodology has been used to test a new theory for spatially accelerating flows. The methodology uses an accelerating moving wall to create an idealised spatial acceleration which replicates many of the key developments found in conventional spatial acceleration. It has been found that the new theory is well-supported by the development of the flow and future work will include testing the new theory on more conventional spatially accelerating flows.

Acknowledgements The authors would like to thank: UK Turbulence Consortium for HPC compute time on ARCHER (Grant EP/R029326/1); CCP-NTH and Dr Wei Wang for the continuous development of the CHAPSim code (Grant EP/T026685/1). A much expanded paper has been submitted for journal publication.

References

1. S. He, M. Seddighi, Turbulence in transient channel flow. *Journal of Fluid Mechanics* **715**, 60–102 (2013). <https://doi.org/10.1017/jfm.2012.498>
2. R.G. Jacobs, P.A. Durbin, Simulations of bypass transition. *Journal of Fluid Mechanics* **428**, 185–212 (2001). <https://doi.org/10.1017/S0022112000002469>
3. R. Narasimha, K. Sreenivasan, Relaminarization of Fluid Flows. *Advances in Applied Mechanics* **19**, 221–309 (1979)
4. R. Narasimha, K.R. Sreenivasan, Relaminarization in highly accelerated turbulent boundary layers. *Journal of Fluid Mechanics* **61**(3), 417–447 (1973)
5. D. Warnack, H.H. Fernholz, The effects of a favourable pressure gradient and of the Reynolds number on an incompressible axisymmetric turbulent boundary layer. Part 2. The boundary layer with relaminarization. *Journal of Fluid Mechanics* **359**, 357–381 (1998). <https://doi.org/10.1017/S0022112097008501>

Dissimilarity Between Heat and Momentum Transfer of Turbulent Heat Transfer over Surfaces with Hemisphere Protrusions



Rika Nagura, Yusuke Kuwata, and Kazuhiko Suga

Abstract To explore how the roughness arrangement affects the turbulent heat transfer, direct numerical simulations of turbulent heat transfer over walls with regularly distributing hemisphere protrusions were performed by the lattice Boltzmann method. The friction Reynolds number was fixed at 660 and the fluid Prandtl number was 0.71 assuming an air flow. The roughness increases the momentum transfer more than the heat transfer. The Reynolds analogy factor, which measures the dissimilarity between the momentum and heat transfer, can be expressed as a function of the skin friction coefficient, inner-scaled equivalent roughness, and Prandtl number regardless of the roughness arrangement.

1 Introduction

The heat transfer over a roughened wall is of great engineering interest because the presence of wall roughness leads to a considerable enhancement of momentum, mass, and heat transfer. As the wall roughness enhances turbulence, secondary or tertiary flow as well as flow mixing, artificial roughness is frequently created to increase the heat transfer performance of engineering devices, such as internal cooling inside turbine blades [1], solar thermal systems [2], and heat transfer pipes [3]. Hence, a great deal of effort has been made to understand the effects of the wall roughness on heat and momentum transfer.

With regard to the momentum transfer, wall roughness hardly affects the momentum transfer provided that the wall roughness is buried within the viscous sublayer but has a considerable impact when the wall roughness protrudes into the logarithmic layer. As a consequence of the enhancement of the momentum transfer, the skin friction coefficient at a rough surface increases resulting in a downward shift in the inner-scaled mean velocity. It is well established that the downward shift in the mean velocity profile, which is referred to as the velocity roughness function, can be expressed as a function of the inner-scaled equivalent roughness [4].

R. Nagura · Y. Kuwata (✉) · K. Suga
Department of Mechanical Engineering, Osaka Prefecture University, Sakai, Japan
e-mail: kuwata@me.osakafu-u.ac.jp

© The Author(s), under exclusive license to Springer Nature Switzerland AG 2021
R. Örlü et al. (eds.), *Progress in Turbulence IX*, Springer Proceedings in Physics 267,
https://doi.org/10.1007/978-3-030-80716-0_16

As for the effects on the heat transfer, wall roughness also leads to a downward shift in the inner-scaled mean temperature profiles due to an increase in the heat transfer over a rough surface. However, as the Reynolds analogy does no longer hold for rough wall turbulence, the temperature roughness function, which is a downward shift in the inner-scaled mean temperature profile, is lower than the velocity roughness function even though the Prandtl number is unity. There is still much controversy about the effects of wall roughness on the dissimilarity between the heat and momentum transfer and no universally-accepted correlation that can accurately predict the heat transfer rate over a rough surface. In this study, for the improvement of the prediction of turbulent heat transfer over a rough surface, we investigate the effects of the roughness arrangement on the dissimilarity between the heat and momentum transfer by means of direct numerical simulations (DNSs) of the turbulent heat transfer over surfaces with hemisphere protrusions.

2 Flow Conditions

A schematic of a rough-walled open-channel flow is shown in Fig. 1. Periodic boundary conditions were applied to the streamwise (x) and spanwise (z) directions, whereas a slip wall was considered for the top wall. The bottom wall was roughened by regularly distributing hemisphere protrusions with relatively large size of $k = 0.3L_y$, where L_y is the open-channel height. The distances between two neighboring hemispheres in the streamwise and spanwise directions (p_x and p_z , respectively) were systematically varied with the roughness density being fixed as shown in Fig. 1. The rough surface is named NXMZ, where $N = p_x/k$ and $M = p_z/k$ stand for the streamwise and spanwise hemisphere pitches, respectively. The surface for case 20X2.5Z in Fig. 1a has the smallest spanwise pitch of $p_z = 2.5k$ yielding the largest streamwise frontal area, whereas the surface for case 2.5X20Z in Fig. 1d has the smallest frontal area. The streamwise and spanwise computational domain size were respectively $L_x = 6L_y$ and $L_z = 3L_y$ for cases 20X2.5Z, 10X5Z, and 5X10Z, but extended to 6δ in the spanwise direction for case 2.5X20Z. A flow was driven by a constant streamwise pressure difference, and the friction Reynolds number was fixed at $Re_\tau = 660$. The fluid Prandtl number was $Pr = 0.71$ assuming an air flow.

The flow field was simulated by the D3Q27 multiple-relaxation-time lattice Boltzmann method (LBM) [5], whereas we used D3Q19 regularized LBM [6] for the scalar field. The computational grid was uniform with equal spacing in all directions, and the grid points across the half channel height were 270 such that the resolution in wall units is comparable to those used in the lattice Boltzmann DNS studies [7].

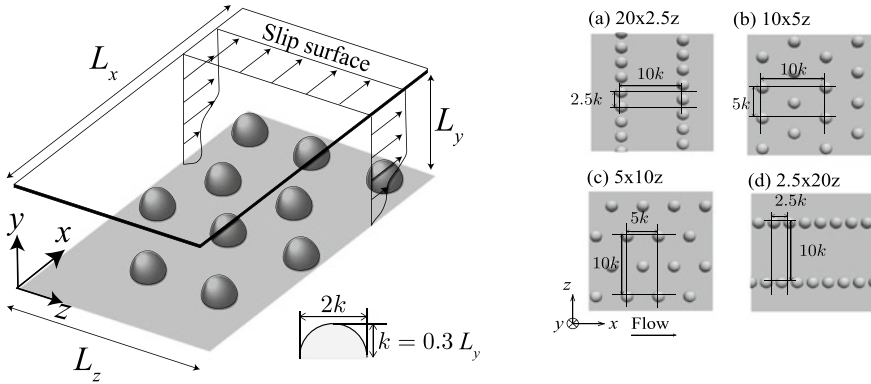


Fig. 1 Computational geometry of a rough-walled open channel flow

3 Results and Discussion

The modification of the mean velocity and temperature profiles are presented in Fig. 2, where the superficial $x - z$ plane-averaged inner-scaled streamwise mean velocity \bar{u}^+ and mean temperature $\bar{\theta}^+$ are shown against the inner-scaled effective wall-normal distance y_e^+ . Here, θ indicates the fluid temperature T relative to the wall temperature T_w : $\theta = T - T_w$, and the effective wall-normal distance y_e is defined as the wall-normal integral of the $x - z$ plane porosity: $y_e = \int_0^y \phi dy$, which accounts for a virtual origin of a rough wall [7]. The figure confirms that the \bar{u}^+ and $\bar{\theta}^+$ profiles for rough wall cases are shifted downward. The figure confirms that the \bar{u}^+ and $\bar{\theta}^+$ profiles for rough wall cases are shifted downward. The hemisphere arrangement affects the \bar{u}^+ profiles considerably, whereas the $\bar{\theta}^+$ profiles remain almost unaffected. The downward shift in \bar{u}^+ is the largest for case 20X2.5Z, followed by 10X5Z, 5X10Z, and 2.5X10Z.

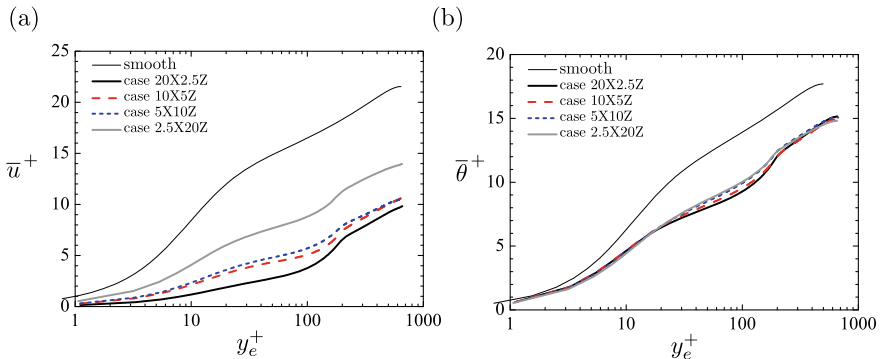


Fig. 2 **a** Inner-scaled streamwise mean velocity profiles, **b** Inner-scaled mean temperature profiles. The DNS data from [8] is also included

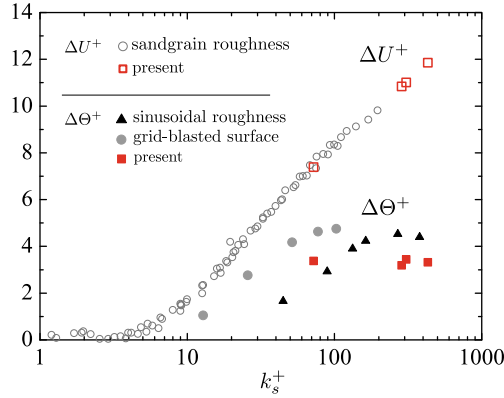


Fig. 3 Velocity and temperature roughness function against the inner-scaled equivalent roughness. The experimental data from [14], and the DNS data for sinusoidal roughness from [10] and grid-blasted surface from [9] are shown

To better understand the behaviors of the downward shift values, the velocity and temperature roughness functions (ΔU^+ and $\Delta \Theta^+$, respectively) are plotted against equivalent roughness height k_s^+ in Fig. 3. For comparison, the DNS data for the sinusoidal roughness from [10] and grid-blasted surface from [9] are also shown. Here, ΔU^+ ($\Delta \Theta^+$) is defined as a mean difference in the \bar{u}^+ ($\bar{\theta}^+$) profile between the smooth wall and rough wall cases in $k < y < \delta$. The trend of $\Delta \Theta^+$ against k_s^+ is found to be very different from that of ΔU^+ : ΔU^+ monotonically increases with k_s^+ , whereas $\Delta \Theta^+$ for the present results exhibits an almost constant value of $\Delta \Theta^+ \simeq 3$ despite the considerable difference in the hemisphere arrangement. This plateau value is seemed to be somewhat smaller than those for the sinusoidal roughness and grid-blasted surface, indicating that the heat transfer enhancement relative to the momentum transfer enhancement is smaller for the present rough surfaces. The possible explanation is that the present rough surfaces tend to yield larger pressure drag which increases the momentum transfer but not the heat transfer. It is well established that ΔU^+ against k_s^+ collapses onto a single curve irrespective of the surface texture in the fully rough regime; however, $\Delta \Theta^+$ against k_s^+ is found to be rather scattered, indicating that $\Delta \Theta^+$ is not expressed as a function of k_s^+ solely but other roughness or flow parameters should be taken into account.

To quantify the augmentation of the heat and momentum transfer, the skin friction coefficient C_f and Stanton number St normalized by the corresponding values C_{f0} and St_0 for smooth wall turbulence are shown in Fig. 4. Note that C_f and St are the averaged values over the rough surfaces. For a better physical understanding, C_f is decomposed into the contribution by the pressure and viscous effects. It is clear that the augmentation of C_f can be attributed to the role of the pressure, and the contribution by the pressure largely depends on the hemisphere arrangement. On the other hand, although St is also enhanced by the wall roughness, the augmentation

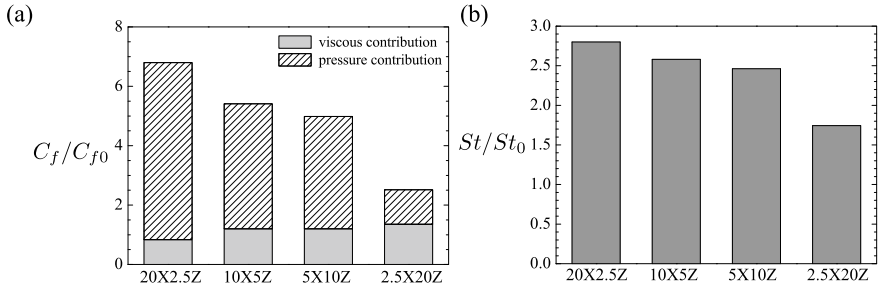
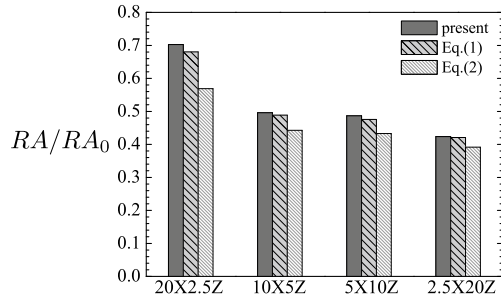


Fig. 4 **a** Augmentation of the skin friction coefficient C_f/C_{f0} and **b** augmentation of the Stanton number St/St_0

Fig. 5 Comparison of the Reynolds analogy factor normalized by the smooth wall value RA/RA_0



of St is much smaller than that of C_f , which is considered to be due to an absence of the pressure term in the energy equation. Both C_f and St show the largest values for case 20X2.5Z where the streamwise frontal area is the largest, whereas the case with streamwise aligned roughness elements (case 2.5X20Z) results in the smallest C_f and St values.

Finally, to explore the predictive method for the dissimilarity between the momentum and heat transfer, we discuss the Reynolds analogy factor, which is defined as the ratio of the doubled Stanton number to the Skin friction coefficient: $RA = 2St/C_f$. When the heat transfer exceeds the momentum transfer, the RA value is greater than unity, whereas it is less than unity in the opposite situation. Figure 5 presents the Reynolds analogy factor RA normalized by a corresponding value for smooth wall turbulence RA_0 , together with the correlation proposed by [12]:

$$RA/RA_0 = \frac{Pr^{2/3}}{1 + \sqrt{0.5C_f} (5.19(k_s^+)^{0.2} Pr^{0.44} - 8.5)}, \quad (1)$$

and that by [11],

$$RA/RA_0 = \frac{Pr^{2/3}}{Pr_t + \sqrt{0.5C_f} ((k_s^+)^{0.2} Pr^{0.44} / C)}. \quad (2)$$

where the turbulent Prandtl number is assumed to be unity, $Pr_t = 1$, and the model constant of $C = 0.35$ is assigned [13]. The figure demonstrates that the RA values predicted by the (1) and (2) are lower than unity, suggesting that both of the models reproduce the dissimilar trend between the heat and momentum transfer. In particular, the correlation by [12] gives solutions that are significantly closer to the present DNS results. This suggests that the Reynolds analogy factor, which measures the dissimilarity between the heat and momentum transfer, can be expressed as a function of the skin friction coefficient, Prandtl number, and the inner-scaled equivalent roughness, irrespective of the roughness arrangement.

4 Conclusion

Direct numerical simulations of turbulent heat transfer over walls with regularly distributing hemisphere protrusions is performed to get insight into how the roughness arrangement affects the turbulent heat transfer. The roughness arrangement largely affects the momentum and heat transfer: the augmentation of the momentum and heat transfer is the largest for the surface with the maximum streamwise frontal area, whereas it is the smallest for the streamwise-aligned hemisphere protrusions. As the hemisphere protrusions particularly increases pressure drag, the roughness increases the momentum transfer more than the heat transfer, resulting in the dissimilarity between the momentum and heat transfer. The Reynolds analogy factor can be expressed as a function of the skin friction coefficient, inner-scaled equivalent roughness, and Prandtl number regardless of the roughness arrangement.

Acknowledgements A part of this study was financially supported by JSPS Japan (No.17K1459) and the Research Association of Automotive Internal Combustion Engines. The numerical calculations were carried out on the TSUBAME3.0 supercomputer at Tokyo Institute of Technology.

References

1. A. Murata, S. Mochizuki, Comparison between laminar and turbulent heat transfer in a stationary square duct with transverse or angled rib turbulators. *International Journal of Heat and Mass Transfer* **44**(6), 1127–1141 (2001)
2. S. Chamoli, N.S. Thakur, J.S. Saini, A review of turbulence promoters used in solar thermal systems. *Renewable and Sustainable Energy Reviews* **16**(5), 3154–3175 (2012)
3. K. Akermann, P. Renze, J. Dietl, W. Schröder, Large-Eddy Simulation of turbulent heat transfer in a multiple-started helically rib-roughened pipe. *International Journal of Heat and Mass Transfer* **154**, 119667 (2020)
4. K.A. Flack, M.P. Schultz, Review of hydraulic roughness scales in the fully rough regime. *Journal of Fluids Engineering* **132**, 4 (2010)
5. K. Suga, Y. Kuwata, K. Takashima, R. Chikasue, A D3Q27 multiple-relaxation-time lattice Boltzmann method for turbulent flows. *Computers & Mathematics with Applications* **69**, 518–529 (2015)

6. K. Suga, R. Chikasue, Y. Kuwata, Modelling turbulent and dispersion heat fluxes in turbulent porous medium flows using the resolved LES data. *International Journal of Heat and Fluid Flow* **68**, 225–236 (2017)
7. Y. Kuwata, Y. Kawaguchi, Direct numerical simulation of turbulence over systematically varied irregular rough surfaces. *Journal of Fluid Mechanics* **862**, 781–815 (2019)
8. F. Lluesma-Rodríguez, S. Hoyas, M. Perez-Quiles, Influence of the computational domain on DNS of turbulent heat transfer up to $Re_\tau = 2000$ for $Pr = 0.71$. *International Journal of Heat and Mass Transfer* **122**, 983–992 (2018)
9. J. Peeters, N. Sandham, Turbulent heat transfer in channels with irregular roughness. *International Journal of Heat and Mass Transfer* **138**, 454–467 (2019)
10. M. MacDonald, N. Hutchins, D. Chung, Roughness effects in turbulent forced convection. *Journal of Fluid Mechanics* **861**, 138–162 (2018)
11. W. Kays, M. Crawford, *Convective Heat and Mass Transfer* (McGraw-Hill, 1993)
12. D. Dipprey, R. Sabersky, Heat and momentum transfer in smooth and rough tubes at various Prandtl numbers. *International Journal of Heat and Mass Transfer* **6**, 329–353 (1963)
13. J.P. Bons, St and Cf augmentation for real turbine roughness with elevated freestream turbulence. *Journal of Turbomachinery* **124**(4), 632–644 (2002)
14. J. Nikuradse (1933) Laws of flow in rough pipes, in *VDI Forschungsheft*

Part III
Data Processing and Scaling

The Diagnostic Plot—A Tutorial with a Ten Year Perspective



P. Henrik Alfredsson, Antonio Segalini, and Ramis Örlü

Abstract The diagnostic plot was introduced in 2010 (Eur. J. Mech. B/Fluids 29: 403–406) but was used already in 2008 during a large measurement campaign as a litmus test to determine if tripped zero-pressure gradient turbulent boundary layers fulfilled basic criteria of being canonical. It used the rms-level of streamwise velocity (u_{rms}) in the outer part of the boundary layer, a region where u_{rms} can give clear indications if insufficient or too tough tripping has been used. In standard plots one needs both the friction velocity and measurement of the full velocity and turbulence profiles. By instead plotting $u_{\text{rms}}/U_{\infty}$ as a function of U/U_{∞} , it was found that this gives rise to a well-defined distribution that could be used as a canonical measure. It was later discovered that it is possible to extend the description to the near wall region. It has also been extended to boundary layers over rough surfaces and with pressure gradients, and some further uses. This paper aims to be both a review of the development of the method during the last 10+ years and a tutorial for those who want to employ it in their research and maybe also find new uses of the methodology.

1 Introduction

Turbulent shear flows, whether boundary layers, channel or pipe flows, as well as jets or wakes, are often analyzed assuming some form of similarity. Two prime examples of such an analysis are the planar turbulent wake and jet, where in the fully developed region (i.e. far from the wake-generating body or the jet exit), one assumes the mean

P. H. Alfredsson (✉) · A. Segalini
Department of Engineering Mechanics, KTH Royal Institute of Technology,
Stockholm, Sweden
e-mail: phal@mech.kth.se

A. Segalini
e-mail: segalini@mech.kth.se

R. Örlü
FLOW, Engineering Mechanics, KTH Royal Institute of Technology,
100 44 Stockholm, Sweden
e-mail: ramis@mech.kth.se

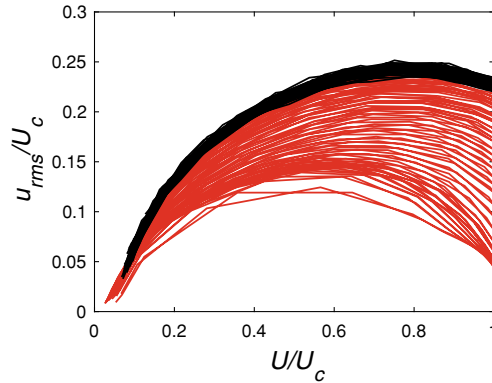


Fig. 1 The diagnostic plot used to evaluate the development towards a self-similar state for a two-dimensional turbulent jet at $Re = 14500$, data replotted from Ref. [8], both sides of the jet are shown. Red lines $0.5 < x/D < 20$, black lines $20 < x/D < 40$, where D is the nozzle width

velocity and higher moments to be expressed in similarity form. As an example, one can describe the jet streamwise (x) mean velocity (U) and variance (\overline{uu}) as

$$U(x, y) = U_c(x)F'[y/\delta(x)] \quad \text{and} \quad \overline{uu} = U_c^2(x)g[y/\delta(x)]$$

where y is the cross-flow coordinate, U_c is the centreline ($y = 0$) velocity and $\delta(x)$ is some suitable cross-flow length scale. This immediately gives the possibility to write

$$\overline{uu}/U_c^2 = H[U(x, y)/U_c(x)] \quad \text{or} \quad u_{\text{rms}}/U_c = h[U(x, y)/U_c(x)]$$

If similarity holds for x/D larger than some value where initial conditions do not play a role, plots of u_{rms}/U_c vs U/U_c should then collapse on a single curve (see Fig. 1 obtained from data in Ref. [8]); such a plot has now become known as the diagnostic plot, Ref. [1]. As can be seen in the figure the data approach a single curve as x/D increases and above approximately $x/D > 20$ similarity seems to hold.

For wall-bounded turbulent flows the situation is more complicated as compared to jets and wakes since the wall-normal distribution depends on two different length scales: the inner or viscous scale and an outer scale related to a measure of the boundary-layer thickness, i.e. the size of the flow. Furthermore there are two different velocity scales, an outer velocity scale (free-stream velocity in boundary layers or centreline velocity in channel and pipe flows) and the friction velocity determined from the wall shear stress. The diagnostic plot was first used for zero pressure gradient turbulent boundary layers (ZPGTBL) [1] and was shown to work well in the outer region when the scaling velocity is the free-stream velocity U_∞ , as can be seen in Fig. 2. An important aspect of this way to plot the data is that neither the friction velocity nor the exact determination of the wall position is necessary which makes

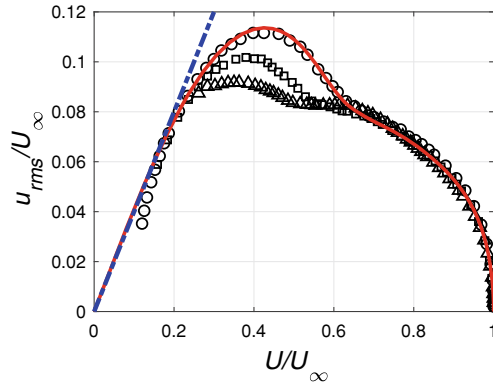


Fig. 2 Original version of the diagnostic plot for zero pressure-gradient turbulent boundary layers at four different Reynolds numbers adapted from Ref. [1]. The red line is a DNS at a momentum-loss based Reynolds number of $Re_\theta = 2510$ from Ref. [17], experimental data from Ref. [12]; \circ : $Re_\theta = 2540$, \square : $Re_\theta = 8100$, \triangle : $Re_\theta = 18700$. Blue dashed line indicates the tangent to the data in the viscous sublayer corresponding to the magnitude of the rms of the wall shear stress fluctuations normalized by its mean, here 0.4

analysing the data in this way much less cumbersome than by scaling both velocity and wall distance with the friction velocity, a quantity that needs to be determined accurately by some independent mean.

As can be seen in Fig. 2 the collapse of the data for the three Reynolds numbers shown is quite good in the range $0.6 < U/U_\infty < 1$ whereas in the range $0.2 < U/U_\infty < 0.6$ they diverge and then start to collapse again for $U/U_\infty < 0.2$. In terms of y^+ , $U/U_\infty \approx 0.6$ is found in the lower part of the logarithmic region (the exact value depends on the Reynolds number), for instance for $Re_\tau = 4 \cdot 10^3$ and $4 \cdot 10^5$ the corresponding y^+ -values are approximately 200 and 2000, respectively.

In this paper we will summarize our own work using the diagnostic concept, show how it can be used to formulate a description of u_{rms} that is valid across the boundary layer (as well as for pipe and channel flows) for arbitrary Reynolds numbers, how it can be used to estimate the thickness and “free-stream velocity” of atmospheric boundary layers from velocity measurements close to the ground, and that the concept actually predicts the existence of an outer peak of u_{rms} at sufficiently high Reynolds numbers. We will also show that the diagnostic concept can be used for higher-order moments, rough-wall boundary layers, for non-zero pressure gradients boundary layers as well as for more complex flows.

2 The Background and Original Diagnostic Plot

In studies of wall-bounded turbulent flows the custom is to scale the mean velocity and the Reynolds stresses using the friction velocity u_τ as the scaling parameter and

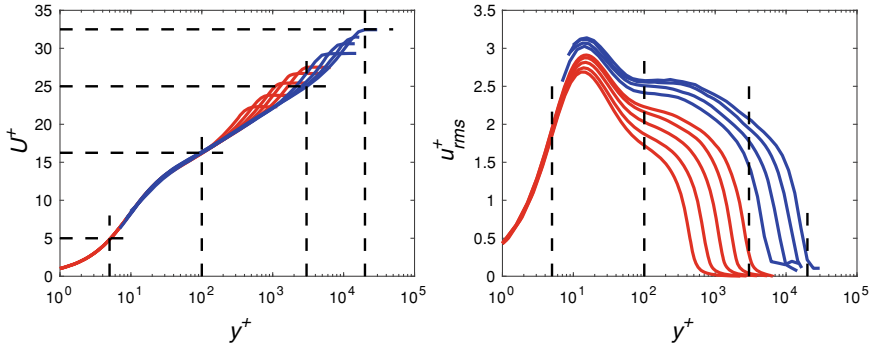


Fig. 3 Mean velocity and u_{rms} distributions of ZPGTBL normalized with inner variables at different Reynolds numbers. Red profiles are from LES by Ref. [7], blue profiles from experiments by Ref. [15]. Vertical dashed lines indicate the limits described in Table 1, where the two outermost ones are for the highest Re case

Table 1 Increments of the streamwise velocity for different regions in the diagnostic plot formulation for the highest friction Reynolds numbers of the LES and the experiments in Fig. 3

Boundary layer region	y range	$Re_\tau = 2500$	$Re_\tau = 20000$
Viscous sublayer	$0 < y^+ < 5$	$0.00 < U/U_\infty < 0.18$	$0.00 < U/U_\infty < 0.15$
Buffer region	$5 < y^+ < 100$	$0.18 < U/U_\infty < 0.59$	$0.15 < U/U_\infty < 0.50$
Logarithmic region	$100 < y^+,$ $y/\delta < 0.15$	$0.59 < U/U_\infty < 0.71$	$0.50 < U/U_\infty < 0.77$
Wake region	$0.15 < y/\delta < 1$	$0.71 < U/U_\infty < 1.00$	$0.77 < U/U_\infty < 1.00$

normalize the distance from the wall with the viscous length scale $\ell_* = \nu/u_\tau$ such that the wall-normal distance y is denoted as $y^+ = y/\ell_*$. To scale the flow far from the wall an outer length scale, such as the boundary layer thickness (δ) or channel half height/pipe radius, is usually used. To illustrate the background to the diagnostic plot, we use a set of nine boundary layer profiles, the five with lowest Re are from LES [7] whereas the four for high Re are from experiments [15]. The mean velocity profiles are plotted in Fig. 3 in the standard semi-logarithmic format where it is divided into four parts; the viscous region $0 < y^+ < 5$, the buffer region $5 < y^+ < 100$, the logarithmic region between $y^+ > 100$ and $y/\delta < 0.15$ and finally the wake region for $y/\delta > 0.15$. Table 1 shows the approximate ranges of the streamwise velocity for the different regions for the highest friction Reynolds numbers of the LES ($Re_\tau = 2500$) and the experiments ($Re_\tau = 20000$). In physical distances the size of the four regions are very different, however in terms of increments in $U^+ (= U/u_\tau)$ or U/U_∞ they are of the same order. As can be observed, the largest change with Reynolds number is within the logarithmic region. Also shown in Fig. 3 are the corresponding u_{rms} profiles for the same nine cases plotted in standard format.

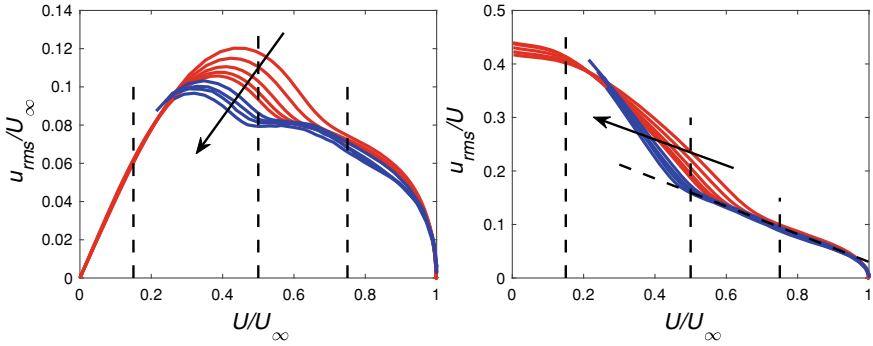


Fig. 4 Same data as in Fig. 3 plotted in original diagnostic form and extended diagnostic form. The dashed slope is from Eq. 1. The arrows indicate increasing Reynolds numbers

In the first published paper [1] on the diagnostic plot it was suggested that if u_{rms} normalized with U_∞ was plotted as function of U/U_∞ one could clearly obtain a “litmus” test both of the data in the viscous sublayer and in the outer region (see Fig. 4). In the viscous sublayer u_{rms} should increase linearly with U up to about $U^+ = 5$, i.e. of the order of $U/U_\infty = 0.2$. In the outer region all data should collapse on a single curve in the approximate region $0.5 \leq U/U_\infty \leq 1$. In a later paper [2] an extended version of the diagnostic plot was suggested by normalizing u_{rms} with the local streamwise velocity. In that scaling the data in the outer region followed a straight line; the higher the Reynolds number the wider the range of U/U_∞ where this line fitted the data (see Fig. 4).

A fitting to the data points in this linear region gives the following expression for the line

$$\frac{u_{rms}}{U} = \alpha - \beta \frac{U}{U_\infty} \tag{1}$$

with $\alpha = 0.29$ and $\beta = 0.26$.

An interesting aspect of this linear relation is that it predicts a maximum in $u_{rms}/U_\infty = \alpha^2/4\beta = 0.08$ at $U/U_\infty = \alpha/2\beta = 0.56$ as long as the data lies along the line given by Eq. 1. As can be seen from Fig. 4 this is only the case if the Reynolds number is high enough and explains why the so called “outer peak” can only be observed if the local turbulence intensity follows the linear behaviour at least down to $U/U_\infty = 0.56$, corresponding to a threshold value of around $Re_\tau = 20000$. It is also interesting to note that the maximum value of u_{rms}/U_∞ and its position in terms of U/U_∞ is independent of Reynolds number. However, in traditional scaling, i.e. u_{rms}/u_τ , the maximum increases with Re as well as its position in wall units. The experimental high Reynolds number data in Fig. 4 barely reaches below this value and only a weak maximum can be discerned for the highest Re .

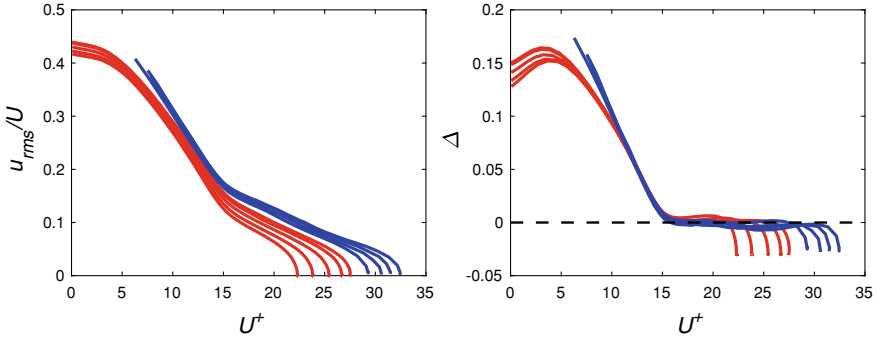


Fig. 5 Same data as in Fig. 3 plotted as function of U^+ , and with the linear relation (Eq. 1) subtracted

3 Extension to the Near Wall Region

As can be seen in Fig. 4, the data in the near wall region do not collapse as expected since it is well known that near the wall viscous scaling applies. If instead u_{rms}/U is plotted versus U^+ as in Fig. 5, one finds a nice collapse in the inner region. By subtracting the linear relationship (Eq. 1) found in the outer region, one obtains a unique collapse of the data in the near wall region. Alfredsson, Örlü & Segalini [3] fitted a difference function Δ to the data and obtained an empirical description of u_{rms}/U across the boundary layer (except in the outermost region where the data deviates from the straight line) which reads:

$$u_{\text{rms}} = U \left[\alpha - \beta \frac{U}{U_{\text{max}}} + \Delta \left(\frac{U}{U_{\text{max}}} U_{\text{max}}^+ \right) \right] \quad (2)$$

In Eq. 2 one observes that the Reynolds number dependence of the u_{rms} profile only enters through U_{max}^+ in the Δ function.

4 How the Diagnostic Idea Can Be Used to Predict High Re Flows

The relations (Eqs. 1, 2) described in Sect. 3 can now be used to predict the u_{rms} distribution in any scaling if the mean velocity distribution is known. Figure 6 shows u_{rms} for a wide range of Reynolds numbers, both in diagnostic form and in standard form, i.e. u_{rms}^+ as function of y^+ . The composite boundary layer profile given in Ref. [11] has been utilized for the mean velocity description. What can be noted is that for high enough Reynolds numbers an outer peak develops that actually overtakes the inner peak at $y^+ \approx 15$. Here outer is maybe a misnomer since this broad peak is located in the logarithmic layer and moves outwards approximately as $Re_\tau^{0.56}$. Another interest-

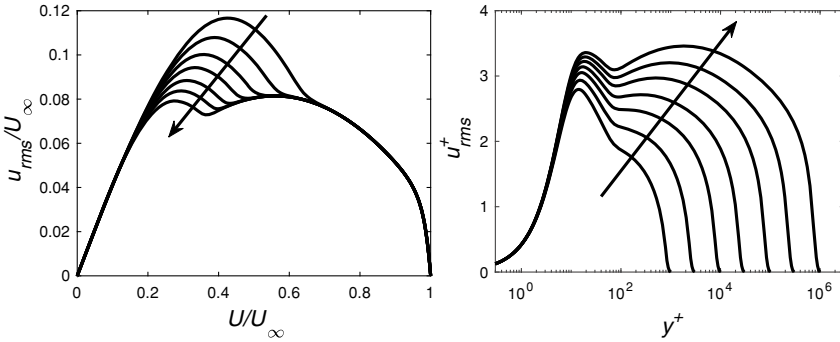


Fig. 6 Prediction of u_{rms} in diagnostic and standard forms. The arrows indicate increasing Reynolds numbers. The Reynolds numbers predicted are $Re_\tau = 10^3, 3 \cdot 10^3, 10^4, 3 \cdot 10^4, 10^5, 3 \cdot 10^5, 10^6$

ing observation is that the model predicts that the inner peak increases with Reynolds number and this is an effect of that the linear region (in the extended diagnostic scaling) expands to lower values of U/U_∞ as the Reynolds number increases. One may interpret this as an increased influence of outer region large scales on the near-wall flow.

If one wants to compare these predictions for high Reynolds numbers with experimental or numerical data, there are few data sets that are available. The ones that exist for truly high Reynolds numbers and have sufficient spatial resolution not to distort the results are from the atmospheric boundary layer; this is a complication for the diagnostic plot methodology since for such data the free-stream velocity is not known *a priori*. As suggested in Ref. [1], an equivalent free-stream velocity can be estimated by fitting the data by varying the value of U_∞ to the description in the outer region (see Fig. 4), assuming that Reynolds number effects are small. This method has been applied to the atmospheric SLTEST data (Ref. [10]) in Fig. 7. Although the atmospheric data show more scatter than typical wind-tunnel data, they nicely follow the trend suggested by the diagnostic plot and an outer maximum is found as predicted. In addition to the atmospheric data in Fig. 7, data from DNS and wind-tunnel experiments, different from those in previous figures, are included. This also shows that the data in previous figures were not “cherry-picked”.

5 Use in Complex Flow Situations—Rough Wall Example

So far we have discussed the diagnostic plot for smooth wall ZPGTBL but it has been found that it can be used with some modifications also in other more complex flow situations, such as rough-wall boundary layers and boundary layers with pressure gradient. Castro, Segalini & Alfredsson [4] found that, if the extended version of the diagnostic plot was used for rough-wall boundary layers, the data still followed a

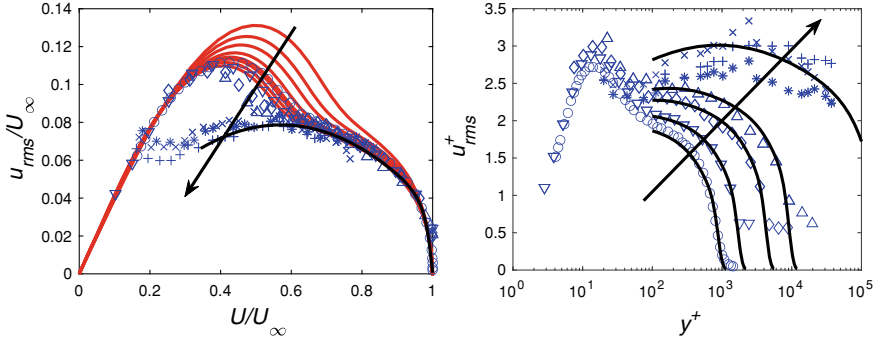


Fig. 7 Data spanning a large Re -range, DNS data [18]: red lines $Re_\tau = 250 - 1300$; hot-wire wind-tunnel data [12] \circ : $Re_\tau = 850$, LDV wind-tunnel data [5] ∇ : $Re_\tau = 1700$, \diamond , $Re_\tau = 4300$, \triangle , $Re_\tau = 10000$, hot-wire measurements from the SLTEST [10]: $*$, \times , $+$, $Re_\tau \approx 10^6$. Data plotted in diagnostic plot and in standard format, i.e. u_{rms}^+ vs y^+

straight line but with increasing slope with increasing roughness strength until the slope saturated at fully rough conditions (see Fig. 8). However they also found that, if the plot was modified by taking the downward shift of the mean velocity (ΔU) in the logarithmic region for the rough boundary layer into account by modifying the normalizing velocities such that the plot was

$$\frac{u_{rms}}{U + \Delta U} \quad \text{vs} \quad \frac{U + \Delta U}{U_\infty + \Delta U},$$

all data followed the smooth-wall line (see Fig. 8). The diagnostic methodology is well adapted to rough-wall boundary layers since neither the exact wall position, nor the friction velocity are needed, both hard to accurately determine for a rough-wall case, as pointed out by e.g. Refs. [9, 14].

Some further examples of the use of the diagnostic plot in more complex flows are TBL with pressure gradients [6] and in three-dimensional flows [19].

6 An Example: How the Diagnostic Plot Can Be Used in Practice

The diagnostic plot was initially proposed as a simple way to determine if a turbulent boundary layer is in a canonical state. This idea was further exploited by Sanmiguel Vila et al. [16]. Figure 9 shows an example where a hot wire is traversed in the streamwise direction inside the boundary layer, whereas the inset shows how u_{rms}/U varies at the measurement position. When the data falls on the line, the boundary layer could be assumed to be in a canonical state. The beauty of this method is that the measurements can be performed at arbitrary y -positions as long as they are

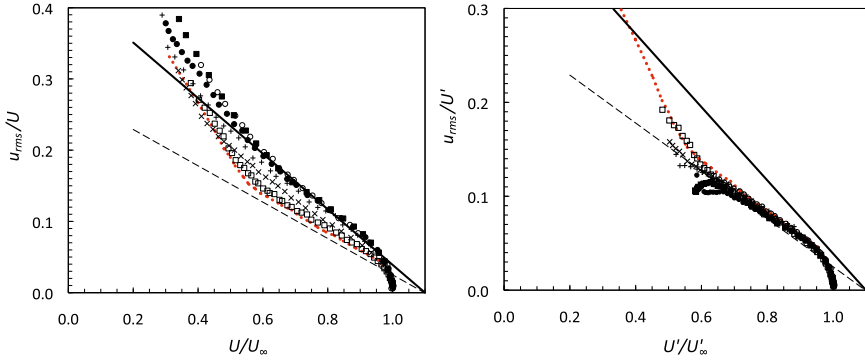


Fig. 8 Rough-wall ZPGTBL data plotted in the extended diagnostic plot and the modified velocity scaling taking the shift ΔU in the logarithmic region into account. $U' = U + \Delta U$ and $U'_\infty = U_\infty + \Delta U$. Figures adapted from Ref. [4]

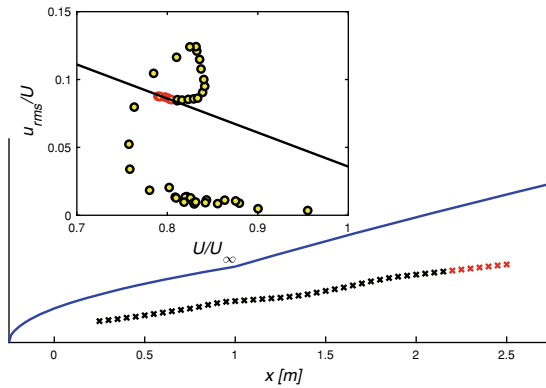


Fig. 9 Illustration on how the diagnostic plot can be used to determine at which x -position a ZPGTBL can be assumed to be in a canonical state. Data from Ref. [16]

within the straight-line region given by Eq. 1, which amounts to a large fraction of the boundary-layer height. The red data points in Fig. 9 indicate at which x -positions the boundary layer is in the canonical state.

7 Summary and Conclusions

The diagnostic-plot methodology was introduced more than 10 years ago as a method to discern if a ZPGTBL reached a canonical state by using rms data of the streamwise fluctuations in and above the logarithmic region. It was also a method that could easily show if measurements in the viscous sublayer were affected by near-wall effects. It was further developed to establish a unique relation of u_{rms} in the buffer

region. One of the strengths of the method is that it does not rely on neither the exact determination of the measurement position with respect to the wall nor the friction velocity. It has furthermore shown that the long-discussed existence of an “outer” peak in the u_{rms} -distribution can only be observed for sufficiently high Reynolds numbers and the method gives a quantitative answer on how large the corresponding Reynolds number needs to be. The method can also be used to determine an effective free-stream velocity for atmospheric boundary layer flows and has been able to fairly accurately predict the u_{rms} -distribution measured in such flows. Furthermore the methodology has found extensions to more complex flow situations, such as rough-wall boundary layers and TBLs with pressure gradients. It should also be pointed out that the methodology is not limited to TBLs but has also been shown to work equally well for channel and pipe flows [3] and can be further generalized to higher-order moments [13].

However one should point out that so far there is no clear explanation for the success of the methodology although one may compare with the successful use a similarity analysis for the analysis of jets and wakes. The analysis has some further implications in the outer region of wall-bounded flows as one can write

$$-\frac{\overline{uv}}{u_{\tau}^2} \approx 1 - \frac{y}{\delta} \quad \text{or} \quad -\frac{\overline{uv}}{u_{\text{rms}}v_{\text{rms}}} \approx \frac{U_{\infty}}{u_{\text{rms}}} \frac{U_{\infty}}{v_{\text{rms}}} \frac{u_{\tau}^2}{U_{\infty}^2} \left(1 - \frac{y}{\delta}\right)$$

Since v_{rms} also seems to follow diagnostic scaling (see Ref. [19], Fig. 5b), this implies that the correlation $-\overline{uv}/u_{\text{rms}}v_{\text{rms}}$ decreases with increasing Reynolds number, i.e. the turbulence within the outer region of a TBL tends towards isotropy.

Acknowledgements We like to acknowledge professor Masaharu Matsubara for making the data from his laboratory available for Fig. 1. We also want to acknowledge the cooperation with professors Ian Castro and Joe Klewicki during the development of extensions of the diagnostic method, as well as many other researchers who have employed the idea and found it useful in various flow situations.

References

1. P.H. Alfredsson, R. Örlü, The diagnostic plot - a litmus test for wall bounded turbulence data. *Eur. J. Mech. B/Fluids* **29**, 403–406 (2010)
2. P.H. Alfredsson, A. Segalini, R. Örlü, A new scaling for the streamwise turbulence intensity in wall-bounded turbulent flows and what it tells us about the outer peak. *Phys. Fluids* **23**, 041702 (2011)
3. P.H. Alfredsson, R. Örlü, A. Segalini, A new formulation for the streamwise turbulence intensity distribution in wall-bounded turbulent flows. *Eur. J. Mech. B/Fluids* **36**, 167–175 (2012)
4. I.P. Castro, A. Segalini, P.H. Alfredsson, Outer layer turbulence intensities in smooth- and rough-wall boundary layers. *J. Fluid Mech.* **727**, 119–131 (2013)
5. D.B. DeGraaff, J. Eaton, Reynolds-number scaling of the flat-plate turbulent boundary layer. *J. Fluid Mech* **422**, 319–346 (2000)
6. A. Drózd, W. Elsner, S. Drobniak, Scaling of streamwise Reynolds stress for turbulent boundary layers with pressure gradient. *Eur. J. Mech. B/Fluids* **49**, 137–145 (2015)

7. G. Eitel-Amor, R. Örlü, P. Schlatter, Simulation and validation of a spatially evolving turbulent boundary layers up to $Re_\theta = 8300$. *Int. J. Heat Fluid Flow* **47**, 57–69 (2014)
8. M. Matsubara, P.H. Alfredsson, A. Segalini, Linear modes in a planar turbulent jet. *J Fluid Mech* **888**, A26 (2020)
9. T. Medjnoun, C. Vanderwel, B. Ganapathisubramani, Characteristics of turbulent boundary layers over smooth surfaces with spanwise heterogeneities. *J. Fluid Mech.* **838**, 516–543 (2018)
10. M. Metzger, B.J. McKeon, H. Holmes, The near-neutral atmospheric surface layer: turbulence and non-stationarity. *Phil. Trans. R. Soc. A* **365**, 859–876 (2007)
11. P.A. Monkewitz, K.A. Chauhan, H.M. Nagib, Self-consistent high-Reynolds number asymptotics for zero-pressure-gradient turbulent boundary layers. *Phys. Fluids* **19**, 115101 (2007)
12. R. Örlü, *Experimental Studies in Jet Flows and Zero Pressure-Gradient Turbulent Boundary Layers* (Royal Institute of Technology, Stockholm, Sweden, 2009). (Ph.D. Thesis)
13. R. Örlü, A. Segalini, J. Klewicki, P.H. Alfredsson, High-order generalisation of the diagnostic scaling for turbulent boundary layers. *J. Turbulence* **17**, 664–677 (2016)
14. M. Placidi, B. Ganapathisubramani, Turbulent flow over large roughness elements: Effect of frontal and plan solidity on turbulence statistics and structure. *Boundary-Layer Meteorol.* **167**, 99–121 (2018)
15. M. Samie, I. Marusic, N. Hutchins, M.K. Fu, Y. Fan, M. Hultmark, A.J. Smits, Fully resolved measurements of turbulent boundary layer flows up to $Re_\tau = 20,000$. *J. Fluid Mech.* **851**, 391–415 (2018)
16. C. Sanmiguel Vila, R. Vinuesa, S. Discetti, A. Ianiro, P. Schlatter, R. Örlü, On the identification of well-behaved turbulent boundary layers. *J. Fluid Mech.* **822**, 109138 (2017)
17. P. Schlatter, R. Örlü, Q. Li, G. Brethouwer, J.H.M. Fransson, A.V. Johansson, P.H. Alfredsson, D.S. Henningson, Turbulent boundary layers up to $Re_\theta = 2500$ studied through simulation and experiment. *Phys. Fluids* **21**, 051702 (2009)
18. P. Schlatter, R. Örlü, Assessment of direct numerical simulation data of turbulent boundary layers. *J. Fluid Mech* **659**, 116–126 (2010)
19. S.J. Zimmerman, S.K. Romero, J. Philip, J.C. Klewicki, Downstream evolution of junction flow three-component velocity fluctuations through the lens of the diagnostic plot. *Int. J. Heat Fluid Flow* **85**, 108665 (2020)

Bayesian Optimisation with Gaussian Process Regression Applied to Fluid Problems



Saleh Rezaeiravesh, Yuki Morita, Narges Tabatabaei, Ricardo Vinuesa, Koji Fukagata, and Philipp Schlatter

Abstract Bayesian optimisation based on Gaussian process regression (GPR) is an efficient gradient-free algorithm widely used in various fields of data sciences to find global optima. Based on a recent study by the authors, Bayesian optimisation is shown to be applicable to optimisation problems based on simulations of different fluid flows. Examples range from academic to more industrially-relevant cases. As a main conclusion, the number of flow simulations required in Bayesian optimisation was found not to exponentially grow with the dimensionality of the design parameters (hence, no curse of dimensionality). Here, the Bayesian optimisation method is outlined and its application to the shape optimisation of a two-dimensional lid-driven cavity flow is detailed.

1 Introduction

Optimisation arises in many problems in CFD (computational fluid dynamics), in general, and in the context of wall-bounded turbulent flows, in particular. The aim is to either maximise or minimise an objective or cost function defined based on the

S. Rezaeiravesh · N. Tabatabaei · R. Vinuesa · P. Schlatter (✉)
SimEx/FLOW, Engineering Mechanics, KTH Royal Institute of Technology, Stockholm, Sweden
e-mail: pschlatt@mech.kth.se

S. Rezaeiravesh
e-mail: salehr@kth.se

N. Tabatabaei
e-mail: nargest@mech.kth.se

R. Vinuesa
e-mail: rvinuesa@mech.kth.se

Y. Morita · K. Fukagata
Department of Mechanical Engineering, Keio University, Yokohama, Japan
e-mail: morita@kth.se

K. Fukagata
e-mail: fukagata@mech.keio.ac.jp

flow quantities of interest (QoIs) through estimating optimal values for a set of design parameters. To this end, different approaches can be used in practice, see e.g. Ref. [9]. The methods can be classified as gradient-based, gradient-enhanced and gradient-free. When the gradients are obtained using the adjoint sensitivity method, gradient-based optimisation methods can be very efficient particularly in large-dimensional space of design parameters. However, these methods may find the local optima and may suffer from an instability of the adjoint for chaotic cases. Moreover, when applied to unsteady simulations of the Navier–Stokes equations, the gradient-based methods may demand a large memory and also add a considerable computational overhead. Another main approach for optimisation in CFD is the response-surface method (RSM) which treats the flow solver as a black-box, see e.g. [4]. These methods are non-intrusive and construct a surrogate for the objective function in the space of design parameters using a limited number of simulations. An efficient way of constructing the surrogate is the use of the Gaussian process regression (GPR) [10]. Although the RSM can find the global optima, in its standard form, it suffers from the curse of dimensionality. The issue can be significantly reduced by including gradient information in RSM, see e.g. Ref. [5].

As detailed in Sect. 2, the Bayesian optimisation employed in the present study is among the response-surface methods, but has a distinctive characteristic: instead of a set of fixed samples, a sequence of samples for the design parameters is drawn which converges to the global optimum [3, 11]. Although the BO has been frequently used in the fields of machine learning and data science [11], its application to CFD and turbulent-flow simulations is rather recent [6, 13]. In a recent study by the present authors [7], the BO based on GPR was shown to be applicable to a wide range of optimisation problems arising in wall-bounded turbulent flows and boundary layers. The considered problems range from purely academic to industrially-relevant setups and include up to 8 design parameters. The BO-GPR was shown to be computationally efficient for finding the global optima, meaning that the number of simulations does not grow exponentially with the dimension of the design parameters.

2 Bayesian Optimisation

Let $p \geq 1$ design parameters be denoted by $\mathbf{q} = (q_1, q_2, \dots, q_p)$. The admissible space of \mathbf{q} is $\mathbb{Q} \subset \mathbb{R}^p$. Corresponding to each sample for \mathbf{q} taken from \mathbb{Q} , a flow simulation can be performed and a realisation for the flow QoI is obtained. Depending on the optimisation problem at hand and using a combination of the QoIs, an objective function $r(\mathbf{q})$ can be defined which can be minimised (or maximised):

$$\mathbf{q}_{\text{opt}} = \arg \min_{\mathbf{q} \in \mathbb{Q}} r(\mathbf{q}). \quad (1)$$

To briefly review the Bayesian optimisation based on GPR (BO-GPR), first a short introduction is given to Gaussian processes. In general, the functional relationship

for $r(\mathbf{q})$ in (1) may not be known in an analytical form. Samples of $r(\mathbf{q})$ can be considered to be generated as,

$$r(\mathbf{q}) = f(\mathbf{q}) + \boldsymbol{\varepsilon}, \quad (2)$$

where $f(\mathbf{q})$ is the computer simulator and $\boldsymbol{\varepsilon}$ represents noise. The samples of $\boldsymbol{\varepsilon}$ are assumed to be independent and identically distributed (*iid*) as $\mathcal{N}(0, \sigma^2)$. An option for constructing the surrogate $\tilde{f}(\mathbf{q})$ is to assume it be a Gaussian process (\mathcal{GP}) [10]:

$$\tilde{f}(\mathbf{q}) \sim \mathcal{GP}(m(\mathbf{q}), c(\mathbf{q}, \mathbf{q}')). \quad (3)$$

Here, $m(\mathbf{q})$ and $c(\mathbf{q}, \mathbf{q}')$ are mean and covariance functions of the \mathcal{GP} , which are dependent on a set of hyperparameters, hereafter denoted by $\boldsymbol{\beta}$. When instantiating $\tilde{f}(\mathbf{q})$, a prior distribution for $\boldsymbol{\beta}$ is assumed. Then within the Bayesian framework, a posterior distribution for $\boldsymbol{\beta}$ is constructed given a set of observed data of size k , i.e. $\mathcal{D}_{1:k} = \{\mathbf{q}^{(i)}, r^{(i)}\}_{i=1}^k$. As a result, the posterior distribution of $r(\mathbf{q})$ is obtained, and it is also a \mathcal{GP} . Using that, mean and variance of $r(\mathbf{q})$ and $\tilde{f}(\mathbf{q})$ at any test sample $\mathbf{q}^* \in \mathbb{Q}$ can be predicted. Note that based on the posterior predictive variance, a confidence interval can be constructed for the predicted mean values. The BO-GPR algorithm can be summarised as the following:

1. Start from a given $\mathcal{D}_{1:k}$.
2. Construct a \mathcal{GP} for $\tilde{f}(\mathbf{q})$ and find the posterior distribution of the hyperparameters $\boldsymbol{\beta}$ using $\mathcal{D}_{1:k}$.
3. Find the next sample $\mathbf{q}^{(k+1)}$ through maximising an acquisition function that is here taken to be the expected improvement (EI) defined as [3]:

$$\text{EI}(\mathbf{q}) = \mathbb{E}[\max(r(\mathbf{q}^\dagger) - r(\mathbf{q}), 0)], \quad (4)$$

where $\mathbf{q}^\dagger = \arg \min_{\mathbf{q} \in \mathcal{D}_{1:k}} r(\mathbf{q})$. For an *iid* Gaussian noise in (3), a closed-form expression for $\text{EI}(\mathbf{q})$ has been derived in [3].

4. Check convergence of the BO-GPR; if not converged, update $\mathcal{D}_{1:k}$ by $\mathbf{q}^{(k+1)}$, $k \leftarrow (k + 1)$, and go to 2.

Defining appropriate convergence criteria in the last step is problem-dependent and can, for instance, be based on the distance between the consecutive samples of \mathbf{q} or having $r(\mathbf{q}^\dagger)$ unchanged over a certain number of samples, see [7] and the references therein. In practice, the computational budget may also impose a limit to the number of simulations. In step 3, when maximising $\text{EI}(\mathbf{q})$, a combination of exploitation, the use of best \mathbf{q} so far, and exploration, reduction of the uncertainty in the GPR surrogate, is considered. The latter, i.e. the active involvement of the predicted uncertainty in the algorithm, is a distinctive characteristic of the BO-GPR approach. As another advantage, the BO-GPR algorithm is versatile meaning that it can be non-intrusively linked to any CFD solver. For instance, a `bash` or `Python` driver can be developed to automatise the whole machinery which comprises of drawing samples in the BO-

GPR, pre-processing the CFD cases, and finally running and post-processing them. In the present study, the BO-GPR algorithm is implemented using GPyOpt [14].

3 Shape Optimisation in a Lid-Driven Cavity Flow

Consider a two-dimensional (2D) cavity flow with the lid moving with a constant velocity U_0 in the positive x direction. The aim is to optimise the shape of the left and right walls of the cavity so that the dissipation, defined as:

$$D = \frac{2}{\text{Re}} \int_{\Omega} S_{ij} S_{ij} d\mathbf{x}, \quad i, j = 1, 2 \quad (5)$$

is minimised or maximised. In this expression, Re is the Reynolds number, $S_{ij} = (\partial u_i / \partial x_j + \partial u_j / \partial x_i) / 2$ is the rate-of-strain tensor, and Ω specifies the flow domain. The optimisation is constrained to keep $\int_{\Omega} d\mathbf{x}$ constant and also retain the length of the lid and bottom surface, l , fixed. The first step to apply the Bayesian optimisation method is to parameterise the left and right walls. To this end, a third-order polynomial is considered for each wall: $\bar{x} = a_0 + a_1 \bar{y} + a_2 \bar{y}^2 + a_3 \bar{y}^3$, where $\bar{x} = x/l$ and $\bar{y} = y/h$ with h denoting the height of the cavity. Considering the origin of the coordinates at $(x, y) = (0, 0)$, the constraint of keeping l fixed leads to $a_{0,L} = 0$ and $a_{3,L} = -(a_{1,L} + a_{2,L})$ for the left wall, and, $a_{0,R} = 1$ and $a_{3,R} = -(a_{1,R} + a_{2,R})$ for the right wall. Therefore, only four distinct design parameters are to be optimised: $\mathbf{q} = (a_{1,L}, a_{2,L}, a_{1,R}, a_{2,R})$. For these, corresponding admissible ranges are arbitrarily chosen as $\mathbb{Q}_{a_{1,L}} = \mathbb{Q}_{a_{1,R}} = [-0.7, 0.7]$ and $\mathbb{Q}_{a_{2,L}} = \mathbb{Q}_{a_{2,R}} = [-0.5, 0.5]$. Assuming the design parameters to be uniform random variables over these ranges, the Sobol sensitivity indices [12] are computed which show a larger sensitivity of \bar{x} to a_1 than a_2 at any $\bar{y} \in [0, 1]$ (not shown here). For any sample of \mathbf{q} taken from the 4D parameter space $\mathbb{Q} = \mathbb{Q}_{a_{1,L}} \times \mathbb{Q}_{a_{2,L}} \times \mathbb{Q}_{a_{1,R}} \times \mathbb{Q}_{a_{2,R}}$, a new shape for the left and right walls is obtained. Corresponding to each configuration of the cavity a computational mesh is automatically generated by gmsh [2]. The flow simulations are performed using Nek5000 [1] which is an open-source highly scalable spectral-element flow solver. In Nek5000, the flow domain is decomposed into a finite number of elements. In each element, a weak form of the incompressible Navier–Stokes equations is solved over Gauss–Lobatto–Legendre (GLL) grid points. In the present study, 30 elements in each of x and y directions are considered, and they are compressed towards the walls. In each element, a 10×10 tensor-product grid of the GLL points is employed.

At $\text{Re} = U_0 l / \nu = 2000$, the cavity shapes with minimum and maximum dissipation are shown in Fig. 1. The optimal parameters for the minimisation and maximisation are found at the 20-th and 15-th iterations, respectively. However, the sampling was continued until 50 iterations to ensure a global optimum had been obtained. The optimal geometries are consistent with the flow physics. In particular, for the shape with maximum dissipation, two large vortices adjacent to the lid are generated which prevent the velocity underneath to increase. The optimal shapes in Fig. 1 can

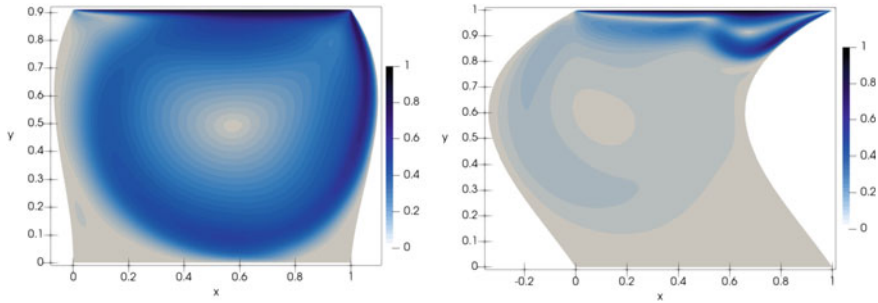


Fig. 1 Contours of the velocity magnitude normalized with the lid velocity U_0 of the 2D cavity flow with (left) minimum and (right) maximum energy dissipation. The flow is steady with $Re = 2000$

be compared to the results reported by Nakazawa [8] using an adjoint method for optimisation. For the minimisation case, the obtained cavity shapes are similar for both BO-GPR and adjoint methods. But this does not hold for the geometry with maximum dissipation. Aside from the difference between the Reynolds number in the two studies, the mismatch can be due to the fact that the BO-GPR finds the global optima. In Fig. 2, the surface of the response $r(\mathbf{q})$ in (3) (here is the dissipation) is plotted in the 2D subspace $a_{1,L} - a_{1,R}$ of the original 4D parameter space. In the plots, the values of $a_{2,L}$ and $a_{2,R}$ are fixed at their computed optima. In Fig. 2a, b, the response surfaces are obtained using the samples generated in minimisation and maximisation, respectively. Clearly, samples are clustered around the global optimum in each case, confirming the fact that the BO is goal-oriented and the sequence of samples quickly moves toward the optima. In the same 2D subspace by combining the samples acquired in minimisation and maximisation problems, more detailed response surfaces are constructed as illustrated in Fig. 2c, d. Through the comparison, the strong point of the BO-GPR algorithm in finding global optima becomes even more visible. An important feature of the GPR is the automatic estimation of the uncertainties of the constructed surrogate over the parameter space, which are represented by the surfaces of the 95% confidence interval in Fig. 2. Reducing such uncertainties is a main driver in the BO algorithm.

4 Conclusion and Outlook

The Bayesian optimisation (BO) based on Gaussian processes regression can be an efficient way of tackling optimisation problems arising in wall-bounded turbulent flows. For such applications, the accuracy and cost-effectiveness of the BO has been recently shown by the authors [7]. The encouraging results have motivated applying the BO to scale-resolving simulations such as large-eddy simulation (LES) and direct numerical simulation (DNS) of wall-bounded turbulent flows. To reduce the overall

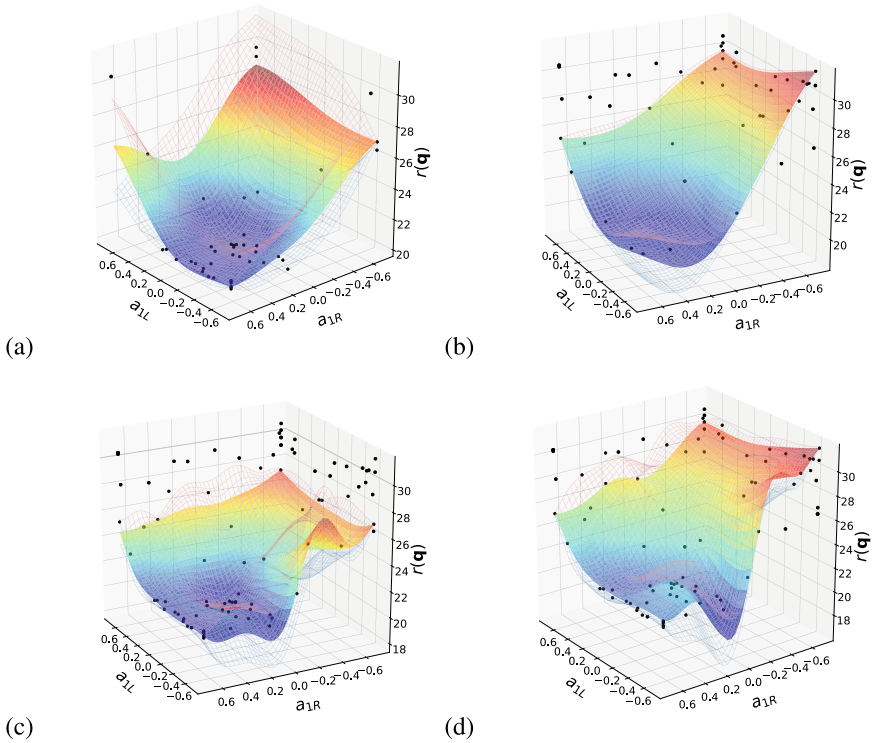


Fig. 2 Posterior surfaces of dissipation in the $a_{1,L} - a_{1,R}$ plane for **a, c** minimisation and **b, d** maximisation of the dissipation in the cavity flow, see Fig. 1. The values of $(a_{2,L}, a_{2,R})$ at these surfaces are fixed at **a, c** $(-0.5, 0.5)$, **b, d** $(0.5, 0.5)$, which are equal to their corresponding optimal values. The GPR in **a, b**, and **c, d** is constructed using the samples taken in the minimisation problem, maximisation problem, and combination of both sets of samples, respectively. The colored surface shows the mean of posterior of dissipation, the red and blue wireframes represent associated upper and lower 95% confidence intervals, and the black symbols are the samples of the design parameters generated during the optimisation

cost in such applications and also account for the observational uncertainties involved in the simulations data, developments are currently ongoing.

Acknowledgements SR acknowledges the financial support from the FLOW Centre at KTH and the EXCELLERAT project which has received funding from the European Union's Horizon 2020 research and innovation programme under grant agreement No 823691. YM acknowledges the Keio-KTH double degree program and the financial support from the NSK Scholarship Foundation. PS, NT and SR also acknowledge funding by the Knut and Alice Wallenberg Foundation via the KAW Academy Fellow programme. KF acknowledges the financial support from the Japan Society for the Promotion of Science (KAKENHI grant number: 18H03758).

References

1. P. F. Fischer, J. W. Lottes, and S. G. Kerkemeier (2008), <http://nek5000.mcs.anl.gov>
2. C. Geuzaine, J.-F. Remacle, *Int J Numer Methods Eng* **79**(11), 1309–1331 (2009)
3. R. Jones, M. Schonlau, W.J. Welch, *J Glob Optim* **13**(4), 455–492 (1998)
4. J. Larson, M. Menickelly, and S. M. Wild. (2019), *Acta Numerica*, 28:287–404
5. J. Laurenceau, M. Meaux, M. Montagnac, P. Sagaut, *AIAA J.* **48**(5), 981–994 (2010)
6. O.A. Mahfoze et al., *Phys. Rev. Fluids* **4**, 094601 (2019)
7. Y. Morita, S. Rezaeiravesh, N. Tabatabaei, R. Vinuesa, K. Fukagata, and P. Schlatter (2021), [arXiv:2101.09985](https://arxiv.org/abs/2101.09985)
8. T. Nakazawa (2016), *Proceedings of ICJWSF2015*, pp. 613–620
9. J. Nocedal, S. Wright, *Numerical Optimization* (Springer, New York, 2006)
10. C.E. Rasmussen, C.K.I. Williams, *Gaussian Processes for Machine Learning (Adaptive Computation and Machine Learning)* (The MIT Press, 2005)
11. B. Shahriari, K. Swersky, Z. Wang, R.P. Adams, N. de Freitas, *Proceedings of the IEEE* **104**(1), 148–175 (2016)
12. I. Sobol, *Math. Comput. Simulat.* **55**(1), 271–280 (2001)
13. C. Talnikar, P. Blonigan, J. Bodart, and Q. Wang (2014), *Proceedings of the CTR*, page 315
14. The GPyOpt authors (2016), <http://github.com/SheffieldML/GPyOpt>

Data-Driven Dynamics Description of a Transitional Boundary Layer



F. Foroozan, V. Guerrero, Andrea Ianiro, and Stefano Discetti

Abstract Cluster analysis is applied to a DNS dataset of a transitional boundary layer developing over a flat plate. The stream-wise-span-wise plane at a wall normal distance close to the wall is sampled at several time instants and discretized into small sub-regions, which are the observations analysed in this work. Using K -medoids clustering algorithm, a partition of the observations is sought such that the medoids in each cluster represent the main local states. The clustering has been carried out on a two-dimensional reduced-order feature space, constructed with the multi-dimensional scaling technique. The clustered feature space provides a partitioning which consists of five different regions. The observations are automatically classified as laminar, turbulent spots, amplification of disturbances, or fully-developed turbulence. The Lagrangian evolution of the regions and the state transitions are described as a Markov process in terms of transition probability matrix and transition trajectory graph to determine the transition dynamics between different states.

1 Introduction

The dynamics of turbulent flows are non-linear and characterized by high dimensionality. The capability of machine-learning (ML) tools to deal with such kind of systems is now paving the way to promising research lines. The purpose of ML fluid dynamics is to provide accurate and efficient reduced-order models that capture the essential dynamical features of fluid flows at a reasonable cost [1]. A comprehensive overview of ML methods used for the turbulence modelling and control is reported in [2]. Dimensionality reduction techniques have received particular attention for flow modelling and control purposes in an automated manner.

In this work we propose an automated flow-modelling method to describe the transition to turbulence of a boundary layer (BL), which has important practical

F. Foroozan (✉) · A. Ianiro · S. Discetti
Aerospace Engineering Research Group, Universidad Carlos III de Madrid, Leganés, Spain
e-mail: firoozeh.foroozan@uc3m.es

V. Guerrero
Department of Statistics, Universidad Carlos III de Madrid, Getafe, Spain

© The Author(s), under exclusive license to Springer Nature Switzerland AG 2021
R. Örlü et al. (eds.), *Progress in Turbulence IX*, Springer Proceedings in Physics 267,
https://doi.org/10.1007/978-3-030-80716-0_19

implications due to the enhanced mixing of momentum, higher skin-friction drag, and heat transfer rates. Here we focus on zero-pressure-gradient BL in the presence of an external flow with free-stream turbulence, with the transition to turbulence being classified as bypass transition [3]. The bypass transition mechanism is described as follows. Firstly, there is a region of streaks i.e. the elongated regions of the perturbation of the stream-wise velocity component. Then these elongated distortions reach large amplitude, which can be larger than 10% of the mean flow speed when the free-stream turbulence intensity is only 3%. The streaks break down locally, to form turbulent spots, precursors of localized regions of turbulence. Once fully formed, these spots continue to grow and spread laterally until they merge with the downstream, fully-turbulent region.

In this work, we aim to obtain an automatic input-free domain partitioning technique, to represent the stages of development of a transitional bypass BL. The availability of well-understood theories for the boundary-layer transition makes it an excellent test case to explore the capabilities of ML to discover a flow theory, and also helps us to evaluate our approach. The use of unsupervised ML techniques to identify regions has already been explored on this dataset. An algorithm has been successfully implemented in the work of [4] to demonstrate the ability of an unsupervised self-organizing map as an automatic tool to identify the turbulent-boundary-layer interface in a transitional flow. In contrast to this method, which separates the points into TBL and non-TBL regions, our focus here is on detecting different stages of the transition based on feature similarity.

The overall approach of this work is presented in Sect. 2, to describe the dataset and also the implemented unsupervised-learning techniques, and the results are presented in two main parts as *kinematic* (in Sect. 3) and *dynamical* analysis (in Sect. 4).

2 Methodology

The dataset used in this work was downloaded from the John Hopkins Turbulence Databases, namely it is the Direct Numerical Simulation (DNS) of the transitional BL of the incompressible flow over a flat plate with an elliptical leading edge. The half-thickness of the plate (L) and the free-stream velocity (U_∞) are used as the reference length-scale and reference velocity respectively. The Reynolds number based on these references quantities is 800. The free-stream turbulence intensity is approximately 3% at the leading edge and slightly less than 0.5% at the outlet of the simulation domain. Stream-wise velocity distribution on a wall-parallel (x - z) plane is sampled. This plane is placed at $y/L = 0.25$ (with y being the wall-normal coordinate), sufficiently close to the wall to be representative of the wall-shear distribution. This selected domain is then discretized into small-sized square cells ($20L \times 20L$) to classify regions by inspecting sub-regions of the domain. The cell size here is of the same order of magnitude as the BL thickness, in order to being large enough to capture significant flow structures, and small enough to guarantee a good mapping of the state of the flow, i.e. a sufficient number of cells. The data in

each cell is captured with the spacing of $0.1L$. Finally, the data is captured at several time instants with the time spacing equal to the convective time to cross a cell with a convection velocity equal to U_∞ . This choice simplifies the analysis since a pseudo-Lagrangian dynamics of observations can be observed by simply stream-wise shift of one cell for each snapshots in time.

Unsupervised learning methods such as Clustering and Multidimensional Scaling (MDS) are applied and evaluated in this work. In order to get a more tractable dataset and remove noisy and redundant features, we propose to reduce the dimensionality before clustering. MDS is a dimensionality reduction technique that maps a set of N points in an original p -dimensional space to a q -dimensional space, where $q \ll p$, given only a proximity matrix. MDS does not require any prior knowledge of the system behavior. It only expects a time-resolved sequence of observations and a problem-dependent definition of a distance measure. Since we work with high-dimensional datasets, taking advantage of MDS we would be able to reduce the dimensionality of the problem while preserving the data structure in the state space.

Clustering partitions the data by introducing few representatives of the system as basis of the reduced-order models. Here we chose an algorithm called K -medoids, which follows the main procedure of K -means but with a different prototyping; K -medoids selects the most centered observation belonging to the cluster as its prototype instead of the average of the observations. This feature is advantageous since we are seeking to find a specific pattern as the representative of each cluster.

After clustering, the dynamical behaviour between different coherent states (or clusters) can be investigated using the Cluster Transition Matrix (CTM) P . It provides the transition of the observations from one cluster to another when advected downstream, that identifies how the groups of observations in the domain belonging to the same cluster change their grouping in one time step. The elements of this matrix P_{jk} , describing the probability of transition from a cluster C_k to C_j in a given forward step, are defined as the number of observations that move from C_k to C_j in Δt divided by the total number of observations (according to [5]).

In addition, to track the transition of cluster states in continuous time-steps, we defined the pseudo-Lagrangian trajectory of observations in the cluster space. Cluster Transition Trajectory (CTT) model the transition between these regions as a Markov process. Having the trajectory of the most probable transitions between clusters, discovers the prevailing sequence of the flow stages. This definition also helps us to track the most upstream observations while travelling downstream. We combine these ideas to develop our low-order model. Since this is a data-driven approach, the model can be as informative as provided by the data. In the present problem the temporal and spatial evolution are considered simultaneously. Here, the aim is not to predict the future states, but rather their interpretability, which means that we need a customized definition with links to the physics of the flow and not a hypothetical transition time-step. Accordingly, we have defined a physics-oriented transition time, which assumes compatible spatial and temporal steps: the convective time to cross a specified space-resolved cell with a convection velocity equal to U_∞ . Since here we have defined a homogeneous coarse-grained spatial domain, this time-step will be fixed throughout the entire domain.

3 Kinematic Analysis

Reducing the dimensions of the dataset enables us to plot all the data in a 2D MDS map with the coordinates of γ_1 and γ_2 that provide a useful interpretability tool to identify the characteristics of the observations which are the stream-wise velocity of the domain captured in small cells. To investigate these characteristics, we examined some of the points along γ_1 and γ_2 to illustrate them in the physical space and observe the flow structure inside each sample cell. Accordingly, we can find the parameters that correlate well with γ_1 and γ_2 . This investigation showed that along γ_1 , the stream-wise variance of the sampled data in the physical space, which is an indicator of the turbulence intensity, is increasing. Along γ_2 , however, the high-variance regions of the sampled data move in span-wise direction. To quantify these characteristics of the observations the span-wise profile of the stream-wise velocity variance inside each cell are evaluated with γ_1 and γ_2 . The mean value of this profile ($\bar{\sigma}$) and the span-wise position of the center of area of this profile (Z^*) are examined and we found that these two parameters have a linear behavior with respect to γ_1 and γ_2 , respectively. This makes a valuable correlation between the axes and these parameters. Thus, it can be stated that the computer has found two consistent metrics to reveal important features. Accordingly, we can confirm that γ_2 is not related to the stream-wise evolution of the structures, thus the transition process.

After reducing the dimensionality of the problem, data clustering is performed on the low-dimensional space (Fig. 1a). In this work the elbow method [6] is used

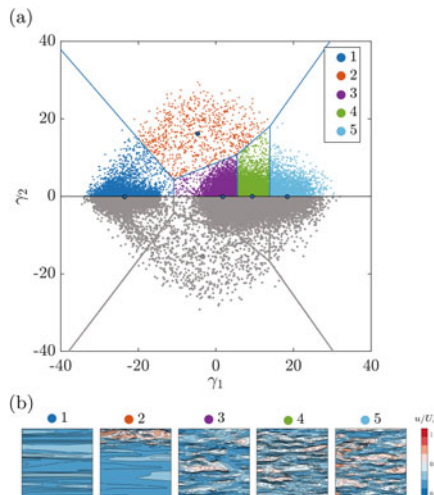


Fig. 1 Kinematic analysis: **a** Clustered two-dimensional MDS map after applying the symmetry. Clusters are specified by colors and the gray points are the merged points. **b** Original contour illustration of the cluster medoids; showing the streaks in medoid 1, turbulent spots in medoid 2, and turbulent stages in medoids 3 to 5 with increasing in intensity

to choose the number of clusters. The result yield to $K = 6$. In addition to what the process found about γ_1 and γ_2 from correlation parameters, the symmetrical configuration of the clusters further confirms that γ_2 relates directly to the asymmetry of the cells rather than to region recognition. Therefore, it is relevant to shrink the 2D map by reflecting all the points to the upper half part of the map. Thus, clusters numbers 2 and 3 are merged into one cluster and five medoids are shown in Fig. 1b, in which we can detect different structures inside them. This difference between their internal structures reveals different flow regimes. We can clearly distinguish different stages of the transitional BL flow from streaks, formation of turbulent spots, high velocity fluctuations turbulent regions and fully turbulent region. There is an overshoot of turbulent activity in the transition region, then the turbulence activity decreases while moving towards fully-turbulent state and is in accordance to [7].

4 Dynamical Analysis

The results shown in Fig. 2 report the CTM containing the probability of transition from one cluster (in columns) to another (in rows) within a forward time-step. It represents the dynamical change of state in the entire flow field. It can be seen that the second cluster play a role as transition phase between the first one and the last three which are coupled and reveal the regions of high turbulence. For cluster 3, it has a large probability to remain in the same state, and thus, it reveals the state of fully turbulent. Distance Matrix also discovers the similarity between clusters in terms of the distance parameter in the low-dimensional space (Fig. 2b). This distance represents the dissimilarity of the primitive cells, the more is the distance, the less similar are the clusters. The same configuration of clusters as the probability matrix can be seen here. It shows that the group of 3 clusters that have the most probability of transition in between are more similar to each other than to other clusters. To track the

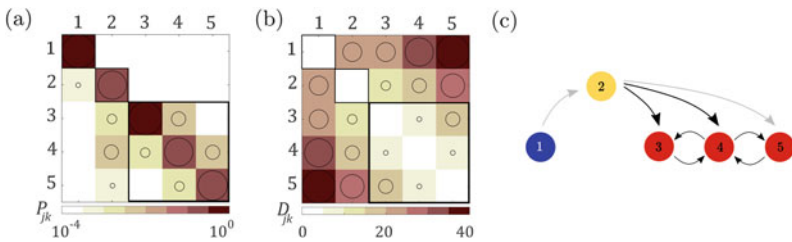


Fig. 2 Dynamical analysis: **a** Cluster Transition Matrix. **b** Cluster Distance Matrix. For the transition matrix the scale is logarithmic, while it is linear for the distance matrix. Cluster subsets are shown in black squares. **c** Graph of Cluster Transition Trajectory. The group of the three final clusters are depicted in one specific color to show their belonging to the turbulent region

transition of cluster states in continuous time-steps, we need to model the transition between these regions as a process, which displays the graph of the trajectories shown in Fig. 2c. Here we assumed that after one time step, each cell travels one-step forward in space. With this assumption, the pseudo-Lagrangian tracking of the cells is captured from the leading edge to the end of the plate and the most probable trajectories are determined. In contrast to the cluster transition matrix that captures all the possible movements in time, this graph captures just the ones that happen between two different clusters. However, the typical path is consistent with the cluster transition matrix, and the cells typically move from laminar to turbulent spots, and finally to regions in the center which is the most spatially homogeneous configuration, thus fully-developed turbulence.

5 Conclusions

With the feature-space discretization, we obtained the regions of development of a transitional BL automatically identified as region containing streaks, turbulent spots, amplification of disturbances, and fully developed turbulent flow. The pseudo-Lagrangian evolution of the regions and the state transitions are employed in terms of transition probability matrix and transition trajectory graph to determine flow dynamics and transition mechanisms between the different states. The development of regions in transitional BL flow presents intermediate stages. The present methodology correctly identifies the bypass transition mechanism. This work thus shows that unsupervised algorithms can identify complex flow dynamics and extract theoretical information.

Acknowledgements This work was partially supported by the research projects:

1. PITUFLOW-CM-UC3M, funded by the call “Programa de apoyo a la realización de proyectos interdisciplinarios de I+D para jóvenes investigadores de la Universidad Carlos III de Madrid 2019–2020” under the frame of the Convenio Plurianual Comunidad de Madrid-Universidad Carlos III de Madrid.
2. COTURB, funded by the European Research Council, under grant *ERC* – 2014.*AdG* – 669505.

References

1. S.L. Brunton, B.R. Noack, P. Koumoutsakos, Machine Learning for Fluid Mechanics. *J Fluid Mech* **52**, 477–508 (2020)
2. S.L. Brunton, B.R. Noack, Closed-Loop Turbulence Control: Progress and Challenges. *Appl. Mech. Rev.* **67**(5), 050801 (2015)
3. T.A. Zaki, From Streaks to Spots and on to Turbulence: Exploring the Dynamics of Boundary Layer Transition. *Flow, Turbulence and Combustion* **91**(3), 451–473 (2013)
4. Z. Wu, J. Lee, C. Meneveau, T.A. Zaki, Application of a self-organizing map to identify the turbulent-boundary-layer interface in a transitional flow. *Physical Review Fluid* **4**, 023902 (2019)

5. E. Kaiser, B.R. Noack, L. Cordier, A. Spohn, M. Segond, M. Abel, G. Daviller, J. Östh, S. Krajnović, and R. Niven, Cluster-based reduced-order modelling of a mixing layer. *J Fluid Mech* **754**, 365–414 (2014)
6. R.L. Thorndike, Who belongs in the family? *Psychometrika* **18**, 267–276 (1953)
7. X. Wu, R.G. Jacobs, J.C.R. Hunt, P.A. Durbin, Simulation of boundary layer transition induced by periodically passing wakes. *J Fluid Mech* **398**, 109–153 (1999)

Identification of a Stochastic Hopf Bifurcation from Stationary Measurement Data of a Turbulent Flow



Moritz Sieber, Christian Oliver Paschereit, and Kilian Oberleithner

Abstract The observation of a Hopf bifurcation in fluid dynamics is commonly associated with the occurrence of a global hydrodynamic instability. The increase of a control parameter above a critical value causes a change from a stable to an unstable flow condition. This behaviour is well understood for the occurrence of instabilities in laminar flows. In turbulent flows, however, the occurrence of hydrodynamic instabilities is similarly observed but less clear. The current work examines the use of stochastic models to describe the supercritical Hopf bifurcation of the global mode in a turbulent swirling jet. The consideration of the interaction between the global mode and the stochastic turbulent perturbations allows a consistent description of the experimental observations. This opens up extensive possibilities for describing and interpreting the occurrence of hydrodynamic instabilities in turbulent flows.

1 Introduction

The observation and description of hydrodynamic instabilities are historically associated with the observation of periodic dynamics in laminar flows that trigger the transition to turbulence. The transition from a stable to an unstable flow state is associated with the change of a control parameter. This parameter is commonly the Reynolds number, which defines the flow states that give rise to instabilities and cause the transition to turbulence. The occurrence of these instabilities is commonly associated with a Hopf bifurcation of the flow [1]. Beyond their well-established role in the transition to turbulence, the occurrence of hydrodynamic instabilities in a turbulent flow is less clear. The change of control parameters other than the Reynolds number can lead to the emergence of hydrodynamic instabilities in fully turbulent flows. In this case, the instability does not develop from an undisturbed steady state,

M. Sieber · K. Oberleithner
Laboratory for Flow Instabilities and Dynamics, Technische Universität Berlin,
10623 Berlin, Germany

M. Sieber (✉) · C. O. Paschereit
Chair of Fluid Dynamics, Technische Universität Berlin, 10623 Berlin, Germany
e-mail: moritz.sieber@tu-berlin.de

but within a stochastically fluctuating flow. The interaction between deterministic dynamics that develop due to the instability and stochastic perturbations that are introduced from the background turbulence is decisive to understand the dynamics in such cases. Phenomenologically, the velocity fluctuations in turbulent flows are categorised by a triple decomposition [2]. Accordingly, the velocity is decomposed into a mean, coherent, and stochastic part that reads

$$v(x, t) = \bar{v}(x) + \tilde{v}(x, t) + v'(x, t), \quad (1)$$

respectively. The mean part \bar{v} , given by the time averaged velocities, constitutes the base flow on which hydrodynamic instabilities may develop. These hydrodynamic instabilities cause the coherent velocity fluctuations \tilde{v} . Further stochastic fluctuations v' are present due to the turbulent flow state.

The observation of coherent dynamics in fully turbulent flows can be attributed to hydrodynamic instabilities. In that context, the instabilities are assumed to develop on the mean velocity field and the turbulent fluctuations act as an increased viscosity [3]. This approach has provided accurate replication of coherent structures extracted from measurements. However, the temporal dynamics observed in the measurement data and the amplification rates suggested by theory do not necessarily coincide [4]. In this work, the experimental observations are explained by a mixed deterministic stochastic model that provides a consistent closure. The stochastic model is based on the analysis of stationary measurement data [5]. It relies on a strict separation of deterministic and stochastic contributions in the data. Accordingly, the deterministic and stochastic part can be accurately modelled which allows an accurate description of the observed dynamics. Previously, the approach was used to characterise thermo-acoustic instabilities in combustion chambers [6].

2 Stochastic Modelling Approach

This section describes the essence of this approach. A detailed derivation of the consecutive steps for the presented approach is given in a related study [7]. Accordingly, the deterministic dynamics of the hydrodynamic instabilities are captured by the Stuart-Landau equation [1]. It describes the oscillatory motion of the instability and the mean-field corrections that lead to a saturation of the oscillation amplitude at the limit-cycle. The background turbulence is covered as a stochastic forcing of the Stuart-Landau equation. This reads

$$\frac{dA}{dt} = (\sigma + i\omega)A - \alpha |A|^2 A + \xi, \quad (2)$$

where A is the complex-valued amplitude of the global mode. The deterministic evolution of the amplitude is governed by the frequency ω , amplification rate σ , and saturation α . The stochastic perturbations are represented by random forcing ξ with

zero mean and variance Γ . In a purely deterministic configuration without stochastic forcing, the amplitude would always converge to the limit cycle. Due to the additional stochastic perturbations, the dynamics is perturbed at the limit cycle. The resulting displacement from the limit cycle and the deterministic return to the limit cycle enables the calibration of state-space models. Since the stochastic perturbations cause continuous disturbances of the system, this is possible with steady-state measured data.

The calibration of the model from the data does not rely on the replication of measured temporal dynamics. Instead, the same statistics are derived from the model and the measurements and then compared. Therefore, the model (2) that describes the evolution of one specific state of the flow is transferred to a Fokker-Planck equation that describes the corresponding probability density of a flow state. The stationary solution of the Fokker-Planck equation provides the average probability density P for the observation of a specific oscillation magnitude $|A|$ as

$$P(|A|) = \mathcal{N}|A| \exp\left(\frac{2\sigma}{\Gamma}|A|^2 - \frac{\alpha}{\Gamma}|A|^4\right). \quad (3)$$

The parameters of this analytical representation are calibrated to match with the measured probability distribution. The calibrated parameters ultimately provide the physical amplification rate σ of the underlying flow.

3 Application to Experimental Data

The approach is used to investigate the global hydrodynamic instability in a swirling jet [3]. The rise of this instability is related to the swirling strength of the flow, which is characterised by the swirl number. Hence, the swirl number is the major control parameter in the investigations. It can be set independently from the Reynolds number allowing investigations at fully turbulent conditions. Through a step-wise increase of the swirl intensity, a supercritical Hopf bifurcation of the flow is observed. The bifurcation is primarily detected from pressure measurements, which allows the recording of the long time series that are necessary to obtain converged statistics. The pressure time series are further filtered to separate the coherent dynamics from stochastic perturbations. The filter uses a spatial Fourier decomposition to reduce the information from eight pressure to a complex coefficient which is further band pass filtered to the frequency range of the instability. The validity of the filter was further checked against dominant structures found in PIV measurements of the flow, as detailed in [7]. From the measurements, the probability distributions of the amplitudes are determined and the analytical model (3) is calibrated to replicate these distributions. The change of the model parameters across the investigated parameters is used to interpret the flow physics.

The measured probability distributions and the calibrated amplification rate are presented in Fig. 1. The probability distributions (Fig. 1a) show a continuous increase

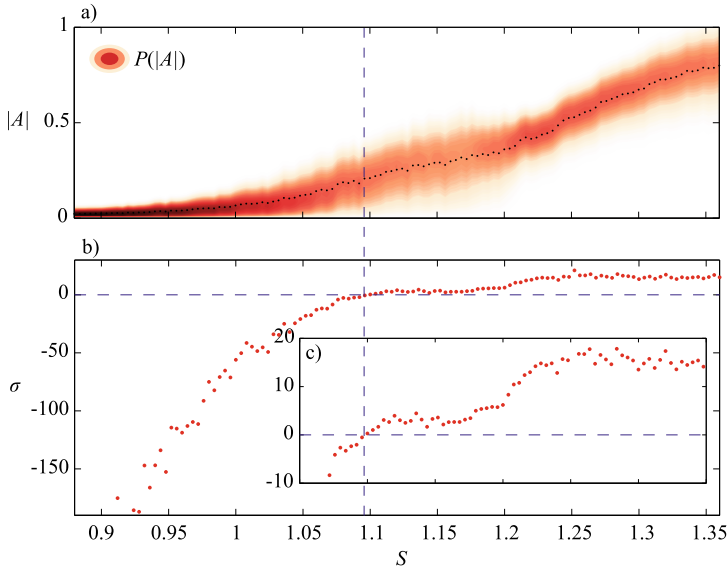


Fig. 1 The graphs show the measured oscillation magnitude $|A|$ (a) and the estimated amplification rate σ (b) against the swirl number S . The insert (c) gives a detail of graph (b). The magnitude is represented by the measured probability distribution $P(|A|)$ at different swirl numbers. The critical swirl number is indicated by a dashed vertical line. (see also [7] for further results)

of the amplitude. The variance of the amplitude does also continuously increase with the swirl number. The sole consideration of the mean amplitude or the variance does not indicate a change of the flow from a stable to an unstable state, it indicates a continuous transition from small to large amplitudes. The parameters from the calibration probability distributions give a much clearer picture. From the amplification rate (Fig. 1b), the sign change that marks the bifurcation point can be identified. The turbulent perturbations obscure the transition in the measured amplitudes, but the stochastic model allows to identify the underlying bifurcation.

The approach is based on the assumption that the flow is actually determined by the stochastic model used. It requires a strict separation of deterministic and stochastic dynamics and does not allow to lump any deterministic dynamics missed in the measurements into the stochastic contributions. The extensive study in [7] shows that the model used here is an oversimplification of the flow. Improving the model accuracy causes minor changes in the trends observed in Fig. 1. However, an increase in the model fidelity (dimensions) comes at the cost of reduced accuracy of the model calibration. This is due to the fixed amount of available measurement data from which the statistics can be derived.

4 Discussion

The proposed method allows to draw completely new conclusions from steady-state measurements of turbulent flows. It allows one to infer a detailed picture of the flow state from relatively simple measurements. This is possible through an accurate separation of deterministic and stochastic dynamics and appropriate modelling of both contributions. Due to the stochastic perturbations, the sole consideration of the mean state does not allow the identification of the bifurcation. This becomes more clear when bifurcation scenarios in laminar and turbulent flows, given in Fig. 2, are investigated side by side. For laminar conditions, the bifurcation from the stable to the unstable state can be seen from the sudden occurrence of the limit cycle oscillation. In a turbulent flow, stochastic forcing causes the occurrence of oscillations even for stable conditions. The closer the flow is to the bifurcation point, on the stable side, the longer it takes for these exited oscillations to decay. Hence, we observe a continuous change of the amplitude across the *stochastic* bifurcation.

The probabilistic interpretation of the flow state and the accurate modelling of deterministic and stochastic contributions allow us to gain deep insights into the dynamics of turbulent flows. The interpretation of the occurrence of a global mode in a turbulent flow as a stochastic Hopf bifurcation allows an accurate description of the experimental observations. The proposed approach requires only stationary measurements and still provides a detailed picture of the dynamic state of the flow. This is possible due to the stochastic forcing that causes the flow to explore the state space in the vicinity of the asymptotic state. Without forcing, the flow would approach the asymptotic state (limit cycle or fixed point) and stay there infinitely. From the balance between the deterministic return to the asymptotic state and the stochastic forcing, which deflects the flow from this state, the flow physics can be identified.

The presented approach has provided great detail for the occurrence of global modes in turbulent swirling flows [4, 7]. Moreover, the authors are confident that it

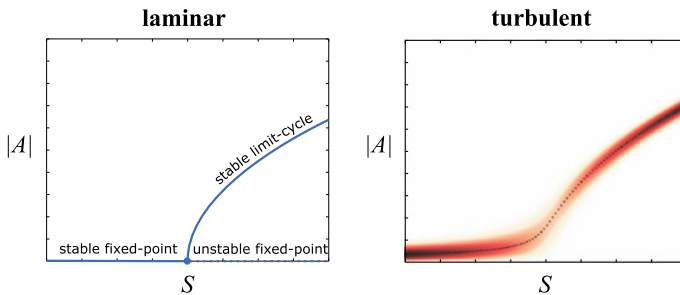


Fig. 2 Different characteristics of a supercritical Hopf bifurcation in a laminar and in a turbulent flow. The graphs show the bifurcation diagram for the magnitude $|A|$ against the swirl number S . The laminar case provides distinct points in the state space whereas the turbulent case allows only a probabilistic description of the state. (as in Fig. 1a)

will help to interpret the occurrence of hydrodynamic instabilities in turbulent flows in many other cases, as well. The consideration of the stochastic forcing in turbulent flows has shown to be the key element for an accurate interpretation of measurement data of instabilities in turbulent flows.

References

1. J. T. Stuart, On the non-linear mechanics of hydrodynamic stability. *Journal of Fluid Mechanics* 4.1 (1958), pp. 1–21. issn: 0022-1120. <https://doi.org/10.1017/S0022112058000276>
2. A. K. M. F. Hussain, W. C. Reynolds, The mechanics of an organized wave in turbulent shear flow. *J. Fluid Mechanics* 41.02 (1970), p. 241. issn: 0022-1120. <https://doi.org/10.1017/S0022112070000605>
3. Kilian Oberleithner, Moritz Sieber, Christian Navid Nayeri, Christian Oliver Paschereit, Christoph Petz, Hans-Christian Hege, Bernd R. Noack, and I. Wygnanski. “Threedimensional coherent structures in a swirling jet undergoing vortex breakdown: stability analysis and empirical mode construction”. In: *Journal of Fluid Mechanics* 679 (2011), pp. 383–414. issn: 0022-1120. <https://doi.org/10.1017/jfm.2011.141>
4. Jens S. Müller, Moritz Sieber, Ivan Litvinov, Sergey Shtork, Sergey Alekseenko, and Kilian Oberleithner. “Prediction of vortex precession in the draft tube of a model hydro turbine using mean field stability theory and stochastic modelling”. In: *30th Symposium on Hydraulic Machinery and Systems 2020*. Lausanne, Switzerland, 2020
5. Rudolf Friedrich, Joachim Peinke, Muhammad Sahimi, and Reza Rahimi Tabar, M. “Approaching complexity by stochastic methods: From biological systems to turbulence”. In: *Physics Reports* 506.5 (2011), pp. 87–162. issn: 03701573. doi: <https://doi.org/10.1016/j.physrep.2011.05.003>
6. Nicolas Noiray and Bruno Schuermans. “Deterministic quantities characterizing noise driven Hopf bifurcations in gas turbine combustors”. In: *International Journal of Non-Linear Mechanics* 50 (2013), pp. 152–163. issn: 00207462. doi: <https://doi.org/10.1016/j.ijnonlinmec.2012.11.008>
7. Moritz Sieber, Christian Oliver Paschereit, and Kilian Oberleithner. “Stochastic modelling of a noise driven global instability in a turbulent swirling jet”. In: *Journal of Fluid Mechanics in press* (2020). url: <https://arxiv.org/abs/2007.07555>

Data-Driven Identification of Robust Low-Order Models for Dominant Dynamics in Turbulent Flows



Y. Schubert, Moritz Sieber, Kilian Oberleithner, and Robert J. Martinuzzi

Abstract This work presents an automated process minimising input parameters for the study of turbulent flows. The goal is to gain insight into the flow dynamics by deriving a data-driven reduced-order model (ROM). Spectral proper orthogonal decomposition (SPOD) is used to efficiently separate the flow dynamics and project the flow field onto a low-dimensional subspace to represent the dominating dynamics with a reduced set of modes. A polynomial combinations of the temporal modal coefficients defines a function library to describe the dynamics by a linear system of ordinary differential equations. In a two-stages cross-validation procedure (conservative and restrictive sparsification), the most important functions are identified and combined in a final ROM. The process is demonstrated for PIV data of a circular cylinder undergoing vortex induced vibration (VIV) $Re = 4000$.

1 Introduction

Over the last decades, experimental studies and simulations of flows have improved significantly in both accuracy and resolution, leading to tremendous amounts of high-fidelity data. Hence, data-driven approaches to investigate turbulent flows are increasingly important. These approaches often aim to derive low-order models with fast and accurate predictions of the flow dynamics to support physical analysis.

The investigation of turbulent flows poses two inherent challenges to data-driven identification of ROM. First, the posterior system identification from observed flow dynamics requires a distinct separation of deterministic dynamics from the stochastic

Y. Schubert · M. Sieber (✉) · K. Oberleithner
Laboratory for Flow Instabilities and Dynamics, Technische Universität Berlin, Berlin, Germany
e-mail: moritz.sieber@tu-berlin.de

Y. Schubert
e-mail: yannick.schubert@hotmail.de

R. J. Martinuzzi
Department of Mechanical and Manufacturing Engineering, University of Calgary, Alberta, Canada
e-mail: rmartinu@ucalgary.ca

fluctuations. Second, the calibration procedure must account for random perturbations of the flow that are extraneous to the candidate model and may lead to over-fitting of the model. In this work a robust approach to handle these challenges using as few exogenous parameters as possible is presented.

Figure 1 illustrates the main idea of the process. Instead of computing the temporal evolution of the velocity field $\mathbf{v}(\mathbf{x}, t)$ by solving the Navier-Stokes-Equations $\mathcal{N}(\cdot)$ directly (slow and very computational costly) the idea is to project the velocity data onto a low-dimensional subspace, isolate the temporal variance $a_i(t)$ of the dynamics and find a representation i. e. operator \mathbf{F} that describes the dynamics.

$$\frac{d}{dt}\mathbf{a}(t) = \mathbf{F}(\mathbf{a}(t)). \quad (1)$$

In a final step, the field is projected back to the original system. The questions arises: What does this operator \mathbf{F} look like and how to derive it?

The first challenge is addressed by an efficient separation of the flow dynamics using a modal decomposition of the flow data [1]. The flow is represented by spatial modes and their corresponding modal coefficients capturing temporal variations. This allows representing the flow dynamics by a reduced set of modes and a simple description of the dynamics by the temporal evolution of the modal coefficients [2]. Here, the velocity is decomposed into a mean field $\overline{\mathbf{v}(\mathbf{x})}$ and fluctuations, which are further decomposed into spatial modes $\Phi_i(\mathbf{x})$ and temporal coefficients $a_i(t)$:

$$\mathbf{v}(\mathbf{x}, t) = \overline{\mathbf{v}(\mathbf{x})} + \sum_{i=1}^N \Phi_i(\mathbf{x})a_i(t). \quad (2)$$

The modal base of low-order models is commonly constructed from a POD. However, this often lacks a clear separation of individual dynamics in different modes making it difficult to build efficient models. This shortcoming is circumvented using the recently introduced SPOD, which helps distinguish different dynamics [3], which is well suited for cyclical but not necessarily periodic signals. The SPOD seeks a short-time temporal coherence in addition to the spatial coherence that is imposed by the modal decomposition. Hence, SPOD requires the specification of a correlation window size, which is the only additional parameter to POD. This results in smooth temporal coefficients, which is beneficial for constructing ROMs. Since coherent flow structures are usually represented by pairs of modes, the spectral proximity between the modes is measured and they are paired accordingly as real and imaginary parts of a complex mode [3]. This allows to simplify the system description and reduces the computational costs.

For the second challenge, the approach builds on recent work introducing strategies from machine-learning [4]. These studies show that efficient representations of canonical fluid dynamic problems can be identified from an automated procedure. The central idea is to describe all interactions of the flow dynamics (even non-linear) with a linear system of ordinary differential equations, where a library of functions Θ accounts for the non-linearities. For this, a reduced number N_m (dependant on the flow complexity) of temporal coefficients \mathbf{A} ,

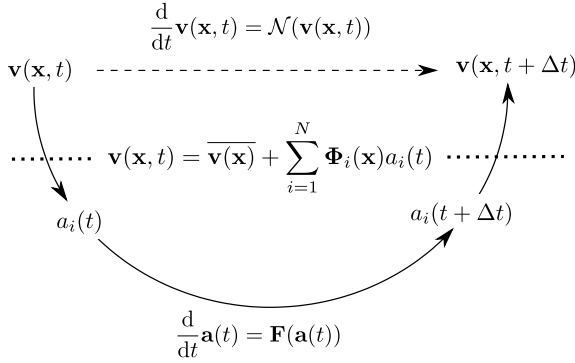


Fig. 1 Conceptual schematic for deriving the temporal evolution of a flow field: the dashed arrow is the direct approach solving Navier-Stokes-Equations (theoretical solution), curved arrows indicates the indirect approach via a modal decomposition (applied solution); the dotted line indicates transition between physical (above) and modal space (below)

$$\mathbf{A} = \begin{bmatrix} \mathbf{a}^T(t_1) \\ \mathbf{a}^T(t_2) \\ \vdots \\ \mathbf{a}^T(t_N) \end{bmatrix} = \begin{bmatrix} a_1(t_1) & a_2(t_1) & \dots & a_{N_m}(t_1) \\ a_1(t_2) & a_2(t_2) & \dots & a_{N_m}(t_2) \\ \vdots & \vdots & \ddots & \vdots \\ a_1(t_{N_t}) & a_2(t_{N_t}) & \dots & a_{N_m}(t_{N_t}) \end{bmatrix}, \tag{3}$$

is used as basis function and combined in all forms of polynomial combinations to define library functions that compose the library

$$\Theta(\mathbf{A}) = \begin{bmatrix} | & | & | & | & | & | & | & | \\ 1 & \mathbf{A} & \overline{\mathbf{A}} & \mathbf{A}^{P_2} & \overline{\mathbf{A}}^{P_2} & (\mathbf{A}\overline{\mathbf{A}})^{P_2} & \mathbf{A}^{P_3} & \dots \\ | & | & | & | & | & | & | & | \end{bmatrix}. \tag{4}$$

Here, \mathbf{A}^{P_2} , \mathbf{A}^{P_3} , $(\mathbf{A}\overline{\mathbf{A}})^{P_2}$ etc. denote higher order polynomials of the state vector $\mathbf{a}(t)$ and its complex conjugated $\mathbf{a}^*(t)$. Hence, (1) can be formulated as

$$\frac{d}{dt}\mathbf{A} = \Theta(\mathbf{A})\Xi, \tag{5}$$

where the matrix Ξ contains the library coefficients, that define which of the library functions contribute for the prediction of each mode. While the number of library functions comprises all sorts of possible combinations, it is assumed that in fact only a few of the corresponding library coefficients $\Xi = [\xi_1 \ \xi_2 \ \dots \ \xi_{N_m}]$ are important i. e. different from zero. Thus, the matrix Ξ is considered to be sparse.

A critical step of the process is the identification of these library coefficients (sparsification). For turbulent flows the stochastic dynamics that are not represented by the low-order model can perturb the modelled dynamics and make the direct application of the recent methodology unreliable. In the present study, a refined approach

is presented that uses two-stage cross-validation for the sparsification procedure to find models with as few parameters as possible without resulting in trivial solutions.

2 Two-Stage Sparsification

The procedure is divided into a conservative sparsification, focused on the approximation of the derivative, and a restrictive sparsification, focused on the model prediction. Hence, the first step identifies candidates and the second retains only a subset of statistically significant coefficients.

2.1 Conservative Sparsification

The principle of this cross-validation step is a bottom-up approach to find the optimal library coefficient in each iteration that improve the approximation of the derivative. The goal is to prefilter the library to reduce computational effort in the restrictive sparsification. Initially, all library coefficients are set to zero. Then coefficients are stepwise activated and their influence on the derivative approximation evaluated. For this, the original signal is divided into equidistant segments based on the SPOD filter to preserve data continuity. The segments are randomly split into training $\mathbf{t}^{\text{train}}$ (20% of segments) and validation \mathbf{t}^{val} (remaining 80%) data. The ratio depends on the available data aiming to maximise the validation data while keeping enough data for training, thus minimising the over-fitting risk. The active coefficients are trained,

$$\xi^{\text{train}} = \underset{\xi}{\operatorname{argmin}} \left\| \frac{d}{dt} a^T(\mathbf{t}^{\text{train}}) - \Theta(a^T(\mathbf{t}^{\text{train}})) \xi \right\| \quad (6)$$

and then a residual r is computed

$$r = \left\| \frac{d}{dt} a^T(\mathbf{t}^{\text{val}}) - \Theta(a^T(\mathbf{t}^{\text{val}})) \xi^{\text{train}} \right\|^2. \quad (7)$$

When all non-active library coefficients are individually tested, the coefficient with the highest improvement is activated permanently. In the following iterations coefficients are evaluated and added in the same way until there is no further improvement in the approximation of the derivative. This is repeated for N_{train} random selections of training and validation data. In a last step, all coefficients that showed an amelioration with respect to the residual are merged into final list of possible candidates.

2.2 Restrictive Sparsification

This procedure is a top-down approach. It starts with the candidate list optimising the coefficient selection based on the model prediction. In comparison to the first stage, the idea is to evaluate if a library coefficient is important not only for the prediction of a single mode, but for the entire system and thereby remove coefficients that are not relevant to describe the dynamics. In an iterative procedure models are built excluding one of the library coefficients candidates, trained and then a short-time integration is performed. Analogously to the the first procedure a subset of randomly chosen training data is used, but this time the entire model is trained simultaneously:

$$\Xi^{\text{train}} = \underset{\Xi}{\operatorname{argmin}} \left\| \frac{d}{dt} \mathbf{a}^T(\mathbf{t}^{\text{train}}) - \Theta(\mathbf{a}^T(\mathbf{t}^{\text{train}})) \Xi \right\|. \quad (8)$$

With short-time integrations (over N_{sim} time steps) from over N_{init} randomly chosen initial values the model performance can be evaluated:

$$r = \int_{t^0}^{t^0 + N_s \Delta t} \left\| \mathbf{a}(t) - \mathbf{a}(t^0) - \int_{t^0}^t f(\mathbf{a}(s)) ds \right\|^2 dt, \quad (9)$$

with function $f = \Theta(\mathbf{a}) \Xi^{\text{train}}$. By iterating over different initial values and various training data sets, a quality function that indicates the relevance of each library coefficient for the ROM can be determined. Coefficients that impact negatively the prediction are excluded permanently. This is repeated until the model converges to a final selection of statistically significant library coefficients.

3 Application to Experimental Data

The procedure is demonstrated for PIV data from the VIV of a cylinder at $\text{Re} = 4000$ [5]. A case in the de-synchronisation regime is chosen to show interactions of forced and natural shedding. The applied process results in the following model using the three most energetic (complex) modes, which is the minimal group of modes to have a meaningful illustration of the process describing the dominating flow dynamics:

$$\begin{aligned} \frac{da_1}{dt} &= \alpha_1 \cdot a_1 + \alpha_2 \cdot a_2 |a_2|^2 + \alpha_3 \cdot a_1 |a_1|^2 + \alpha_4 \cdot a_1 |a_2|^2 + \alpha_5 \cdot a_2 a_3 a_1^* + \alpha_6 \cdot a_1 a_1 a_3^* \\ \frac{da_2}{dt} &= \beta_1 \cdot a_2 + \beta_2 \cdot a_2 a_2 a_1^* + \beta_3 \cdot a_2 a_3 + \beta_4 \cdot a_1 a_1 a_3^* + \beta_5 \cdot a_1 |a_3|^2 \\ \frac{da_3}{dt} &= \gamma_1 \cdot a_3 + \gamma_2 \cdot a_2 a_1^* + \gamma_3 \cdot a_3 |a_1|^2 + \gamma_4 \cdot |a_1|^2. \end{aligned}$$

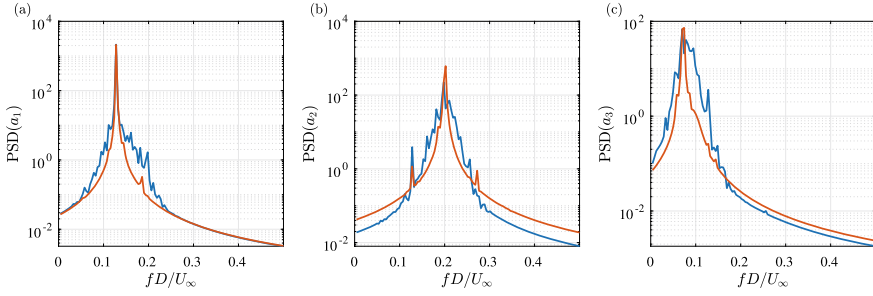


Fig. 2 Power spectrum of the mode coefficients obtained from the SPOD of PIV measurement (blue), a simulation of the calibrated low-order model (orange). The graphs show the mode **(a)** of the natural frequency of the cylinder, **(b)** the vortex shedding and **(c)** of the mode related to the interaction of the forced shedding and the cylinder motion

Following the two-step sparsification the number of possible library coefficients is reduced from 252 to only 15. These statistically significant coefficients and the corresponding library functions provide insight to the flow physics. As the model only represents the deterministic dynamics of the dominating structure, long-term predictions show deviations after approximately two periods of the natural cylinder oscillation, since the model does not account for stochastic perturbations and only uses a reduced number of modes to represent flow structures. However, Fig. 2 shows, that the model captures the general, spectral characteristics of the flow.

4 Conclusion

The presented approach provides an objective strategy for the investigation of turbulent flows. It uses SPOD for an efficient separation of the flow dynamics, which allows to isolate individual physical phenomena and results in smooth temporal coefficients. With a two-stage cross-validation procedure the essential analytical functions can be identified, so that flow dynamics can be represented with a linear system of ODEs. The selection of the analytical functions also provides insight of the flow physics. Finally, this is achieved with a very limited number of input parameters, which can either be derived from physical properties of the flow or address the number of repeated iterations on different parts of the data, i.e. without the need to define an arbitrary threshold.

References

1. K. Taira, S.L. Brunton, S.T.M. Dawson, C.W. Rowley, T. Colonius, B.J. McKeon, O.T. Schmidt, S. Gordeyev, V. Theofilis, L.S. Ukeiley, Modal Analysis of Fluid Flows: An Overview. *AIAA J* **55**, 4013–4041 (2017)
2. B.R. Noack, K. Afanasiev, M. Morzyński, G. Tadmor, F. Thiele, A hierarchy of low-dimensional models for the transient and post-transient cylinder wake. *J Fluid Mech* **497**, 335–363 (2003)
3. M. Sieber, C.O. Paschereit, K. Oberleithner, Spectral proper orthogonal decomposition. *J Fluid Mech* **792**, 798–828 (2016)
4. S.L. Brunton, J.L. Proctor, J.N. Kutz, Discovering governing equations from data by sparse identification of nonlinear dynamical systems. *PNAS USA* **113**, 3932–3937 (2016)
5. G. Riches, C. Morton, One degree-of-freedom vortex-induced vibrations at constant Reynolds number and mass-damping. *Exp. Fluids* **59**, 1–16 (2018)

Experimental Assessment of Symmetry Induced Higher-Moment Scaling Laws in Turbulent Pipe Flow



Spencer Zimmerman, Joseph Klewicki, and Martin Oberlack

Abstract The total velocity moment scaling law that can be obtained through the symmetry group analysis described by Oberlack et al. (Mech. Eng. Rev., vol. 2, 2015) is assessed using experimental pipe flow velocity measurements previously published in Zimmerman et al. (J. Fluid Mech., vol. 869, 2019, pp. 182–213) and Baidya et al. (J. Fluid Mech., vol. 871, 2019, pp. 377–400). Although the streamwise velocity data are well described by the proposed scaling law, we show that the observed level of agreement is primarily reflective of the role played by the mean velocity rather than of the details of the fluctuations. Indeed, recalculation of moment profiles using Gaussian standardized central moments in place of the measured ones results in very little change, and does not affect the overall quality of agreement. We also show that the influence of the mean makes discrimination between these turbulent and Gaussian total streamwise moment profiles via hotwire anemometry essentially infeasible. Finally, we find that in its present form the proposed scaling law is not suitable to describe the azimuthal total moment profiles using the same coefficients obtained from the streamwise total moment profiles.

1 Background

Both classical and statistical symmetries admitted by the multi-point moment (MPM) equations, which can be derived from the Navier Stokes equations, may be exploited to derive functional forms for statistical moments of the instantaneous total velocity $\tilde{u}_i \equiv U_i + u_i$ in turbulent wall-bounded flows [1]. The same symmetry conditions that yield logarithmic dependence of the mean velocity U_1 on wall-distance x_2 can

S. Zimmerman (✉) · J. Klewicki
Department of Mechanical Engineering, University of Melbourne, Parkville, VIC 3010, Australia
e-mail: spencer.zimmerman@unimelb.edu.au

J. Klewicki
e-mail: klewicki@unimelb.edu.au

M. Oberlack
Chair of Fluid Dynamics, Technische Universität Darmstadt, 64289 Darmstadt, Germany
e-mail: oberlack@fdy.tu-darmstadt.de

© The Author(s), under exclusive license to Springer Nature Switzerland AG 2021
R. Örlü et al. (eds.), *Progress in Turbulence IX*, Springer Proceedings in Physics 267,
https://doi.org/10.1007/978-3-030-80716-0_22

also yield power-law dependence of higher-order moments of the instantaneous total velocity (to arbitrarily high order), as well as linear dependence of the scaling exponent on order number [2]. That is, if the MPM tensor of rank n is given as:

$$H_{i_{\{n\}}}(\mathbf{x}, \mathbf{r}_{\{n-1\}}, t) = \overline{\tilde{u}_{i_{(1)}}(\mathbf{x}, t) \cdot \tilde{u}_{i_{(2)}}(\mathbf{x}, \mathbf{r}_{(1)}, t) \cdot \dots \cdot \tilde{u}_{i_{(n)}}(\mathbf{x}, \mathbf{r}_{(n-1)}, t)}, \quad (1)$$

then the symmetries consistent with a mean velocity profile of the form:

$$U_1^+ = \frac{1}{\kappa} \log(x_2^+ + A) + B \quad (2)$$

can also yield the following form for moments $n \geq 2$ when all $\mathbf{r}_{\{n-1\}} = 0$ (i.e. for the single-point case):

$$H_{i_{\{n\}}}^+ = C_{i_{\{n\}}}(x_2^+ + A)^{\omega(n-1)} - B_{i_{\{n\}}}. \quad (3)$$



Note that the overbar implies time-averaging, the superscript ‘+’ implies normalization by the wall-shear-stress scales, $B_{\{n\}}$ and $C_{i_{\{n\}}}$ are constants of integration, and κ , A and ω are functions of the symmetry group parameters associated with the infinite set of MPM equations. The integration constants are constrained to be of the functional forms $C_{i_{\{n\}}} = \alpha_i e^{\beta_i n}$ and $B_{\{n\}} = \tilde{\alpha}_i e^{\tilde{\beta}_i n}$. For the remainder of this paper, normalization by the wall-shear-stress scales will be implied, and the superscript ‘+’ will be omitted for compactness of notation. In this paper, we assess the adherence to these predictions of the turbulent pipe flow measurements of Zimmerman et al. 2019 [3] and Baidya et al. 2019 [4].

In order to contextualize the fidelity of the experimental data to the proposed scaling law, it is useful to establish a baseline for comparison. To do so, we also test the fidelity to (3) of hybrid synthetic/experimental data, prescribed in a way that is intentionally inconsistent with (3). This process can be described by first rewriting (1) (for the $\mathbf{r}_{\{n-1\}} = 0$ case) in terms of contributions from the mean and the fluctuations:

$$H_{i_{\{n\}}} = \sum_{k=0}^n \binom{n}{k} \overline{u_i^k} U_i^{n-k}, \quad (4)$$

i.e. as a binomial expansion of $\tilde{u}_i^n \equiv (U_i + u_i)^n$. Any probability distribution can then be assigned to the fluctuations by making the substitution $\overline{u_i^k} = M_k \overline{u_i^2}^{k/2}$, where M_k are the standardized central moments (e.g. skewness, kurtosis, etc.). For the present purposes, we will use the values of M_k associated with a Gaussian distribution (i.e. $M_k = (k-1)!!$ for even k , and $M_k = 0$ otherwise). While the log-layer turbulent fluctuations are qualitatively quasi-Gaussian, it can be shown explicitly that the Gaussian values of M_k are inconsistent with (3). For example, if we write (4) for $n = 3$ and substitute the M_3 -based term for $\overline{u_i^3}$:

Table 1 Datasets used in this study. R represents the pipe radius, l_w represents the length of each individual hotwire sensor, t_s represents the sample time, and U_{cl} represents the mean velocity at the pipe centreline. Darker shaded lines are used to denote higher R^+ within each dataset

Colours	Study	Method	Cases	R^+	l_w^+	$t_s U_{cl} / R$
	[3]	x-wire	4	5400–14000	13–35	$5\text{--}25 \times 10^3$
	[4]	SN-wire	3	10000–35000	11–39	$5\text{--}100 \times 10^3$

$$H_{i(3)} = M_3 \overline{u_i^2}^{3/2} + 3\overline{u_i^2} U_i + U_i^3, \tag{5}$$

we can see from an order of magnitude analysis that M_3 must not be constant for (3) to hold. That is, if we write out the order of each term implied by (3) (and employ the substitution $\overline{u_i^2} = H_{i(2)} - U_i^2$), we obtain:

$$\mathcal{O}(x_2^{2\omega}) = M_k \cdot \mathcal{O}\left((x_2^\omega - U_i^2)^{3/2}\right) + \mathcal{O}\left((x_2^\omega - U_i^2) U_i\right) + \mathcal{O}(U_i^3). \tag{6}$$

This expression implies that $M_k = \mathcal{O}\left(x_2^{\omega/2}\right)$ (to leading order) for (3) to be valid (note that $U_1 = \mathcal{O}(\log(x_2))$ and $U_2 = U_3 = 0$). The same argument also applies to higher orders. As the experimental data are able to establish that the fluctuations are non-Gaussian based on M_k to a high degree of certainty, we posit that their adherence to (3) must be clearly different from that of ‘Gaussian’ profiles (reconstructed from measured U_i and $\overline{u_i^2}$ and Gaussian M_k) for the result to be significant. It is shown below that this is not the case for the $i = 1$ data, and that it is likely infeasible for hotwire-based experimental data to realize this level of significance.

2 Results

The experimental data presented herein are summarised in Table 1 below. More detail regarding these datasets can be found in [3] and [4]. Figure 1a shows the family of streamwise $H_{i(n)}$ profiles for $n = 2 - 8$ on logarithmic axes. The curves from all different cases appear to be relatively independent of Reynolds number in the logarithmic region in this ‘macroscopic’ representation. These moment profiles are plotted again in Fig. 1b, but with their log-layers explicitly highlighted, and with all curves shifted by the additive constants $B_{1(n)}$. These profiles are then compared to the best-fit family of power laws of the form implied by (3) (with $B_{1(n)}$ added to both sides), which are shown as black dashed lines. Figure 1b illustrates that it is possible to obtain fits that closely describe the measured data across all present Reynolds numbers (at least relative to their overall variation in magnitude) using the five free fitting parameters $\alpha_1, \beta_1, \tilde{\alpha}_1, \tilde{\beta}_1$, and ω .

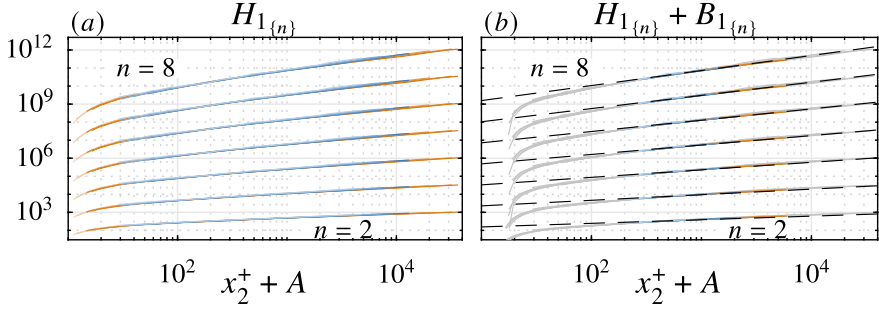


Fig. 1 **a** $H_{1\{n\}}$ profiles for $n = 2-8$. Line colors as in Table 1. **b** $H_{1\{n\}}$ profiles shifted by the additive constants $B_{1\{n\}}$, using $\tilde{\alpha}_1 = -0.434$ and $\tilde{\beta}_1 = 2.64$ (see text). Coloured segments of each profile in **b** highlight the log-layer, bounded by $3\sqrt{R^+} < x_2^+ < 0.15R^+$. Dashed lines represent the best-fit family of power laws, i.e. $\omega = 0.118$, $\alpha_1 = 1.83$, and $\beta_1 = 2.33$

In order to detect any systematic deviations between the fit and the data that might otherwise be obscured by the ‘macroscopic’ view, we now show in Fig. 2 the *difference* between the two (for the highest Re case only), measured in decades. That is, Fig. 2 shows the deviations of the measured data from the best-fit lines computed as follows:

$$\Delta_{1\{n\}} \equiv \log_{10} (H_{1\{n\}} + B_{1\{n\}}) - \log_{10} (C_{1\{n\}} (x_2^+ + A)^{\omega(n-1)}). \quad (7)$$

The plot in Fig. 2 is therefore analogous to the indicator plot commonly used to detect logarithmic behaviour in the mean velocity profile (or, more precisely, x_2^{-1} power law behaviour in its gradient). Figure 2 also helps illustrate the effects of both the functional form of $C_{1\{n\}}$ as well as the details of M_k , as will be explained below. Figure 2a shows the deviations of the measured data from the five-parameter functional form,

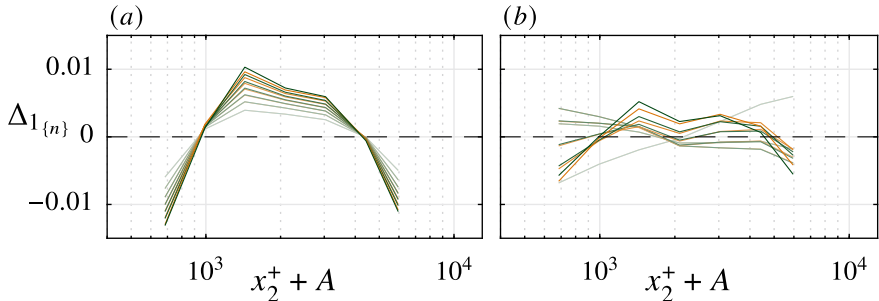


Fig. 2 Deviation of $R^+ \approx 35000$ actual (orange) and synthetic (green) data from log-layer best fit for: **a** five-parameter case, using $\alpha_1 = 1.83$, $\beta_1 = 2.33$, $\tilde{\alpha}_1 = -0.434$, $\tilde{\beta}_1 = 2.64$, and $\omega = 0.118$; and **b** relaxed $C_{1\{n\}}$ constraint case (see text), using $\tilde{\alpha}_1 = 1.8374$, $\tilde{\beta}_1 = 2.7817$, and $\omega = 0.102$

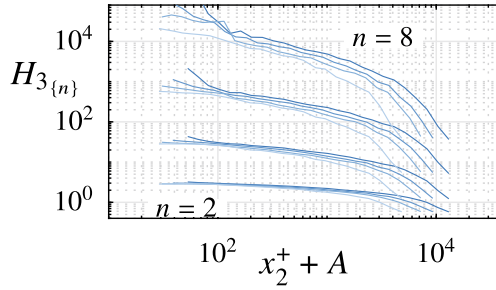


Fig. 3 Azimuthal total moment profiles for (even) $n = 2-8$ for all present data. Profiles increase in magnitude monotonically with n . Line colors as in Table 1. Note that darker shades represent higher Reynolds numbers

while Fig. 2b shows the deviations under the relaxed condition $C_{1(n)} = f(n)$ (as opposed to $C_{1(n)} = \alpha e^{\beta n}$). The measured data are consistently concave down relative to the full five-parameter fit. This concavity can be reduced dramatically by removing the exponential functional constraint from $C_{1(n)}$, which illustrates the potential effects of measurement uncertainty. That is, measurements that suffer from some degree of precision *and* bias errors may still produce roughly ‘correct’ slopes via regression, but bias in particular could diminish the fit quality when an additional magnitude constraint (i.e. $C_{1(n)} = \alpha e^{\beta n}$) is imposed. Furthermore, the magnitudes of the deviations from the fit for the measured (orange) and the Gaussian (green) profiles are essentially the same. Thus, we posit that the present data neither support nor refute the proposed scaling law for the $i = 1$ case.

This begs the question of the root cause of the insensitivity to the fluctuations, and the related question of what might be required to overcome it experimentally. Essentially, the insensitivity comes down to the relative magnitudes of U_1 and $u_{1,rms}$ in the log-layer. Using the representative values of $U_1 \approx 20$ and $u_{1,rms} \approx 2.5$, it can be shown numerically that $U_1^n > (n - 1)!! u_{1,rms}^n$ for $n < 174$. That is, when computing $H_{1(n)}$ from (4) (and assuming Gaussian M_k), the contribution of the mean-only term will exceed the contribution from the fluctuation-only term until $n \geq 174$. This estimate is also likely too low for streamwise fluctuations in wall-bounded flows, as these are known to be sub-Gaussian in the tails [3, 5] (at least out as far as has been converged). This is not to say, however, that non-Gaussianity could not be detected at lower n . It can also be shown numerically that a term involving M_4 (i.e. kurtosis) or higher does eventually becomes larger than U_1^n when $n = 16$. This term, i.e. $\binom{16}{4} U_1^{12} u_1^4$, would still however be highly sensitive to measurement errors in U_1 . Given the tendency of hotwire sensors to suffer from calibration drift, and the extremely long sample times required to converge such high moments (here we converge up to $n \approx 10$), it is unlikely that one could obtain (via hotwire) data that could conclusively support or refute the proposed scaling law.

In order to avoid the aforementioned challenges in assessing the fit for the $i = 1$ case, we now turn to the $i = 3$ case for which the mean contribution is zero (i.e.

$U_3 = 0$). Figure 3 shows profiles of $H_{3(n)}$ for $n = 2-8$. Several issues are immediately apparent that point towards 3 being unsatisfactory for the $i = 3$ case, at least over the present range of Reynolds numbers. The first issue is that the profiles tend to increase in magnitude in the log-layer with increasing Reynolds number rather than being Re -invariant. The second issue is that the best-fit power law slopes are negative (and increasingly-so with increasing n), which implies $\omega < 0$. This is in conflict with the $\omega > 0$ condition implied by the $i = 1$ profiles. This discrepancy motivates further analysis to determine whether the symmetries that lead to (3) for the $i = 1$ case are applicable to the $i = 3$ (or $i = 2$) case.

3 Conclusions

The present analyses show that it is not possible to use the present datasets to conclusively support or refute the proposed higher-moment scaling law for the $i = 1$ case. This is related to the relative magnitudes of U_1 and $u_{1,rms}$, which causes contributions to $H_{1(n)}$ from the mean to overwhelm those of the fluctuations out to very high n . Indeed, the overall fit quality is largely unaffected even when the fluctuation moments M_k are prescribed so as to be inconsistent with the proposed scaling law. This issue is likely insurmountable for hotwire-based experiments, owing to the extreme sample times that would be required and the tendency of hotwire sensors to suffer calibration drift. To avoid the issue of the mean contribution altogether, we also consider the $i = 3$ case. Here we show that the $H_{3(n)}$ profiles are not Re -invariant over the present parameter space, and that their slopes imply that the same value of ω cannot be used to describe both the $i = 1$ and $i = 3$ profiles. Further analysis is thus required to determine if modifications to (3) are necessary for the $i = 3$ case.

Acknowledgements The authors would like to acknowledge the support of the Australian Research Council as well as the researchers involved in the CICLoPE project.

References

1. M. Oberlack, M. Waławczyk, A. Rosteck, V. Avsarkisov, Symmetries and their importance for statistical turbulence theory. *Mech. Eng. Rev.* **2**(2), (2015)
2. S. Hoyas, M. Oberlack, S. Kraheberger, F. Alcantara-Avila, Turbulent channel flow at $Re_\tau = 10000$. *Bull. Amer. Phys. Soc. Seattle* (2019)
3. S. Zimmerman et al., A comparative study of the velocity and vorticity structure in pipes and boundary layers at friction Reynolds numbers up to 10^4 . *J. Fluid Mech.* **869**, 182–213 (2019)
4. R. Baidya et al., Simultaneous skin friction and velocity measurements in high Reynolds number pipe and boundary layer flows. *J. Fluid Mech.* **871**, 377–400 (2019)
5. L.W.B. Browne, A. Dinkelacker, Turbulent pipe flow: pressures and velocities. *Fluid Dyn. Res.* **15**(3), 177–204 (1995)

Characteristics of Reynolds Shear Stress in Adverse Pressure Gradient Turbulent Boundary Layers



Sylvia Romero, Spencer Zimmerman, Jimmy Philip, and Joseph Klewicki

Abstract The focus of the present work is to characterize the features of the turbulent inertia term (the wall-normal gradient of Reynolds shear stress) through the mean momentum balance and the Reynolds shear stress correlation coefficient (ρ_{uv}). Effects of the Reynolds number and Clauser pressure-gradient parameter, β , are discussed. Large eddy simulations of low Reynolds number adverse pressure gradient turbulent boundary layers from Bobke et al. [1], low Reynolds number experimental data from Vila et al. [2] and Volino [3], and newly acquired experimental data at higher Reynolds number from the Flow Physics Facility at The University of New Hampshire are utilized for this analysis. Observations are compared to zero pressure gradient turbulent boundary layer direct numerical simulations of Schlatter and Örlü [4] and Sillero et al. [5], and experimental data from Zimmerman et al. [6] and Zimmerman [7]. These cases show that the correlation coefficient (ρ_{uv}) decreases in magnitude with increasing Reynolds number and β . However, from these initial observations we find that ρ_{uv} is more sensitive to changes in the Reynolds number in comparison to the examined range of β . We also find that the location of zero-crossing of the turbulent inertia term seems to scale with $\sqrt{\delta^+}$ while the minimum of ρ_{uv} scales with δ .

1 Introduction

The effects of pressure gradients on turbulent boundary layers are often parameterized in terms of the Clauser pressure-gradient parameter $\beta = (\delta^*/\tau_w)(dP/dx)$, where δ^* is the displacement thickness, τ_w is the wall shear stress, and dP/dx is the streamwise pressure gradient. Positive and negative values of β respectively reflect adverse pressure gradient (APG) and favorable pressure gradient conditions, while $\beta = 0$ reflects zero pressure gradient (ZPG) conditions. The Clauser parameter can

S. Romero (✉) · S. Zimmerman · J. Philip · J. Klewicki
Department of Mechanical Engineering, University of Melbourne, Parkville, VIC 3010, Australia
e-mail: sylvia.r@student.unimelb.edu.au

S. Zimmerman
e-mail: spencer.zimmerman@unimelb.edu.au

© The Author(s), under exclusive license to Springer Nature Switzerland AG 2021
R. Örlü et al. (eds.), *Progress in Turbulence IX*, Springer Proceedings in Physics 267,
https://doi.org/10.1007/978-3-030-80716-0_23

also be characterized as a ratio of turbulence time scale $t_{turb} = \Delta/u_\tau$ to pressure gradient time scale $t_{PG} = 1/|dU_\infty/dx|$, where Δ is the Rotta-Clauser thickness and u_τ the friction velocity. For the APG flow to be in equilibrium, the ratio of two time-scales, i.e., $|\beta| = t_{turb}/t_{PG}$, has to be a constant. Therefore, under a non-constant β , the flow would take time to reach equilibrium, a history-effect would be present. This history-effect is anticipated to be different when β increases or decreases and also depends on how rapidly β is changing. In order to avoid these potentially confounding history-effects, this paper focuses on cases where β is nearly constant in numerical simulations taken from Bobke et al. [1] as well as experimental cases where β is only changing mildly with Reynolds number obtained from Vila et al. [2] and Volino [3] and newly acquired data at the Flow Physics Facility of the University of New Hampshire.

1.1 Mean Momentum Balance

The mean momentum balance (MMB) is the time-averaged statement of Newton's second law. The MMB for the ZPG turbulent boundary layer (TBL) consists of three terms: viscous force (VF), turbulent inertia (TI), and mean inertia (MI):

$$\underbrace{\frac{\partial^2 U^+}{\partial y^{2+}}}_{VF} + \underbrace{\frac{\partial \overline{-uv^+}}{\partial y^+}}_{TI} + \underbrace{\left[-U^+ \frac{\partial U^+}{\partial x^+} - V^+ \frac{\partial U^+}{\partial y^+} \right]}_{MI} = 0. \quad (1)$$

In (1) x and y respectively represent the streamwise and wall-normal coordinate directions and the superscript '+' denotes normalization by the mean wall shear stress and the fluid kinematic viscosity, or 'viscous' scales. The VF term is the gradient of the viscous stress and the TI term is the gradient of the Reynolds shear stress. The zero-crossing of the TI term corresponds to the peak location of the Reynolds shear stress. Prior to the zero-crossing, the TI term acts as a source of momentum (i.e., $TI > 0$), whereas after the zero-crossing the TI term becomes negative and acts as a momentum sink. These source and sink regions balance to zero, (i.e. it must integrate to zero across the boundary layer), which implies that the TI term is merely redistributive. The MI term reflects boundary layer development, and so when cast as a force represents a source of momentum. The MMB for the APG TBL includes a fourth term, the pressure gradient (PG) term, which is constant and negative:

$$\underbrace{\frac{\partial^2 U^+}{\partial y^{2+}}}_{VF} + \underbrace{\frac{\partial \overline{-uv^+}}{\partial y^+}}_{TI} + \underbrace{\left[-U^+ \frac{\partial U^+}{\partial x^+} - V^+ \frac{\partial U^+}{\partial y^+} \right]}_{MI} + \underbrace{U_\infty^+ \frac{\partial U_\infty^+}{\partial x^+}}_{PG} = 0. \quad (2)$$

As an example, Fig. 1 shows the distribution of the different terms in (1) and (2). Changes in the MMB indicate structural changes in the APG TBL flow from the

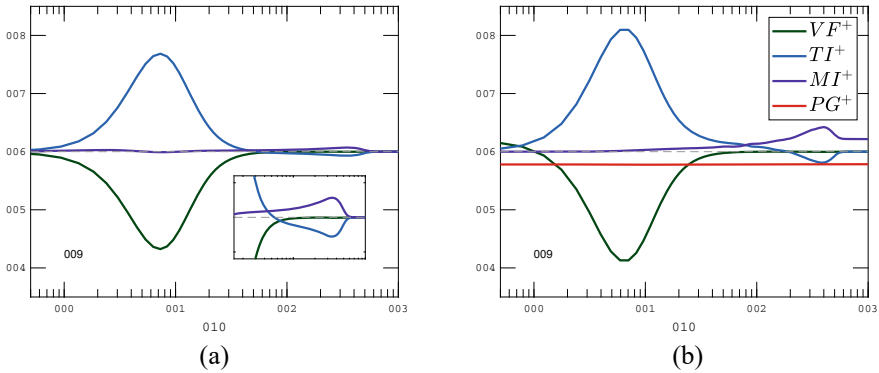


Fig. 1 **a** MMB of ZPG TBL at $Re_\tau = 490$, from [4]. **b** MMB of APG TBL at $Re_\tau = 490$ at $\beta = 1$, from [1]

ZPG TBL flow. In (1) the effect of turbulence is represented by the Reynolds shear stress \overline{uv} via the TI term. The focus of the present work is to understand changes in the TI term through the Reynolds shear stress \overline{uv} and the associated Reynolds shear stress correlation coefficient $\rho_{uv} = \overline{uv}/(u_{rms}v_{rms})$, where u_{rms} and v_{rms} are streamwise and wall-normal fluctuating r.m.s. velocities. The Reynolds shear stress correlation coefficient represents an “efficiency” of turbulent momentum transport while the Reynolds shear stress itself may be affected by the available fluctuation energy (as represented by u_{rms} and v_{rms}). We want to know if the larger changes in the Reynolds stresses due to Re_τ (the friction Reynolds number) and β are accompanied by a change to this efficiency.

1.2 Experimental and Computational Data Summary

The APG cases are compared to canonical ZPG TBL data to provide context for the APG TBL analysis. A summary of the computational and experimental data is given in Table 1.

Table 1 Summary of data sets and corresponding symbols

Type of flow	Type of Data	Source of Data	Data Symbol	Re_τ	β
ZPG TBL	DNS	[5]	—	250 - 1300	0
ZPG TBL	DNS	[6]	—	1300 - 2000	0
ZPG TBL	Experiment	[3]	▷	1800	0
ZPG TBL	Experiment	[7] and [8]	○	3300 - 10000	0
APG TBL	LES	[1]	—	360-830	0.9 - 4.5
APG TBL	Experiment	[3]	▷	1800	1.1
APG TBL	Experiment	[2]	*	1900	1.3-2.4
APG TBL	Experiment	recent experiments	○	7100	1.1

2 Results

The effects of Reynolds number and β on the peak location of the Reynolds shear stress, i.e. the zero-crossing of the TI term of the MMB, and the minimum of ρ_{uv} are discussed in the following sections.

2.1 ZPG TBL for Increasing Reynolds Number

Before moving to the APG cases, the ZPG case is observed over a range of Reynolds numbers in Fig. 2. As the Reynolds number increases ρ_{uv} decreases in magnitude; see Fig. 2 (left). This decrease in magnitude reflects the increasing intensity of the u and v fluctuations in the outer region while $-\overline{uv}^+$ gets closer to its theoretical maximum value of 1 [8]. The peak of $-\overline{uv}^+$ and minimum of ρ_{uv} are marked by green \diamond and blue \diamond symbols, respectively. As can be seen in Fig. 2 (right) the peak in ρ_{uv} scales nominally with δ , which is why it appears to move outward when plotted relative to y^+ or $y^+/\sqrt{\delta^+}$. The maximum of $-\overline{uv}$ however, seems to scale with $\sqrt{\delta^+}$. Note that $\delta^+ := \delta u_\tau / \nu =: Re_\tau$, and we interchangeably use δ^+ and Re_τ . There is more scatter for the high Reynolds number markers due to the difficulty of identifying the peak locations within the experimental data. This scaling is well-established for ZPG TBLs despite the scatter in the present experimental data.

2.2 ZPG TBL and APG TBL at Matched Reynolds Number

A ZPG case is compared to several APG cases at matched Reynolds number, $Re_\tau = 490$, for $0.99 < \beta < 4.5$ in Fig. 3 (left). Note that when comparing data sets at the same Re_τ one cannot determine whether certain features occur at fixed y^+ , $y^+/\sqrt{\delta^+}$, or y/δ . One clear feature that distinguishes the Reynolds shear stress of the APG

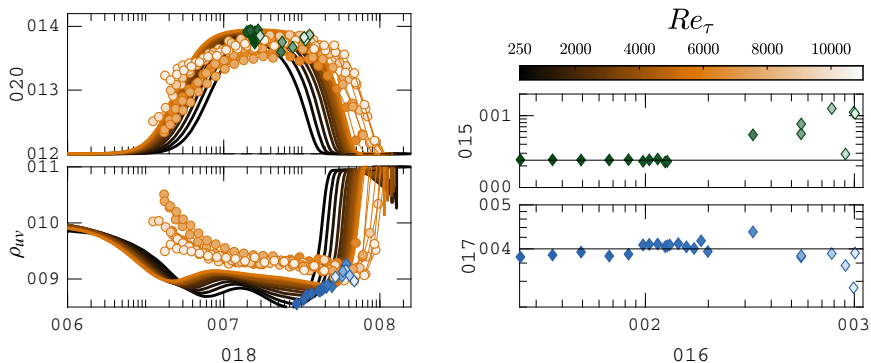


Fig. 2 (left): $-\overline{uv}^+$ and ρ_{uv} at $\beta = 0$. Reynolds number increasing from dark to light colors. $250 < Re_\tau < 2000$, from [4] and [5] plotted with—lines. $3300 < Re_\tau < 10000$ from [6] and [7] plotted with \circ symbols. Maximum of $-\overline{uv}^+$ and minimum of ρ_{uv} marked by green \diamond and blue \diamond symbols, respectively. (right): The corresponding wall-normal locations plotted versus Reynolds number

cases from the ZPG case is the emergence of a peak that exceeds unity, i.e. $-\overline{uv}^+ > 1$. The peak of $-\overline{uv}^+$ is marked by green \diamond symbols. The increased peak magnitude is enabled by the presence of the pressure gradient; the maximum Reynolds shear stress is not capped by the maximum viscous stress (i.e. u_τ^2) as in the ZPG case. Surprisingly, there is relatively little change in ρ_{uv} at the outer minimum, marked by blue \diamond symbols, despite the emergence of outer peaks in u_{rms}^+ and v_{rms}^+ with increasing β . The insensitivity of this ‘efficiency’ to β in the outer region suggests that the observed outer peaks in u_{rms}^+ and v_{rms}^+ are more reflective of changes of the scaling factor u_τ than of fundamental changes to the local turbulence. The wall-normal location of the outer minimum of ρ_{uv} remains fairly constant with increasing β , as seen in Fig. 3 (right) for $Re_\tau = 490$ in diamond symbols. Over the range of positive β examined, the peak of $-\overline{uv}^+$ remains nominally constant. However, the peak of the APG cases has shifted outwards from the ZPG case. This indicates that the TI term has remained positive further away from the wall and is acting as an additional source of momentum in the APG cases.

2.3 ZPG TBL and APG TBL: Effects of β and Re_τ

ZPG cases are compared to APG cases for $\beta \approx 1$. The corresponding $-\overline{uv}^+$ in Figs. 4b, d indicate that the peak location of $-\overline{uv}^+$ maintains $\sqrt{\delta^+}$ scaling for both the ZPG and APG cases examined. Note that the outer minimum of ρ_{uv} remains at nominally the same wall-normal location when normalized by δ in Fig. 4c. In Fig. 4a, c there is minimal change between the ZPG and APG ρ_{uv} profiles at matched Reynolds number as β increases from 0 to ≈ 1 . In comparison, both the ZPG and

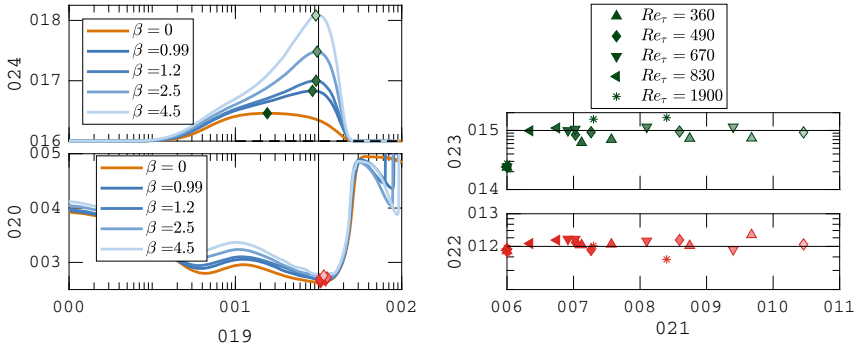


Fig. 3 (left): $-\overline{uv}^+$ and ρ_{uv} . ZPG TBL and APG TBL at constant Reynolds number, $Re_\tau = 490$, from [4] and [1], respectively. Maximum of $-\overline{uv}^+$ and ρ_{uv} marked by green \diamond and blue \diamond symbols, respectively. (right): The corresponding wall-normal locations plotted versus β for $360 \leq Re_\tau \leq 830$. For $Re_\tau = 1900$: ZPG TBL from [5] and APG TBL from [2]

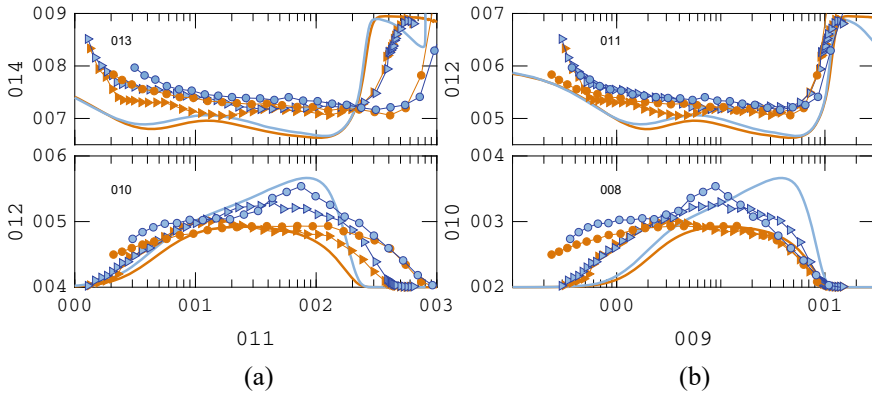


Fig. 4 **a, c** ρ_{uv} of $\beta = 0$ and $\beta \approx 1$ for increasing Reynolds number. **b, d** $-\overline{uv}^+$ of $\beta = 0$ and $\beta \approx 1$ for increasing Reynolds number. $Re_\tau = 490$: $\beta = 0$ and $\beta = 1.0$ plotted with orange – and blue – lines from [4] and [1], respectively. $Re_\tau = 1800$: $\beta = 0$ and $\beta = 1.1$ plotted with orange \triangleright and blue \triangleright symbols from [3]. $Re_\tau = 7800$: $\beta = 0$ and $Re_\tau = 7100$: $\beta = 1.1$ plotted with orange \circ and blue \circ symbols from [7] and recent experiments, respectively

APG ρ_{uv} curves decrease in magnitude as the Reynolds number increases. It appears that ρ_{uv} is more sensitive to changes in Reynolds number than the change from $\beta = 0$ to $\beta \approx 1$.

3 Conclusion

We find that ρ_{uv} is more sensitive to changes in Reynolds number in comparison to the examined range of β . Overall there is little change in the ‘efficiency’ of turbulent momentum transport as characterized by ρ_{uv} , for increases in β . It is reasoned that the effects of β diminish as Reynolds number increases, i.e., the same effect requires a larger β . Furthermore, the location of the zero-crossing of the TI term seems to scale with $\sqrt{\delta^+}$ for the APG cases examined while the minimum of the Reynolds shear stress correlation coefficient scales with δ .

References

1. A. Bobke, R. Vinuesa, R. Örlü, P. Schlatter, History effects and near equilibrium in adverse-pressure-gradient turbulent boundary layers. *J. Fluid Mech.* **820**, 667–692 (2017)
2. C. Vila, R. Örlü, R. Vinuesa, P. Schlatter, A. Ianiro, S. Discetti, Adverse-pressure-gradient effects on turbulent boundary layers: statistics and flow-field organization. *Flow Turbul. Combust.* **99**(3), 589–612 (2017)
3. R. Volino, Non-equilibrium development in turbulent boundary layers with changing pressure gradients. *J. Fluid Mech.* **897**, (2020)
4. P. Schlatter, R. Örlü, Assessment of direct numerical simulation data of turbulent boundary layers. *J. Fluid Mech.* **659**, 116–126 (2010)
5. J. Sillero, J. Jiménez, R. Moser, One-point statistics for turbulent wall-bounded flows at Reynolds numbers up to $\delta^+ \approx 2000$. *Phys. Fluids* **25**(10), 105102 (2013)
6. S. Zimmerman, J. Philip, J. Monty, A. Talameli, I. Marusic, B. Ganapathisubramani, J. Hearst et al., A comparative study of the velocity and vorticity structure in pipes and boundary layers at friction Reynolds numbers up to 10^4 . *J. Fluid Mech.* **869**, 182–213 (2019)
7. S. Zimmerman, Experimental investigation of velocity and vorticity in turbulent wall flows. Doctoral Dissertation, 2019
8. T. Wei, Properties of the mean momentum balance in turbulent Taylor–Couette flow. *J. Fluid Mech.* **891**, (2020)

Energy Transfer in Turbulent Boundary Layers with Adverse Pressure Gradient



Taygun R. Gungor, Ayse G. Gungor, and Yvan Maciel

Abstract Turbulent boundary layers (TBLs) under the effect of an adverse pressure gradient (APG) are significantly different from canonical wall-bounded flows because of the increasing momentum deficit. In this study, the effect of velocity defect on energy-transferring structures is investigated in a non-equilibrium APG TBL with Re_θ reaching 8000. The spectral distributions of production and pressure-strain of $\langle u^2 \rangle$ have been employed. The findings show that energy-transferring structures in APG TBLs may remain fairly similar within one layer (inner or outer) as the defect increases.

1 Introduction

Turbulent boundary layers (TBLs) that are subjected to a strong or prolonged adverse-pressure-gradient (APG) behave differently than canonical wall-bounded flows such as channel flows or zero-pressure-gradient (ZPG) TBLs because of the effect of the pressure gradient [1]. The presence of such a pressure gradient leads to an increasing momentum deficit and substantially changes the nature of the flow. As this defect increases, inner layer turbulence loses its importance, and outer layer turbulence becomes dominant [2]. This is one of the main distinctions between APG TBLs and canonical wall-bounded flows.

Regarding the coherent structures in APG TBLs, as the outer layer structures become dominant, the inner layer structures weaken. The inner layer streaks become disorganized or vanish as the flow approaches separation [3]. Furthermore, the number of sweeps and ejections in the inner layer is less in APG TBLs than in ZPG TBLs

T. R. Gungor (✉) · Y. Maciel
Department of Mechanical Engineering, Laval University, Quebec City, QC G1V 0A6, Canada
e-mail: taygun-recep.gungor.1@ulaval.ca

Y. Maciel
e-mail: Yvan.Maciel@gmc.ulaval.ca

T. R. Gungor · A. G. Gungor
Faculty of Aeronautics and Astronautics, Istanbul Technical University, 34469 Istanbul, Turkey
e-mail: ayse.gungor@itu.edu.tr

[4]. Moreover, energetic structures are found more frequently in the outer layer in APG TBLs [5]. The outer layer structures become shorter with increasing velocity defect.

Despite research efforts on coherent structures carrying $\langle u^2 \rangle$ and $\langle uv \rangle$ in APG TBLs, spectral analysis of Reynolds stress transport equations has been performed only for canonical wall-bounded flows so far. The energy cascade, scale separation and energy transferring structures were investigated for Couette [6] and channel flows [7].

To understand the energy transfer mechanisms in APG TBLs, the spectral distributions of the production and pressure-strain terms of $\langle u^2 \rangle$ are analyzed in a non-equilibrium APG TBL.

2 The Flow Case

The current study employs a direct numerical simulation (DNS) database of a non-equilibrium APG TBL with an increasing mean velocity deficit. The DNS was performed using a box domain with a no-slip smooth bottom wall. The Reynolds number based on momentum thickness (Re_θ) spans 2000–8000 and the shape factor (H) increases from 1.5 to 3.2. The dimensions of the computational box are $(L_x, L_y, L_z)/\delta_0 = 81, 16, 24$, where δ_0 is the boundary layer thickness at the inlet. The number of grid points are $N_x, N_y, N_z = 4609 \times 736 \times 1920$.

Figure 1 shows the spatial evolution of $\langle u^2 \rangle$ as a function of x/δ_0 and y/δ_0 . The maximum value of $\langle u^2 \rangle$ is in the inner layer at the beginning of the domain. It is found in the outer layer after approximately $x = 25\delta_0$ when the shape factor reaches approximately 1.75. It is seen that the dominant turbulence energy is in the outer layer when the defect is large. In order to investigate the effect of velocity defect on turbulent structures, energy transfer is examined at two streamwise positions corresponding to small and large velocity defect cases, where the shape factor is 1.65 and 2.63, respectively.

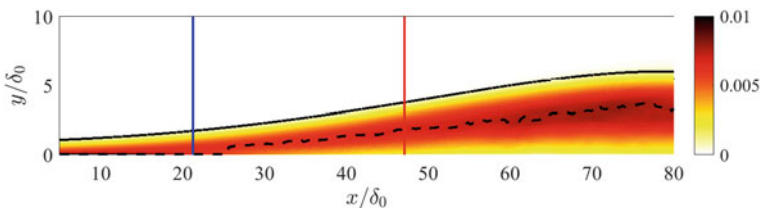


Fig. 1 The spatial evolution of $\langle u^2 \rangle / U_{e,0}^2$ as a function of x/δ_0 and y/δ_0 , where $U_{e,0}$ is the edge velocity at the inlet. The straight and dashed black lines indicate boundary layer thickness and the wall-normal position of maxima of $\langle u^2 \rangle$. Blue and red vertical lines indicate the streamwise positions of $H = 1.65$ and 2.63, respectively

3 Results

3.1 The Reynolds Stress Budgets

First, the energy transfer mechanisms in the APG TBL are investigated through the transport equations for the Reynolds stresses. Figure 2 shows the Reynolds stress budget of $\langle u^2 \rangle$ for the small and large velocity defect cases. In the small defect case, all terms exhibit a strong inner peak. This strong inner layer activity suggests that the small defect case has similarities with canonical wall-bounded flows, where the inner layer turbulence is dominant.

As the defect increases, the inner layer loses its importance, and the outer layer becomes dominant. All transfer terms increase in the outer region except viscous diffusion. Furthermore, production and pressure-strain peak in the outer layer, roughly around $y/\delta = 0.5$. There is still inner layer activity, but it is much weaker than in the outer layer for production and pressure-strain. In addition, the energy levels are different in both defect cases.

3.2 The Spectral Distributions

The Reynolds stress budgets provide information about the wall-normal distribution of the energy transfer mechanisms but not about coherent structures that are linked to these mechanisms. To investigate the role that coherent structures play in the energy transfer, the spectral distribution of production and pressure-strain of $\langle u^2 \rangle$ are analyzed using the transport equation for the two-point velocity correlation tensor. The reason for using the two-point correlation equation is that the spectral information about energy transfer mechanisms can only be obtained through two-point corre-

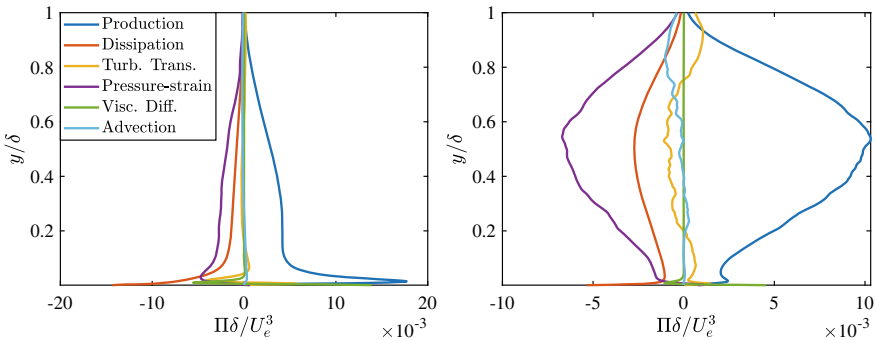


Fig. 2 The energy transfer mechanisms of $\langle u^2 \rangle$ as a function of y/δ for the small (left) and large (right) defect cases. U_e is the the edge velocity and δ is the local boundary layer thickness

lations. The transport equation for the two-point correlation tensor ($\langle u_i \tilde{u}_j \rangle$) can be written as follows.

$$0 = \left[-U_k \langle \tilde{u}_j \frac{\partial u_i}{\partial x_k} \rangle - U_k \langle u_i \frac{\partial \tilde{u}_j}{\partial \tilde{x}_k} \rangle \right] + \left[-\langle \tilde{u}_j u_k \rangle \frac{\partial U_i}{\partial x_k} - \langle u_i \tilde{u}_k \rangle \frac{\partial U_j}{\partial \tilde{x}_k} \right] + \frac{1}{\rho} \left[-p \left(\frac{\partial \tilde{u}_j}{\partial x_i} \right) - \tilde{p} \left(\frac{\partial u_i}{\partial \tilde{x}_j} \right) \right] + \frac{1}{\rho} \left[-\left(\frac{\partial p \tilde{u}_j}{\partial x_i} \right) - \left(\frac{\partial \tilde{p} u_i}{\partial \tilde{x}_j} \right) \right] + \left[-\langle \tilde{u}_j \frac{\partial u_k u_i}{\partial x_k} \rangle - \langle u_i \frac{\partial \tilde{u}_k \tilde{u}_j}{\partial \tilde{x}_k} \rangle \right] + \left[v \langle \tilde{u}_j \frac{\partial^2 u_i}{\partial x_k \partial x_k} \rangle + v \langle u_i \frac{\partial^2 \tilde{u}_j}{\partial \tilde{x}_k \partial \tilde{x}_k} \rangle \right]$$

where U_j and u_i are the mean and fluctuation velocities, x_i and \tilde{x}_i are vector coordinates of the two points where the correlations are computed. The terms on the RHS of the equation are, in order, mean convection, production, pressure-strain, pressure transport, turbulent transport and viscous terms. This study focuses only on production and pressure-strain, the latter being the inter-component energy transfer between $\langle u^2 \rangle$, $\langle v^2 \rangle$ and $\langle w^2 \rangle$. In addition, only spanwise separation is considered for the two-point correlations. Therefore, the spectral distributions are functions of x , y and only spanwise wavenumber in wavenumber space.

Figure 3 displays the premultiplied energy, production and pressure-strain spectra of $\langle u^2 \rangle$ as a function of λ_z/δ and y/δ for the small and large defect cases using a linear scale for y to emphasize the outer region. It is important to note that the pressure-strain spectra have predominantly negative values because the pressure-strain of $\langle u^2 \rangle$ acts as a sink term since $\langle u^2 \rangle$ transfers energy to $\langle v^2 \rangle$ and $\langle w^2 \rangle$. It is negative except for the very near-wall region. Some characteristics of outer layer energy transferring structures remain similar with increasing velocity defect even though the shape of the spectra is different. The production and pressure-strain structures are at similar

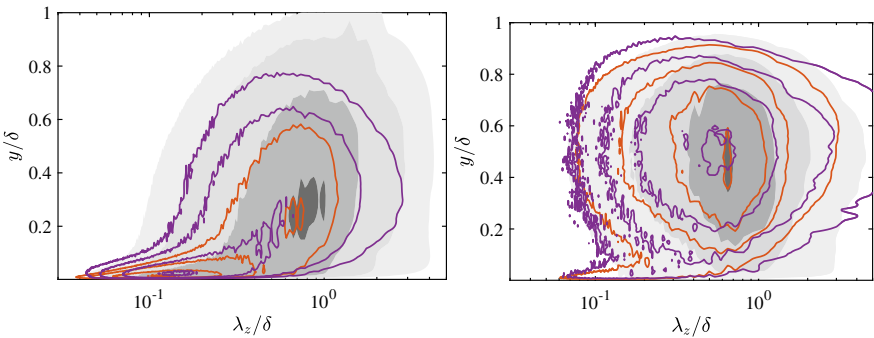


Fig. 3 The energy (shaded), production (red), and pressure-strain (purple) spectra of $\langle u^2 \rangle$ as a function of λ_z/δ and y/δ for the small (left) and large (right) defect cases. The contours are 0.1, 0.2, 0.45, and 0.9 of the absolute maximum of each spectrum and negative for the pressure-strain spectra. δ is the local boundary layer thickness

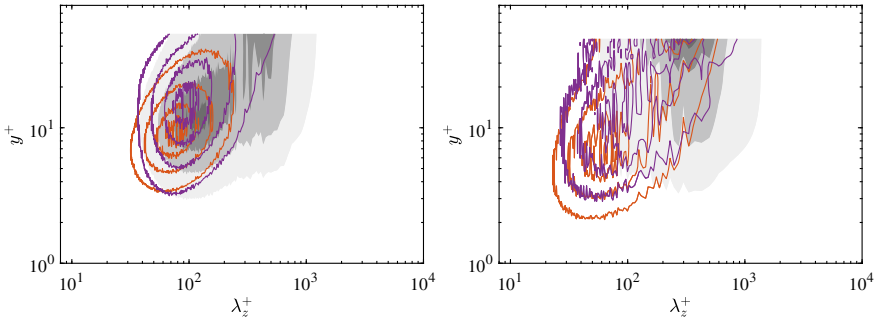


Fig. 4 The energy (shaded), production (red), and pressure-strain (purple) spectra of $\langle u^2 \rangle$ as a function of λ_z^+ and y^+ for the small (left) and large (right) defect cases. Only the inner layer ($y^+ < 50$) is shown. The contours are 0.25, 0.5, 0.75, and 0.9 of the absolute maximum of each spectrum in the inner layer and negative for the pressure-strain spectra

y -locations as the most energetic structures. Moreover, λ_z of energy-transferring structures are in the same order of magnitude in both cases. In addition, the pressure-strain structures are slightly narrower than the production structures in the outer layer of both defect cases.

Regarding the inner layer, Fig. 4 presents the same spectral distributions as in Fig. 3 but masking the outer layer to examine the inner layer in more detail, especially for the large defect case. The reason for masking the outer layer is to prevent the dominant outer peak from hiding the spectral distribution in the inner layer. The inner peak in the energy spectra completely vanishes in the large defect case. On the other hand, the spectral distributions of both production and pressure-strain exhibit an inner peak, although the spectra are noisy in the large defect case because the levels are low. Furthermore, the shape of both spectral distributions is very similar in both defect cases. Moreover, the relationship between the production and pressure-strain spectra remains very similar with increasing velocity defect. The main difference between both defect cases is that the y -position and λ_z of the inner peak of production and pressure-strain spectra are different, but this is expected since friction-viscous units are not appropriate scales for APG TBLs with large velocity defect [1].

4 Conclusion

The effects of the velocity defect on the energy-transferring structures are examined through the spectral distributions of energy, production and pressure-strain of $\langle u^2 \rangle$ in a non-equilibrium APG TBL. Two streamwise positions that correspond to small ($H = 1.65$) and large ($H = 2.63$) velocity defect cases of the APG TBL are chosen.

The examination of energy, production and pressures-strain spectra suggests that the production and pressure-strain structures have some similarities within one layer regardless of the velocity defect. In the inner layer, there is a peak in production and

pressure-strain spectra in both defect cases, even though the inner peak completely vanishes in the energy spectra of the large defect case. Moreover, the shape of the production and pressure-strain spectra do not significantly change with increasing velocity defect. In the outer layer, the y -position of production and pressure-strain structures with respect to the most energetic structures are similar. Regarding their size, the spanwise wavelengths of production and pressure-strain structures remain in the same order of magnitude as the defect increases. Furthermore, the pressure-strain structures are slightly narrower than the production structures in both cases.

To have a more complete picture of energy-transfer mechanisms and energy-transferring structures and come to a more solid conclusion, 1D spectra as a function of streamwise wavelength and 2D spectra of energy and all energy transfer terms should be investigated in future studies.

Acknowledgements AGG and TRG were supported by the Research Funds of Istanbul Technical University (project numbers: MGA-2019-42227 and MDK-2018-41689). TRG and YM were supported by NSERC of Canada. We acknowledge PRACE for awarding us access to Marconi100 at CINECA, Italy and Calcul Québec (www.calculquebec.ca) and Compute Canada (www.computecanada.ca) for awarding us access to Niagara HPC server.

References

1. Y. Maciel, T. Wei, A.G. Gungor, M.P. Simens, Outer scales and parameters of adverse-pressure-gradient turbulent boundary layers. *J. Fluid Mech.* **844**, 5–35 (2018)
2. A.G. Gungor, Y. Maciel, M.P. Simens, J. Soria, Scaling and statistics of large-defect adverse pressure gradient turbulent boundary layers. *Int. J. Heat Fluid Flow* **59**, 109–124 (2016)
3. S. Rahgozar, Y. Maciel, Statistical analysis of low-and high-speed large-scale structures in the outer region of an adverse pressure gradient turbulent boundary layer. *J. Turbul.* **13**, N46 (2012)
4. Y. Maciel, M.P. Simens, A.G. Gungor, Coherent structures in a non-equilibrium large-velocity-defect turbulent boundary layer. *Flow, Turbul. Combust.* **98**(1), 1–20 (2017)
5. Z. Harun, J.P. Monty, R. Mathis, I. Marusic, Pressure gradient effects on the large-scale structure of turbulent boundary layers. *J. Fluid Mech.* **715**, 477 (2013)
6. T. Kawata, P.H. Alfredsson, Inverse interscale transport of the Reynolds shear stress in plane Couette turbulence. *Phys. Rev. Lett.* **120**(24), 244501 (2018)
7. M. Lee, R.D. Moser, Spectral analysis of the budget equation in turbulent channel flows at high Reynolds number. *J. Fluid Mech.* **860**, 886–938 (2019)

Influence of Rough Surface Morphology on Boundary Layer Flow



K. Jurčáková, P. Procházka, R. Kellnerová, P. Antoš, and V. Skála

Abstract The flow over nine different surfaces with sharp-edged roughness elements were measured by single wire anemometry. The intensity of turbulence did increase with the plan/frontal solidity of the roughness elements. We used a diagnostic plot to assess the quality of boundary-layer flows. All investigated boundary layers revealed linear dependence of the turbulence intensity on the relative mean wind speed in the outer layer. The slope of the diagnostic plot was dependent on the frontal solidity of the elements but not on their size. The intensity of turbulence exceeds the maximal slope of the diagnostic plot for rough-wall flows showed in (J. Fluid Mech.727:119–131) in six cases.

1 Introduction

Outer-layer similarity for smooth- and rough-wall flows is still an unresolved problem. Townsend's hypothesis [1] suggests that it is only the inner layer (approx. up to five roughness heights) that is affected by surface roughness and studies of e.g., [2] and [3] support this hypothesis. On the other hand, there are studies (e.g. [4]) which suggest that the entire boundary layer is affected and that the difference is also dependent on the roughness topology. The roughness topology can be very variable, for example, the classical sandpaper roughness, a wire mesh, long rods or bars oriented across the flow, or three-dimensional regularly placed obstacles. In our study, turbulence is very effectively generated by spatially placed sharp-edged obstacles, which suppress along-wind dimensions (i.e. plates).

K. Jurčáková (✉) · P. Procházka · R. Kellnerová · P. Antoš · V. Skála
The Czech Academy of Sciences, Institute of Thermomechanics, Dolejškova 5, 182 00 Prague,
Czech Republic
e-mail: klara.jurcakova@it.cas.cz

© The Author(s), under exclusive license to Springer Nature Switzerland AG 2021
R. Örlü et al. (eds.), *Progress in Turbulence IX*, Springer Proceedings in Physics 267,
https://doi.org/10.1007/978-3-030-80716-0_25

2 Experimental Setup

Turbulent boundary layers over 9 surfaces were experimentally investigated by hot-wire anemometry. A constant-temperature anemometer, DISA M10, together with a single-wire probe, Dantec 55P11, were utilized. The sensor used was a tungsten wire with a diameter of $5 \mu\text{m}$ and a length of 1.25 mm . The temperature of the sensor was $200 \text{ }^\circ\text{C}$. The sampling frequency was 75 kHz and the sampling time was 30 s , which corresponded to more than 3500 boundary-layer turnover times. The measurement campaign was conducted in an open blowing-type wind tunnel with dimensions of $0.25, 0.25$ and 4.20 m (width, height and length). Operational free-stream wind speed was around 14 m/s and there was no tripping. The non-dimensional pressure gradient parameter, defined as

$$\beta = \frac{\delta^*}{u_\tau \rho} \frac{dp}{dx} \quad (1)$$

where δ^* is displacement thickness, u_τ is friction velocity, and ρ is the air density, had negligible value: $-0.22 < \beta < -0.15$. Therefore, all boundary layers can be considered as zero pressure-gradient flows.

We investigated one nearly smooth surface (non-polished block material) and 8 rough surfaces with plate roughness elements. All roughness elements had a uniform height of $k = 4 \text{ mm}$ and a length $l = 1 \text{ mm}$, they were arranged in staggered rows, and they covered the whole extent of the wind tunnel floor. The spacing of elements in one row was the same as the rows' spacing. The first set of 4 rough surfaces S4_8, S4_6, S4_4, and S4_2 (the first row in Fig. 1) had identical roughness elements with decreasing element spacing and, consequently, with increasing plan solidity λ_p and frontal solidity λ_f . The second set of rough surfaces S7_5, S10_6, S15_7, and S20_8 (the second row in Fig. 1) was derived from the surface S4_4. The width of the elements and their spacing were increased to keep λ_p and λ_f constant. The roughness layout details are given in Table 1.

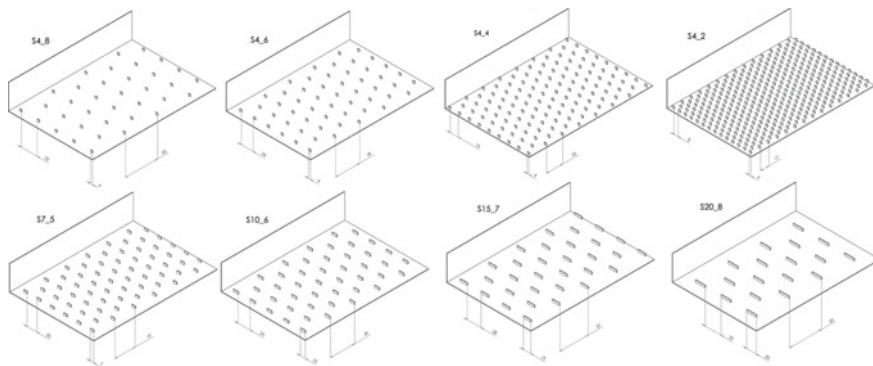


Fig. 1 Sketches of rough surfaces. Only parts of the surfaces are shown

Table 1 Surface characteristics. All surface names are in the format $S_{x,y}$ where x is the element width in mm and y is the element spacing as a multiple of the element height ($k = 4$ mm)

	S4_8	S4_6	S4_4	S4_2	S7_5	S10_6	S15_7	S20_8
Element's width (mm)	4	4	4	4	7	10	15	20
Spacing (mm)	32	24	16	8	20	24	28	32
Plan solidity (%)	0.3	0.6	1.2	3.7	1.2	1.2	1.2	1.2
Frontal solidity (%)	1.3	2.3	4.7	14.8	4.9	4.7	4.8	4.7

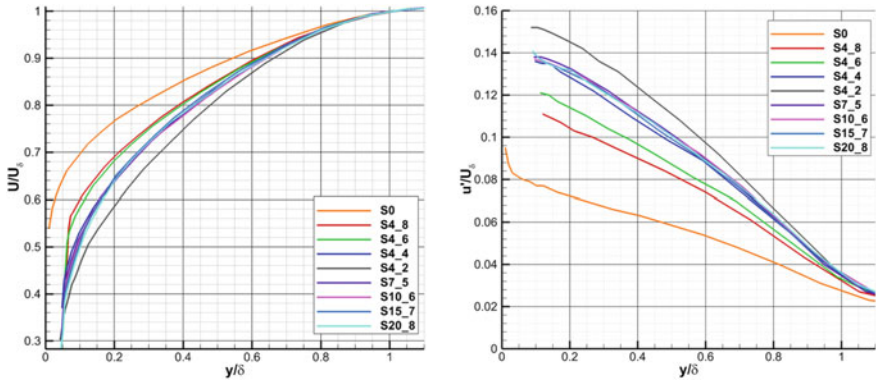


Fig. 2 Wall-normal profiles of mean velocity (left) and velocity standard deviation (right) in the outer scaling measured at $x = 3450$ mm

3 Mean Flow Profiles

Mean velocity profiles in outer scaling showed the influence of the surface roughness, see Fig. 2, left. The profiles lined up according to the plan and frontal solidities. The profiles over the second set of surfaces with the constant λ_p and λ_f (S4_4, S7_5, S10_6, S15_7, and S20_8, various blue colours) collapsed into identical profiles of the mean stream-wise velocity U/U_δ and its standard deviation u'/U_δ in the outer region (within the experimental error). The roughness sublayer ($z < 2k$), where the individual profiles varied according to the proximity of individual roughness elements, was excluded from the graphs.

4 Diagnostic Plot

There is some doubt whether a boundary layer created by flow over large and sharp-edged roughness elements is properly developed and whether there is adequate scale separation or if it is just a superposition of bluff-body wakes. The diagnostic plot proposed in Alfredsson and Örlü [5] was created and used to analyse wall-bounded turbulence profiles. In the outer region, including the inertial sublayer, the dependence between stream-wise fluctuation intensity u'/U and local velocity in outer scaling U/U_δ can be, according to Alfredsson and Örlü [6], expressed linearly as

$$\frac{u'}{U} = a + b \frac{U}{U_\delta} \quad (2)$$

where a and b are empirical constants. The diagnostic plot shows different slopes for flows over rough and smooth walls. Alfredsson and Örlü [6] set the constants for the boundary-layer flows over a smooth wall as: $a = 0.286$ and $b = -0.255$. Castro and Segalini [7] compiled various rough-wall data and found $a = 0.436$ and $b = -0.389$ as an asymptote line for the fully rough boundary-layer flows. The compiled dataset included flows over sand grains, grits, meshes, cubes, bars, and sparsely placed plates. Based on their observation, they stated that any examined surface roughness does not change the outer layer turbulence intensity.

Diagnostic plots for all 9 profiles are shown in Fig. 3 together with the asymptotic line for the smooth (dashed line) and rough (solid line) walls. The lines for surfaces S0 and S4_8 lie between the smooth and rough wall lines which show that the boundary layers are transitionally rough and not fully developed. The values of Re_τ and roughness function ΔU (see Table 2) support this observation. Surface S4_6 agrees with Castro's rough line very well. The other profiles have a higher turbulence intensity in the whole extent of the outer layer and it keeps the linear dependence on U/U_δ . The S4_2 surface, which has the highest λ_p and λ_f , has the steepest slope and a new asymptotic line can be parametrized with the $a_{\text{new}} = 0.499$ and $b_{\text{new}} = -0.445$. Our sharp-edged roughness elements are more effective in turbulence production than the surfaces compiled in Castro and Segalini [7]. The values of roughness function (defined in (4)) of our profiles ΔU^+ in the range of 11–15 (see Table 2) is on the upper limit and higher than the data in Castro and Segalini [7]. Their maximum was $\Delta U^+ = 13.9$ for 2D bars roughness. We repeated the measurement of all surfaces for the free-stream velocity 23 m/s with the same results. The only weak point of our data is the rather small ratio $\delta/k \approx 25$. This leads to a higher relative thickness of the roughness sublayer and loss of the lower part of the logarithmic layer, i.e. the region where $U/U_\delta \lesssim 0.6$.

The difference between smooth and rough diagnostic-plot slopes can be associated with the difference in roughness function ΔU . All data in Castro and Segalini [7] collapsed in one line using a modified version of the diagnostic plot

$$\frac{u'}{U'} = \tilde{a} + \tilde{b} \frac{U'}{U'_\delta}, \quad \text{where } U' = U + \Delta U \text{ and } U'_\delta = U_\delta + \Delta U. \quad (3)$$

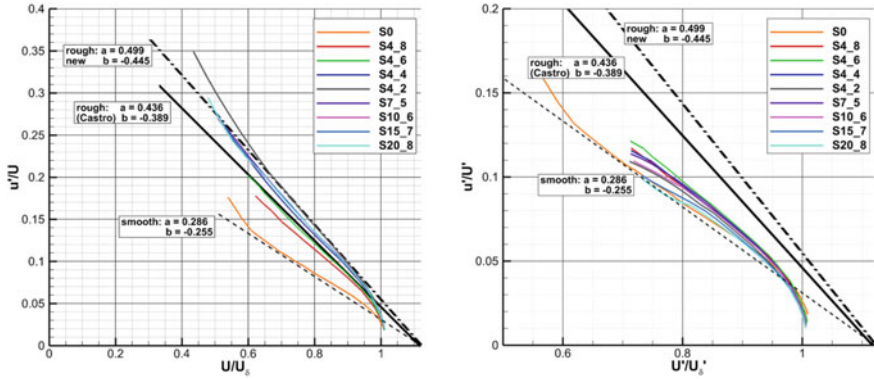


Fig. 3 Diagnostic plot for all surfaces. Dashed and bold line adopted from Castro and Segalini [7], dash-dotted line is the new asymptote

Table 2 Boundary-layer parameters for investigated surfaces

	S0	S4_8	S4_6	S4_4	S4_2	S7_5	S10_6	S15_7	S20_8
δ [mm]	49	75	80	93	105	96	94	97	99
U_δ [m/s]	13.6	14.0	14.3	14.7	14.9	14.5	14.5	14.4	14.3
δ/k	–	19	20	23	26	24	24	24	25
u_τ [m/s]	0.40	0.66	0.72	0.85	0.97	0.86	0.88	0.94	0.96
ΔU [m/s]	0.3	4.5	5.7	9.5	14.3	10.1	10.8	12.8	13.6
ΔU^+	0.75	6.8	7.9	11.2	14.7	11.7	12.3	13.6	14.2
Re_τ	1307	3300	3840	5270	6790	5504	5515	6079	6336

At the limit for the smooth wall $\Delta U = 0$, (2) and (3) will be the same. Roughness parameter ΔU can be calculated from the composite velocity profile (adapted from Chauhan et al. [8])

$$\frac{U}{u_\tau} = \frac{1}{\kappa} \ln\left(\frac{y u_\tau}{\nu}\right) + A - \frac{\Delta U}{u_\tau} + \frac{2\Pi}{\kappa} W\left(\frac{y}{\delta}\right) \quad (4)$$

where κ is the von Karman constant, ν is the kinematic viscosity, $A = 5.2$ is the smooth surface additive constant, Π is known as the wake parameter, δ is the boundary layer height, and W is the wake function, which is defined to satisfy the normalization conditions $W(0) = 0$ and $W(1) = 1$. We used the exponential wake function from Chauhan et al. [9]. We also tested the composite profile fit with non-zero displacement height, but the values of displacement height were negligible and the fit error did not decrease. Therefore, zero-plane displacement was set to zero for all setups. This is a valid assumption since the maximal plan solidity λ_p was 3.7%.

We had no direct measurement of the surface shear stress and the inner layer was overridden by the roughness sublayer. Therefore, friction velocity u_τ and roughness function ΔU were obtained by the least-square fit of the composite profile (4) to the measured vertical profiles of U in the range $2.2k < y < 0.95\delta$. Boundary-layer parameters as boundary-layer height δ and free stream velocity U_δ as well as the fitted parameters u_τ and ΔU for all surfaces are listed in Table 2.

The values of roughness functions obtained by the fit of measured profiles to (4) are not large enough to unify all profiles onto the smooth line, see Fig. 3, right. The ΔU values would have to be much higher (up to 100% for surfaces S4_8 and S4_6) for the modified diagnostic plot (3) to reach the smooth-wall line. Please note, that the dependency of u'/U' on U'/U'_δ is not linear (by definition) but the curvature is small. However, the curvature is increasing for the higher values of ΔU and it is probably not feasible for such turbulent boundary layers to collapse into the smooth-wall line.

There is no visible difference in the mean velocity profiles for the surfaces with a constant λ_p and λ_f if plotted in outer scaling (see Fig. 2). However, there is an increasing trend in the values of boundary-layer depth δ and roughness function ΔU^+ with the increasing width of the elements (S4_4 \rightarrow S20_8). We plan to investigate the flow over these surfaces by particle image velocimetry to reveal possible structural changes in the flow.

5 Conclusion

We confirmed that roughness elements in the shape of erected plates are extremely effective in turbulence production. The boundary layers created above surfaces with such elements are relatively shallow ($19 < \delta/k < 26$) but their turbulence intensity u'/U is linearly dependent on relative velocity U/U_δ in the outer layer. The slope of this dependence increases with the density of roughness elements. Six of the investigated setups exceed the line for fully rough boundary-layer flow as proposed in Castro and Segalini [7]. The new asymptote has parameters: $a_{\text{new}} = 0.499$ and $b_{\text{new}} = -0.445$.

Acknowledgements The financial support for the present project was provided by the *Czech Science Foundation* under the *Grant No.18-09539S* and by the institutional support RVO 61388998.

References

1. A.A. Townsend, *Turbulent Structure of Turbulent Shear Flow*, (Cambridge University Press, 1976)
2. K.A. Flack, M.P. Schultz, T.A. Shapiro, Experimental support for townsend's reynolds number similarity hypothesis on rough walls. *Phys. Fluids* **17**, (2005)
3. P.-A. Krogstad, V. Efron, About turbulence statistics in the outer part of a boundary layer developing over two-dimensional surface roughness. *Phys. Fluids* **24**, (2012)

4. M. Placidi, B. Ganapathisubramani, Turbulent flow over large roughness elements: effect of frontal and plan solidity on turbulence statistics and structure. *Bound. Layer Meteorol.* **167**, 99–121 (2018)
5. P.H. Alfredsson, R. Örlü, The diagnostic plot—a limitus test for wall bounded turbulence data. *Eur. J. Mech. B/Fluids* **29**, 403–406 (2010)
6. P.H. Alfredsson, R. Örlü, A. Segalini, A new formulation for the streamwise turbulence intensity distribution in wall-bounded turbulent flows. *Eur. J. Mech. B/Fluids* **36**, 167–175 (2012)
7. I.P. Castro, A. Segalini, P.H. Alfredsson, Outer-layer turbulence intensities in smooth- and rough-wall boundary layers. *J. Fluid Mech.* **727**, 119–131 (2013)
8. K.A. Chauhan, P.A. Monkewitz, H.M. Nagib, Criteria for assessing experiments in zero pressure gradient boundary layers. *Fluid Dyn. Res.* **41**(2), (2009)
9. K.A. Chauhan, H.M. Nagib, P.A. Monkewitz, On the composite logarithmic profile in zero pressure gradient turbulent boundary layers (2007)

Part IV

Theory

Similarity Scaling of a Free, Round Jet in Air



Preben Buchhave, Chunyue Zhu, and Clara M. Velte

Abstract Natural phenomena adhere to certain conservation laws that follow from fundamental symmetries in nature. We assume a simplified model for a free, round, fully developed turbulent jet in air and apply the conservation laws to this model to see what we can predict concerning the physical properties of such a jet. We compare these results to carefully conducted laser Doppler anemometry (LDA) measurements in a fully developed turbulent round jet. We find that both first, second and third order statistical quantities are controlled by a single scaling factor—the downstream distance x .

1 Background

It is well known that some fluid flows, that are free and unhindered of physical boundaries, develop into a state that to some degree replicate statistical properties describing the flow upstream. This phenomenon is called self-preservation or self-similarity [1–9]. The concept of self-similarity is of great practical importance because it simplifies the mathematical description of such flows and reduces the computational load when it can be used in engineering models.

The phenomenon is also interesting from a theoretical point of view: What is the underlying reason for the development of self-similarity? When does it occur? And how many parameters are needed to describe self-similarity in a flow?

The free, axisymmetric jet is an example of a canonical flow, which has been studied thoroughly over the years [10–14]. In our laboratory, we have worked with a jet with an initial 10 mm diameter top-hat profile issuing into a large nylon tent.

P. Buchhave (✉)
Intarsia Optics, Birkerød, Denmark

C. Zhu · C. M. Velte
Department of Mechanical Engineering, Technical University of Denmark, Kgs. Lyngby,
Denmark
e-mail: zhucy_hhu@outlook.com

C. M. Velte
e-mail: cmve@dtu.dk

We find that this jet in a matter of a few milliseconds develops into a state that scales downstream in a self-reproducing manner. Most treatments of the self-similar jet consider this as an observation of an experimental fact and, based on that, create mathematical relations describing the already assumed similarity properties. It is then shown that the scaling relations satisfy the equation of motion, in this case the Navier-Stokes equation. Finally, the theory is confirmed by comparison to experimental data.

We believe that the development of a self-similar state is governed by basic, underlying principles resulting from fundamental properties of space and time, the so-called symmetry properties of classical space-time. These symmetry relations are equivalent to conservation relations governing mathematical physical quantities such as momentum, energy and angular momentum. In the following we begin by applying these conservation relations to a simplified model of a jet without assuming anything about the jet except that it issues in a given axial direction and is symmetric about this axis with a constant velocity profile. We then derive how various first, second and third order statistical functions and moments of the velocity are expected to scale downstream in the jet.

We then describe laser Doppler measurements of the axial velocity component and present results of calculations of statistical functions that convincingly confirm the predictions from the simple model and imply that the similarity scaling is controlled by a single, geometrical scaling factor. In two companion papers to be published [15, 16], we present more details regarding the derivation of the scaling behavior expected from the simple model and more details about the measurements and the computed statistical functions.

2 Space-Time Symmetries and Conservation Laws

The basic symmetry properties of classical space-time in which the jet exists are (see e.g. Frisch [3]):

- Space translation symmetry
- Time translation symmetry
- Rotational symmetry

In addition, we assume a Newtonian fluid described fully by

- Navier Stokes equation (NSE)

As is well known from Noether's theorem [17], the symmetries lead to corresponding basic physical-mathematical conservation laws:

- Conservation of momentum
- Conservation of energy
- Conservation of angular momentum

In addition, we know that non-dimensionalizing the Navier-Stokes equation for $Re \gg 1$ leads to (see e.g. Monin and Yaglom [1])

- Reynolds number similarity,

which, as we shall see, in connection with momentum conservation, leads to the linear growth of the jet and the velocity decrease being inversely proportional to the distance from the origin.

3 Simple Jet Model

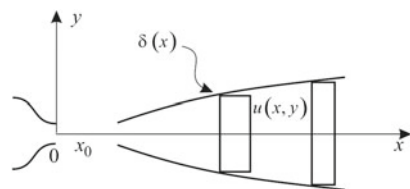
We consider a simple model for the jet in a cylindrical coordinate system, see Fig. 1, where we assume constant mean velocity $u(x, y)$ in the axial direction, x , that is zero outside the jet radius, $\delta(x)$, in the radial direction, y , but do not otherwise assume anything about the form of the jet except rotational symmetry about the jet axis. We then apply momentum conservation. Because the jet is not influenced by boundaries, the initial momentum flux at the jet exit in the direction of the jet axis must be conserved downstream. The momentum flux, \dot{B} , is: $\dot{B} = \rho \pi \delta^2 u dt u/dt = \rho \pi \delta^2 u^2 = \text{constant}$, where ρ is the constant mass density of air. It then follows that $\delta^2 u^2 = \text{constant}$ and therefore the large-scale Reynolds number $Re_L = u\delta/\nu = \text{constant}$ along the jet axis.

As detailed in the companion paper [15] we can then invoke Reynolds number similarity and conclude that the jet width must increase linearly along the jet axis and that the velocity must decrease inversely proportional to the distance from the origin. Further, the jet mass must increase linearly with distance from the origin and entrainment defined as the influx of mass per unit axial length must be constant. The actual rate of increase depends on the initial structure of the jet [18, 19].

If we then apply energy conservation to equal thickness sections of the jet, we find that the energy density and thus the variance must decrease as x^{-2} and that the spectral energy density must decrease as x^{-1} and that the wavenumber k describing the spatial scales must also decrease as x^{-1} . It follows that the turbulence intensity must be constant along the jet axis.

Seeing that spatial structures and velocity scale with a single, geometrical scaling factor, we can expect higher order statistical functions to scale according to the dimension of velocity and spatial structures entering the formula for the statistical functions. We reiterate that all these considerations are based on a simplified model for the mean values of the velocity and that these predictions must be compared to experimental results in order to find to which degree they can be verified.

Fig. 1 Simplified jet model with arbitrary $u(x, y)$ and $\delta(x)$ to be determined from first principles



4 Measurements

The measurements were performed on a free, axisymmetric jet in air. The jet orifice was $D = 10$ mm, the Reynolds number based on the jet diameter was 32.000. Measurements were made at 70 positions from $x = 30D - 100D$ and across the full width of the jet. The axial velocity component was measured with a laser Doppler anemometer (LDA) with variable optical frequency shift optimized for bias-free, high signal-to-noise Doppler signals. Between 100 and 400 records of 1 second duration were sampled at each measurement point. All-digital signal processing provided sample time, velocity and transit time. The data processing provided velocity data separated spatially by the convection record method. Thus, all statistical functions were spatially sampled, corrected for the convection velocity sweeping effect [20]. We present selected results; a complete description will be published separately [16].

Figure 2 presents first order scaling properties of the jet. The scaling along the axis adheres quite well to the predictions from the simple model. Figure 3 shows the spatial power spectral density along the jet axis and Fig. 4 shows the same in cross sections at $30D, 60D$ and $90D$. The axial spectra have been scaled, first along the ordinate and then the abscissa for optimum collapse of the spectra in the velocity and spatial scalings, respectively, to the one at $30D$. The transverse spectra have been scaled only with the total energy.

Figures 5 (left) and (middle) show the second and third order structure functions, respectively, scaled to collapse to the one at $30D$. The scaling factor allows us to compute the mean rate of dissipation and the Kolmogorov scale. Figure 5 (right)

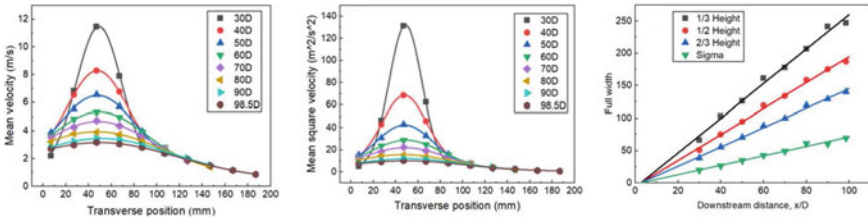


Fig. 2 Axial development of mean velocity profiles with a Gaussian fit (left), the mean square velocity (middle) and the jet width indicating a virtual origin at $x_0/D \approx 5 - 8$ (right)

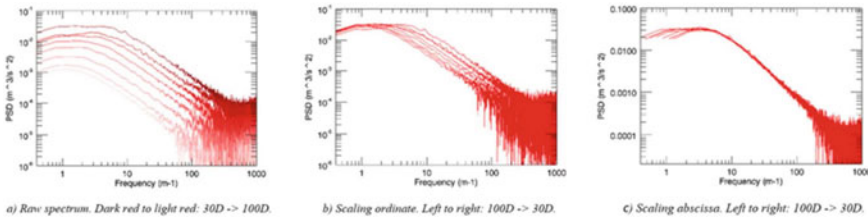


Fig. 3 Axial developments of scaled spatial power spectra along the jet centerline. $x/D = 30, 40, 50, 60, 70, 80, 90, 100$

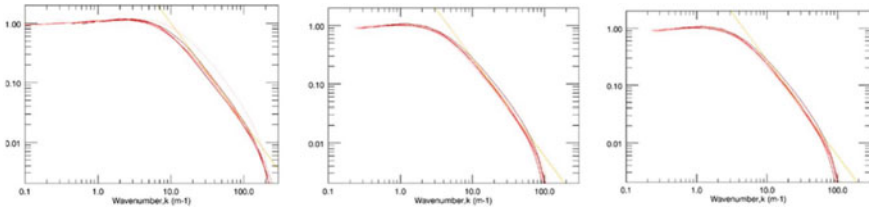


Fig. 4 Spatial power spectra along the radial direction at $x/D = 30, 60$ and 90 ; $r = 0, 20, 40, 60, 80, 100, 120$ mm. These spectra have been scaled only by the local total energy. Yellow line: $-5/3$ slope

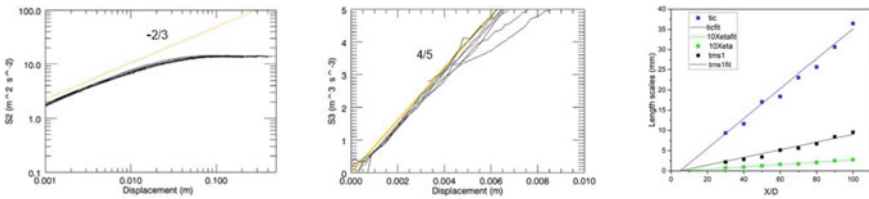


Fig. 5 Left and middle: Second and third order structure functions at axial downstream distances of $x/D = 30, 40, 50, 60, 70, 80, 90, 100$, scaled to collapse. Right: Spatial scales as a function of axial distance

shows the spatial scales along the jet axis. The integral scale is computed from the spatial one-point correlation functions. The Taylor microscale is computed in Fourier space from the Fourier components in the inertial range and the Kolmogorov scale is computed from the measured scaling factor to fit the third order structure function to a $4/5$ slope.

5 Conclusion

The overall result of the detailed measurements and computations is that all first and second order statistical quantities can be referred to a single scaling parameter, the downstream distance x , in agreement with the conservation laws applied to the simple conical model. The third order spatial structure function can be scaled to fit a $4/5$ slope and thus provide results for average dissipation and Kolmogorov scale. All the scaling functions needed to make the various statistical functions collapse do so as expected from their dimension. We thus conclude that the statistical functions measured for this high Reynolds number jet scale according to a single geometrical scaling factor, namely the axial distance x from a virtual origin given within experimental uncertainty to lie between 5 and 8 jet orifice diameters. The scaling functions needed to make the statistical functions collapse and thus display self-similarity adhere well to the predictions from a simple, conical model for the mean velocity.

Acknowledgements Professor Poul Scheel Larsen is acknowledged for helpful discussions. Financial support from the Poul Due Jensen Foundation (Grundfos Foundation) for this research is gratefully acknowledged.

References

1. A.S. Monin, A.M. Yaglom, *Statistical Fluid Mechanics*, vol. 1 (MIT Press, Cambridge, 1971)
2. H. Tennekes, J.L. Lumley, *A First Course in Turbulence* (MIT Press, Cambridge, 1972)
3. U. Frisch, *Turbulence: The Legacy of A* (Cambridge University Press, N. Kolmogorov, 1995)
4. S.B. Pope, *Turbulent Flows* (Cambridge University Press, 2000)
5. L. Prandtl, Bericht über Untersuchungen zur Ausgebildeten Turbulenz. ZAMM **5**(2), 136–139 (1925)
6. T. von Kármán, Mechanische Ähnlichkeit und Turbulenz. Nachr. Ges. Wiss. Göttingen, Fachgruppe I (Mathematik) **5**, 58–76 (1930)
7. G.I. Taylor, Some recent developments in the study of turbulence, in *Proceedings of the Fifth International Congress on Applied Mechanics, Cambridge MA*, ed. by J.P. Den Hartog, H. Peters. (John Wiley, New York, 1938), pp. 294–310
8. Y.B. Zel'dovich, Limiting laws for turbulent flows in free convection. Zhurnal Experimental'noi Teoreticheskoi Fiziki (J. Exp. Theor. Phys.) **7**(12), 1463 (1937)
9. W.K. George, The self-preservation of turbulent flows and its relation to initial conditions and coherent structures, in *Recent Advances in Turbulence*. ed. by R.E.A. Arndt, W.K. George. (Hemisphere, New York, 1989)
10. I. Wygnanski, H. Fiedler, Some measurements in the self-preserving jet. J. Fluid Mech. **38 part 3**, 677–612 (1969)
11. N.R. Panchapakesan, J.L. Lumley, Turbulence measurements in axisymmetric jets of air and helium, Part 1. Air jet. J. Fluid Mech. **246**, 197–223 (1993)
12. J.H. Hussein, S.P. Capp, W.K. George, Velocity measurements in a high-Reynolds-number, momentum-conserving, axisymmetric, turbulent jet. J. Fluid Mech. **258**, 31–75 (1994)
13. P. Burattini, R.A. Antonia, L. Danaïla, Similarity in the far field of a turbulent round jet. Phys. Fluids **17**, 025101 (2005). <https://doi.org/10.1063/1.1833414>
14. D. Ewing, B. Frohnäpfel, W.K. George, J.M. Pedersen, J. Westerweel, Two-point similarity in the round jet. J. Fluid Mech. **577**, 309–330 (2007)
15. P. Buchhave, C.M. Velte, Similarity scaling of the axisymmetric turbulent jet. Part 1. To be submitted (2021)
16. C. Zhu, Y. Tian, P. Buchhave, C.M. Velte, Experimental verification of similarity scaling of axisymmetric turbulent jet. To be submitted (2021)
17. E. Noether, Invariante Variationsprobleme. Nachr. D. König. Gesellsch. D. Wiss. Zu Göttingen, Math-Phys. 235–257, (1918)
18. F.P. Ricout, D.B. Spalding, Measurements of entrainment by axisymmetrical turbulent jets. J. Fluid Mech. **11**, 21–32 (1961)
19. C.B. da Silva, J.N. dos Reis Ricardo, J.C.F. Pereira, The intense vorticity structures near the turbulent/non-turbulent interface in a jet. J. Fluid Mech. **685**, 165–190 (2011)
20. P. Buchhave, C.M. Velte, Measurement of turbulent spatial structure and kinetic energy spectrum by exact temporal-to-spatial mapping. Phys. Fluids **29**, 085109 (2017). <https://doi.org/10.1063/1.4999102>

Topological Differences in Mean Wakes of Circular and Square Cantilevered Cylinders



Matthew G. Kindree, Dekun Yan, and Robert J. Martinuzzi

Abstract The turbulent quasi-periodic wake of a circular and a square cross-section cantilevered finite aspect ratio cylinder protruding a thin laminar boundary layer is investigated experimentally. The mean wake vortical structure and flow topology are found to be more complex for the square than the circular geometry. The differences arise from interactions involving periodically shed Kármán-like vortices. For the square cylinder, the circulation of the shed vortices is significantly stronger, giving rise to more complex interactions between shed vortices and the redeveloping boundary layer. The strength of the shed vortices is related to the rate vorticity, generated on the obstacle faces, is transported along the separated shear layers. The obstacle surface topology thus plays an important role by modifying the separation process.

1 Introduction

Flows over circular and square cross-section, finite aspect ratio cantilevered cylinders are commonly studied as heuristic simplifications for wind engineering and industrial aerodynamics. These are often discussed interchangeably, yet their surface topology are distinct. When compared to the circular cylinder, the additional discontinuities at the sharp edges and corners of the square geometry require topological differences in the flow domain to satisfy the Poincaré–Hopf theorem [1]. The surface influences the rate vorticity is generated and convected into the wake, thus affecting the dynamics of Kármán-like vortex shedding. In this study, it is shown that these differences result in more complex wake structures for square than for circular geometries.

M. G. Kindree · D. Yan

University of Calgary, 2500 University Dr. NW, Calgary, Alberta T2N 1N4, Canada
e-mail: mgkindree@ucalgary.ca

D. Yan

e-mail: dekun.yan2@ucalgary.ca

R. J. Martinuzzi (✉)

Department of Mechanical and Manufacturing Engineering, University of Calgary, Alberta, Canada

e-mail: rmartinu@ucalgary.ca

The influence of the boundary layer state on the wake structure and dynamics is poorly documented for cantilevered cylinders with height-to-width ratios $h/d > 2$. For on-coming thin boundary layers of thickness $\delta < \sim 0.3h$, the wake dynamics are characterized by the quasi-periodic shedding of Kármán-like vortices. Whereas for the square cylinder shedding is observed over most of the obstacle height, for the circular cylinder it is typically restricted to regions closer to the ground plane below $\sim h/2$ [2]. The dominant mean wake features are a lee region recirculation from which two counter-rotating stream-wise vortices, commonly referred to as a dipole, extend downstream [3]. The dipole is the mean signature of the shed vortices, which are tilted upstream with increasing elevation from the ground plane, and are thus observed at lower elevations for circular than square cylinders.

For thin laminar boundary layers, the wake structure is qualitatively similar to that for turbulent boundary layers, but the existence of low-frequency instabilities near the free-end have been reported. In contrast, for the square cylinder, the wake structure differs significantly with multiple mean vortex structures [2, 4]. These observations motivate more detailed studies to elucidate the role of the boundary layer state.

2 Methodology

The turbulent wakes of cantilevered circular and square cylinders of height-to-width, h/d , aspect ratio 4 protruding a thin laminar boundary layer are investigated using planar, time-resolved Stereoscopic Particle Image Velocimetry (SPIV) synchronized with surface-pressure measurements. For each SPIV plane, 16,000 snapshots were collected at a sampling rate corresponding to about 11 points per shedding cycle. The nominal Reynolds number, based on the free-stream velocity U_∞ , the kinematic viscosity ν and d , is 10,500. Further experimental details can be found in Kindree et al. [2]. The on-coming boundary layer satisfies the Blasius profile and its undisturbed thickness at the obstacle location is $0.05h$ ($0.2d$).

Data are reported for a Cartesian coordinate system with (x, y, z) representing (stream-wise, flow-normal, plate-normal) directions and (u, v, w) the corresponding velocity components. Mean and fluctuating components of velocity are denoted (U, V, W) and (u', v', w') , respectively. Coordinate variables are normalized by d , with $z_h = z \cdot d/h$, and velocity by U_∞ . Over 30 SPIV z -planes are synchronized with the surface pressure measurements to obtain volumetric, phase-average representations of the wake dynamics. The common reference phase-angle was obtained using a Hilbert transform of the surface pressure fluctuations. A phase-averaged shedding cycle was represented by 40 phase-bins.

3 Results and Discussion

Mean streamlines overlaying flooded iso-contours of the $\overline{w'^2}$ -distributions in the symmetry plane $y = 0$ are compared in Fig. 1. Also shown are sectional streamlines overlaying iso-contours of W close the ground at an elevation of $z_h = 0.03$ ($z =$

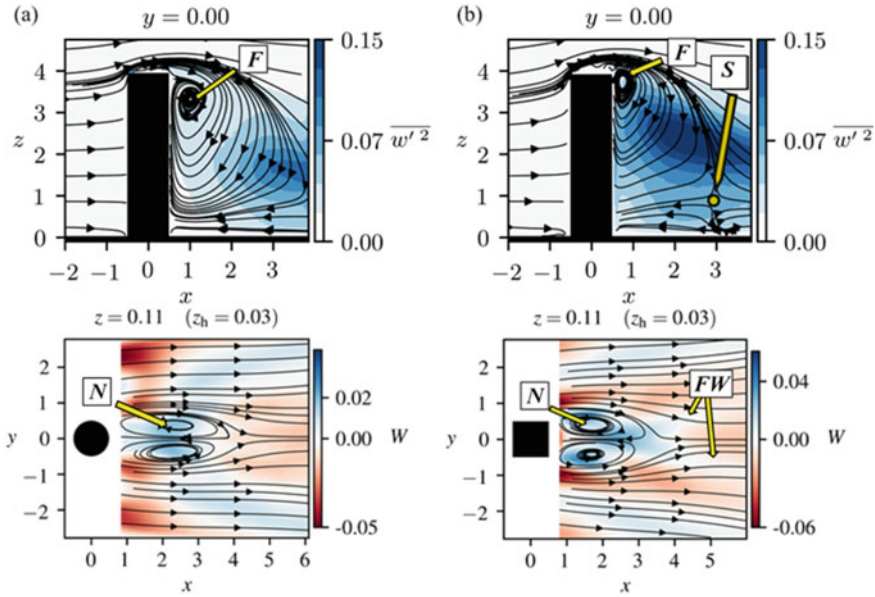


Fig. 1 Mean flow field for **a** circular cylinder and **b** square cylinder. Top: Iso-contours of $\overline{w'^2}$ overlaid by mean flow streamlines in the symmetry plane $y = 0$. Bottom: Iso-contours of W overlaid by sectional streamlines in the plane $z = 0.11$ ($z_h = 0.03$)

0.11). The flow separates at the top leading edges giving rise to a mean recirculation over the obstacle free-end. For the square cylinder, however, the separated shear layer reattaches intermittently. For both obstacles, the separated shear layer exhibits a flapping motion. This process gives rise to a low-frequency, f_L , instability in the wake near the free-end at $f_L d / U_\infty \approx 0.04$ and 0.01 for circular and square cylinders, respectively [2]. For the square cylinder, due to the intermittent reattachment, the amplitude of the low-frequency instability is weaker than for the circular cylinder. The dominant contribution to the wake fluctuations is due to the Kármán-like shedding of vortices at frequencies f_S corresponding to $St = f_S d / U_\infty = 0.146$ and 0.110 for circular and square cylinders, respectively. Concentrations of high $\overline{w'^2}$ show dominant spectral contributions at $2St$ and are located closer to the ground for the circular cylinder. As is further elaborated below, these observations are consistent with the passage of vortex strands connecting alternately shed vortices.

Important topological differences are noted near the wake attachment. For the circular cylinder, the bifurcation line originating over the free-end impinges on the the ground resulting in a simple attachment half-saddle. In contrast, for the square cylinder, the bifurcation connects to a free-saddle S . Flow is directed up from the ground to S giving rise to a secondary vortex structure downstream of the attachment point along regions of $W > 0$ marked FW in the plane $z_h = 0.03$.

The extent and nature of the topological differences are more clearly appreciated by comparing the isometric views of the mean vortical structures shown in Fig. 2.

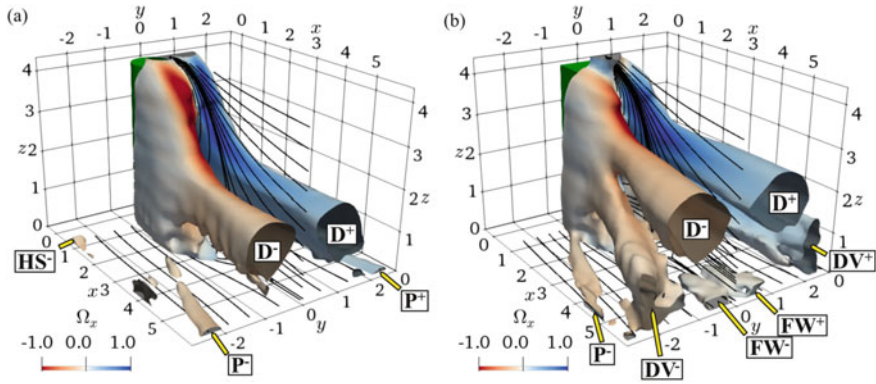


Fig. 2 Mean vortical structures in the wake of the **a** circular and **b** square cylinder visualized as isosurfaces of $\lambda_2 = 0$ coloured by stream-wise vorticity Ω_x . Identified are: **D** dipole; **P** junction; **DV** descending; **FW** far wake and **HS** horseshoe vortices. Superscripts $^+/-$ indicate sense of rotation

This figure shows the iso-surfaces of $\lambda_2 = 0$ coloured by mean streamwise vorticity. While both mean wakes show dipole (**D**) tip vortices and junction (**P**) vortices, the square cylinder wake also shows a descending vortex pair (**DV**) and far wake (**FW**) structures extending downstream.

Differences in the mean wake structures are due to the signature of the instantaneous, interacting large-scale vortices associated with the shedding process. Phase-averaged reconstructions of the wake structure are shown for the circular cylinder, Fig. 3, and square cylinder, Fig. 4, for an arbitrary, but similar, shedding phase. In these figures, features are numbered chronologically with respect to the shedding cycle. The principal cores, **PC**, extend vertically from the ground plane. These cores tilt stream-wise forming connector strands, **CS**, which cross the symmetry plane and connect to the upstream opposite-rotating **PC**. This process results in a continuous chain linking successive shed vortices [3] as seen from the loci of vortex centroids.

The mean signature of the connector strands corresponds to the dipole vortices, **D** in Fig. 2. Maxima of $\overline{w'^2}$ along $y = 0$ occur along the trajectories of the connector strands as these cross the symmetry plane. During each shedding cycle, two strands, one from each opposing shed vortex, cross the symmetry plane such that the dominant w' -fluctuation frequency is $2St$ in this region.

Closer consideration of the phase-resolved wake structure indicates important differences in the wake dynamics and vortex interactions between the two cases. For the circular cylinder in Fig. 3, the connector strands attach to the upstream **PC** at an elevation around $z = 2$ ($z_h = 0.5$). A more resolved view of the process can be gleaned from the loci of the vortex centroids. The loci for the **CS** and **PC** remain distinct, indicating that the vortices have not fully merged. Note that the loci along the **PC** are located on the outer side of the wake, compared to those for the **CS**, which are located closer to the symmetry plane after connecting.

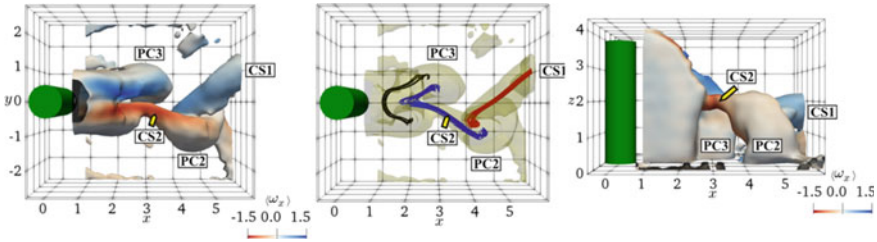


Fig. 3 Phase-averaged vortical structures in the wake of the circular cylinder for an arbitrary shedding phase visualized as isosurfaces of $\lambda_2 = 0$ coloured by streamwise vorticity $\langle \omega_x \rangle$. Middle frame shows loci connecting vortex centroids estimated from the second moments of vorticity

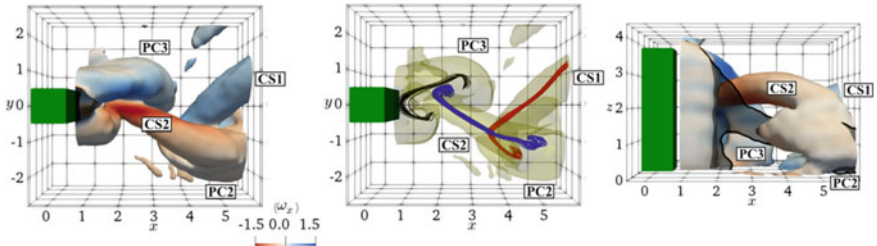


Fig. 4 Phase-averaged vortical structures in the square cylinder wake for an arbitrary shedding phase visualized as isosurfaces of $\lambda_2 = 0$ coloured by $\langle \omega_x \rangle$. Middle frame shows loci connecting vortex centroids. The semi-transparent region in the right frame marks the **DV**-trajectory

For the square cylinder, Fig. 4, the **CS** connect to the upstream vortices at greater elevation ($z \approx 3, z_h \approx 0.75$). In contrast to the circular cylinder wake, the loci of the connected **CS** are located on the outer side of the wake and those of the **PC** closer to the symmetry plane. The connector strands are effectively entrained around the principal core. Due to this wrapping motion, the vorticity vector along the centroid rotates almost 180° stream-wise as the connector wraps around the **PC**. From the right-hand frame of Fig. 4, this wrapping motion occurs along the trajectory of the **DV**, which are thus the mean signature due to the re-orientation of the **CS**.

These differences in the wake dynamics appear related to the strength of the shed vortices. The circulation of the principal cores were estimated for each reconstructed shedding phase for five planes below the **CS** according to $\Gamma = \int \int \langle \omega_z \rangle dA$, where A is the area of the vortex core in the z -plane enclosed by the $\lambda_2 = 0$ iso-contour. For each geometry, the estimated Γ varied less than 5% for each plane or shedding phase. The ensemble average of Γ for the circular cylinder wake is $\Gamma/dU_\infty = 3.8$, which is significantly less than $\Gamma/dU_\infty = 4.8$ for the square cylinder.

The greater strength of the shed vortices for the square cylinder wake results in stronger induced velocities. These observations are consistent with the stronger $W < 0$ observed in the wake along the symmetry plane and the stronger entrainment of the connector strands. The stronger entrainment helps explain why the connector strands wrap around the principal core, giving rise to the descending vortices, for the

square cylinder. For the circular cylinder wake, the **CS** are not entrained as strongly and descending vortices are not observed.

For the square cylinder, the principal cores are located more closely to the symmetry plane. These are thus expected to induce the upward flow ($W > 0$) near the attachment region ($x \sim 3$) from the ground plane, which is consistent with the appearance of the free saddle point S in Fig. 1b. This motion induced by these principal cores is further believed to induce the formation of the the far-wake vortices **FW** downstream of S . For the circular cylinder, the principal cores do not approach the symmetry plane are much weaker, such the flow attaches at a simple half-saddle (in the $y = 0$ plane) and **FW** are not observed.

4 Concluding Remarks

Significant differences have been shown in the mean wake structure and flow topology of circular and square cantilevered cylinders protruding a thin laminar boundary layer. For both cases, the wake is turbulent and quasi-periodic. These differences are related to changes in the wake dynamics and vortex interactions due to the strength of the shed vortices. The surface topology of the obstacles affects the nature of the separation and thus the rate at which surface-generated vorticity is transported to the wake. These changes also affect interactions with the junction vortices and horseshoe vortices, which were not discussed for brevity. The influence of the low-frequency instability on the wake remains unclear and is the subject of on-going research.

Acknowledgements We thank the financial support of the Natural Sciences and Engineering Research Council of Canada through the Discovery Grant and Research Tools & Equipment programs.

References

1. H. Hornung, A.E. Perry, Some aspects of three-dimensional separation, part I: streamsurface bifurcations. *Zeit. Flug. Weltraumforsch.* **8**, 77–87 (1984)
2. M.G. Kindree, M. Shahroodi, R.J. Martinuzzi, Low-frequency dynamics in the turbulent wake of cantilevered square and circular cylinders protruding a thin laminar boundary layer. *Exp. Fluids* **59**, 186 (2018)
3. J.A. Bourgeois, B.R. Noack, R.J. Martinuzzi, Generalized phase average with applications to sensor-based flow estimation of the wall-mounted square cylinder wake. *J. Fluid Mech.* **736**, 316–350 (2013)
4. D. Zhang, L. Chang, H. An, M. Zhao, Direct numerical simulation of flow around a surface-mounted finite square cylinder at low Reynolds numbers. *Phys. Fluids* **29**, 045101 (2017)

Large-Scale-Motions and Self-excited Clustering of Coherent Structures in Wall Turbulence



Sedat Tardu

Abstract We revisit clustering of coherent Reynolds shear stress producing eddies in wall bounded turbulent flows. We question the plausibility of the strict alignment of the packets of vortices that supposedly lead to very-large-scale motions. Attention is later drawn to the self-exciting Hawkes stochastic processes to model and understand the organization of coherent vortices into clusters, and their spatial organization in the logarithmic layer.

1 Introduction

The main aim of this short note is to introduce and propose adequate stochastic point processes to describe and model large-scale (LSM) and very-large scale (VLSM) motions occurring in wall bounded turbulent flows. The LSM originate from the packets of Reynolds (Re) shear stress producing eddies in the buffer layer (quasi-streamwise vortices, QSV), at small-medium and large Re numbers [5, 7]. The origin of very-large-scale motions (VLSM) at large Re is still not clearly understood, but one of the conjectures is the coherent alignment of LSM and the wakes they induce into the subsequent packets [5] and their immersion in the logarithmic layer. Figure 1 shows the top view of the quasi-streamwise vortices populating a turbulent channel flow obtained through direct numerical simulations (DNS) in particularly large computational domains at $Re_\tau = \frac{h\bar{u}_\tau}{\nu} = h^+ = 590$. Here h is the channel half width and \bar{u}_τ and ν are respectively the shear velocity and the viscosity. Hereafter (+) denotes the quantities scaled by \bar{u}_τ and ν . Note the large spanwise extend of the cluster. It is also seen that the very-large scale motions have a direct impact on the weighted spectra of the turbulent streamwise velocity intensity in the logarithmic layer.

S. Tardu (✉)
Université Grenoble Alpes, LEGI, Grenoble, France
e-mail: sedat.tardu@legi.grenoble-inp.fr

© The Author(s), under exclusive license to Springer Nature Switzerland AG 2021
R. Örlü et al. (eds.), *Progress in Turbulence IX*, Springer Proceedings in Physics 267,
https://doi.org/10.1007/978-3-030-80716-0_28

209

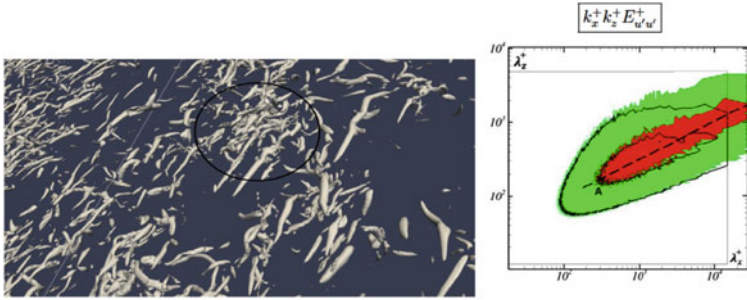


Fig. 1 Left: Top view of QSV's in a turbulent channel flow at $Re_\tau = 590$ resulting from our own DNS. Clusters of QSV appear as amalgamation of LSM's at different wall normal positions into a large bulge. The radius of the circle is about $10h$. Right: weighted streamwise velocity fluctuations spectra in the log-layer. Black and colour contours correspond to $h^+ = 395$ and 1100 respectively [10]

2 Coherent Alignment of One-Dimensional (1D) Clusters. Structuration of VLSM

The cumulative probability distribution (cpd) of the QSV interarrival times in the buffer layer shown in Fig. 2-left, is reminiscent of a double Poisson process. The passage of the QSV are detected by single point measurements through different identification schemes combined with a self-similar pattern recognition technique [7]. The results in Fig. 2 have been obtained in a turbulent channel flow at $h^+ = 560$. Two categories of events emerge, those that are close (packets) and the solitary single-events. A Markov chain that contains 3 states is introduced here to model this double Poisson process as in [3] (Fig. 2, right). The state 0 stands for the presence of a QSV within a given interval of time δt . The states 1 and 2 are the waiting states with absence of QSV. The arrows are annotated with their respective probabilities of occurrence. The quantity A is a measure of clustering and t_e is the mean regeneration period of the structures. The Markov chain perfectly estimates the cpd of the interarrival times (squares in Fig. 2 left) as expected. The evaluation of the supposed coherent alignments of the packets that presumably result in VLSM requires the use of a hidden Markov chain. Yet the part of the Markov chain shown by the circle in broken lines in Fig. 2 allows us to estimate the *stricto sensu* alignment probability of the clusters. We found that the probability of having Ξ aligned 1D clusters, which uniformly contain N individual vortices, is proportional to

$$\log p(\Xi > 1) \propto (\Xi - 1)(N + 1) \log A \quad (1)$$

and since the measure of clustering is $A < 1$, this probability decreases both with N and Ξ . That is, the larger the LSM, the rarer their coherent alignment into VLSM. Coherent alignment of clusters of structures originating from roughly the same buffer

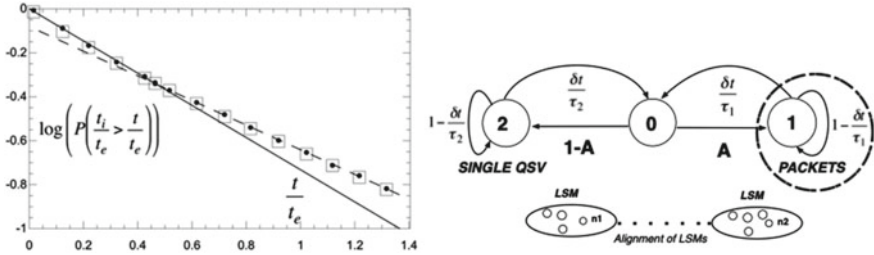


Fig. 2 Left: Cumulative probability distribution (cpd) of the interarrival times of QSV's in the buffer layer. Further details of the methodology can be found in [7]. Circles and squares show the measurements and the model estimations respectively. Right: Markov chain modelling the double Poisson distribution

layer streak, as suggested by [5] is therefore unlikely. This constitutes, at least a formal argument justifying the observations and discussions related to the vortex clusters in the logarithmic region in [2].

3 Self-exciting Processes and Regeneration of Large-Scale-Motions

The clusters of the near wall structures are provoked by a primary structure which is sufficiently intense, and/or close to the wall (Fig. 3 left). This has been shown both experimentally and through direct numerical simulations in [7, 11]. A mother structure with large $s^+ = \Gamma/a^{+2}$, wherein Γ is the circulation of the primary vortex and a^+ is its distance to the wall gives birth to a cascade of active eddies. The characteristic time-scale of the viscous-inviscid response related to the primary structure is $1/s^+$.

We propose to model the buffer layer clusters through a self-exciting non-homogeneous Hawkes Poisson point process [4]. In the Hawkes terminology, the primary intense vortex of the cluster is an immigrant and the provoked subsequent structures are the offsprings. These processes are commonly used in seismology (earthquake

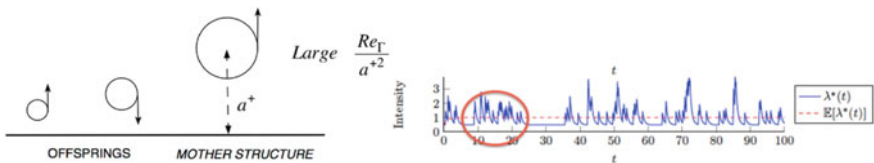


Fig. 3 Left: ‘mother’ structure with a large enough intensity, and close to the wall regenerates secondary structures according to [7, 11]. Right adapted from [6] with the consent of the authors: The arrival rate in time of a typical Hawkes process [6]. The red circle shows a typical ‘packet’

and subsequent aftershocks), neuroscience, epidemiology, insurance and finance. They are long-range dependent. Our aim in this short note is to draw our community's attention to these peculiarities. Consider the process with arrival (occurrence) rate in time:

$$\lambda^*(t) = \lambda + \sum_{t_i < t} \alpha e^{-\beta(t-t_i)} \quad (2)$$

Each arrival in the system increases the arrival intensity by α , then this arrival's effect decays at rate β [6]. This is a non-homogeneous Poisson process in which the intensity explicitly depends on previous events. The excitation function which is exponential, is connected to the regeneration of the QSV packets in the buffer layer. The red circle in Fig. 3b, which is adapted from [6] shows such a self-excited packet. The covariance density of this point process is:

$$R^c(\tau) = \bar{\lambda}^* \delta(\tau) + \frac{\alpha\beta\lambda(2\beta - \alpha)}{2(\beta - \alpha)^2} e^{-(\beta-\alpha)\tau} \quad (3)$$

The first term of this equation, wherein δ is the Dirac function, stands for a classical non-excited Poisson process and $\bar{\lambda}^* = \frac{\lambda}{1-\alpha/\beta}$. The second term shows that the process is long range dependent, with a typical relaxation time $t_r = (\beta - \alpha)^{-1}$. The original Hawkes's process is one of the self-exciting processes, but other types of excitation processes can also be considered. In the present context, the parameter α is typically the rate of arrivals of the structures into packets. The parameter β is such that at the trailing edge (the end) of a packet the arrival rate α is substantially reduced. We have experimental data to roughly estimate α and β in the buffer layer, but unfortunately only at $h^+ = 560$ [7], and we are not aware of more data analyzing the regeneration process this way. Thus, $\alpha \propto 1/\Delta t_P$ where Δt_P is the time interval separating the consecutive events within the packets. Supposing that β dumps the arrival rate by two decades at the leading edge of a cluster, gives $\beta \propto 5/T_P$ where T_P is the typical time duration of the packet. Using the data in [7] one obtains $\alpha^+ \propto 0.05$, $\beta^+ \propto 0.08$ resulting in the memory time of the process $t_r^+ \propto 30$ which is as large as the outer time scale at this Re_τ . Using a convection velocity of 10 wall units in the buffer layer results in the streamwise extends of $l_\alpha^+ = 200$ and $l_\beta^+ = 125$ that are within the range of the lengths of QSV. It has to be emphasized here that the choice (estimation) of α and β is crucial as significantly longer memory periods can result when approaching the excessive case $\beta \rightarrow \alpha$. Maximum likelihood estimations are needed to determine these parameters more precisely [6]. The packets form large wakes of typical streamwise lengths $L_w \approx 5h$ in the low buffer [1, 7]. The clusters transport the wakes into the outer region by the lift-up velocity field they induce according to the Biot-Savart law. Hence, the streamwise and spanwise length of the multiple-wakes increase linearly with the wall distance [2]. The wake structure stays self-similar during the long memory time t_r , as the tall self-similar attached clusters grow self-similarly in time in [2]. The lifetime of the wakes is much larger than t_r . Once the wake clusters merge in the log-layer they lose their initial memory and the trails of the streamwise velocity fluctuations they transport adapt themselves to the

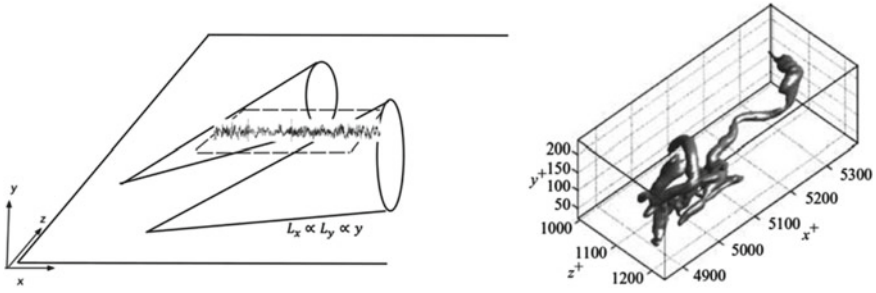


Fig. 4 Conceptual model of the merging of LSM induced wakes into the logarithmic layer (left). Two clusters of wakes coming from different origins shifted in the spanwise direction can lead to persistent streamwise velocity fluctuations in the intersection plane. Right: an attached cluster according to [2] adapted with permission

outer scales. According to our estimations given above, the multiple-wakes reach $y^+ \approx 300$ self-similarly during t_r . Their streamwise and spanwise scales increase by the same amount, attaining roughly $6h$. Although the *stricto sensu* coherent alignment of the clusters is unlikely as discussed before, the alignment of the multiple wakes formed by different buffer-layer clusters with different past stories and that are close in the streamwise direction and (or) shifted in the spanwise one, now becomes plausible. This is schematically shown in Fig. 4, which also shows a typical attached cluster explored in [2] and originating roughly from a region of about 100 wall units spanwise extend. Last but not least, the cluster excitation parameter α and consequently β depends on the Reynolds number. Indeed, the regeneration of offsprings depends on the vorticity intensity of the mother structure and the streamwise vorticity intensity at the wall is Re dependent [9].

4 Conclusion

Self excited processes are good candidates to model the clustering of coherent structures and of their wakes emerging into VLSM in the logarithmic layer. It is unlikely that the vortex clusters originating, say from the same streak in the buffer layer, get coherently aligned to form VLSM in the logarithmic region. The main point is the spanwise expansion of the wakes generated by individual clusters. This consequently makes possible the amalgamation of different wake clusters with different histories, coming from different, but close enough streamwise and spanwise locations. The VLSM result from a self-exciting spatio-temporal Poisson cluster process, in which the spanwise direction plays a capital role in the present context. Existing models such as the Townsend-Perry hierarchy should be modified to take these specific features into account (see [8] for a review). To be short, the contribution of the hierarchies to the shear stresses in the fully developed turbulent region is related to the

probability density for the length scale in the hierarchy. This probability density has to be extended to contain informations on the streamwise and spanwise extends of the clusters. The events in the clusters have to be marked by the wake they induce, which is an additional important variable. The self-exciting feature of the regeneration process has to be taken into account. We are currently working on these key issues.

References

1. R.J. Adrian, C.D. Meinhart, C.D. Tomkins, Vortex organization in the outer region of the turbulent boundary layer. *J. Fluid Mech.* **422**, 1–53 (2000)
2. J.C. Alamo, J. Jimenez, P. Zandonade, R.D. Moser, Self-similar vortex clusters in the turbulent logarithmic region. *J. Fluid Mech.* **561**, 329–358 (2006)
3. P.R. Field, R. Wood, P.R.A. Brown, Ice particle interarrival times measured with a fast FSSP. *J. Atmos. Oceanic Technol.* **131**, 1997–2017 (2003)
4. A.G. Hawkes, Spectra of some self-exciting and mutually exciting point processes. *Biometrika* **58**, 83–90 (1971)
5. K.C. Kim, J. Adrian, Very large-scale motion in the outer layer. *Phys. Fluids* **11**, 417–422 (1999)
6. P.J. Laub, T. Taimre, P.K. Pollett, Hawkes processes (2015). [arXiv:1507.02822](https://arxiv.org/abs/1507.02822)
7. S. Tardu, Characteristics of single and clusters of bursting events. *Exp. Fluids* **33**, 640–652 (2002)
8. S. Tardu, *Statistical Approach to Wall Turbulence*, 336 pp. (Wiley, 2011)
9. S. Tardu, F. Bauer, Vorticity transport in low Reynolds number turbulent channel flows. *Eur. J. Mech. B* **55**, 272–278 (2016)
10. S. Tardu, F. Bauer, Fine structure of production in low to medium Reynolds number wall turbulence. *Comput. Fluids* **148**, 82–102 (2017)
11. J. Zhou, R.J. Adrian, S. Balachandar, T.M. Kendall, Mechanisms for generating coherent packets of hairpin vortices in channel flow. *J. Fluid Mech.* **387**, 353–396 (1999)

The Conservative Pressure Hessian and the Free Fluid Particle Model



Maurizio Carbone, Andrew Bragg, Josin Tom, Michael Wilczek,
and Michele Iovieno

Abstract In this work we aim to understand the interplay between deformation and energy of a fluid particle in a turbulent flow, focusing on the role of the pressure Hessian. A new decomposition of the Hessian is proposed, defining a conservative Hessian which contains the stabilizing effects of the full Hessian on energy and deformation of fluid elements. This conservative Hessian is then used to construct models for the velocity gradient which allow controlling alignments and singularities.

1 Introduction

Small-scale turbulence exhibits complex and intriguing features, such as quasi log-normality of the dissipation rate, extreme intermittency of vorticity [1] and exponential stretching/contraction of fluid elements [2, 3]. The velocity gradient, together with the Cauchy-Green tensor, comprehensively characterize small-scale turbulence, including strain/rotation rates and the deformation of fluid elements. The velocity

M. Carbone (✉) · M. Wilczek
Max Planck Institute for Dynamics and Self-Organization, Am Faßberg 17,
37077 Göttingen, Germany
e-mail: maurizio.carbone@ds.mpg.de

M. Wilczek
e-mail: michael.wilczek@ds.mpg.de

A. Bragg · J. Tom
Department of Civil and Environmental Engineering, Duke University,
Durham, NC 27708, USA
e-mail: andrew.bragg@duke.edu

J. Tom
e-mail: josin.tom@duke.edu

M. Iovieno
Dipartimento di Ingegneria Meccanica e Aerospaziale, Politecnico di Torino,
Corso Duca degli Abruzzi 24, Torino, Italy
e-mail: michele.iovieno@polito.it

gradient drives the evolution of the Cauchy-Green tensor while undergoing non-linear and non-local dynamics. The pressure Hessian encodes most of the non-localities.

We analyze the interplay between the pressure Hessian, kinetic energy and the deformation of fluid elements. In particular, we aim to extract simple dynamical features introduced by pressure, possibly concealed by chaotic behaviours and intermittency. The usual decomposition of the pressure Hessian is purely kinematic, consisting of an isotropic part that ensures incompressibility and a non-local/anisotropic part [4]. In contrast, we define a dynamical decomposition of the pressure Hessian into a conservative and a non-conservative part, based on the equations for the dynamics of fluid elements [5]. Taken by itself, the conservative Hessian introduces a first integral of motion in the dynamics of fluid elements. This conserved quantity hinders the formation of singularities in the gradient dynamics and opposes the exponential deformation of material lines. Also, the conservative part of the Hessian does not apply any torque to the fluid element. In this sense, the conservative Hessian acts on a free fluid particle: angular momentum and energy are conserved.

We employ the conservative pressure Hessian to construct models that allow controlling the statistical alignments and the onset of singularities. The resulting class of closures includes the well-known Restricted Euler model [4] and the inviscid tetrad closure [6] as limiting cases. Those classical closures provide relevant insight into the velocity gradient dynamics but also have some shortcomings, yielding, for example, Hessians that are either positive or negative definite [6, 7]. Contrarily, the pressure Hessian in turbulence has a rich set of preferential configurations, as shown through an invariant triangle in [8] or a symmetry analysis in [9].

2 Constructing the Conservative Pressure Hessian

The dynamics of the velocity gradient $\mathbf{A} = \nabla \mathbf{u}(\mathbf{x}, t)$ in an incompressible flow is governed by the equations

$$\text{Tr}(\mathbf{A}) = 0, \quad \text{d}_t \mathbf{A} \equiv (\partial_t + \mathbf{u} \cdot \nabla) \mathbf{A} = -\mathbf{A}^2 - \mathbf{H} + \nu \nabla^2 \mathbf{A} + \mathbf{F}, \quad (1)$$

where $\text{Tr}(\cdot)$ indicates the matrix trace, \mathbf{H} is the pressure Hessian, ν is the kinematic viscosity and \mathbf{F} is an external forcing. In the following, we analyze the role of \mathbf{H} on the dynamics of a fluid element, and we neglect viscous stresses and forcing. The Cauchy-Green tensor characterizes the shape of an infinitesimal fluid element, and its evolution is driven by the velocity gradients

$$\mathbf{C} = \mathbf{D} \mathbf{D}^\top, \quad \text{d}_t \mathbf{C} = \mathbf{A} \mathbf{C} + \mathbf{C} \mathbf{A}^\top, \quad (2)$$

where $\mathbf{D} = \partial \mathbf{X}(t; \mathbf{x}) / \partial \mathbf{x}$ is the deformation tensor, describing the dependence of the fluid particle trajectory $\mathbf{X}(t; \mathbf{x})$ on the initial position \mathbf{x} . Equations (1) and (2) allow deriving the evolution equations for the angular momentum $\mathbf{L} = \mathbf{C} \mathbf{A}^\top - \mathbf{A} \mathbf{C}$ and the kinetic energy $E = \text{Tr}(\mathbf{A} \mathbf{A}^\top \mathbf{C}) / 2$ of an infinitesimal ideal fluid element [5]

$$d_t \mathbf{L} = [\mathbf{H}, \mathbf{C}], \quad d_t E = -\text{Tr}(\mathbf{H} \mathbf{A} \mathbf{C}), \quad (3)$$

where $[\cdot, \cdot]$ indicates the matrix commutator. Equation (3) implies that the angular momentum of the fluid element is conserved if \mathbf{C} and \mathbf{H} commute. In such a case, \mathbf{H} and \mathbf{C} share the same eigenvectors, or, more generally, the space of the eigenvectors of \mathbf{H} is \mathbf{C} -invariant. Based on that, we define the conservative pressure Hessian

$$\mathbb{H} = \varphi_{-1} \frac{\mathbf{C}^{-1}}{\text{Tr}(\mathbf{C}^{-1})} + \varphi_0 \left(\frac{\mathbf{I}}{3} - \frac{\mathbf{C}^{-1}}{\text{Tr}(\mathbf{C}^{-1})} \right) + \varphi_1 \left(\frac{\mathbf{C}}{\text{Tr}(\mathbf{C})} - \frac{\mathbf{C}^{-1}}{\text{Tr}(\mathbf{C}^{-1})} \right), \quad (4)$$

where \mathbf{I} is the identity matrix and coefficients $\varphi_i(\mathbf{C}, \mathbf{A})$ are functions of the invariants formed through the velocity gradient and the Cauchy-Green tensor. We also require that this conservative part ensures incompressibility through $\text{Tr}(\mathbb{H} + \mathbf{A}^2) = 0$. We further constrain the conservative Hessian \mathbb{H} to conserve a potential energy function, which is achieved if φ_0 and φ_1 are a function of \mathbf{C} only. In such a case, the Hessian defined in (4) does work on fluid elements according to (3) by conserving a pressure-induced potential energy function U

$$\text{Tr}(\mathbb{H} \mathbf{A} \mathbf{C}) = \frac{\varphi_0}{6} d_t c_1 + \frac{\varphi_1}{4c_1} d_t c_2 \equiv d_t U(c_1, c_2), \quad (5)$$

where $c_1 = \text{Tr}(\mathbf{C})$ and $c_2 = \text{Tr}(\mathbf{C}^2)$ are the principal invariants of the Cauchy-Green tensor. The conservative Hessian components φ_i are related to the velocity gradient and pressure-induced energy U through

$$\varphi_0 = 6 \frac{\partial U}{\partial c_1}(c_1, c_2), \quad \varphi_1 = 4c_1 \frac{\partial U}{\partial c_2}(c_1, c_2), \quad \varphi_{-1} = -\text{Tr}(\mathbf{A}^2). \quad (6)$$

By introducing the decomposition of the pressure Hessian into conservative and non-conservative parts, $\mathbf{H} = \mathbb{H}[U] + \mathbf{H}'$, the energy balance in (3) becomes $d_t(E + U) = -\text{Tr}(\mathbf{H}' \mathbf{A} \mathbf{C})$. Therefore, the tensor $\mathbb{H}[U]$, taken by itself, conserves a modified energy function $F = E + U$, consisting of the sum of the kinetic energy E and a pressure-induced potential energy U .

3 Conservative Pressure Hessian from DNS Data

We compute the conservative Hessian using data from a direct numerical simulation of incompressible, statistically steady and isotropic turbulence. The computational grid size is 256^3 and the Reynolds number based on the Taylor micro-scale is $Re_\lambda \simeq 110$. In the simulations, a statistically steady state is maintained in a deterministic fashion by reintroducing at large scales the energy lost to viscous dissipation.

A requirement of minimum statistical distance between the conservative and full pressure Hessians is employed, we search for components φ_i that yield

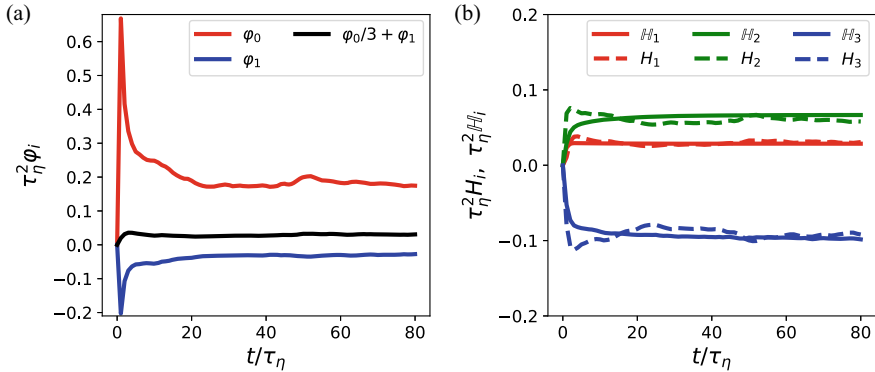


Fig. 1 **a** Components φ_i of the conservative pressure Hessian (4) as functions of time. The results are from DNS and all quantities are normalized through the Kolmogorov time-scale. **b** Effect of conservative and full pressure Hessian $H_i = \mathbf{w}_i^\top \mathbf{H} \mathbf{w}_i$ along the principal deformation directions

$\min(\text{Tr}((\mathbf{H} - \mathbb{H})^2))$. Equation (4) is projected along the basis tensors formed through normalized powers of \mathbf{C} and the resulting linear system yields the conservative Hessian components φ_0 and φ_1 , while incompressibility specifies φ_{-1} . The conservative Hessian components, φ_0 and φ_1 depend only on the \mathbf{C} eigenvalues, which approach almost everywhere the same exponential growth rate for long times, namely the Lyapunov exponents [3]. Therefore φ_0 and φ_1 are independent of spatial coordinates for long times. Figure 1a shows the components φ_i of the conservative Hessian as a function of time. After a short transient, the components approach constant values. The conservative Hessian does work on fluid elements preserving the potential energy U which, with constant components φ_0 and φ_1 , is asymptotically $U \sim (\varphi_0/3 + \varphi_1)c_1/2$. This potential energy is analogous to that of a spring with stiffness $\mathcal{K} = \varphi_0/3 + \varphi_1$. The stiffness coefficient from our DNS data is $\mathcal{K} \simeq 0.03/\tau_\eta^2$, where τ_η is the Kolmogorov time-scale. Therefore, the conservative part of the pressure Hessian introduces a positive stiffness of the fluid element: the fluid element behaves as if it could react to deformations. Of course, an isolated blob of ideal fluid does not react to deformation. This stiffness arises through interaction with other fluid elements mediated by pressure.

The stabilizing effect of the pressure Hessian due to the introduction of stiffness of fluid elements impacts the dynamics of velocity gradients. To see how, we project the equation for the gradient (1) along instantaneous directions of the eigenvectors \mathbf{w}_i of \mathbf{C} . The eigenvectors are ordered such that the first corresponds to the major stretching direction, the second to the intermediate (which also stretches in turbulence [2]), and the third to the exponentially shrinking direction. Figure 1b shows that pressure Hessian hinders all stretching/shrinking of fluid elements. Indeed, the Hessian components $\mathbf{w}_i^\top \mathbb{H} \mathbf{w}_i$ induce negative strain along the major and intermediate stretching directions \mathbf{w}_1 and \mathbf{w}_2 , while inducing positive strain along direction \mathbf{w}_3 .

4 The Free Fluid Particle and the Control of Singularities

We now employ the pressure-induced potential energy to construct models for the velocity gradient dynamics that allow controlling preferential alignments and singularity onsets. As a first step, we neglect all non-conservative contributions, namely the non-conservative part of the pressure Hessian, the viscous stresses and the external forcing. These rather extreme simplifications allow us to focus on the time-reversible part of the velocity gradient dynamics. We leave the introduction of dissipation for future work. We propose an ansatz in which the pressure-induced potential energy U is proportional to the anisotropy degree of the fluid element. This results in the model equations

$$d_t \mathbf{A} = -\mathbf{A}^2 - \mathbb{H}[U], \quad d_t \mathbf{C} = \mathbf{A}\mathbf{C} + \mathbf{C}\mathbf{A}^\top, \quad U = \gamma E_0 \frac{\text{Tr}((\mathbf{C} - \mathbf{I})^2)}{\text{Tr}(\mathbf{C}^2)}, \quad (7)$$

where E_0 is the initial kinetic energy of the fluid element and γE_0 is the maximum potential energy. Equations (7) are integrated in time through a second-order Runge–Kutta scheme, featuring QR decomposition of the Cauchy–Green tensor at each time step. The conservative Hessian $\mathbb{H}[U]$ corresponding to the potential energy U follows from Equations (4) and (6) and we would recover the tetrad closure [6] by setting $\gamma = 0$. The parameter γ controls the amount of kinetic energy relative to potential energy of the fluid element. The gradients cannot be singular when $\gamma > 1$ since the energy balance $d_t(E + U) = 0$ bounds both the kinetic and potential energy. The resulting deformations are also bounded so that this time-reversible model rules out the exponential chaotic separation of fluid particles. Despite these simplifications, the model can surprisingly replicate characteristic features of small-scale turbulence. For example, the model predicts very well the preferential alignment between vorticity and intermediate strain-rate eigenvector, as shown in Fig. 2a. The inset shows that this preferential alignment is stronger as γ decreases, corresponding to more extreme deformations of fluid elements. The proposed time-reversible model already encodes relevant information about the turbulent dynamics, thus providing a good starting point to introduce forcing and dissipation for more realistic turbulence modelling.

Figure 2b shows the joint PDF of the principal velocity gradient invariants obtained from the proposed model. It resembles the PDF from a Gaussian random field and does not show very pronounced tails along the zero-discriminant curve [4]. Despite this resemblance to Gaussian random fields, the strain and vorticity are well correlated, showing pronounced alignments. A drawback of the energy balance $d_t(E + U) = 0$ is that the kinetic energy and the deformations are bounded. Therefore, the gradients cannot take on extreme values, and the PDF of its invariants decays very fast compared to the same PDF in turbulence. This drawback is also observed in closures based on the recent deformation approximation [10].

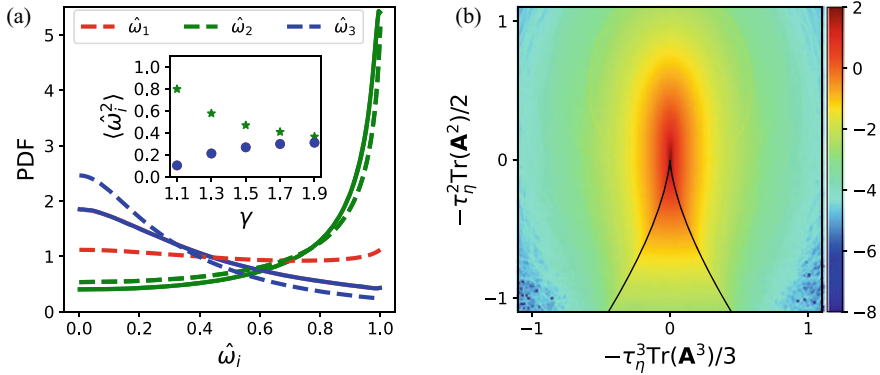


Fig. 2 **a** PDF of the alignment between vorticity and strain-rate eigenvectors $\hat{\omega}_i = \mathbf{v}_i \cdot \boldsymbol{\omega} / \|\boldsymbol{\omega}\|$. The first strain eigenvector corresponds to most positive eigenvalue. Solid lines refer to the model, dashed lines refer to the DNS. Note that the solid red and blue lines overlap due to time reversibility. Inset: mean square alignment as a function of the model parameter γ . **b** Joint PDF of the principal invariants of the velocity gradient \mathbf{A} . Results are for $\gamma = 1.3$

5 Concluding Remarks and Outlook

We have defined a conservative pressure Hessian that highlights the effects of the pressure on energy and deformation of fluid elements. The conservative Hessian, taken by itself, introduces first integrals of motion. These induce a dynamical stabilizing effect, hindering extreme velocity gradients and material lines deformation. The newly observed stabilizing mechanism is mainly related to strain rate, thus being complementary to the reduction of non-linearity, which relies on the stabilizing role of vorticity. The conservative Hessian is used to construct models for the velocity gradient that allow controlling alignments and singularities. Despite its extreme simplifications, the presented time-reversible model can predict alignments between strain rate and vorticity, thus representing a good starting point to construct more realistic models for turbulence.

References

1. D. Buaria, A. Pumir, E. Bodenschatz, P.K. Yeung, Extreme velocity gradients in turbulent flows. *New J Phys* **21**(4), 043004 (2019)
2. S.S. Girimaji, S.B. Pope, Material-element deformation in isotropic turbulence. *J Fluid Mech* **220**, 427–458 (1990)
3. P.L. Johnson, C. Meneveau, Large-deviation joint statistics of the finite-time Lyapunov spectrum in isotropic turbulence. *Phys Fluids* **27**(8), 085110 (2015)
4. P. Vieillefosse, Local interaction between vorticity and shear in a perfect incompressible fluid. *J Phys France* **43**(6), 837–842 (1982)

5. P. Vieillefosse, Internal motion of a small element of fluid in an inviscid flow. *Physica A* **125**(1), 150–162 (1984)
6. M. Chertkov, A. Pumir, B.I. Shraiman, Lagrangian tetrad dynamics and the phenomenology of turbulence. *Phys Fluids* **11**(8), 2394–2410 (1999)
7. L. Chevillard, C. Meneveau, L. Biferale, F. Toschi, Modeling the pressure Hessian and viscous Laplacian in turbulence: Comparisons with direct numerical simulation and implications on velocity gradient dynamics. *Phys Fluids* **20**(10), 101504 (2008)
8. J. Tom, M. Carbone, A.D. Bragg, Exploring the turbulent velocity gradients at different scales from the perspective of the strain-rate eigenframe. *J Fluid Mech* **910**, A24 (2021)
9. M. Carbone, M. Iovieno, A.D. Bragg, Symmetry transformation and dimensionality reduction of the anisotropic pressure Hessian. *J Fluid Mech* **900**, A38 (2020)
10. P.L. Johnson, C. Meneveau, A closure for Lagrangian velocity gradient evolution in turbulence using recent-deformation mapping of initially Gaussian fields. *J Fluid Mech* **804**, 387–419 (2016)

Modelling The Pressure Hessian in Turbulence Through Tensor Function Representation Theory



Maurizio Carbone and Michael Wilczek

Abstract One of the main challenges in Lagrangian modelling of velocity gradients in isotropic turbulence is to capture the non-local effects of the pressure Hessian and viscous diffusion. In statistical models of the velocity gradient tensor, the non-local effects give rise to unclosed conditional averages, making the statistical framework ideal for tensor function representation theory. By employing data from direct numerical simulation (DNS) of incompressible, statistically steady and isotropic turbulence, we analyze the mean non-local pressure Hessian conditional on the local velocity gradient tensor configuration. We define a basis consisting of velocity gradients products and investigate the trend of the associated Hessian components as functions of the velocity gradient invariants. Results show that some of the Hessian components display a pronounced dependence on the gradient invariants, undergoing sharp variations in specific phase space regions. Thus, our analysis lays the foundation for improved dynamical velocity gradient models that are accurate across the whole phase space.

1 Introduction

Many important characteristics of small-scale turbulence, such as dissipation, enstrophy, and the topology of small-scale structures, are encoded in the velocity gradient. For example, the teardrop-shaped probability density function (PDF) of the velocity gradient's principal invariants, together with the preferential statistical alignments between strain-rate eigenvectors and vorticity, are distinguishing marks of turbulent motion [1]. The dynamics of the velocity gradient is non-linear and non-local. The anisotropic part of the pressure Hessian encodes most of the non-locality, thus contributing to prevent singularities that the non-linear terms alone would induce [2].

M. Carbone (✉) · M. Wilczek
Max Planck Institute for Dynamics and Self-Organization, Am Faßberg 17,
37077 Göttingen, Germany
e-mail: maurizio.carbone@ds.mpg.de

M. Wilczek
e-mail: michael.wilczek@ds.mpg.de

In single-particle models for the velocity gradient, the non-local contributions are unclosed and require modelling. Classical closures are constructed, for example, by approximating the geometrical features of motion [3], by employing analytically tractable random fields [4], or by combinations of both [5]. A more recent alternative consists of tensorial neural networks that can predict the non-local pressure Hessian statistics given the local velocity gradients [6]. Such machine learning approaches rely on tensor function representation theory [7]. Tensor function representation can also be directly employed to build stochastic models for the velocity gradient dynamics. For example, a recent work [8] assumed constant components of the pressure Hessian in a basis consisting of products of velocity gradients. The resulting stochastic model accurately reproduces the dynamics of the gradient invariants in vorticity-dominated regions. However, it leaves room for improvement at a large strain rate. Here, we explore how to refine such dynamical models for the velocity gradient, using data from direct numerical simulations and tools from information theory. We systematically characterize the tensor function representation of the non-local Hessian in terms of the velocity gradient, featuring variable Hessian components with respect to the prescribed basis.

2 Statistical Dynamics of Velocity Gradients and Tensor Function Representation Theory

The equations governing the dynamics of the velocity gradient $\mathbf{A}(\mathbf{r}, t) = \nabla \mathbf{u}(\mathbf{r}, t)$ are obtained by taking the gradient of the incompressible Navier-Stokes equations, resulting in

$$(\partial_t + \mathbf{u} \cdot \nabla) \mathbf{A} = -\mathbf{A}^2 - \mathbf{H} + \nu \nabla^2 \mathbf{A} + \mathbf{F}, \quad \text{Tr}(\mathbf{A}) = 0, \quad (1)$$

where $\text{Tr}(\cdot)$ denotes the matrix trace, ν is the kinematic viscosity, \mathbf{H} is the pressure Hessian divided by the constant fluid density, and \mathbf{F} is an external large-scale forcing. The pressure Hessian can be decomposed into a local part, entirely determined by incompressibility, and a non-local part $\tilde{\mathbf{H}} = \mathbf{H} - \text{Tr}(\mathbf{H})\mathbf{I}/3$, which can be expressed as a spatial convolution. From a single-point perspective, this anisotropic/non-local part is unclosed, and we need to express it in terms of local quantities to obtain a closed set of equations for the velocity gradient. Modelling every single realization of the pressure Hessian in terms of the local velocity gradient is probably infeasible. However, in a statistical framework based on a Fokker-Planck equation, the pressure Hessian enters the velocity gradient dynamics in ensembles of fluid particles only through its mean conditional on the gradient itself. The corresponding Langevin equation takes the form [4]

$$d\mathbf{A} = \left(-\tilde{\mathbf{A}}^2 - \langle \tilde{\mathbf{H}}(\mathbf{r}, t) | \mathbf{A} \rangle + \langle \nu \nabla^2 \mathbf{A}(\mathbf{r}, t) | \mathbf{A} \rangle \right) dt + d\mathbf{F}, \quad (2)$$

where the tilde indicates the traceless part and brackets denote the conditional average. The key advantage here is that the conditional averages are by definition tensor functions of the velocity gradient so that tensor function representation theory applies. It allows representing any tensor in terms of other basis tensors derived from a generating tensor [7].

In the following, we specify the independent invariants and basis tensors that can be formed through the velocity gradient. We split \mathbf{A} into strain-rate $\mathbf{S} = (\mathbf{A} + \mathbf{A}^\top)/2$ and rotation-rate $\mathbf{W} = (\mathbf{A} - \mathbf{A}^\top)/2$. The independent invariants that can be constructed through \mathbf{S} and \mathbf{W} read

$$\begin{aligned} x_1 &= \text{Tr}(\mathbf{S}^2), \quad x_2 = -\text{Tr}(\mathbf{W}^2), \quad x_3 = \text{Tr}(\mathbf{S}^3), \\ x_4 &= \text{Tr}(\mathbf{S}\mathbf{W}^2), \quad x_5 = -\text{Tr}(\mathbf{S}^2\mathbf{W}^2). \end{aligned} \tag{3}$$

These invariants determine a sixth invariant only up to a sign [7]. We will not consider the sixth invariant as an independent variable since it cannot vary continuously and independently from the other invariants. Regarding the basis tensors, only five symmetric and traceless basis tensors can be linearly independent in three dimensions. Therefore, given the basis tensors

$$\begin{aligned} \mathbf{B}_1 &= \widetilde{\mathbf{S}}^2, \quad \mathbf{B}_2 = \widetilde{\mathbf{W}}^2, \quad \mathbf{B}_3 = \mathbf{S}\mathbf{W} - \mathbf{W}\mathbf{S}, \\ \mathbf{B}_4 &= \sqrt{x_1 + x_2}\mathbf{S}, \quad \mathbf{B}_5 = \frac{1}{\sqrt{x_1 + x_2}} (\widetilde{\mathbf{S}\mathbf{W}^2} + \widetilde{\mathbf{W}^2\mathbf{S}}), \end{aligned} \tag{4}$$

all the others can be retrieved by means of the Cayley-Hamilton equation. Two additional tensors would be necessary to fix possible degeneracies of the basis [7], which however occur with vanishingly small probability.

A realization of the non-local pressure Hessian at each point and time can be expressed as a linear combination of the basis tensors \mathbf{B}_i defined in (4)

$$\widetilde{\mathbf{H}}(\mathbf{r}, t) = \sum_{i=1}^5 \varphi_i(\mathbf{r}, t) \mathbf{B}_i(\mathbf{A}(\mathbf{r}, t)). \tag{5}$$

This is a local representation of the pressure Hessian, and the coefficients $\varphi_i(\mathbf{r}, t)$ are the components of $\widetilde{\mathbf{H}}(\mathbf{r}, t)$ in the considered basis. On the other hand, the conditional pressure Hessian is an isotropic tensor function of the velocity gradient, so that its components $\bar{\varphi}_i$ are functions only of the invariants x_j defined in (3)

$$(\widetilde{\mathbf{H}}(\mathbf{r}, t) | \mathbf{A}) = \sum_{i=1}^5 \bar{\varphi}_i(x_1(\mathbf{A}), x_2(\mathbf{A}), \dots, x_5(\mathbf{A})) \mathbf{B}_i(\mathbf{A}). \tag{6}$$

Equations (5) and (6) highlight the differences in local modelling strategies and statistical closures for the Hessian: the conditional pressure Hessian is completely deter-

mined by the phase-space variable \mathbf{A} , while the single realization $\tilde{\mathbf{H}}(\mathbf{r}, t)$ encodes additional information through the space-time dependency of its components.

3 Pressure Hessian Components as Functions of the Velocity Gradient Invariants

We aim to retrieve the functional dependency of the conditional pressure Hessian components on the velocity gradient invariants. We do this numerically, using data from a 1024^3 DNS of incompressible, statistically steady and isotropic turbulence, with one-half truncation for de-aliasing to fulfil the constraint $\text{Tr}(\mathbf{H} + \mathbf{A}^2) = 0$ [9]. The Reynolds number based on the Taylor micro-scale is $Re_\lambda \simeq 140$.

The local velocity gradient invariants $x_j(\mathbf{A}(\mathbf{r}, t))$ are random variables representing the local state of the fluid particle. On the other hand, the corresponding pressure Hessian components $\varphi_i(\mathbf{r}, t)$ encode non-local information and represent the random variables we aim to predict based on the known velocity gradient invariants. This interplay between given and unknown random variables is typical in information theory, and we analyze the information that each invariant $x_j(\mathbf{A}(\mathbf{r}, t))$ provides about the corresponding Hessian component $\varphi_i(\mathbf{r}, t)$. The mutual information of two random variables is

$$I(\varphi_i, x_j) = \left\langle \log_2 \frac{f_2(\varphi_i, x_j)}{f_1(\varphi_i) f_1(x_j)} \right\rangle, \quad (7)$$

where f_1 and f_2 indicate single-quantity and joint probability densities, respectively. Figure 1a shows the mutual information between the local velocity gradient invariants x_j and anisotropic pressure Hessian components φ_i . The components $\varphi_i(\mathbf{r}, t)$ are obtained by projecting (5) along $\mathbf{B}_i(\mathbf{A}(\mathbf{r}, t))$ at each point \mathbf{r} and time t . The local enstrophy x_2 provides most of the information about the Hessian components, especially concerning the second component of the Hessian φ_2 . Therefore, we expect to observe a well-defined trend of $\bar{\varphi}_2$ regarded as a function of x_2 .

Based on the mutual information analysis, we approximate the conditional Hessian components $\bar{\varphi}_i$ as functions of only the enstrophy. These components $\bar{\varphi}_i(x_2)$ are shown in Fig. 1b. As expected based on the information analysis, the second component of the conditional Hessian $\bar{\varphi}_2(x_2)$ strongly and smoothly varies with the enstrophy. In particular, it displays a clear trend with the inverse norm of vorticity. Our results indicate that the fit $\bar{\varphi}_2(x_2) \simeq a + b/\sqrt{x_2}$ works very well for various Reynolds numbers and different forcing schemes (not shown). We also notice from Fig. 1a that the relative information between φ_5 and x_2 is also high, but $\bar{\varphi}_5$ is almost constant when regarded as a function of only x_2 . The high relative information is not reflected in the functional trend in this case, the variations of $\bar{\varphi}_5$ are suppressed by conditional averaging on the single invariant x_2 .

It is insightful to further analyze the first two conditional pressure Hessian components as functions of the gradient invariants. Indeed, for a conditional Hessian computed from a Gaussian random field, the first two components, $\bar{\varphi}_1$ and $\bar{\varphi}_2$, are

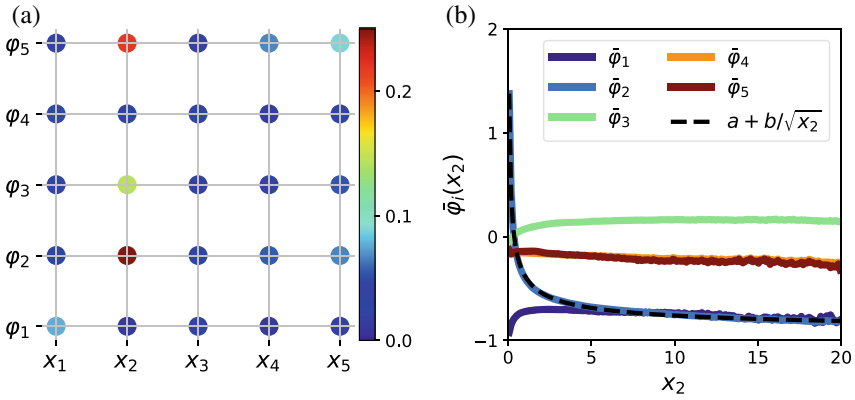


Fig. 1 **a** Mutual information $I(\varphi_i, x_j)$ between the invariant $x_j(\mathbf{A}(\mathbf{r}, t))$ and the pressure Hessian component $\varphi_i(\mathbf{r}, t)$. **b** Conditional pressure Hessian components $\bar{\varphi}_i(x_2)$ as functions of the enstrophy. As expected based on the information analysis, $\bar{\varphi}_2$ displays a prominent trend in terms of x_2 . All quantities are normalized through the Kolmogorov time-scale $\tau_\eta = 1/\sqrt{2\langle x_1 \rangle}$

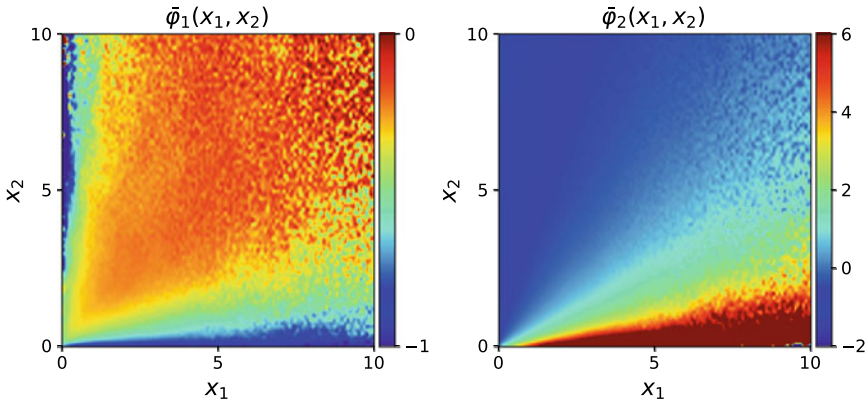


Fig. 2 Conditional pressure Hessian components $\bar{\varphi}_1(x_1, x_2)$ and $\bar{\varphi}_2(x_1, x_2)$ as functions of the strain-rate magnitude x_1 and enstrophy x_2 . The components correspond to basis tensors $\tilde{\mathbf{S}}^2$ and $\tilde{\mathbf{W}}^2$ and quantities are normalized through the Kolmogorov time-scale

constant and do not depend on the spatial correlations of the flow field [4]. Therefore, variations of the first two components highlight the effects of non-Gaussianity of the turbulent velocity field. Figure 2 shows the conditional Hessian components as functions of the strain-rate magnitude and enstrophy, $\bar{\varphi}_1(x_1, x_2)$ and $\bar{\varphi}_2(x_1, x_2)$. The components exhibit a well-defined functional trend with almost straight contour levels. The second component displays the strongest variation, being positive at small enstrophy and then becoming negative at large enstrophy. This trend is consistent with what we observed for the quantity $\bar{\varphi}_2$ regarded as a function of only x_2 . However, the results also unveil the dependency of the conditional Hessian components on the

strain-rate magnitude x_1 . Remarkably, this dependency averages out when the $\bar{\varphi}_i$ are regarded as functions of the single invariant x_1 (not shown).

These observations can be useful to further improve stochastic models for the velocity gradient dynamics. For example, a recent model for the velocity gradient dynamics [8] assumed constant conditional Hessian components in a basis consisting of powers of the velocity gradient. The model leaves room for improvement in strain-dominated regions, and our results reveal the reason for this. At small enstrophy, most of the pressure Hessian components undergo sharp variations. The sign of $\bar{\varphi}_2$ even flips between strain- and vorticity-dominated configurations (cf. Figs. 1b, 2b), leading to qualitatively different dynamical behaviours of the conditional Hessian along \widetilde{W}^2 .

4 Concluding Remarks

We characterized the conditional pressure Hessian components as functions of the velocity gradient invariants in a basis consisting of powers of the velocity gradients. When focusing on individual invariants, a mutual information analysis shows that the enstrophy encodes most of the information on the Hessian components. In particular, the component along the squared rotation-rate varies as the inverse of the square root of enstrophy. The sharpest variations of the conditional Hessian components occur in strain-dominated regions where current models for the velocity gradient are not accurate. Therefore, this work constitutes the first step towards improving such models through analysis of DNS data. Also, the systematic interpretation of the DNS results, together with mutual information analyses, can be effectively employed to improve machine learning approaches to the velocity gradient dynamics in turbulence.

References

1. C. Meneveau, Lagrangian dynamics and models of the velocity gradient tensor in turbulent flows. *Annu. Rev. Fluid Mech.* **43**(1), 219–245 (2011)
2. P. Vieillefosse, Local interaction between vorticity and shear in a perfect incompressible fluid. *J. Phys. Fr.* **43**(6), 837–842 (1982)
3. L. Chevillard, C. Meneveau, Lagrangian dynamics and statistical geometric structure of turbulence. *Phys. Rev. Lett.* **97**, 174501 (2006)
4. M. Wilczek, C. Meneveau, Pressure Hessian and viscous contributions to velocity gradient statistics based on Gaussian random fields. *J. Fluid Mech.* **756**, 191–225 (2014)
5. P.L. Johnson, C. Meneveau, A closure for Lagrangian velocity gradient evolution in turbulence using recent-deformation mapping of initially Gaussian fields. *J. Fluid Mech.* **804**, 387–419 (2016)
6. N. Parashar, B. Srinivasan, S.S. Sinha, Modeling the pressure-Hessian tensor using deep neural networks. *Phys. Rev. Fluids* **5**, 114604 (2020)
7. R.S. Rivlin, J.L. Ericksen, Stress-deformation relations for isotropic materials. *Arch. Ration. Mech. Anal.* **4**, 323–425 (1955)

8. L.A. Leppin, M. Wilczek, Capturing velocity gradients and particle rotation rates in turbulence. *Phys. Rev. Lett.* **125**, 224501 (2020)
9. J. Tom, M. Carbone, A.D. Bragg, Exploring the turbulent velocity gradients at different scales from the perspective of the strain-rate eigenframe. *J. Fluid Mech.* **910**, A24 (2021)

Stretched Amplitude Decaying Fourier Modes in the Jet Far-Field



Azur Hodžić, K. E. Meyer, W. K. George, and Clara M. Velte

Abstract A framework is presented for decomposing the self-similar region of the round jet along the streamwise direction using an analytical series expansion deduced from the four dimensional (space-time) Proper Orthogonal Decomposition (POD) integral. A specific inner product weight function is introduced in order to deduce the Stretched Amplitude Decaying Fourier Modes. The inner product weight function, maps the POD kernel into a displacement invariant kernel. The SADFM are demonstrated to be orthogonal with respect to the weighted inner product and therefore constituting a basis for the weighted Hilbert space, $L_w^2(\Omega, \mathbb{C}^3)$, over the domain $\Omega \subset \mathbb{R}^4$. The SADFM allow for an Fast Fourier Transform (FFT) algorithm to be used along the streamwise inhomogeneous direction reducing the computational workload for the four-dimensional POD of the jet far-field. Applying a Galerkin projection to the governing equations using the SADFM provides additional insight into the far-field dynamics.

1 Introduction

The common polynomial expansions combined with the Proper Orthogonal Decomposition (POD) are the regular trigonometric polynomials, which have aptly been applied along coordinate direction for which the flow is periodic, homogeneous, or statistically stationary, see e.g. [1–4]. The Fourier-based POD methods in general

A. Hodžić (✉) · K. E. Meyer · C. M. Velte
Department of Mechanical Engineering, Technical University of Denmark,
2800, Kgs. Lyngby, Denmark
e-mail: azuhod@mek.dtu.dk

K. E. Meyer
e-mail: kem@mek.dtu.dk

C. M. Velte
e-mail: cmve@dtu.dk

W. K. George
Department of Aeronautics, Imperial College London, London SW7 2AZ, UK

allow for the implementation of efficient decomposition algorithms for the decomposition of turbulent flows with reduced memory demands, [5]. The latter is due to the fact that Fourier-based decompositions imply that the eigenvalue problem at hand can be solved separately for each wavenumber/frequency, thereby breaking up a large matrix-eigenvalue problem into a number of smaller ones.

Similarity solutions to statistical moments in turbulent flows have been investigated in e.g. [6–8], and are a manifestation of statistical symmetries that certain turbulent flows may exhibit. One such flow is the far-field region of the turbulent round jet, which is self-similar in the streamwise direction. The present work (based on [9–11]) builds on the previous work of [7, 12] and aims to extend to statistically-inhomogeneous directions the set of polynomials that may be combined with the POD for the analysis of the jet. In the current work we present the framework for decomposing the far-field region of the turbulent round jet using Stretched Amplitude Decaying Fourier Modes (SADFM) by introducing an inner product weight (window) function that maps the POD kernel into a displacement invariant kernel, characterized by its exclusive dependence on the coordinate *difference* along the streamwise direction. From here one can argue that the solution to the POD integral in the streamwise direction consists of Fourier modes, analogous to the case of homogeneous turbulence.

2 Proper Orthogonal Decomposition

The formulations from this point on are specific for the self-similar region of the jet far-field. Let the fluctuating velocity field of the turbulent jet far-field be represented by vector-valued functions, $v \in L_w^2$, where the vector space is defined as

$$L_w^2(\Omega, \mathbb{C}^3) := \left\{ \varphi : \Omega \mapsto \mathbb{C}^3 \left| \int_{\Omega} |\varphi(x)|^2 w(x) dx < \infty \right. \right\}, \quad w(x) > 0, \quad (1)$$

where $w : \Omega \mapsto \mathbb{R}_{>0}$ is a weight function, and the spatio-temporal domain is defined by $\Omega \subset \mathbb{R}^4$. Equipping (1) with the inner product

$$(\varphi, \psi)_w = \int_{\Omega} \varphi(x) \psi^*(x) w(x) dx, \quad \psi \in L_w^2(\Omega, \mathbb{C}^3), \quad (2)$$

where the asterisk denotes complex conjugation, and the norm

$$\|\varphi\|_w = \sqrt{(\varphi, \varphi)_w}, \quad (3)$$

makes the vector space in (1) a Hilbert space. The POD is then given by the following integral eigenvalue problem

$$\int_{\Omega} R(x, x') \varphi(x') w(x') dx' = \lambda \varphi(x), \tag{4}$$

where the two-point correlation function $R(x, x')$ is given by

$$R(x, x') = \langle v(x) \otimes v(x') \rangle. \tag{5}$$

Here the angle braces denote ensemble averaging, $v \in L_w^2(\Omega, \mathbb{C}^3)$ represent the fluctuating part of the turbulent velocity field, and \otimes is the tensor product over the velocity components of $v(x)$ and $v(x')$.

2.1 SADFM

Introducing a radially-stretched spherical coordinate system (ξ, θ, ϕ) , defined wrt. Cartesian coordinates as follows

$$x(\xi, \theta, \phi) = C e^{\xi} \cos \theta + x_0, \tag{6}$$

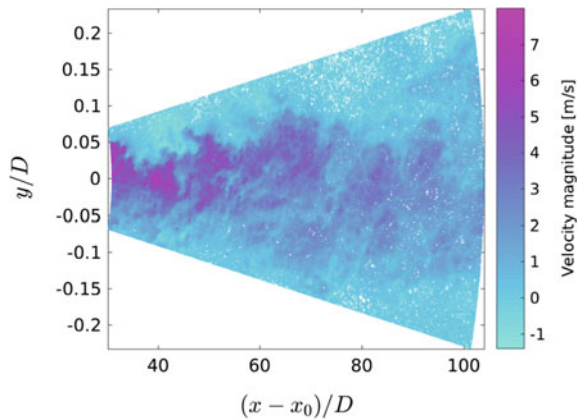
$$y(\xi, \theta, \phi) = C e^{\xi} \sin \theta \cos \phi, \tag{7}$$

$$z(\xi, \theta, \phi) = C e^{\xi} \sin \theta \sin \phi, \tag{8}$$

where $x = y = z = 0$ denotes the center of the nozzle at the lip, and the line $y = z = 0$ denotes the jet centerline. ξ is the logarithmically stretched streamwise coordinate and $C = x_s - x_0$, is a constant where x_s is the start of the self-similar and x_0 is the virtual origin.

One realization of the velocity magnitude in this region of the jet is shown in Fig. 1 sampled with two-component Particle Image Velocimetry, [10].

Fig. 1 Velocity magnitude of the jet in the fully developed self-similar region, where x_0 is the virtual origin and D is the nozzle diameter. The overall velocity is shown to decay downstream



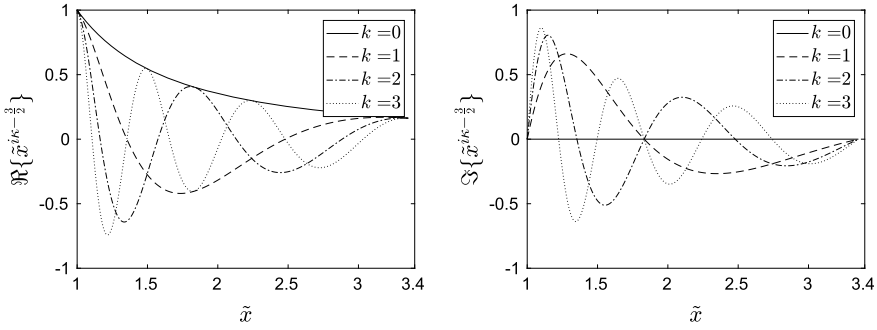


Fig. 2 Real- and imaginary parts of the streamwise part of the POD modes, $f(\xi)$, in the jet far-field for the choice of weight $w = ((e^{L_\xi} - 1)/L_\xi)e^{-\xi}$. The wavenumber, κ , is defined in terms of k by $\kappa = 2\pi k/L_\xi$, where L_ξ is the spatial domain length

In order to express (4) in this system the Jacobian is needed, which evaluates to $|J| = C^3 e^{3\xi} \sin \theta$. Choosing the weight to be $w(\xi) = ((e^{L_\xi} - 1)/L_\xi)e^{-\xi}$ and exploiting that the kernel in this case is displacement invariant in ξ yields that the modes in the streamwise direction are given by

$$f_\kappa(\xi) = \tilde{x}^{i\kappa - \frac{3}{2}} = e^{i\kappa\xi - \frac{3}{2}\xi}, \quad (9)$$

where $\tilde{x} = (x - x_0)/C$. We note that $(e^{L_\xi} - 1)/L_\xi$ is a constant included in the definition of the window function to ensure that the turbulence kinetic energy of the field in Ω equals the case where $w = 1$. The scaling of the window function by $((e^{L_\xi} - 1)/L_\xi)$ corresponds to the normalization factors used on windows/filters for the reduction of spectral leakage. The real- and imaginary parts are shown in Fig. 2 for $k = 0, 1, 2, 3$ where $\kappa = 2\pi k/L_\xi$ where L_ξ is the length of the domain in the streamwise direction.

3 Results and Discussion

A Galerkin projection of the production term of the turbulence kinetic energy (TKE) transport equation is then performed using the SADFM in combination with the numerical θ -component of the POD modes. Normalizing by the product of the fluid density and the eigenvalues, $\rho\lambda$, one obtains the energy normalized production spectra, $\mathcal{P}_{\rho\lambda}$, [11], as a function of the wavenumber κ and POD mode number α . Figure 3 shows the absolute value of $\mathcal{P}_{\rho\lambda}$, revealing the relative production-to-energy rate of the modes as a function of κ and α . The relative production rate appears localized in the spectral domain, characterized by the high values in Fig. 3. The SADFM projection coefficients for the streamwise and spanwise fluctuating velocity components are defined as $c^\xi(\kappa, \theta) = \frac{1}{\sqrt{2\pi}} \int_0^{L_\xi} v^\xi f_\kappa^*(\xi) d\xi$ and $c^\theta(\kappa, \theta) = \frac{1}{\sqrt{2\pi}} \int_0^{L_\xi} v^\theta f_\kappa^*(\xi) d\xi$,

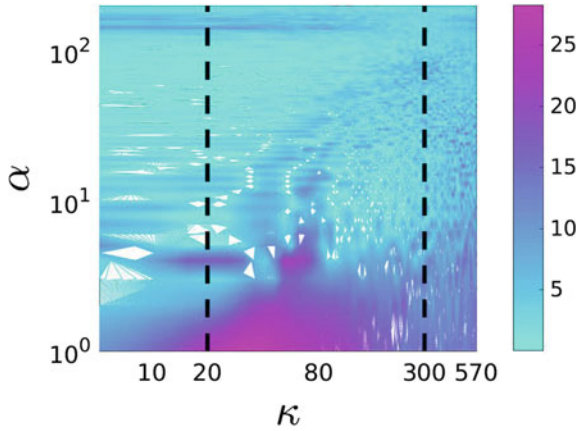


Fig. 3 Absolute value of the Galerkin projection of the energy normalized production term integrated over the domain, $\mathcal{P}_{\rho\lambda}$, obtained from the TKE transport equation shown as a function of wavenumber, κ , related to the streamwise SADFM decomposition as well as the POD mode number α . $\mathcal{P}_{\rho\lambda}$ shows significant levels even in the $-5/3$ -region identified for $20 < \kappa < 300$

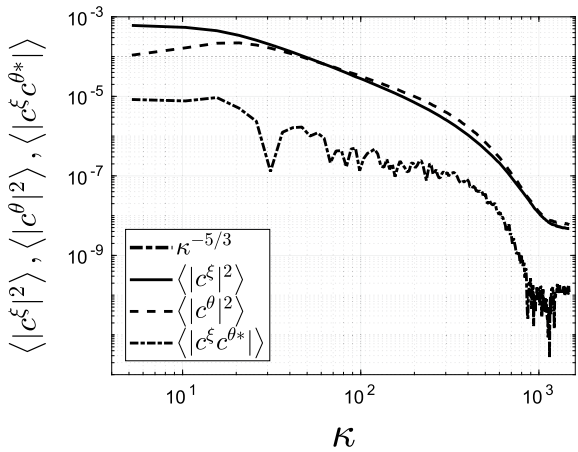


Fig. 4 Spatial SADFM energy spectra along the centerline of the jet shows the $-5/3$ -region for $20 < \kappa < 300$. Here $\langle |c^\xi|^2 \rangle$ and $\langle |c^\theta|^2 \rangle$ represent the component energy spectra for the ξ - and θ -components, respectively, and $\langle |c^\xi c^{\theta*}| \rangle$ is the cross spectrum

respectively, from which energy spectra may be obtained (Fig.4). Combined with Fig.3 these reveal that $\mathcal{P}_{\rho\lambda}$ shows significant values even in the $-5/3$ -region identified for $\kappa \in [20 : 300]$. This shows that even the modes related to the $-5/3$ -region of the spectrum are able to produce significant levels of their energy content. This sort of behavior was hypothesized by [12].

4 Summary

The present study proposes that the streamwise part of the POD modes in the self-similar far-field region of the steady turbulent round jet can be represented by Stretched Amplitude Decaying Fourier Modes (SADFM) by introducing a streamwise decaying inner product weight function, $w = ((e^{L\xi} - 1)/L\xi)e^{-\xi}$. The latter allows for a FFT-based POD of the far-field region of the jet along the streamwise direction. The inner product definition ensures that the resulting POD modes are orthogonal and may be used to span the $L_w^2(\Omega, \mathbb{C}^3)$ vector space. The introduction of the weight function inevitably redistributes the energy across the eigenvalues, thereby reducing the convergence rate of the eigenspectrum relative to a choice of weight $w = 1$. Nevertheless, the use of the weight function has the advantage of reducing the computational resources needed for the decomposition by making use of the efficient FFT-algorithm.

Acknowledgements Financial support from the Poul Due Jensen Foundation (Grundfos Foundation) for this research is gratefully acknowledged.

References

1. J.H. Citriniti, W.K. George, Reconstruction of the global velocity field in the axisymmetric mixing layer utilizing the proper orthogonal decomposition. *J. Fluid Mech.* **418**, 137–166 (2000)
2. S. Gamard, D. Jung, W.K. George. Downstream evolution of the most energetic modes in a turbulent axisymmetric jet at high Reynolds number. Part 2. The far-field region. *J. Fluid Mech.* **514**, 205–230 (2004)
3. J.L. Lumley, The structure of inhomogeneous turbulent flows, in *Atmospheric Turbulence and Radio Wave Propagation* (Nauka, Moscow, 1967), pp. 166–178
4. O.T. Schmidt, A. Towne, G. Rigas, T. Colonius, G.A. Brès, Spectral analysis of jet turbulence. *J. Fluid Mech.* **855**, 953–982 (2018)
5. Oliver T. Schmidt, Aaron Towne, An efficient streaming algorithm for spectral proper orthogonal decomposition. *Comput. Phys. Commun.* **237**, 98–109 (2019)
6. W.K. George, The self-preservation of turbulent flows and its relation to initial conditions and coherent structures, in *Advances in Turbulence* (1989), p. 3973
7. D. Ewing, B. Frohnäpfel, W.K. George, J.M. Pedersen, J. Westerweel, Two-point similarity in the round jet. *J. Fluid Mech.* **577**, 309–330 (2007)
8. Martin Oberlack, A unified approach for symmetries in plane parallel turbulent shear flows. *J. Fluid Mech* **427**, 299–328 (2001)
9. A. Hodžić. A tensor calculus formulation of the Lumley decomposition applied to the Turbulent Axi-symmetric Jet Far-field (2018)
10. A. Hodžić, K.E. Meyer, C.M. Velte, W.K. George, Lumley decomposition of the Turbulent round jet far-field. Part 1 - kinematics (2019) [arXiv:1908.05134](https://arxiv.org/abs/1908.05134)
11. A. Hodžić, K.E. Meyer, W.K. George, C.M. Velte, Lumley decomposition of the Turbulent round jet far-field. Part 2 - Dynamics (2019), [arXiv:1909.01307](https://arxiv.org/abs/1909.01307)
12. M. Wänström, Spatial decompositions of a fully-developed turbulent round jet sampled with particle image velocimetry. Ph.D. thesis, Chalmers University of Technology (2009)

Generalizable Theory of Reynolds Stress



T.-W. Lee

Abstract We generalize the Lagrangian transport theory to include the normal and shear Reynolds stresses, so that a complete tensor can be constructed. The ideology is based on imposition of the momentum and energy balance to a control volume moving at the local mean velocity, which bears the effect of de-coupling the mean from the fluctuation components. The resulting transport equations are verified, with available DNS data. Representation of the fluxes in this form leads to the dissipation scaling, which collapses the u'^2 , v'^2 and $u'v'$ gradient profiles for all Reynolds numbers. Addition of the energy spectra, derivable from the maximum entropy principle, completes the Reynolds stress theory, to fully prescribe the turbulence structures in canonical geometries.

1 Introduction

In prior works [1–4], we have set forth a set of Galilean-transformed transport equations to produce explicit inter-dynamical relations for u'^2 , v'^2 and $u'v'$. This formalism is based on momentum ((1) and (2)) and energy balances ((3)), wherein the fluctuation velocities represent flux vectors. The derivations and validations can be found in [1–4].

u' momentum transport:

$$\frac{d(u'v')}{dy} = -C_{11}U \frac{d(u'^2)}{dy} + C_{12}U \frac{d(v'^2)}{dy} + C_{13} \frac{d^2 u'_{\text{rms}}}{dy^2} \quad (1)$$

T.-W. Lee (✉)
Arizona State University, Tempe, AZ, USA
e-mail: attwl@asu.edu

v' momentum transport:

$$\frac{d(v'^2)}{dy} = -C_{21}U \frac{d(u'v')}{dy} + C_{22}U \frac{d(v'^2)}{dy} + C_{23} \frac{d^2 v'_{\text{rms}}}{dy^2} \quad (2)$$

u'^2 transport:

$$\frac{d(u'^3)}{dy} = -C_{31} \frac{1}{U} \frac{d(u'v' \cdot u')}{dy} + C_{32} \frac{1}{U} \frac{d(v' \cdot u'v')}{dy} + C_{33} \frac{1}{U} \left(\frac{du'_{\text{rms}}}{dy} \right)^2 \quad (3)$$

In this work, we complete the theoretical formulation through analysis of the scaling in the “dissipation” space, i.e. at the first- and second-gradient levels, and by adding the spectral function for the turbulence kinetic energy, derivable from the maximum entropy principle [5, 6].

2 Dissipation Scaling

We have shown in recent works that gradient structures in wall-bounded flows are self-similar [7]. This “dissipation” scaling emerges if we examine the first gradients of the u'^2 profiles for channel flows in Fig. 1, where an intrinsic order is observed. The DNS data in Fig. 1 and subsequent figures are from [8–10]. All the previous scaling efforts have attempted to find some relationships at the surface level, which did have some utility, e.g. invariant peak location at $y^+ \sim 15$ [11]. However, ordered structures are found at the first- (u'^2) and second-gradient (v'^2 , $u'v'$) levels [7], which facilitate the collapse of the gradient structures, as illustrated in Figs. 2, 3 and 4. After normalizing by local extrema (initial peak height or magnitude of the second nadir), $\frac{du'^2}{dy^+}$, $\frac{d^2 v'^2}{dy^{+2}}$, and $\frac{d^2 u'v'}{dy^{+2}}$ profiles collapse onto single respective curves, as shown in Figs. 2, 3 and 4. Similar to the abbreviated notations in (1)–(3), here u'^2 represents $\frac{\langle u'^2 \rangle}{u_\tau^2}$, etc; fluctuation velocities are Reynolds-averaged and normalized by the friction velocity squared. The secondary peaks (-/+) have also been ratioed relative to the first (+/-), so that the same peak-to-peak amplitudes are retained in the profiles. There are some deviatoric data points near the wall, possibly due to insufficient numerical resolution, and also in the far field caused by the subtle differences in the outer boundary conditions. Nonetheless, the unification of the profiles is nearly complete, at least at these Reynolds numbers, and applies across wall-bounded geometries: channel (CF) and boundary-layer flow over a flat plate (FP). The scaling factors simply are functions of the Reynolds number, but asymmetrical [7]. It is interesting to note that u'^2 -structure scales at the first-gradient level, while v'^2 and $u'v'$ do so at the second. The fact that (1) and (2) are momentum-conserving, while (3) is an expression of the energy balance, may have some bearing on this: momentum

Fig. 1 Scalability of the u'^2 profiles at the first gradient level. Self-similarity is observable with asymmetrical monotonicity. DNS data are from [8, 9]

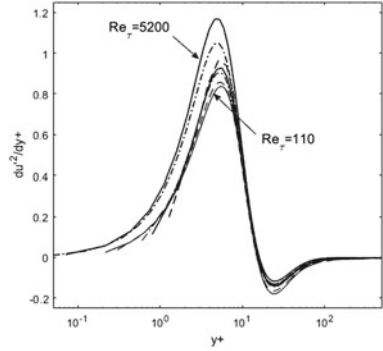


Fig. 2 The above scaling leads to a unitary, collapsed profile for asymmetrically normalized $\frac{du'^2}{dy+}$

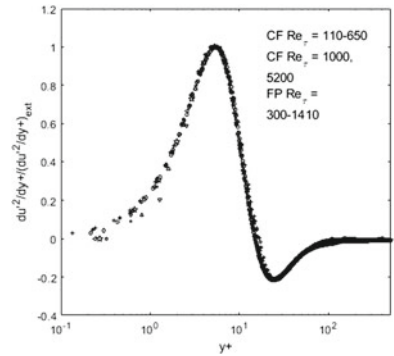
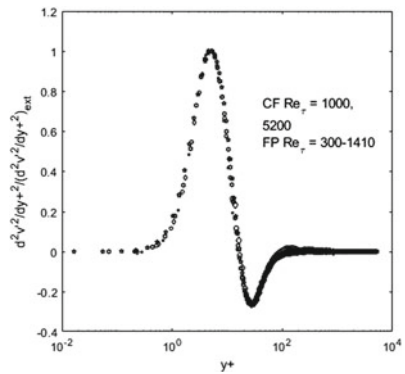
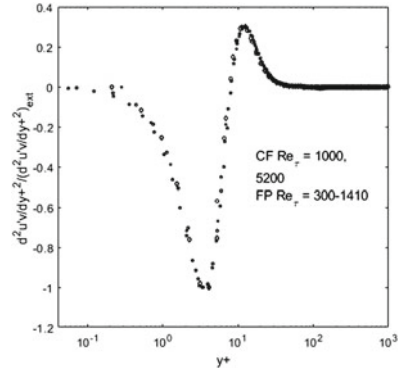


Fig. 3 Similar scaling holds for v'^2 , except at the second-gradient level



diffuses proportionately to the second-gradient, whereas energy dissipation has a linear dependence on the first-derivative squared. For the free jet flows, r/x or y/x scaling already accomplishes the same effect [12].

Fig. 4 The Reynolds shear stress also collapses onto a single profile, for the second gradients



3 Turbulence Flux Dynamics

We can examine the transport dynamics in this context, starting from $\frac{du'^3}{dy^+}$ ((3)) and $\frac{dv'^2}{dy^+}$ ((2)). Both of these fluxes are important contributors to the Reynolds shear stress in (1), and scripting these two root variables would suffice in full reconstruction of $u'v'$, de-necessitating any turbulence models. Equation (3) shows that $u'v'$ and v'^2 in turn re-combine to prescribe the kinetic energy flux gradient, $\frac{du'^3}{dy^+}$, forming a triad of energy terms to produce the observed turbulence structure. Here, we take the Lagrangian interpretation of u'^3 as $(u'^2)^{3/2}$, just as u'_{rms} is set equal to $(u'^2)^{1/2}$ in (1), so that u'^2 profiles can be obtained directly from integration of $\frac{du'^3}{dy^+}$. We can see in Fig. 5 that the agreement between the current theory (3) and DNS data [9] is quite good, until we reach the “far-field”, $y^+ > 30$. The main composition of the kinetic energy flux are the lateral transport (C_{31} term) and the pressure work (C_{32}). The viscous dissipation (C_{33}) term is quite small at this Reynolds number ($Re_\tau = 1000$), and its omission does not subtract from the current accuracy. Thus, a succinct visualization emerges wherein the streamwise flux of kinetic energy, $\frac{du'^3}{dy^+}$, is balanced by the cross-stream transport (C_{31}) and expended through pressure work (C_{32}) and viscous dissipation ($\ll 1$).

It is a simple matter to numerically integrate and see that this gradient structure will result in a sharp peak near the wall, followed by an increasingly abrupt bend toward gradual decline to the centerline boundary condition [7, 13]. For $\frac{dv'^2}{dy^+}$, the set of flux terms in (2) prescribe the composition of the v' -momentum content also accurately (Fig. 6).

We have already shown the flux balances for the Reynolds shear stress in previous works [1–4]. As described therein, by substituting u'^2 and v'^2 -gradients in (1), $\frac{du'v'}{dy}$ is directly computed, which upon integrations and insertion in the Reynolds-averaged Navier-Stokes equation results in the mean velocity profile [3, 4]. For jet flows, the situation is made yet simpler due to absence of the pressure terms in ((1)–(3)), and solutions scaled by y/x are iteratively achieved [1]. The above flux balances occur through the transport equations of (1)–(3). The dynamical processes can also

Fig. 5 $\frac{du'^3}{dy^+}$ profile as prescribed by the terms in (3). In (3), C_{32} term represents the pressure work

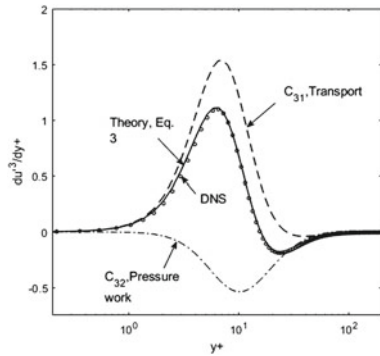
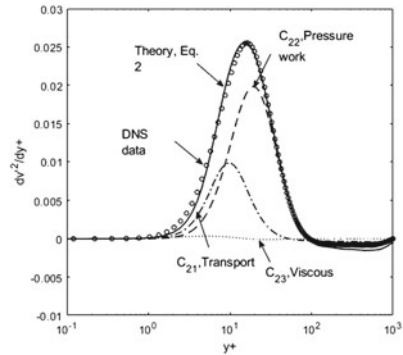


Fig. 6 $\frac{dv'^2}{dy^+}$ profile as prescribed by the terms in (2)

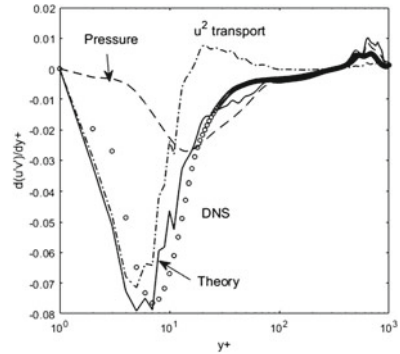


be intuitively visualized by conjuring an observer on a vessel (the control volume), which is moving at the local mean velocity. If the observer opens the windows, no effects of the mean flow velocity can be felt due to the zero relative motion. However, the fluctuation momentum must still be balanced: streamwise u'^2 -flux must be offset by the lateral flux ($u'v'$) plus the forces (pressure and viscous). Algebraically, these flux balances lead to ((1)–(3)), which prescribe the turbulence transport processes quite accurately and logically, as shown above. Figure 7 demonstrates the efficacy of the transport equations in another geometry: adverse pressure-gradient flow (DNS data are from [14]). Therefore, the flux dynamics of ((1)–(3)) are generalizable due to its applicability for each of the Reynolds stress components, and across different flow geometries.

4 Energy Spectra

Finally, the final component for a full description of turbulent flows is the energy distribution or spectra. Since u'^2 and v'^2 also represent the mean turbulence kinetic energy, enumeration of their spectral contents will complete the statistical prescrip-

Fig. 7 The applicability of the current theory is extended to more complex flows: boundary layer flow over a flat plate in adverse pressure gradient. DNS data are from [14]



tion. In this regard, we drew upon yet another fundamental principle of the Second Law, in the corollary form of the maximum entropy method [5, 6], which derives the full spectral function, parameterizable with the root turbulence variables, as shown below [5, 6].

$$E(k) = \frac{C_1}{k^4} \exp \{-C_2 u'^2 - C_3 k^2 u'^2\} \quad (4)$$

This spectral function, along with the kinematic scaling for $u' \sim m \log(k)$, is found to be applicable in two-, three-dimensional homogeneous turbulence, and in channel flows [5, 6], reproducing the full observed energy distributions continuously from the energy-containing, inertial to the viscous dissipation range. Further confirmation would be useful in other turbulence geometries, but the above set of findings constitute a foundation for theoretical analysis of canonical turbulence.

5 Summary

Resolution of the turbulence structure has been a long-standing, “millennial” problem in fluid physics. In this work, a formalism is demonstrated to encapsulate and predict the main features of turbulent flows in canonical geometries, including the energy spectra.

References

1. T.-W. Lee, Lagrangian transport equations and an iterative solution method for turbulent jet flows. *Phys. D* **403**, 132333 (2020)
2. T.-W. Lee, The Reynolds stress in turbulence from a Lagrangian perspective. *J. Phys. Commun.* **2**(5), 055027 (2018)
3. T.-W. Lee, J. Park, Integral formula for determination of the Reynolds stress in canonical flow geometries, in *Progress in Turbulence VII.*, vol. 196, eds. by R. Örlü, A. Talamelli, M. Oberlack, J. Peinke (Springer, Cham, 2017), pp. 147–152; Springer Proceedings Phys

4. T.-W. Lee, Origin of turbulence in wall-bounded turbulent flows, from a Lagrangian perspective. Submitted to a fluid journal. An alternate version is viewable and citable as, [arXiv:2006.01634](https://arxiv.org/abs/2006.01634) (2021)
5. T.-W. Lee, Lognormality in turbulence energy spectra. *Entropy* **22**(6), 669 (2020)
6. T.-W. Lee, Scaling of the maximum-entropy turbulence energy spectra. *Eur. J. Mech. B Fluids* **87**, 128–134 (2021a)
7. T.-W. Lee, Asymmetrical order in wall-bounded turbulent flows. Submitted to a physics journal. An alternate version is viewable and citable as, [arXiv:2006.01634](https://arxiv.org/abs/2006.01634) (2021)
8. K. Iwamoto, Y. Suzuki, N. Kasagi, Reynolds number effect on wall turbulence: toward effective feedback control. *Int. J. Heat Fluid Flow* **23**(5), 678–689 (2002)
9. J. Graham, K. Kanov, X.I.A. Yang, M. Lee, N. Malaya, C.C. Lalescu, R. Burns, G. Eyink, A. Szalay, R.D. Moser, C. Meneveau, A web services accessible database of turbulent channel flow and its use for testing a new integral wall model for LES. *J. Turbul.* **17**(2), 181–215 (2016)
10. P.R. Spalart, Direct simulation of a turbulent boundary layer up to $Re_\theta = 1410$. *J. Fluid Mech.* **187**, 61–98 (1988)
11. G.I. Barenblatt, A.J. Chorin, V.M. Prostokishin, Scaling laws for fully developed turbulent flow in pipes. *Appl. Mech. Rev.* **50**(7), 413–429 (1997)
12. E. Gutmark, I. Wygnanski, The planar turbulent jet. *J. Fluid Mech.* **73**(3), 465–495 (1976)
13. I. Marusic, B.J. McKeon, P.A. Monkewitz, H.M. Nagib, A.J. Smits, K.R. Sreenivasan, Wall-bounded turbulent flows at high Reynolds numbers: recent advances and key issues. *Phys. Fluids* **22**(6), 065103 (2010)
14. V. Kitsios, C. Atkinson, J. Sillero, G. Borrell, A. Gungor, J. Jiménez, J. Soria, Direct numerical simulation of a self-similar adverse pressure gradient turbulent boundary layer. *Int. J. Heat Fluid Flow* **61**, 129–136 (2016)

Spectral Energetics of a Quasilinear Approximation in Uniform Shear Turbulence



Carlos G. Hernández and Yongyun Hwang

Abstract The spectral energetics of a quasilinear (QL) model is studied in uniform shear turbulence. For the QL approximation, the velocity is decomposed into a mean averaged in the streamwise direction and the remaining fluctuation. The equations for the mean are fully considered, while the equations for the fluctuation are linearised around the mean. The QL model exhibits an energy cascade in the spanwise direction, but this is mediated by highly anisotropic small-scale motions unlike that in direct numerical simulation mediated by isotropic motions. In the streamwise direction, the energy cascade is shown to be completely inhibited in the QL model, resulting in highly elevated spectral energy intensity residing only at the streamwise integral length scales. Finally, the QL model is shown to generate anisotropic turbulence throughout the entire wavenumber space and inhibit the nonlinear regeneration of streamwise vortices in the self-sustaining process.

1 Introduction

In wall-bounded turbulent shear flows, linear instability does not arise from the mean velocity. In this type of flows, the evolution of disturbance has been studied by examining the response of the linearised Navier–Stokes equations to various excitation mechanisms [11, 12], such as initial condition (transient growth) [4, 16] and deterministic/stochastic forcing (analysis of resolvent and gramian) [1, 7].

The earliest work utilising the quasilinear (QL) framework can be found in [8], which ignored the self-interactions in the second group with the ‘marginal stability’ for the closure of the quasilinear system. The modern approaches share similar ideas with these early ones, but they take more flexible and delicate approaches for modelling of the self-interaction term of the second group (e.g. stochastic forcing,

C. G. Hernández (✉) · Y. Hwang
Department of Aeronautics, Imperial College London, South Kensington,
London SW7 2AZ, UK
e-mail: cg1116@ic.ac.uk

Y. Hwang
e-mail: y.hwang@imperial.ac.uk

eddy viscosity, etc.). Of particular interest here is the type of RNL (Restricted Non-linear) model without any parametric stochastic excitation. This type of quasilinear model was recently applied to parallel wall-bounded shear flows [5, 10, 13–15], in which the key dynamics of coherent structures has been understood in terms of the so-called ‘self-sustaining process’ [6, 17]. An important feature of this type of model is that it typically activates only a handful number of streamwise Fourier modes for self-sustaining velocity fluctuations [5, 13, 15]. A judicious choice of the active streamwise Fourier modes appears to reproduce sound first-order turbulence statistics [3].

The present study aims to explore spectral energy transfer of the aforementioned QL model in order to gain the fundamental understanding of its precise modelling capability. Here we consider uniform shear turbulence where only single integral length scale is retained by prescribing the size of computational domain.

2 Problem Formulation

We consider a turbulent flow under a uniform mean shear. The flow field is decomposed into a streamwise mean and the remaining fluctuation, the former of which is solved by considering the full nonlinear equations whereas the latter is obtained from the linearised equations around the former: $\mathbf{u} = \mathbf{U}_m + \mathbf{u}_r$, with $\mathbf{U}_m = \langle \mathbf{u} \rangle_x$, where $\langle \cdot \rangle_x$ indicates the streamwise average. Following [10], we introduce two linear projection operators defined as $\mathcal{P}_m[\mathbf{u}] \equiv \langle \mathbf{u} \rangle_x = \mathbf{U}_m$, $\mathcal{P}_r[\mathbf{u}] \equiv \mathbf{u} - \langle \mathbf{u} \rangle_x = \mathbf{u}_r$. The Navier–Stokes equations are first projected onto the \mathcal{P}_m and \mathcal{P}_r subspaces. The subsequent linearisation of the equations for \mathbf{u}_r about \mathbf{U}_m leads to the QL system:

$$\frac{\partial \mathbf{U}_m}{\partial t} + (\mathbf{U}_m \cdot \nabla_{yz}) \mathbf{U}_m = -\frac{1}{\rho} \nabla_{yz} \mathbf{P}_m + \nu \nabla_{yz}^2 \mathbf{U}_m - \mathcal{P}_m[(\mathbf{u}_r \cdot \nabla) \mathbf{u}_r] \quad (1a)$$

$$\frac{\partial \mathbf{u}_r}{\partial t} + (\mathbf{U}_m \cdot \nabla) \mathbf{u}_r + (\mathbf{u}_r \cdot \nabla) \mathbf{U}_m = -\frac{1}{\rho} \nabla \mathbf{p}_r + \nu \nabla^2 \mathbf{u}_r, \quad (1b)$$

where P_m and p_r are defined to enforce $\nabla_{yz} \cdot \mathbf{U}_m = \mathbf{0}$ and $\nabla \cdot \mathbf{u}_r = \mathbf{0}$, respectively, with $p = P_m + p_r$. The self-interaction term $\mathcal{P}_r[(\mathbf{u}_r \cdot \nabla) \mathbf{u}_r]$ in (1b) will be ignored. The TKE equation is considered in the streamwise/spanwise Fourier space:

$$\underbrace{\left\langle \left\{ -\widehat{u}'_i(k) \widehat{v}'(k) \frac{dU}{dy} \right\} \right\rangle_{r^\perp, y, t}}_{\widehat{P}(k)} + \underbrace{\left\langle \left\{ -\nu \frac{\partial \widehat{u}'_i(k)}{\partial x_j} \frac{\partial \widehat{u}'_i(k)}{\partial x_j} \right\} \right\rangle_{r^\perp, y, t}}_{\widehat{\varepsilon}(k)} + \underbrace{\left\langle \left\{ -\widehat{u}'_i(k) \left(\frac{\partial}{\partial x_j} \left(\widehat{u}'_i u'_j(k) - \mathcal{P}_r \left[\widehat{u}'_{r,i} \widehat{u}'_{r,j}(k) \right] \right) \right) \right\} \right\rangle_{r^\perp, y, t}}_{\widehat{T}(k)} = 0, \quad (2)$$

Table 1 L_x^* , L_y^* and L_z^* indicate the domain size in the x -, y - and z directions in the Kolmogorov unit, respectively. Here, $Re = U_0 L_y / (2\nu)$, $Re_{\tau, Lz} = L_z^*$ and Re_λ is the Reynolds number based on Taylor microscale. The grid spacings in the x - and z -directions are Δ_x^* and Δ_z^* (after aliasing). $N_{x,F}$ indicates the number of the positive-wavenumber streamwise Fourier modes

Case	Re	$Re_{\tau, Lz}$	Re_λ	L_x^*	L_z^*	Δ_x^*	Δ_z^*	$N_{x,F}$	$N_y \times N_z$	δ_y^*
H-DNS	25000	514	63	1542	1714	14.3	5.7	54	497×108	257
H-QL-FULL	25000	617	108	1852	2056	17.1	8.6	54	497×108	308
H-QL-NX4	25000	580	103	1739	1932	869	8.1	1	497×108	289
H-QL-NX16	25000	628	108	1883	2094	188	8.7	5	497×108	313
H-QL-NX32	25000	626	112	1877	2086	89	8.7	10	497×108	312
H-QL-NX48	25000	629	111	1888	2096	59	8.7	16	497×108	314

where the overbar indicates the complex conjugate, and $Re\{\cdot\}$ the real part. $\widehat{P}(k)$ is the rate of turbulence production, $\widehat{\varepsilon}(k)$ is the viscous dissipation and $\widehat{T}(k)$ is the (nonlinear) turbulent energy transport, at a given wavenumber, respectively. Since $\int_0^\infty \widehat{T}(k) dk = 0$, the exact statistical balance between the production and dissipation of TKE is obtained for both of the full and QL systems through (2). A simulation is first set up for plane Couette flow where the two parallel sliding walls with the velocity $\pm U_0$ are located at $y = \pm L_y/2$, respectively (Table 1). The spanwise domain of the simulation is designed to be highly restricted, such that the size of the largest eddies in the bulk region is determined by L_z . The bulk region of the flow in effect simulates a uniform shear flow [18]. The numerical solver used is `diablo` [2].

3 Results and Discussion

The QL model is found to generate more anisotropic velocity fluctuations: u_{rms}^* and v_{rms}^* are increased in the QL model regardless $N_{x,F}$ considered, whereas w_{rms}^* is decreased (see Table 2). This behaviour is a little different from that observed in wall-bounded shear flows (e.g. [5, 14]), where only u_{rms}^* is increased by the QL

Table 2 One-point turbulence statistics

Simulation	dU^*/dy^*	$-\langle u'^* v'^* \rangle_{x,y,z,t}$	u_{rms}^*	v_{rms}^*	w_{rms}^*
H-DNS	0.017	0.99	1.72	1.15	1.42
H-QL-FULL	0.007	0.99	1.80	1.35	1.30
H-QL-NX4	0.007	0.99	1.9	1.35	1.1
H-QL-NX16	0.006	0.99	1.75	1.35	1.25
H-QL-NX32	0.006	0.99	1.81	1.35	1.25
H-QL-NX48	0.006	0.99	1.80	1.35	1.25

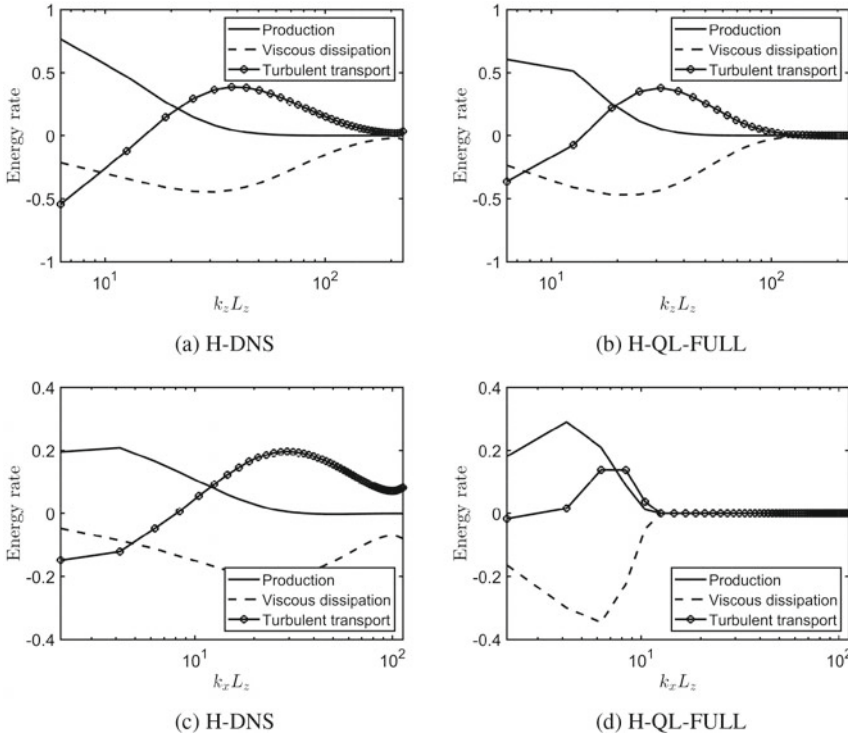


Fig. 1 Premultiplied spanwise (first row) and streamwise (second row) wavenumber spectra of energy budget per unit mean shear for the H-DNS and H-QL-FULL cases

approximation while the others are decreased. The QL model exhibits one-point turbulence statistics well converged for $N_{x,F} \geq 5$ (see Table 2). This implies that only a reasonably small number of the streamwise Fourier modes are active in the QL model, consistent with the previous observations made in wall-bounded flows (e.g. [5, 13–15]). The premultiplied one-dimensional spanwise wavenumber spectra of the production, turbulent transport and dissipation per unit mean shear from DNS and QL model are plotted in Fig. 1 (first row). Production takes place at large scales ($k_z L_z \lesssim 20$) and this energy appears to be transferred almost equally to turbulent transport and viscous dissipation, the latter phenomenon of which is presumably due to the still relatively low Reynolds number considered in the present study. At small scales ($k_z L_z \gtrsim 50$), the production becomes negligible and the other two terms balance each other with the turbulent transport term being positive. The premultiplied streamwise wavenumber spectra of the energy budget per unit mean shear are shown in Fig. 1 (second row). While the spectra of DNS show the typical features of energy cascade and turbulent dissipation observed in Fig. 1, the QL model does not develop such features even with the streamwise resolution used in DNS. In particular, both turbulent transport and dissipation spectra are highly localised within the wavenum-

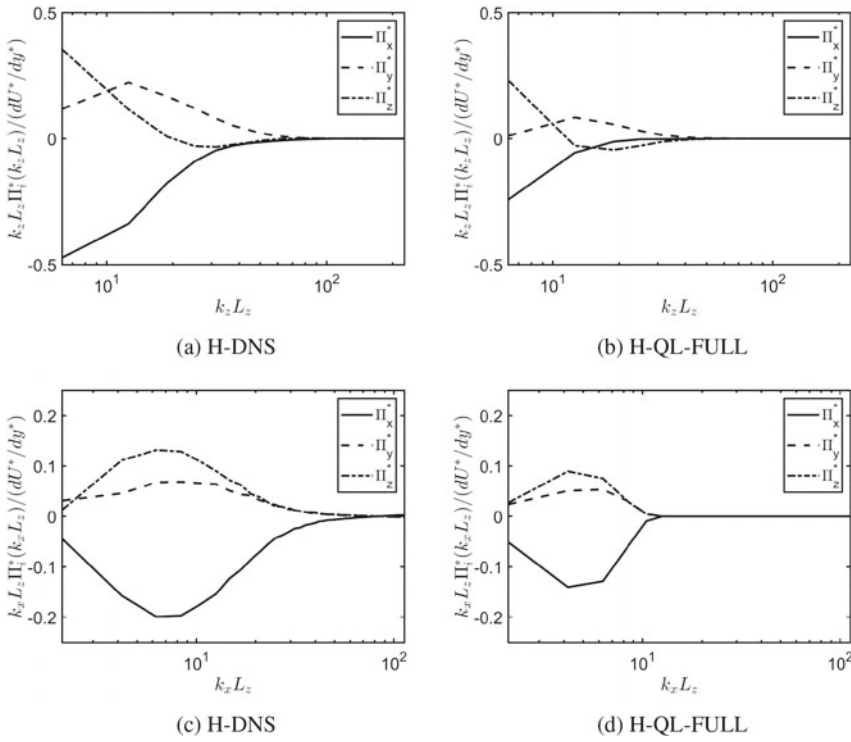


Fig. 2 Premultiplied spanwise (first row) and streamwise (second row) wavenumber spectra of pressure strain per unit mean shear for the H-DNS and H-QL-FULL cases

ber space where turbulence production is active $k_x L_z \lesssim 1$. However, it should also be pointed out that there are still a non-negligible number of wavenumbers actively involved in the spectral TKE balance: for example, in the case of H-QL-FULL, there are still approximately five streamwise Fourier modes highly active, and they form the spectral TKE balance in the streamwise wavenumber space. Furthermore, the nonlinear turbulent transport is not completely inactive in the streamwise wavenumber space.

The pressure-strain spectra are finally explored to understanding the mechanism of the componentwise TKE distribution in the QL model. Figure 2 shows the spectra of the pressure-strain terms for DNS and QL model. A negative $\widehat{\Pi}_x$ and a positive $\widehat{\Pi}_y$ are observed for both DNS and QL model throughout the spanwise scales. The $\widehat{\Pi}_z$ takes a positive value at small wavenumbers ($k_z L_z \lesssim 20$ in DNS and $k_z L_z \lesssim 10$ in QL model) and a negative value at large wavenumbers. The QL model appears to reproduce the pressure-strain spectra similar to those of DNS, but it largely fails to do so quantitatively. In particular, the absolute values of the pressure-strain spectra of the QL model are considerably smaller than those of DNS in the entire range of the spanwise wavenumbers. Similar behaviours are also observed in the streamwise

wavenumber spectra of pressure strain. Here, the only notable qualitative difference from the spanwise wavenumber spectra is that the pressure-strain spectra of the QL model is also highly localised for $k_x L_z \lesssim 1$. This is evidently due to the lack of nonlinear energy transport (energy cascade) of the QL model in the streamwise wavenumber space.

4 Concluding Remarks

The overall turbulence statistics and the spectral energetics of the QL model found in the present study are reminiscent of those of under-resolved direct numerical simulation: in fact, the monochromatic QL model (i.e. the QL model with $N_{x,F} = 1$) is mathematically identical to direct numerical simulation with single streamwise Fourier mode. Having pointed this out, the observations made in the present study suggest that the QL model considered in the present study may be improved, if the mechanisms of nonlinear turbulent transport in the streamwise wavenumber space is further incorporated. One such way might be realised by adding an eddy-viscosity-based diffusion model to (1b), as the enhanced diffusion at the integral length scale would replace the role of nonlinear turbulent transport without creating energy cascade. Given the translational invariance of the statistical features of uniform shear turbulence in all the spatial directions, a realistic and simplest form of the eddy viscosity would be an isotropic constant diffusion tensor. In this respect, the GQL [9, 15] would be an interesting direction to pursue, as it would incorporate some minimal role of the slow pressure. Ultimately, combination of an additional turbulence model (e.g. based on an eddy viscosity) with the GQL might be a direction towards a reliable low-dimensional description of turbulent flows.

References

1. B. Bamieh, M. Dahleh, *Phys. Fluids* **13**, 3258–69 (2001)
2. T.R. Bewley (Renaissance Press, Richardson, 2014)
3. J.U. Bretheim, C. Meneveau, D.F. Gayme, *Phys. Fluids* **27**(1), (2015)
4. K.M. Butler, B.F. Farrell, *Phys. Fluids A: Fluid Dyn.* **5**(3), 774–777 (1993)
5. B. Farrell, P. Ioannou, J. Jiménez, N. Constantinou, A. Lozano-Durán, M.-A. Nikolaidis, *J. Fluid Mech.* **809**, 290–315 (2016)
6. J.M. Hamilton, J. Kim, F. Waleffe, *J. Fluid Mech.* 317–348 (1995)
7. M.R. Jovanović, B. Bamieh, *J. Fluid Mech.* **543**, 145–83 (2005)
8. W.V.R. Malkus, S. Chandrasekhar, *Phil. Trans. R. Soc. A* **225**(1161), 196–212 (1954)
9. J.B. Marston, G.P. Chini, S.M. Tobias, *Phys. Rev. Lett.* **116**, (2016)
10. M. Pausch, Q. Yang, Y. Hwang, B. Eckhardt, *Fluid Dyn. Res.* **51**(1), (2019)
11. P.J. Schmid, *Ann. Rev. Fluid Mech.* **39**(1), 129–162 (2007)
12. P. J. Schmid, D.S. Henningson (Springer, Berlin, 2001)
13. V.L. Thomas, B.F. Farrell, P.J. Ioannou, D.F. Gayme, *Phys. Fluids* **27**(10), (2015)
14. V.L. Thomas, B.K. Lieu, M.R. Jovanović, B.F. Farrell, P.J. Ioannou, D.F. Gayme, *Phys. Fluids* **26**(10), (2014)

15. S.M. Tobias, J.B. Marston, *J. Fluid Mech.* **810**, 412–428 (2017)
16. L.N. Trefethen, A.E. Trefethen, S.C. Reddy, T.A. Driscoll, *Science* **261**(5121), 578–584 (1993)
17. F. Waleffe, *Phys. Fluids* **9**(4), 883–900 (1997)
18. Q. Yang, A.P. Willis, Y. Hwang, *J. Fluid Mech.* **834**, 531–554 (2018)

Part V
Miscellaneous Topics

Turbulence and Uncertainty for Future Renewable Energy Reliability



P. Tavner and D. Zappalá

Abstract Current climate change concerns accelerate interest in developing reliable renewable energy sources. Two of the most significant, in the wind and sea, are subject to turbulence, where its mathematics are at the forefront and the topic of this Conference.

At the heart of renewable energy extraction are aero/hydrodynamic and electrical/mechanical/control machines, all subject to fault processes, some initiated by that turbulence. Humans, animals and plants are also subject to fault processes and health degradation, but plants and animals have cellular structures, incorporating growth and self-repair, dependent on genes. Machines of human construction, however, do not have these benefits, but there are similarities. Renewable energy extraction reliability depends on:

- Application: such as wind or tidal turbines, or wave devices. Figure 1 shows an early wind power spectrum while Figs. 2 and 3 show the turbulence encountered by renewable devices;
- Design: by virtue of device rating, load and materials used;
- Physics: energy transfer by thermodynamically reversible processes accompanied by irreversible fault processes, mitigated by design, but degrading energy conversion through uncertain failures.

In time, these irreversible loss processes, or root causes, accumulate, worsening machine reliability and triggering conversion failure, a stochastic integration process. Brand et al. [2] point out the gap in the Fig. 1 spectrum is absent over land, the wind speed distribution is non-Gaussian under unstable maritime conditions, and off-shore

P. Tavner (✉)

Department of Engineering, Durham University, Durham, UK

e-mail: peter.tavner@durham.ac.uk

D. Zappalá

Faculty of Aerospace Engineering, TU Delft, Delft, Netherlands

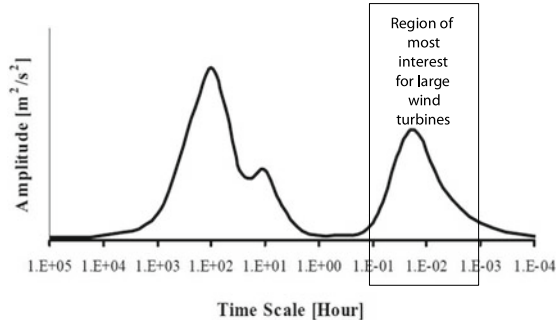


Fig. 1 Classical wind speed time variation assumption [1]. This is expressed as $fS(f)$, not $S(f)$ as used in current turbulence work, thus Kolmogorov decay in double-log presentation would be $f^{-2/3}$, as expressed in current turbulence concepts, [2–3]

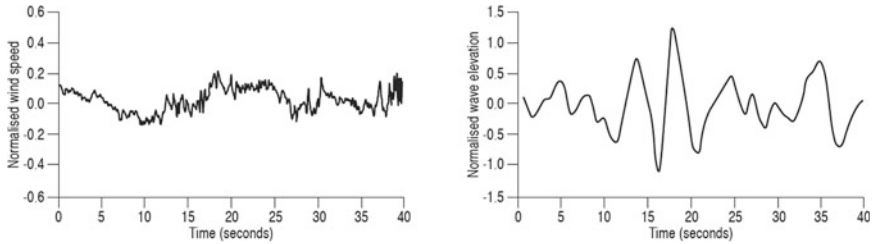
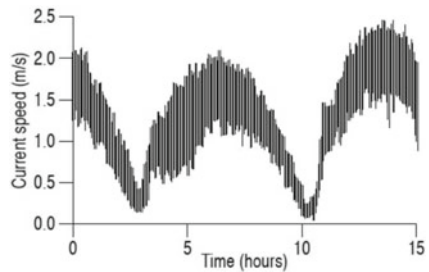


Fig. 2 Practical turbulence encountered by an onshore wind turbine (left) and an offshore wave energy device (right), [4]

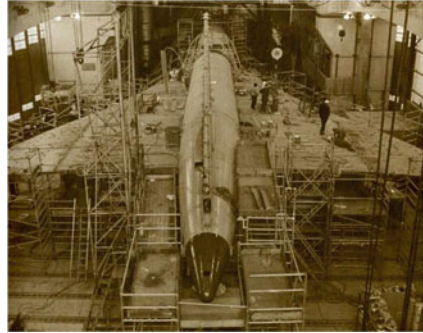
Fig. 3 Practical, unpredictable tidal energy device turbulence superimposed on predictable diurnal variation, [4]



wind speed profiles differ from onshore. Recent insights from Nandi et al. [3] confirm some of Fig. 1’s turbulence assumptions.

However, the purpose of this brief paper is to draw turbulence researchers’ attention to the connection between the mathematical continuity of turbulence and the integration of uncertain failure physics processes. The intent is to explain the impact on wind and sea renewable energy extraction of aero-dynamic and hydro-dynamic turbulence and the integrating effect of subsequent uncertain irreversible failure processes on those renewable energy devices.

Fig. 4 Concorde full-size fatigue air-frame test, Aerospatiale/BAe, Farnborough, UK, 1973–75, [5]



This is not new, scientists and engineers experienced similar issues in the early days of transonic jet aircraft flight, summarized by:

- Slow fuselage skin stress variation, due to pressurization or depressurization, as aircraft descend from or ascend to high altitude, initiating low-cycle skin fatigue failure;
- Rapid air-frame and skin stress changes as aircraft accelerate or decelerate through the sound barrier, initiating high-cycle fatigue failure.

Figure 4, from the 1970s [5], shows for the Concorde supersonic aircraft airframe how such structural issues were resolved, by full-size physical fatigue and pressurization/depressurization tests.

We make this comparison between the aeronautic and renewable industries, emphasizing structural fatigue failure in the former, whereas renewable industry failure processes penetrate further into the device than the structure, because these devices are fully robotic and risk overall failure if one part fails, whether in the structure or conversion system.

To analyze such issues cost-effectively, devices cannot be subjected to full-size, Concorde-like tests but must be modelled. To do that for wind and sea renewables we need a mathematical understanding that links turbulent causes to uncertain cumulative consequences, not only in device structures but also in their energy collection systems, generators, electronics and controls. There needs to be a mathematical connection between the continuity of turbulence mathematics and the integration processes of uncertain failure physics, across combined structural, mechanical, electrical and control technologies [6]. A first attempt at this process has been taken by Lin et al. [7].

References

1. I. van der Hoven, Power spectrum of horizontal wind speed in the frequency range from 0.0007 to 900 cycles per hour. *J. Atmos. Sci.* **14**(2), 160–164 (1957)
2. A.J. Brand, J. Peinke, J. Mann, Turbulence and wind turbines. *J. Phys.: Conf. Ser.* **318** (2011)
3. T.N. Nandi, A. Herrig, J.G. Brasseur, Non-steady wind turbine response to daytime atmospheric turbulence. *Phil. Trans. R. Soc. Lond. A* **375**(2091), (2017)
4. P. Tavner, *Wave and Tidal Generation Devices: Reliability and Availability* (IET, 2017)
5. <https://www.heritageconcorde.com>. Accessed 27 Mar 2021
6. R. Yan, X. Chen, W. Li, S. Sheng, Mathematical methods and modelling in machine fault diagnosis. *Math. Probl. Eng.* (2014)
7. Z. Lin, D. Cevasco, M. Collu, A methodology to develop reduced-order models to support the operation and maintenance of offshore wind turbines. *Appl. Energy* **259**(114228), (2020)

Instability on Rotating Sharp Cones—Revisited



K. Kato, P. Henrik Alfredsson, and R. J. Lingwood

Abstract We analyse the azimuthal velocity fluctuation in the boundary layer driven by a rotating slender cone with a half-cone apex angle of 30° . The flow is dominated by a centrifugal instability, which develops into randomly occurring spiralling vortices travelling on the cone surface. Such non-stationary vortices are observed as an irregular wave packet-like fluctuation signal by a hot wire fixed in the lab frame of reference and the spectral map at different radial positions forms a smooth ridge, which is in contrast to the periodic time signal due to stationary crossflow vortices on broad cones, which gives rise to sharp spectral ridges. The present analysis decomposes the wave packet-like fluctuation using a short-time Fourier transform (STFT), revealing that the smooth spectral peak at a given radial position consists of waves with different frequencies. The most probable fundamental frequency follows the most unstable frequency according to linear stability theory. Also, we evaluate the amplitude of the harmonics of the most energetic mode around transition; quadratic nonlinear growth is observed until the amplitude of the fundamental mode saturates at transition. This behaviour is similar to that on broad cones although the primary instability and vortex structures are different.

K. Kato (✉) · P. H. Alfredsson · R. J. Lingwood
Department of Engineering Mechanics, KTH, Stockholm, Sweden
e-mail: kentaro.kato@mech.kth.se

P. H. Alfredsson
e-mail: phal@mech.kth.se

R. J. Lingwood
e-mail: Rebecca.Lingwood@brunel.ac.uk

R. J. Lingwood
Department of Mechanical and Aerospace Engineering,
Brunel University London, London, UK

© The Author(s), under exclusive license to Springer Nature Switzerland AG 2021
R. Örlü et al. (eds.), *Progress in Turbulence IX*, Springer Proceedings in Physics 267,
https://doi.org/10.1007/978-3-030-80716-0_35

1 Introduction

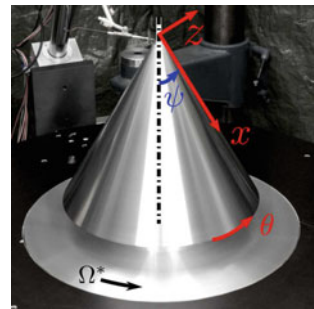
Instability in boundary layers driven by rotating cones in still fluid has been studied to understand transition in three-dimensional boundary layers. The early work showed that two different instabilities dominate the flow depending on the half-cone apex angle ψ (see Fig. 1); on a broad cone (including $\psi = 90^\circ$, i.e., the disk) the cross-flow instability develops into spiral vortices that are stationary with respect to the surface and an abrupt collapse of the vortices leads to transition, whereas a centrifugal instability forms larger spiral vortices (with a smaller azimuthal wavenumber n) on sharper cones (including $\psi = 0^\circ$, i.e., the cylinder) [5]. For the latter case, however, the transition process has not been studied in detail.

We define an orthogonal coordinate system with the origin located at the apex of the cone as shown in Fig. 1; x , θ and z are the coordinates along the generatrix of the cone, azimuthal and wall-normal directions, respectively. Lengths are normalised by $\delta_v^* = \sqrt{\nu^*/(\Omega^* \sin \psi)}$ (ν^* and Ω^* are the kinematic viscosity of the surrounding fluid and the cone angular velocity, respectively). Note that the Reynolds number based on x^* and the local wall velocity is the square of x .

Recent work on a sharp cone [4] shows that the centrifugal instability can be characterized by a Görtler number $G = \sqrt{x \delta_2^3} / \sin \psi$, where δ_2 is the measured momentum thickness scaled by δ_v^* . The instability develops into a slightly inclined non-stationary vortex (see Fig. 1c in [6]), that modifies the mean flow at $G \approx 10$ and saturates in the range $14 \lesssim G \lesssim 20$.

In the present work, we analyse the azimuthal velocity fluctuations v inside of the boundary layer on the slender cone obtained by the previous hot-wire measurements [4]. An example of the characteristic transition is illuminated in the power spectrum density (PSD) map shown in Fig. 2, compared with ones on broad cones; the colour shows the amplitudes of different frequency components as a function of x . On the disk and broad cone (a, b), around 30 and 24 stationary crossflow vortices exist, respectively. A hot wire fixed in the laboratory detects 30 and 24 waves per cone revolution, which are observed as multiple sharp peaks at the frequency $\omega \approx 30$ and 24 (normalised by Ω^*) developing from $x \approx 450$ (a) and 370 (b). For increasing x , higher harmonics are observed due to nonlinearity. At $x \approx 570$ (a) and

Fig. 1 The coordinate system (x, θ, z) on the cone with a half-cone apex angle of $\psi = 30^\circ$. The azimuthal velocity fluctuation v was measured by a single hot wire. All data for $\psi = 30^\circ$ analysed in the present work are for a case with $\Omega^* = 900$ rpm [4]



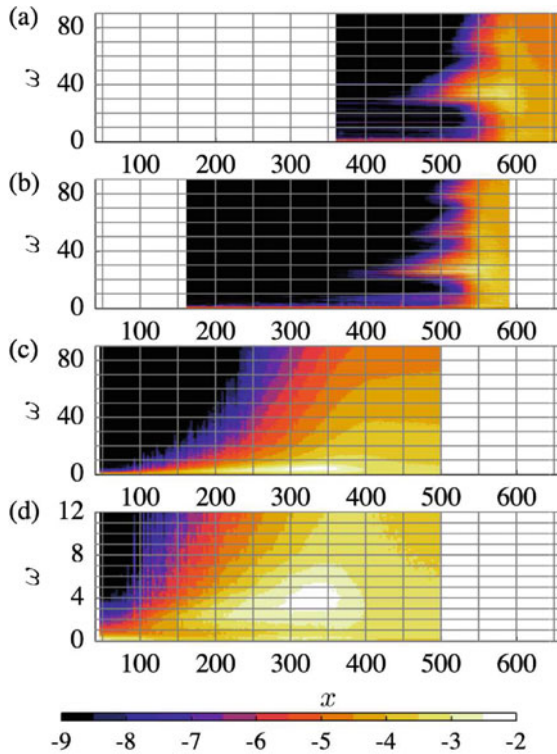


Fig. 2 Power spectrum density (PSD) $\log(E)$ map of the azimuthal velocity fluctuation v close to the centre of the boundary layer on cones with different apex angles: **a** $\psi = 90^\circ$, 1400 rpm [1], **b** $\psi = 60^\circ$, 900 rpm [2, 3], **c** $\psi = 30^\circ$, 900 rpm [4] and **d** blow-up of **c**. ω is the frequency normalized by the rotational rate Ω^* . For **a** and **b**, the spectra of the full fluctuation are shown. For **c** and **d**, the spectrum of the stationary component was subtracted and only the non-stationary component is shown; this was done to reduce the effect of an imbalance at $\omega = 1$ (in the lab frame of reference); no significant effect was observed at other frequencies. Data were taken from the corresponding references and further detailed explanations on the experiments can be found in [1–4]

537 (b), the disturbance level abruptly increases for all frequencies indicating the breakdown [1–3]. In contrast, no distinct harmonics and breakdown are observed on the slender cone (c, d). In this work, we analyse and discuss the transition process in the centrifugal-dominated flow on the slender cone ($\psi = 30^\circ$).

2 Time-Frequency Decomposition Using STFT

The velocity fluctuation v subtracted by the stationary fluctuation \hat{v} (obtained by phase-averaging v according to the cone revolution) is shown in Fig. 3(i). For small x , wave packet-like fluctuations appear spontaneously (ai); and as x increases, both the number of packets and their amplitude increase (bi). At larger x -locations, the wave packets fill up the signal (ci). STFT using a short time window (for 10 cone revolutions) provides the corresponding PSDs (ii); when the wave packets are separated (a), it is clear that the packet consists of several frequency components, in which we call the one with the maximum amplitude the fundamental mode (with the frequency ω_0 marked by the black line in (ii)) and other higher ones with frequencies of multiples of ω_0 as harmonics. For larger x , the more frequent appearances of the packets partly obscure the harmonics (bii) and they cannot be distinguished in (cii).

Applying this analysis to the whole data length (3600 cone revolutions), we accumulate the PSDs and detected ω_0 . The probability density function (PDF) of ω_0 as a function of x is shown through the colour map in Fig. 4; just beyond the neutral curve ($50 \lesssim x \lesssim 120$), the detected ω_0 is found in the region $0.5 \lesssim \omega_0 \lesssim 1$. As x increases, more modes become unstable and variation of ω_0 increases gradually ($150 \lesssim x \lesssim 350$). It is interesting that the most probable ω_0 follows the most unstable frequency (white lines) at a given x -location according to linear stability analysis with a certain shift in the x -direction $100 \lesssim \Delta x \lesssim 150$. It may be interpreted that the most unstable mode at a given x -location X does not necessarily have the largest amplitude there and needs some distance until the amplitude exceeds that of the lower-frequency mode that has the largest amplitude at X . At $x \approx 350$, the variation of ω_0 spreads suddenly, indicating breakdown. Thus, the sudden transition is detected clearly by evaluating only the fundamental mode whereas this is masked by harmonics in Fig. 2d.

Also, we can evaluate the quadratic nonlinear development of the harmonics by extracting the PSDs with the particular ω_0 . Figure 5 shows the case selecting $\omega_0 = 4$ as the fundamental frequency, which is the most energetic mode at transition. The amplitudes of harmonics are plotted in a similar way as in Fig. 6b in [2] (as the representative of samples, median of the amplitudes are taken, which is more robust against outliers than the average). The amplitude of the k th harmonic $v'_{rms, \omega_k} \sim [v'_{rms, \omega_0}]^{k+1}$ grows following the slope of $k + 1$ (without significant effect of the mean flow modification at $G = 10$, marked by \times), and rapidly increases at transition where the amplitude of the fundamental saturates at $G = 20$ (marked by $+$). Thus, this analysis reveals a quadratic nonlinear growth of the harmonics, which is not observable in the time-averaged spectra (Fig. 2c, d). Interestingly, Fig. 5 shows a similar behaviour to the broad cone [2] and may indicate a common mechanism for transition in three-dimensional boundary layers in general.

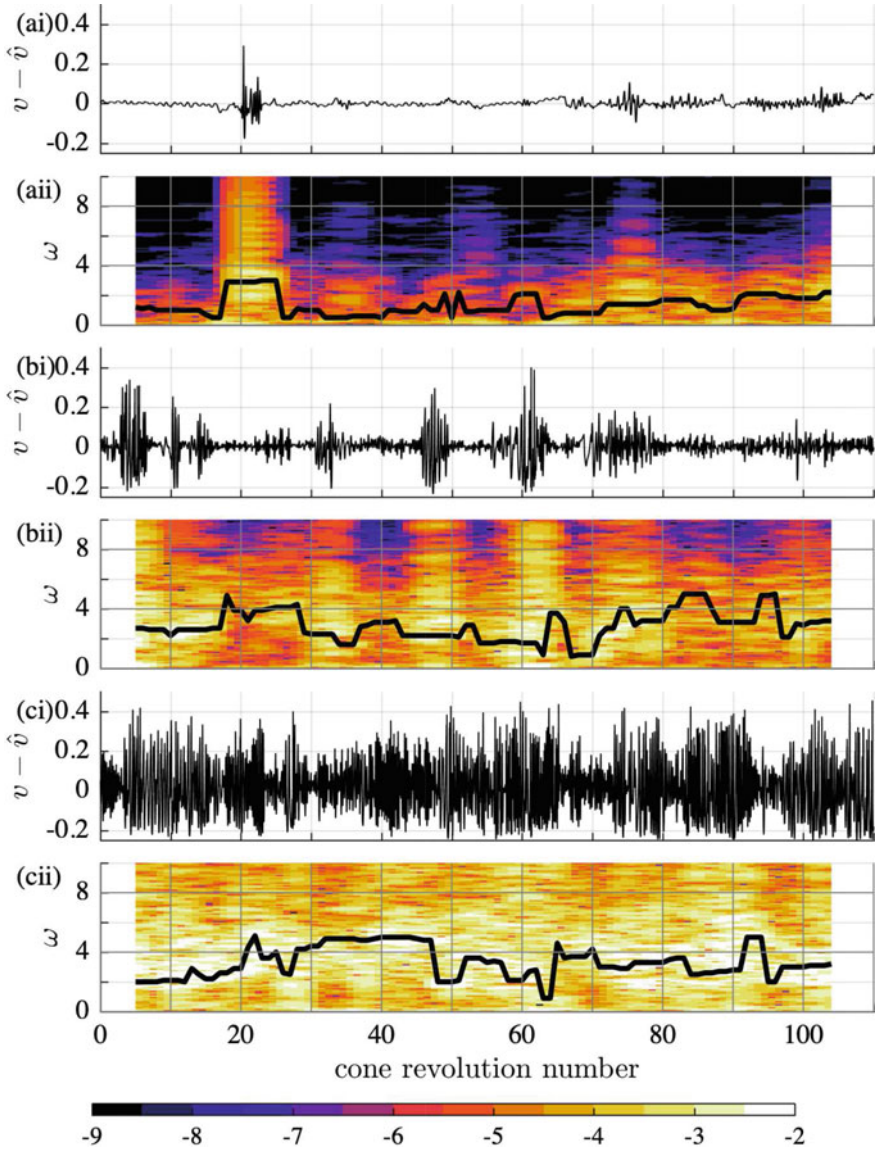


Fig. 3 The non-stationary velocity fluctuation $v - \hat{v}$ (i) and the PSDs $\log(E)$ using STFT or spectrogram (ii) at different x -locations: **a** $x = 151$, **b** $x = 250$, **c** $x = 301$. The fluctuation is normalised by the local wall velocity. The thick lines (ii) indicate the fundamental frequency ω_0 where the maximum amplitude is detected in the frequencies $\omega > 0.3$ in each short segment for 10 cone revolutions (providing a frequency resolution of $\Delta\omega = 0.1$ and overlapping 90%)

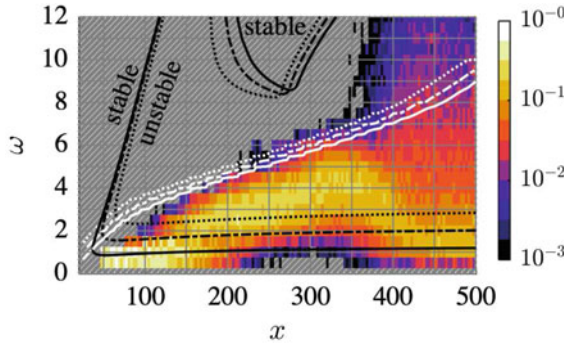


Fig. 4 PDF of the detected fundamental frequency ω_0 . The shadowed area shows where no fundamental frequency was detected. The black and white lines indicate the neutral curves and the frequency with the highest growth rate according the linear stability analysis [4] for different azimuthal wave numbers: $n = -1$ (solid line), $n = 0$ (dash-dotted line), $n = 1$ (dotted line)

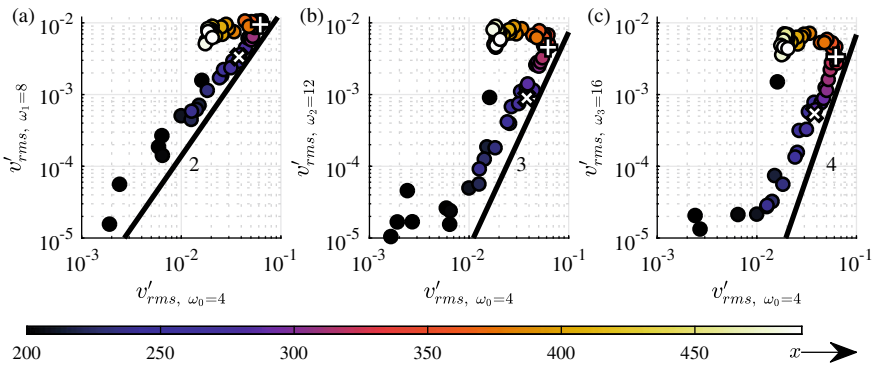


Fig. 5 Median of the harmonics' amplitudes as a function of the median of amplitude of the fundamental disturbance $v'_{rms, \omega_0=4}$: **a** the first harmonic, **b** the second harmonic, **c** the third harmonic. The colour indicates x -location. The white \times and $+$ indicate the points at $G = 10$ and 20 , respectively ($x \approx 270$ and 334 at 900 rpm). The amplitude was calculated by integrating the premultiplied spectrum in the single frequency bin $\Delta\omega = 0.1$. Only every second measured point is shown for ease of visibility

3 Conclusion

The instability and transition scenario in the boundary layer induced by a rotating sharp cone ($\psi = 30^\circ$) in still fluid is studied through a temporal-spectral analysis of the azimuthal velocity fluctuations. The fluctuations caused by the centrifugal-dominated non-stationary vortices appear as irregular wave packets in time and give a smooth peak in the frequency domain (Fig. 3). On the other hand the STFT provides the spectrum and fundamental frequency ω_0 of each wave packet. The most probable ω_0 follows the frequency with the largest spatial growth rate predicted by local

linear stability analysis with a certain radial offset (Fig. 4). For the most energetic mode around transition ($\omega = 4$), the developments of the harmonics are evaluated; their amplitudes grow in a quadratic manner until the fundamental mode saturates, and increases suddenly around transition (Fig. 5) though these harmonics and sudden breakdown are not observable in the time-averaged spectrum (Fig. 2c, d). This behaviour, which is first reported here, may indicate a similar transition scenario with the one on broad cones that are dominated by a crossflow instability.

Acknowledgements This work was supported by the Swedish Research Council through the ASTRID and SERAFINA projects (VR Contract No. 2013-5786, 2016-05200).

References

1. S. Imayama, P.H. Alfredsson, R.J. Lingwood, On the laminar-turbulent transition of the rotating-disk flow: the role of absolute instability. *J. Fluid Mech.* **745**, 132–163 (2014)
2. K. Kato, P.H. Alfredsson, R.J. Lingwood, Boundary-layer transition over a rotating broad cone. *Phys. Rev. Fluids* **4**, 071902 (2019)
3. K. Kato, T. Kawata, P.H. Alfredsson, R.J. Lingwood, Investigation of the structures in the unstable rotating-cone boundary layer. *Phys. Rev. Fluids* **4**, 053903 (2019)
4. K. Kato, A. Segalini, P.H. Alfredsson, R.J. Lingwood, Instability and transition in the boundary layer driven by a rotating slender cone. *J. Fluid Mech.* **915**, R4 (2021)
5. R. Kobayashi, H. Izumi, Boundary-layer transition on a rotating cone in still fluid. *J. Fluid Mech.* **127**, 353–364 (1983)
6. Y.P. Kohama, Three-dimensional boundary layer transition study. *Curr. Sci.* **79**(6), 800–807 (2000)

Rotational Effects on Layered Structures in Inhomogeneous Stratified Turbulence



Oaki Iida

Abstract Effects of buoyancy force stabilizing the disturbances and system rotation are investigated on turbulent structure of inhomogeneous flow. Fourier spectral method is used for inhomogeneous flow stirred by the artificial body force in the fringe region at the right side of the cuboid computational box of periodic boundary condition; thus stirred disturbances are dispersed from turbulent to non-turbulent flow field in the x_1 , i.e., streamwise direction. Moreover, a constant mean temperature gradient $d\Theta/dx_3$ is imposed in the x_3 direction i.e., vertical direction, to make a flow dynamically stable. As a result, internal gravity waves are radiated from the disturbed region, contributing to the dispersion of turbulent fluctuations, which generates the layered structures of u_1 , i.e., streamwise velocity elongated in the x_1 direction. Moreover, system rotation imposed in the x_3 direction results in an asymmetry between the positive and negative vertical vorticity; negative anticyclonic vorticity, surrounded by positive cyclonic vorticity, tends to become dominant flow structures.

1 Introduction

In the environmental flow, combined effects of density stratification and system rotation seriously affect turbulence and its diffusion. For example, the emergence of turbulent patches generated by the breaking of the internal gravity waves and the subsequent effect of Earth's rotation on them is the feature common in oceanic mixing and dispersion.

In this study, the effects of stable density stratification on turbulent diffusion from the locally disturbed region are numerically investigated in the very simple flow configuration of the periodic boundary conditions in all three directions. As shown in Fig. 1, attaching the fringe region excited by the artificial body force, Fourier spectral method can be used for inhomogeneous flow stirred at the right side of the

O. Iida (✉)

Department of Mechanical Engineering, Nagoya Institute of Technology,
Nagoya 466-8555, Japan
e-mail: iida.oaki@nitech.ac.jp

© The Author(s), under exclusive license to Springer Nature Switzerland AG 2021
R. Örlü et al. (eds.), *Progress in Turbulence IX*, Springer Proceedings in Physics 267,
https://doi.org/10.1007/978-3-030-80716-0_36

267

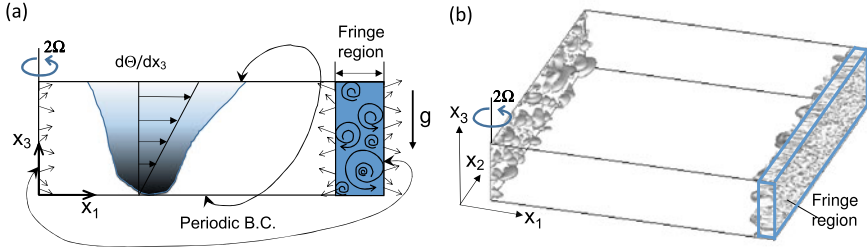


Fig. 1 **a** flow configuration with the coordinate system, and **b** bird view of the entire computational region including the isosurfaces of streamwise velocity $u_1=0.1$ at the early period of the calculation in the case without system rotation. At the inlet (left edge of the computational region), the buoyancy Reynolds number defined as $Re_b = \epsilon/\nu N^2$ is less than 2 in all cases of N2F, S10, S1, and S01 over the entire computational period, while the Froude number $Fr = \epsilon/kN$ is less than 0.03, indicating that the flow is so-called at the viscosity dominated regime; k and ϵ are the turbulent kinetic energy and its dissipation rate at the inlet, respectively, while ν and N are the kinematic viscosity and buoyancy frequency, respectively. Reproduced from [Phys. Fluids 33, 025102 (2021)], with the permission of AIP Publishing

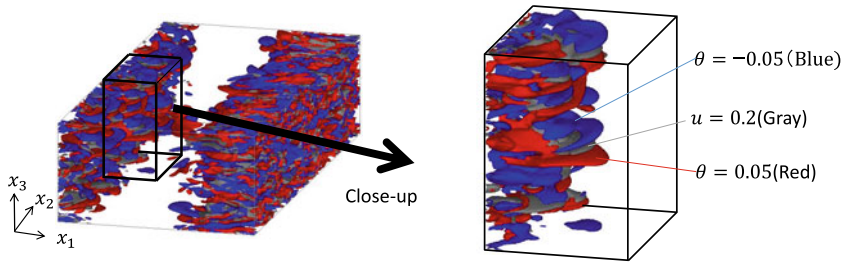


Fig. 2 Isosurfaces of temperature θ and streamwise velocity u_1 in case N2F [1], where system rotation is not imposed; blue and red isosurfaces are $\theta=-0.05$ and 0.05 , respectively, while grey is $u_1=0.1$; the entire computational regions are visualized, including the fringe region at the right-hand side

cuboid computational box, from which disturbances are dispersed from turbulent to non-turbulent flow field in the x_1 , i.e., streamwise direction. Moreover, a constant mean temperature gradient $S_\theta = d\Theta/dx_3$ is imposed in the x_3 direction i.e., vertical direction, to make a flow dynamically stable.

Our previous study [1] without system rotation shows that internal gravity waves are radiated from the disturbed region, which contributes to the dispersion of turbulent fluctuations and generation of the layered structure. As shown in Fig. 2, the layered structures of u_1 , i.e., streamwise velocity elongated in the x_1 direction, are observed, though layers are sandwiched by upper cold fluids and lower hot fluids, indicating the generation of gravity currents where the potential energy is reconverted into the horizontal kinetic energy, as indicated by our previous study [1].

In this study, however, the entire flow is also assumed to rotate in the vertical direction, i.e., x_3 , with the angular frequency Ω as shown in Fig. 1. Although the results of numerical simulations are identical with the previous study [2], effects of system rotation on the layered structures are more visually presented by using the different figures from our previous studies [1, 2].

2 Numerical Methods

In this study, a buoyancy force is approximated by the linear Boussinesq equation, and the rotational axis is assumed to be vertical axis. The physical parameters included in the governing equations are kinematic viscosity ν , thermal diffusivity α , S_θ , the rotation frequency $f = 2\Omega$, and buoyancy parameter $g\beta$, where β represents the volume-expansion rate.

The Boussinesq-approximated Navier–Stokes equations attaching the fringe term, the continuity equation, and the equation of temperature fluctuations θ take the following forms:

$$\frac{\partial u_i}{\partial x_i} = 0 \quad (1)$$

$$\frac{\partial u_i}{\partial t} + u_j \frac{\partial u_i}{\partial x_j} = -\frac{\partial p}{\partial x_i} + \nu \frac{\partial^2 u_i}{\partial x_j \partial x_j} + g\beta\delta_{i3}\theta + \epsilon_{3ij}2\Omega u_j + F_i(x_1) \quad (2)$$

$$\frac{\partial \theta}{\partial t} + u_j \frac{\partial \theta}{\partial x_j} = -S_\theta u_3 + \alpha \frac{\partial^2 \theta}{\partial x_j \partial x_j} + F_\theta(x_1), \quad (3)$$

where $F_i(x_1)$ and $F_\theta(x_1)$ are body force terms working in the fringe region. In above equations, u_i and p are the i th component of the velocity vector and pressure, respectively, while θ is temperature fluctuation.

Moreover, when non-dimensionalized by the appropriate length scale L , the velocity scale U , and the temperature scale $\Delta T (= |S_\theta|L)$, the following equations are obtained:

$$\frac{\partial u_i}{\partial x_i} = 0 \quad (4)$$

$$\frac{\partial u_i}{\partial t} + u_j \frac{\partial u_i}{\partial x_j} = -\frac{\partial p}{\partial x_i} + \frac{1}{\text{Re}} \frac{\partial^2 u_i}{\partial x_j \partial x_j} + \epsilon_{3ij} \frac{1}{\text{Ro}} u_j + \frac{1}{\text{Fr}^2} \delta_{i3} \theta + \frac{L\lambda(x_1)}{U} (v_r - u_i), \quad (5)$$

$$\frac{\partial \theta}{\partial t} + u_j \frac{\partial \theta}{\partial x_j} = -u_3 + \frac{1}{\text{RePr}} \frac{\partial^2 \theta}{\partial x_j \partial x_j} + \frac{L\lambda(x_1)}{U} (\theta_r - \theta). \quad (6)$$

The last term in the right side of (5) and (6) is the fringe term and supposed to force disturbances to be the ideal inflow condition v_r and θ_r [3]. Also, $Re = UL/\nu$, $Fr = U/LN$ and $Ro = U/Lf$ are the Reynolds, Froude, and Rossby numbers, respectively; the reference length and velocity scales are set to be unity in our previous studies [1, 2]. In contrast, $Pr = \nu/\alpha$, $N = \sqrt{g\beta S_\theta}$, and Ro/Fr are the Prandtl number, buoyancy frequency, and $S = N/2\Omega$, respectively. In all cases, Pr and N are set to be 0.71 and 2, respectively. The case without system rotation is defined as N2F. Moreover, S is set to be 10, 1, and 0.1 in the same flow configuration and grids resolution as case N2F; cases of $S = 10, 1,$ and 0.1 are coined as case S10, S1, and S01, respectively.

The computational box is set to be $8\pi \times 8\pi \times 2\pi$ in $x_1, x_2,$ and x_3 directions, respectively, while the grid resolutions are set to be $512 \times 512 \times 128$ in $x_1, x_2,$ and x_3 directions, respectively. In contrast, the fringe region is put in the region of $x_1 = 7\pi$ to 8π , where flow is artificially disturbed by the fringe term, which is switched on, when the velocities are deviated from the ideal disturbances, i.e., v_r and θ_r , which are the artificial random numbers as discussed in our previous studies.

In these numerical simulations, all equations are solved by the Fourier spectral and second-order Runge–Kutta methods, while alias error is removed by the truncation. The periodic boundary condition is imposed in all three directions.

3 Results and Discussions

Figure 3 shows the isosurfaces of the vertical vorticity ω_3 at $t = 12$. It is noted that in cases S01 and S1, the isosurfaces of ω_3 tend to be thin columns elongated in the vertical direction. In contrast, in cases S10 and N2F, the isosurfaces become flatten pancake structures. A close-up of Fig. 3 in cases S1 and S10 is shown in Fig. 4, where the effects of system rotation are observed, i.e., suppression of the horizontal enlargement of the vertical vorticity and its vertical elongation. In both cases, however, the anticyclones ($\omega_3 < 0$) become dominant in comparison to cyclones ($\omega_3 > 0$); intense cyclones are observed only at the periphery of the intense anticyclones.

Figure 5 shows the instantaneous velocity vectors colored by ω_3 in case N2F and case S10. It is noted that because of relatively small rotational effects, the structure of diffusion has a high similarity between these two cases. However, the rotation makes the layered structures large-scale anticyclonic vortices, and their periphery is rimmed by the cyclonic vorticity as observed in Figs. 3 and 4. Similar anticyclones are also observed in case S1, as shown in Fig. 3.

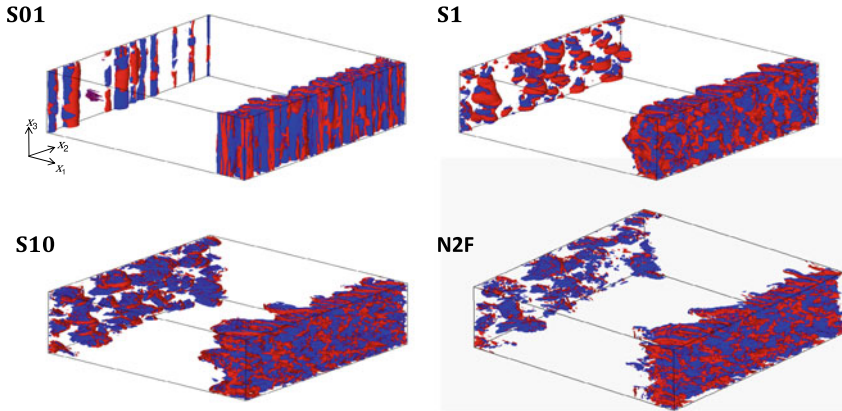


Fig. 3 Isosurfaces of vertical vorticity ω_3 at $t = 14$ in the entire computational regions of cases S01, S1, S10, and N2F; red and blue represent $u_1 = 0.1$ and -0.1 , respectively

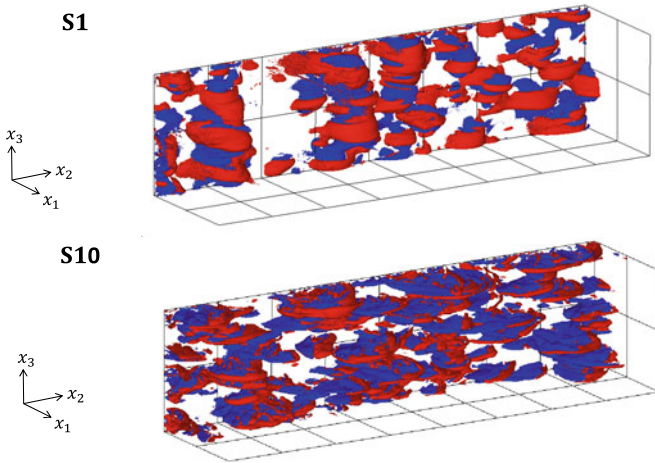


Fig. 4 Close-up of Fig. 3 in cases S1 and S10; regions of $2\pi \times 8\pi \times 2\pi$ are visualized in the x_1 , x_2 , and x_3 directions, respectively

4 Conclusions

The rotational effects on the diffusion of the disturbances injected into the laminar region under a stable density stratification are discussed by the direct numerical simulations of spectral methods with the fringe region, where the disturbances are excited by the artificially imposed body force. We find that by imposing the system rotation, disturbances diffused from the inlet generate anticyclonic vortices of the negative vertical vorticity, though their periphery is rimmed by the weak positive

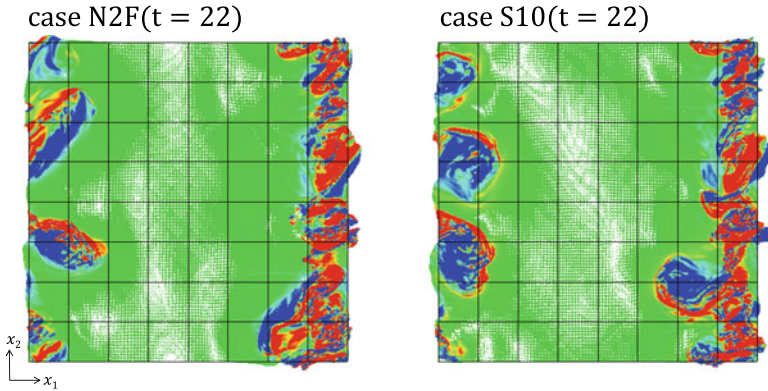


Fig. 5 Horizontal velocity vectors colored by the vertical vorticity ω_3 at $t = 22$ in the entire horizontal planes ($8\pi \times 8\pi$) of cases N2F and S10; red and blue represent positive and negative values, respectively, while green represents zero. Reproduced from [Phys. Fluids **33**, 025102 (2021)], with the permission of AIP Publishing

vorticity. With an increase in system rotation, the vertical length of the vorticity increases, while its horizontal scales decrease.

Acknowledgements Gratitude is expressed to author's former students of graduate school, M. Hayashi and Y. Inagaki for their contributions to this research study.

References

1. O. Iida, Turbulent structure of stably stratified inhomogeneous flow. Phys. Fluids **30**, 045101 (2018)
2. O. Iida, Effects of system rotation on diffusion of the disturbances in inhomogeneous strongly stratified flow. Phys. Fluids **33**, 025102 (2021)
3. J. Nordstorm, N. Nordin, D. Henningson, The fringe region technique and the Fourier method used in the direct numerical simulation of spatially evolving viscous flows. SIAM J. Sci. Comput. **20**, 1365 (1999)

Magnetoclinicity Instability



Nobumitsu Yokoi and Steven M. Tobias

Abstract In strongly compressible magnetohydrodynamic turbulence, obliqueness between the large-scale density gradient and magnetic field gives an electromotive force mediated by density variance (intensity of density fluctuation). This effect is named “magnetoclinicity”, and is expected to play an important role in large-scale magnetic-field generation in astrophysical compressible turbulent flows. Analysis of large-scale instability due to the magnetoclinicity effect shows that the mean magnetic-field perturbation is destabilised at large scales in the vicinity of strong mean density gradient in the presence of density variance.

1 Magnetoclinicity: Dynamo at Strong Compressibility

With the aid of the two-scale direct-interaction approximation (TSDIA), a multiple-scale renormalised perturbation expansion theory for inhomogeneous turbulence [1, 2], the turbulent electromotive force (EMF) is written as [3, 4]

$$\begin{aligned} \langle \mathbf{u}' \times \mathbf{b}' \rangle = & -(\beta + \zeta) \nabla \times \mathbf{B} + \alpha \mathbf{B} - (\nabla \zeta) \times \mathbf{B} + \gamma \nabla \times \mathbf{U} \\ & - \chi_\rho \nabla \bar{\rho} \times \mathbf{B} - \chi_Q \nabla Q \times \mathbf{B} - \chi_D \frac{D\mathbf{U}}{Dt} \times \mathbf{B}, \end{aligned} \quad (1)$$

where \mathbf{u}' is the velocity fluctuation, \mathbf{b}' the magnetic fluctuation, \mathbf{B} the mean magnetic field, \mathbf{U} the mean velocity, $\bar{\rho}$ the mean density, Q the mean internal energy,

N. Yokoi (✉)

Institute of Industrial Science, University of Tokyo, 4-6-1 Komaba, Meguro,
Tokyo 153-8505, Japan
e-mail: nobyokoi@iis.u-tokyo.ac.jp

Visiting researcher at the Nordic Institute for Theoretical Physics (NORDITA), Stockholm, Sweden

S. M. Tobias

Department of Applied Mathematics, University of Leeds, Leeds LS2 9JT, UK
e-mail: S.M.Tobias@leeds.ac.uk

$D/Dt = \partial/\partial t + \mathbf{U} \cdot \nabla$, and $\langle \dots \rangle$ denotes ensemble averaging. Here, the transport coefficients $\eta_T (= \beta + \zeta)$, α and γ represent the turbulent magnetic-diffusivity, residual-helicity and cross-helicity effects, respectively, which are present even in the incompressible case [5]. On the other hand, the transport coefficients χ_ρ , χ_Q , and χ_D have no counterparts in the incompressible case. They are related to the obliqueness of mean magnetic field to the gradients of density, internal energy, etc., and are called ‘‘magnetoclinicity’’. Note that in the TSDIA framework, they depend on the response functions and the compressible energy spectra with the multiplicative wavenumber factor k^2 . This corresponds to the square of turbulent dilatation, $(\nabla \cdot \mathbf{u}')^2$, and is directly connected to the magnitudes of density and internal-energy fluctuations.

The physical origin of the magnetoclinicity effect can be obtained as follows. Through simplest linear relations, the density and internal-energy fluctuations can be expressed in terms of the turbulent dilatation as

$$\rho' = -\tau_\rho \bar{\rho} \nabla \cdot \mathbf{u}', \quad q' = -(\gamma_s - 1) \tau_q Q \nabla \cdot \mathbf{u}', \quad (2)$$

where γ_s is the ratio of the specific heats at the constant pressure and volume, and τ_ρ and τ_q are the characteristic times for the density and internal-energy fluctuations, respectively. These relations naturally show that the density and internal-energy fluctuations are reduced or enhanced respectively with turbulent expansion ($\nabla \cdot \mathbf{u}' > 0$) or contraction ($\nabla \cdot \mathbf{u}' < 0$). From the equation of state, the fluctuation pressure is linearly related to the density and internal energy as $p' = (\gamma_s - 1) (q' \bar{\rho} + \rho' Q)$. Then the velocity fluctuation is related to the turbulent dilatation as

$$\begin{aligned} \frac{\partial \mathbf{u}'}{\partial t} &= \dots - \frac{1}{\bar{\rho}} \nabla p' + \dots \simeq \dots - (\gamma_s - 1) \frac{q'}{\bar{\rho}} \nabla \bar{\rho} - (\gamma_s - 1) \frac{q'}{\bar{\rho}} \nabla Q + \dots \\ &\simeq \dots + (\gamma_s - 1)^2 \tau_q \frac{Q}{\bar{\rho}} (\nabla \cdot \mathbf{u}') \nabla \bar{\rho} + (\gamma_s - 1) \tau_\rho (\nabla \cdot \mathbf{u}') \nabla Q + \dots \end{aligned} \quad (3)$$

Here, use has been made of (2) on the final evaluation of (3), which suggests that positive (negative) turbulent dilatation leads to velocity fluctuation parallel (anti-parallel) to the mean density gradient. On the other hand, from the induction equation of fluctuating magnetic field, we have

$$\frac{\partial \mathbf{b}'}{\partial t} = \dots - (\nabla \cdot \mathbf{u}') \mathbf{B} + \dots \quad (4)$$

This represents the effect of magnetoacoustic wave. Positive (negative) turbulent dilatation induces the magnetic fluctuation whose direction is opposite (parallel) to the mean magnetic field (Fig. 1).

Integrating (3) and (4) with respect to time, we get approximate expressions for \mathbf{u}' and \mathbf{b}' . Then, the EMF due to turbulent dilatation, $\langle \mathbf{u}' \times \mathbf{b}' \rangle_{TD}$, is given as

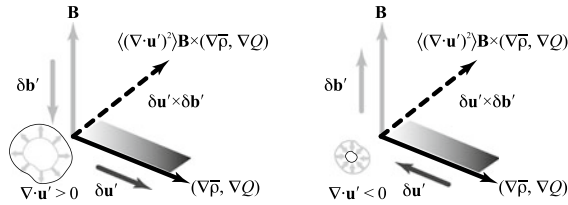


Fig. 1 Turbulent electromotive force due to the mis-alignment of the mean magnetic field \mathbf{B} from the gradient of mean density or internal energy, $\nabla\bar{\rho}$ or ∇Q . Cases for the local expansion (positive dilatation) (left) and the local contraction (negative dilatation) (right)

$$\begin{aligned} \langle \mathbf{u}' \times \mathbf{b}' \rangle_{\text{TD}} &\simeq -(\gamma_s - 1)^2 \tau_u \tau_b \tau_q \langle (\nabla \cdot \mathbf{u}')^2 \rangle \frac{Q}{\rho} \nabla \bar{\rho} \times \mathbf{B} \\ &\quad - (\gamma_s - 1) \tau_u \tau_b \tau_\rho \langle (\nabla \cdot \mathbf{u}')^2 \rangle \nabla Q \times \mathbf{B}, \end{aligned} \quad (5)$$

where τ_u and τ_b are the characteristic times of velocity and magnetic-field evolutions, respectively. Equation (5) infers that in the presence of the obliqueness between the mean magnetic field \mathbf{B} and the gradient of mean density, $\nabla\bar{\rho}$, and/or the gradient of mean internal energy, ∇Q , the EMF is induced in the direction of $\mathbf{B} \times \nabla\bar{\rho}$ and/or $\mathbf{B} \times \nabla Q$, mediated by the turbulent dilatation. It is important to note that the direction of $\langle \mathbf{u}' \times \mathbf{b}' \rangle_{\text{TD}}$ is always in the direction of $\mathbf{B} \times \nabla\bar{\rho}$ and/or $\mathbf{B} \times \nabla Q$, independent of the sign of turbulent dilatation (Fig. 1).

2 Equilibrium State and Disturbance

In this work, we study a large-scale instability of compressible MHD turbulence: How do the mean or large-scale fields evolve under the influence of the turbulent transport represented by turbulent correlations such as the turbulent mass flux $\langle \rho' \mathbf{u}' \rangle$, Reynolds stress $\langle \mathbf{u}' \mathbf{u}' \rangle$, turbulent Maxwell stress $\langle \mathbf{b}' \mathbf{b}' \rangle$, turbulent internal-energy flux $\langle q' \mathbf{u}' \rangle$, EMF $\langle \mathbf{u}' \times \mathbf{b}' \rangle$, etc. appearing in the mean-field equations. For this purpose, a mean-field quantity F is divided into the equilibrium unperturbed state F_0 and the deviation from it or disturbance, δF , as $F = F_0 + \delta F$ with the disturbance being much smaller than the equilibrium field: $|\delta F| \ll |F_0|$.

In this work, for the sake of simplicity, we assume simplified equilibrium mean fields for the velocity and magnetic field in the rectangular coordinate system (x, y, z) :

$$\mathbf{U} = \mathbf{U}_0 + \delta \mathbf{U} = \delta \mathbf{U} = (\delta U^x, \delta U^y, \delta U^z), \quad (6)$$

$$\mathbf{B} = \mathbf{B}_0 + \delta \mathbf{B} = (B_0, 0, 0) + (\delta B^x, \delta B^y, \delta B^z). \quad (7)$$

The mean equilibrium velocity \mathbf{U}_0 is assumed to be zero ($\mathbf{U}_0 = 0$), and the mean equilibrium magnetic field \mathbf{B}_0 is put in the x direction transverse to the mean equilibrium density gradient $\nabla\rho_0$ and uniform ($B_0 = \text{const.}$).

We decompose the mean-field equations into F_0 and δF with (6) and (7), we have equations of disturbances:

$$\frac{\partial \delta \rho}{\partial t} + (\delta \mathbf{U} \cdot \nabla) \rho_0 + \rho_0 \nabla \cdot \delta \mathbf{U} = -\nabla \cdot \langle \rho' \mathbf{u}' \rangle_1, \quad (8)$$

$$\begin{aligned} \frac{\partial}{\partial t} \rho_0 \delta U^\alpha &= -\frac{\partial \delta P}{\partial x^\alpha} + \frac{\partial}{\partial x^\alpha} \mu \left(\frac{\partial \delta U^\alpha}{\partial x^\alpha} + \frac{\partial \delta U^a}{\partial x^\alpha} \right) + (\mathbf{J}_0 \times \delta \mathbf{B})^\alpha + (\delta \mathbf{J} \times \mathbf{B}_0)^\alpha \\ &- \frac{\partial}{\partial x^\alpha} \left[\delta \rho \left(\langle u'^a u'^\alpha \rangle_0 - \frac{1}{\mu_0 \rho_0} \langle b'^a b'^\alpha \rangle_0 \right) + \delta U^a \langle \rho' u'^\alpha \rangle_0 + \delta U^\alpha \langle \rho' u'^a \rangle_0 \right], \quad (9) \end{aligned}$$

$$\begin{aligned} \frac{\partial}{\partial t} (\rho_0 \delta Q + \delta \rho Q_0) + \nabla \cdot (\rho_0 \delta \mathbf{U} Q_0) \\ &= \nabla \cdot \left(\frac{\kappa}{C_v} \nabla \delta Q \right) - \nabla \cdot (\delta \bar{\rho} \langle q' \mathbf{u}' \rangle_0 + \delta Q \langle \rho' \mathbf{u}' \rangle_0) \\ &+ \delta \mathbf{U} \langle \rho' q' \rangle_0 - (\gamma_s - 1) [\rho_0 Q_0 \nabla \cdot \delta \mathbf{U} + \delta \rho \langle q' \nabla \cdot \mathbf{u}' \rangle_0 + \delta Q \langle \rho' \nabla \cdot \mathbf{u}' \rangle_0], \quad (10) \end{aligned}$$

$$\frac{\partial \delta \mathbf{B}}{\partial t} = \nabla \times (\delta \mathbf{U} \times \mathbf{B}_0) + \eta \nabla^2 \delta \mathbf{B} + \nabla \times \langle \mathbf{u}' \times \mathbf{b}' \rangle_1 \quad (11)$$

and the solenoidal condition of the magnetic field: $\nabla \cdot \delta \mathbf{B} = 0$.

The pressure and internal-energy perturbations, δP and δQ , can be expressed in terms of the density perturbation $\delta \rho$ with the speed of sound c_s as

$$\delta P = (\gamma_s - 1) (\rho_0 \delta Q + Q_0 \delta \rho) = c_s^2 \delta \rho. \quad (12)$$

Then, there is no need to solve the internal-energy equation.

The turbulent correlations in the mean-field perturbation equations are given as

$$\langle \rho' \mathbf{u}' \rangle_0 = -\kappa_\rho \nabla \rho_0, \quad \langle \rho' \mathbf{u}' \rangle_1 = -\kappa_\rho \nabla \delta \rho, \quad (13)$$

$$\langle u'^\alpha u'^\beta \rangle_0 - \frac{1}{\mu_0 \bar{\rho}} \langle b'^\alpha b'^\beta \rangle_0 = -\nu_K \left(\frac{\partial U_0^\beta}{\partial x^\alpha} + \frac{\partial U_0^\alpha}{\partial x^\beta} \right) + \nu_M \left(\frac{\partial B_0^\beta}{\partial x^\alpha} + \frac{\partial B_0^\alpha}{\partial x^\beta} \right) / \mu_0 \bar{\rho} = 0, \quad (14)$$

$$\langle \mathbf{u}' \times \mathbf{b}' \rangle_1 = -\eta_T \delta \mathbf{J} + \alpha \delta \mathbf{B} + \gamma \delta \boldsymbol{\Omega} + \chi_\rho \mathbf{B}_0 \times \nabla \delta \rho + \chi_\rho \delta \mathbf{B} \times \nabla \rho_0, \quad (15)$$

where κ_ρ , ν_K , and ν_M are the transport coefficients. Note that (14) gives no contribution because of the assumptions (6) and (7).

3 Normal Mode Analysis of the Mean-Field Equations

We analyse an arbitrary disturbance into a complete set of normal modes, and examine the stability of each of these modes characterised by a wave number k . The disturbances are expressed in terms of two-dimensional periodic waves as

$$\delta F = \hat{f}(z) \exp[i(k^x x + k^y y) - i\omega_{\mathbf{k}} t], \quad (16)$$

where $\delta F = (\delta\rho, \delta\mathbf{U}, \delta\mathcal{Q}, \delta\mathbf{B})$ and $\hat{f} = (\hat{\rho}, \hat{\mathbf{u}}, \hat{q}, \hat{\mathbf{b}})$. In general this formalism leads to a two-point boundary eigenvalue problem for the functions $\hat{f}(z)$. Here, as the simplest possible case, we assume that the amplitudes of disturbances, \hat{f} , do not depend on the vertical coordinate z and constant, which will be relaxed in subsequent papers. Under this assumption, the equations of perturbations are

$$(-k^2 \kappa_\rho + i\omega_{\mathbf{k}}) \hat{\rho} + ik^x \rho_0 \hat{u}^x + ik^y \rho_0 \hat{u}^y + \frac{d\rho_0}{dz} \hat{u}^z = 0, \quad (17)$$

$$-ik^x c_s^2 \hat{\rho} + \left(\kappa_\rho \frac{d^2 \rho_0}{dz^2} + i\omega_{\mathbf{k}} \rho_0 \right) \hat{u}^x = 0, \quad (18)$$

$$-ik^y c_s^2 \hat{\rho} + \left(\kappa_\rho \frac{d^2 \rho_0}{dz^2} + i\omega_{\mathbf{k}} \rho_0 \right) \hat{u}^y - ik^y B_0 \hat{b}^x + ik^x B_0 \hat{b}^y = 0, \quad (19)$$

$$ik^x \kappa_\rho \hat{u}^x + ik^y \kappa_\rho \hat{u}^y + \left(\kappa_\rho \frac{d^2 \rho_0}{dz^2} + i\omega_{\mathbf{k}} \rho_0 \right) \hat{u}^z + ik^x B_0 \frac{d\rho_0}{dz} \hat{b}^z = 0, \quad (20)$$

$$k^2 \gamma \hat{u}^x - ik^y B_0 \hat{u}^y + \left(-k^2 \eta_T + \chi_\rho \frac{d^2 \rho_0}{dz^2} + i\omega_{\mathbf{k}} \right) \hat{b}^x + ik^y \alpha \hat{b}^z = 0, \quad (21)$$

$$(k^2 \gamma + ik^x B_0) \hat{u}^y + \left(-k^2 \eta_T + \chi_\rho \frac{d^2 \rho_0}{dz^2} + i\omega_{\mathbf{k}} \right) \hat{b}^y - ik^x \alpha \hat{b}^z = 0, \quad (22)$$

$$ik^x B_0 \hat{u}^x + k^2 \gamma \hat{u}^z - ik^y \alpha \hat{b}^x + ik^x \alpha \hat{b}^y + (-k^2 \eta_T + i\omega_{\mathbf{k}}) \hat{b}^z = 0. \quad (23)$$

This system of equations (17)–(23) with the solenoidal conditions for the magnetic field is analysed. One of the dispersion relations is given by

$$\chi_\rho \frac{d^2 \rho_0}{dz^2} - \eta_T k^2 + i\omega_{\mathbf{k}} = 0. \quad (24)$$

From this, the α component of large-scale magnetic-field disturbance is written as

$$\delta B^\alpha = \hat{b}^\alpha \exp \left[\left(-\eta_T k^2 + \chi_\rho \frac{d^2 \rho_0}{dz^2} \right) t \right] \exp[i(k^x x + k^y y)]. \quad (25)$$

The first term in the temporal evolution part arises from the turbulent magnetic diffusivity η_T . The growth of the mean-field perturbations are suppressed by η_T . This effect is strongest at small scales where the wave number k is large. On the other hand, in the presence of a strong mean density inhomogeneity such that

$$\chi_\rho \frac{d^2 \rho_0}{dz^2} > \eta_T k^2, \quad (26)$$

the second or χ_ρ -related term in the temporal evolution part contributes to the growth of mean-field perturbations. This large-scale instability, the magnetoclinicity instability, is important only in the region where the density variance is strong enough since it also depends on $\chi_\rho (\propto \langle \rho^2 \rangle)$.

4 Instability Across the Strong Density Variation

In order to quantitatively evaluate the magnetoclinicity effect, we consider a simplest possible spatial profile of the unperturbed density $\rho_0(z)$ as

$$\rho_0(z) = \rho_m - \rho_d \tanh(z/z_d), \quad (27)$$

where $\rho_m [= (\rho_> + \rho_<)/2]$ is the reference (average) density, $\rho_d [= (\rho_> - \rho_<)/2]$ the density difference, and z_d the depth of mean density variation. For the spatial distribution of unperturbed density (27), the first and second derivatives are given as

$$\frac{d\rho_0(z)}{dz} = -\frac{\rho_d}{z_d} \frac{1}{\cosh^2(z/z_d)}, \quad \frac{d^2\rho_0(z)}{dz^2} = +\frac{2\rho_d}{z_d^2} \frac{\tanh(z/z_d)}{\cosh^2(z/z_d)}. \quad (28)$$

The schematic spatial distribution of the unperturbed density, its first and second derivatives, as well as the setup considered, are depicted in Fig. 2.

With this density configuration, the second derivative is positive in the upper layer (low density region) and negative in the lower layer (high density region) as

$$\frac{d^2\rho_0}{dz^2} \begin{cases} > 0 & (z > 0, \rho_< : \text{low density}), \\ < 0 & (z < 0, \rho_> : \text{high density}). \end{cases} \quad (29)$$

It follows from (25) that the mean magnetic-field disturbance can increase in the low density (positive z) side, and decays in the high-density (negative z) side. The lower the wave number k is, the larger the growth rate of the perturbed magnetic field is.

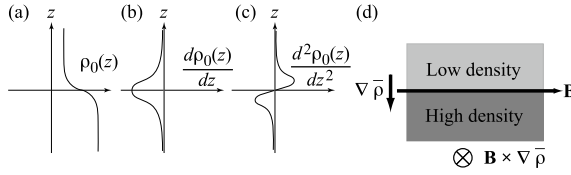


Fig. 2 Schematic spatial distributions of **a** the unperturbed density $\rho_0(z)$, **b** its first derivative with respect to z , $d\rho_0/dz$, **c** the second derivative $d^2\rho_0/dz^2$, and **d** the setup with transverse \mathbf{B}

In this sense, this magnetoclinicity effect is more suitable for producing large-scale magnetic-field structures than small-scale ones. The growth rate also depends on how much large transport coefficient χ_ρ is. The magnitude of χ_ρ reflects the magnitude of density variance $\langle \rho'^2 \rangle$. If the high χ_ρ region is spatially localised, the instability region of the large magnetic field is also spatially localised. A region with a strong mean density gradient $\nabla \bar{\rho}$ is favourable for high density variance $\langle \rho'^2 \rangle$, since $\langle \rho'^2 \rangle$ is generated by strong $\nabla \bar{\rho}$ coupled with $-\langle \rho' \mathbf{u}' \rangle$. We stress again here that although the arguments here make physical sense, a global analysis involving a two-point boundary value problem is necessary to elucidate the mechanisms.

Acknowledgements This work was supported by Japan Society for the Promotion of Science (JSPS) Grants-in-Aid for Scientific Research: 18H01212.

References

1. A. Yoshizawa, Statistical analysis of the deviation of the Reynolds stress from its eddy-viscosity representation. *Phys. Fluids* **27**, 1377–1387 (1984)
2. N. Yokoi, Turbulence, transport and reconnection, in *Topics in Magnetohydrodynamic Topology, Reconnection and Stability Theory*, ed. by D. MacTaggart, A. Hillier. CISM International Centre for Mechanical Sciences, vol. 591 (Springer, Berlin, 2020), pp. 177–265
3. N. Yokoi, Electromotive force in strongly compressible magnetohydrodynamic turbulence. *J. Plasma Phys.* **84**, 735840501-1–26 (2018)
4. N. Yokoi, Mass and internal-energy transports in strongly compressible magnetohydrodynamic turbulence. *J. Plasma Phys.* **84**, 7758140603-1–30 (2018)
5. N. Yokoi, Cross helicity and related dynamo. *Geophys. Astrophys. Fluid Dyn.* **107**, 114–184 (2013)

Beginning of Taylor's and Wavy Vortices at the Loss of Stability of a Conducting Liquid Flow Produced by the Rotating Magnetic Field



Alexander Zibold

Abstract The non-stationary instability of the axisymmetric laminar flow of a viscous incompressible conducting liquid arising in infinitely long circular cylinder under the influence of coaxially homogeneous rotating magnetic field is investigated in linear representation. Calculation of critical parameters of a flow at which the primary azimuthal flow loses stability and Taylor's or wavy vortices arise was completed. It is established, that wavy vortices can arise directly at the loss of stability of a primary flow, omitting the stage of Taylor's vortices formation. The results have been compared to those of stability of Couette flow between concentric rotating cylinders in conventional hydrodynamics.

1 Introduction

It is well known that the flows arising in technological devices under the influence of the rotating magnetic field (RMF), as a rule, are three-dimensional. At the loss of stability of primary azimuthal laminar flow, not a turbulent but secondary laminar-vortical mode appears. Thus, the system periodic along the vessel axis meridional vortices is imposed on primary laminar flow: depending on flow parameters it is either Taylor's vortices or wavy vortices. This feature of rotary flows has extremely high value for the theory and practical applications.

The nearest analogue of such type a flow is Couette flow between two concentric cylinders from which internal one rotates and external remains motionless. Analyzing stability of such flow, Lin [1] has noticed, that the first approximation equations for small perturbations of velocity and pressure allow for periodic solution with respect to φ and z :

$$f = f(r) \cdot \exp(\gamma t + in\varphi + iaz), \quad (1)$$

where n is the integer number (azimuth wave number), and a is the real (dimensionless axial wave number).

A. Zibold (✉)
Donetsk, Ukraine

Using analogy to Couette flow for a flow excitable of RMF we will consider a special case of rotary symmetry $n = 0$. In this case a primary flow is independent of φ , but disturbances of velocity u_r , u_φ , u_z and pressure q are not zero. The stability of a primary azimuthal flow and three-dimensional hydrodynamic structures of thus arising ‘Taylor’s vortices’ have been investigated by us in sufficient detail [2, 3]. With the use of Galerkin method for a wide range of flow parameters we obtained the curves of neutral stability, separating the area of one-dimensional azimuthal flow from that of the three-dimensional laminar-vortical flow. Apparently, in low-frequency approximation ($\bar{\omega} = \mu_0 \sigma \omega R_0^2 < 1$) the stability is characterized by two independent criteria— $\text{Re}_\omega = \omega R_0^2 / \nu$ and $\text{Ha}_{ac} = B_0 R_0 \sqrt{\sigma / 2\eta}$. At the increase in relative frequency there is a one-parametrical family of neutral curves depending on Prandtl magnetic number. For all investigated ranges of values of parameters of a flow calculations we got one-vortical (in the radial direction) structure of Taylor’s vortices. We studied the influence of flow parameters on the change of the characteristic size of Taylor’s vortex, and on the displacement of the centre of a vortex along cylinder’s radius.

The case of $n \neq 0$ corresponds to the occurrence of the so-called wavy vortices. In this case stability of a primary azimuthal flow in relation to non-axially symmetrical disturbances is investigated. Thus, the vortical structure is transformed in such a manner that the centres of Taylor’s vortices form a wave extending in an azimuthal direction. As the number of waves along the azimuth can be only integer it is clear why n is the integer. Initially, the stability of a primary azimuthal flow in relation to non-axially symmetrical disturbances was investigated in stationary statement [4]. It has been established, that the loss of stability of a primary flow can lead both to the occurrence of Taylor’s vortices (in sufficiently limited range of parameters of a flow), and to the occurrence of directly wavy vortices of this or that mode, bypassing of a Taylor’s vortices stage. Actually, we deal with the whole cascade of bifurcations, thus the axial wave number varies step-wise (the characteristic size of a vortical cell decreases).

In hydrodynamic experiments with the Couette flow, in some cases the motion of wavy vortices in the azimuthal direction with a certain phase angular velocity was observed. Therefore, non-stationary statement of a problem about stability of a primary flow will be more correct. Thus, contrary to the Taylor’s vortices problem, where, according to the principle of stability change in expression (1), $\gamma = 0$, the eigenvalue γ will now be complex. It describes waves, moving in an azimuthal direction with phase angular velocity $\omega_{ph} = \text{Im}\{\gamma\} / n\omega$.

2 Presentation of the Problem

Non-stationary instability of axisymmetric laminar flow of a viscous conducting liquid in infinitely long circular cylinder, arising under the influence of coaxially homogeneous RMF, is investigated in a linear statement. Stability is investigated both in relation to axially and to non-axially symmetrical disturbances. The problem is studied both in the low-frequency approximation, and for any value of relative frequency. As the most interesting results have been received in low-frequency approach, we will dwell upon such statement of a problem. In cylindrical coordinate system the problem is described by the following system of the dimensionless equations

$$\frac{\partial u_r}{\partial t} + \frac{V_{\varphi 0}}{r} \frac{\partial u_r}{\partial \varphi} - \frac{2V_{\varphi 0}u_{\varphi}}{r} = -\frac{\partial q}{\partial r} + \frac{1}{\text{Re}_{\omega}} \left(Lu_r - \frac{2}{r^2} \frac{\partial u_{\varphi}}{\partial \varphi} \right) - \frac{\text{Ha}_{ac}^2}{\text{Re}_{\omega}} u_r \quad (2)$$

$$\frac{\partial u_{\varphi}}{\partial t} + \left(\frac{dV_{\varphi 0}}{dr} + \frac{V_{\varphi 0}}{r} \right) u_r + \frac{V_{\varphi 0}}{r} \frac{\partial u_{\varphi}}{\partial \varphi} = -\frac{1}{r} \frac{\partial q}{\partial \varphi} + \frac{1}{\text{Re}_{\omega}} \left(Lu_{\varphi} + \frac{2}{r^2} \frac{\partial u_r}{\partial \varphi} \right) - \frac{\text{Ha}_{ac}^2}{\text{Re}_{\omega}} u_{\varphi} \quad (3)$$

$$\frac{\partial u_z}{\partial t} + \frac{V_{\varphi 0}}{r} \frac{\partial u_z}{\partial \varphi} = -\frac{\partial q}{\partial z} + \frac{1}{\text{Re}_{\omega}} \Delta u_z - \frac{2\text{Ha}_{ac}^2}{\text{Re}_{\omega}} u_z \quad (4)$$

$$\frac{\partial u_r}{\partial r} + \frac{u_r}{r} + \frac{1}{r} \frac{\partial u_{\varphi}}{\partial \varphi} + \frac{\partial u_z}{\partial z} = 0 \quad (5)$$

with boundary conditions

$$\mathbf{u} |_{r=1} = 0, \quad \mathbf{u} |_{r=0} < \infty, \quad (6)$$

where

$$\Delta = \frac{\partial^2}{\partial r^2} + \frac{1}{r} \frac{\partial}{\partial r} + \frac{1}{r^2} \frac{\partial^2}{\partial \varphi^2} + \frac{\partial^2}{\partial z^2}, \quad L = \Delta - \frac{1}{r^2},$$

$V_{\varphi 0} = r - \frac{I_1(\text{Ha}_{ac}r)}{I_1(\text{Ha}_{ac})}$ – a primary axisymmetric flow, arising of homogeneous RMF.

The problem (2)–(5) with boundary conditions (6) solved with use of Galerkin method. The universal computer program which allows to investigate various cases of supercritical transitions has been created. Calculation of critical parameters of a flow at which the primary azimuthal flow loses stability and at $n = 0$ Taylor’s or at $n \neq 0$ wavy vortices appear, have been completed. By results of calculations curves of neutral stability (Fig. 1), representing projections space curves of neutral stability on corresponding coordinate planes, are constructed. Instability in relation to non-axially symmetrical disturbances ($n \neq 0$) arises at lower critical parameters in

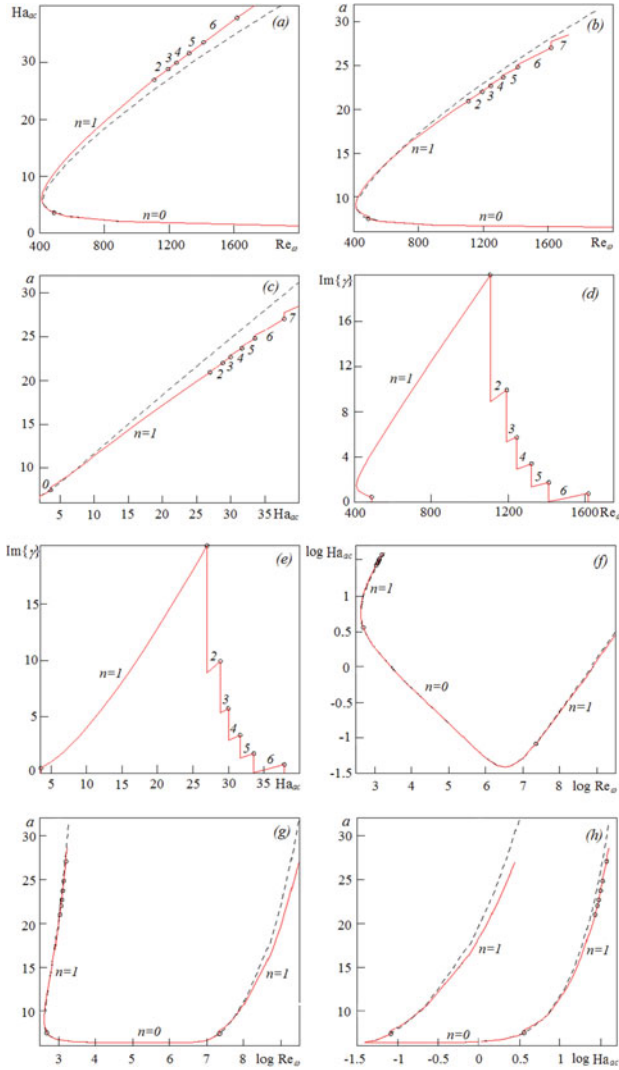


Fig. 1 Projections of curves of the neutral stability (**a–e**—low-frequency approximation): **a** in planes Re_ω, Ha_{ac} ; **b** in planes Re_ω, a ; **c** in planes Ha_{ac}, a ; **d** in planes $Re_\omega, Im\{\gamma\}$; **e** in planes $Ha_{ac}, Im\{\gamma\}$; **f** in planes Re_ω, Ha_{ac} ; **g** in planes Re_ω, a ; **h** in planes Ha_{ac}, a

comparison with a case of axially symmetrical ($n = 0$) disturbances (a dashed lines on Fig. 1). In addition to the features obtained by solving of a stationary problem of stability [4], calculations of a non-stationary problem have led to unexpected results. For sufficiently big Hartmann numbers interesting regularity has been discovered: critical numbers Re_ω coincide for various axial and neighboring azimuthal wave numbers. Calculations of $Im\{\gamma\}$ have shown that for each concrete azimuthal wave number n , $Im\{\gamma\}$ increases with the increase in the Reynolds and Hartmann numbers (Fig. 1d, e). With the increase of n in points of bifurcation, the value $Im\{\gamma\}$ (and furthermore ω_{ph}) decreases step-wise. It is logical to assume, that at coinciding critical Re_ω the variant with the least phase angular velocity ω_{ph} , so with the greatest n , will be realized. Numerical experiment has shown, that in low-frequency approach for certain ranges of Ha_{ac} change there is an area in which critical Re_ω coincide to within 4 significant digits for 4 neighboring azimuthal wave numbers (with $n = 1$ to $n = 4$). Taking into account the aforesaid it is logical to assume, that the variant with $n = 4$ (corresponding to the wave with four periods round an axis) will be the most preferable to realization. It is interesting to develop comparison with classical Couette flow in common hydrodynamics. So, for example, one of the important results of Coles experiments [5] about transitions in Couette flow was the detection of non-uniqueness of spatial structure: at the same Reynolds's number waves with various axial and azimuthal wave numbers can be observed. From Coles experiment it follows, that the wave mode with $n = 4$ is preferable. As well, the experiments of other authors confirm the special status of non-axially symmetrical mode with $n = 4$ among other modes. Apparently, noted earlier formal analogy to Couette flow has appeared to be deeper up to the similarity of the results.

It is necessary to notice, that in low-frequency approximation besides unique area with coinciding critical Re_ω for 4 neighboring azimuthal wave numbers there are areas in which critical Re_ω coincide for 2 and for 3 neighboring azimuthal wave numbers. Localisation of these areas and transitions between them are reflected in Table 1. Various conditions for Re_ω are singled out by various colours of fonts. Not realised Re_ω —a black colour; realised critical Re_ω —a red colour: possible—a font *slanted*, preferable (with maximum n)—a font **boldface**.

When solving a problem on stability of a primary azimuthal flow in statement for any values of relative frequency the numerical solution of a full induction problem about primary laminar axisymmetric flow received in [6] has been used. For wide enough investigated ranges of values of parameters of a flow only transition from Taylor's vortices ($n = 0$) to wavy vortices with azimuthal wave number $n = 1$ has been noted. Curves of the neutral stability received in low-frequency statement and for any values of relative frequency (results of calculations for $Pr_m = 10^{-6}$ are reduced) are well compatible among themselves (Fig. 1f–h).

Table 1 Critical values of the parameters characterizing the instability onset

Ha_{ac}	Re_{ω}								
	$n = 0$	$n = 1$	$n = 2$	$n = 3$	$n = 4$	$n = 5$	$n = 6$	$n = 7$	$n = 8$
0.20	65140	67190	77560						
3.59	490.8	490.9	536.6						
3.60	<i>489.9</i>	489.9	535.4	623.1					
3.62	<i>488.1</i>	488.1	533.1	620.1					
3.63	487.2	487.1	532.0	618.7					
26.95	1189	1106	1107	1108					
26.96	1189	<i>1107</i>	1107	1109	1111				
28.84	1282	<i>1192</i>	1192	1193	1194				
28.85	1283	<i>1193</i>	<i>1193</i>	1193	1194	1197			
29.97	1340	<i>1244</i>	<i>1244</i>	1244	1245	1247			
29.98	1340	<i>1245</i>	<i>1245</i>	<i>1245</i>	1245	1247	1252		
30.71	1378	<i>1279</i>	<i>1279</i>	<i>1279</i>	1279	1280	1284		
30.72	1378	1280	<i>1279</i>	<i>1279</i>	1279	1280	1284		
31.10	1398	1298	<i>1297</i>	<i>1297</i>	1297	1298	1301		
31.11	1399	1298	1298	<i>1297</i>	1297	1298	1301		
31.63	1426	1323	1322	<i>1321</i>	1321	1322	1324		
31.64	1426	1324	1323	<i>1322</i>	<i>1322</i>	1322	1325	1338	
32.40	1466	1360	1359	<i>1358</i>	<i>1358</i>	1358	1359	1371	
32.41	1467		1360	1359	<i>1358</i>	1358	1359	1371	
33.05	1501		1391	1390	<i>1388</i>	1388	1389	1399	
33.06	1501			1390	1389	1388	1389	1399	
33.55	1528			1414	1412	1411	1412	1421	
33.56	1528			1414	1413	<i>1412</i>	1412	1421	1445
34.45	1576			1457	1456	<i>1454</i>	1454	1461	1483
34.46	1577				1456	1455	1454	1461	1483
37.84	1764				1624	1620	1617	1618	1632
37.85	1765				1625	1621	<i>1618</i>	1618	1632
38.30	1790				1648	1644	<i>1640</i>	1640	1653
38.31	1791					1644	1641	1640	1653
40.00	1888					1730	1726	1723	1732

3 Conclusions

The executed research allows one to expand our views about the mechanisms of the rise in instability of the conducting liquid flow generated by the RMF in infinitely long cylindrical vessel. The results obtained thus far allow us upon the loss of stability of a primary flow, to predict the occurrence of a secondary flow in Taylor's vortices or wavy vortices of this or that mode depending on the value of the power affecting the liquid. The fact of coincidence of critical Reynolds numbers for various wave modes is noted (the conclusion about preference of a mode with the greatest value of azimuth wave number is given a reason). Apparently, noted features of beginning of Taylor's and wavy vortices would likely be true for sufficiently long cylinders of finite length as well, when it is possible to neglect the influence of end faces, on a flow in the central part of the vessel.

References

1. C.C. Lin, *The Theory of Hydrodynamic Stability* (Cambridge University Press, Cambridge, 1955)
2. A.B. Kapusta, A.F. Zibold, Stationary instability of axisymmetric flow of a liquid in a rotating magnetic field. *Magnetohydrodynamics* **13**, 312–319 (1977)
3. A.B. Kapusta, A.F. Zibold, The effect of rotating magnetic field symmetry on the stability of steady axially symmetric flow. *Magnitnaya Gidrodinamika* **17**, 134–136 (1981). (in Russian)
4. A.F. Zibold, Effect of the symmetry of a rotating magnetic field on the instability of a flow of the conducting liquid: Taylor's and wavy vortices, in *Proceedings of the 10th PAMIR International Conference- Fundamental and Applied MHD*, Cagliari, Italy, June 20–24 (2016), pp. 12–16
5. D. Coles, Transition in circular Couette flow. *J. Fluid Mech.* **21**, 385–425 (1965)
6. A.F. Zibold, A.B. Kapusta, Some results of numerical simulation of laminar flow in a rotating magnetic field. *Magnetohydrodynamics* **16**, 364–368 (1980)

Investigation of the Flow Generated by the Surface Discharge on the Cylinder Body in the Quiescent Air



A. V. Ivchenko and V. G. Shakhov

Abstract By using the shadow and PIV methods, the flow patterns induced by the surface discharge on the circular cylinder in the stationary air are presented. It is shown that the flow around cylinder is a superposition of the near-wall vortex structure and radially-propagating jets. The averaged and pulsation components of the jet velocity for two levels of discharge power consumption (8.2 and 39 W) are determined by the LDA method. Based on the analysis of the velocity pulsation spectra, the presence of two inertial intervals with decrements round ‘ $-5/3$ ’ for $f < 20\text{--}30$ Hz and ‘ -7 ’ for $f > 40$ Hz is shown. For description flow pulsating near a plasma sheet, it is proposed to use a double-cascade model of turbulence.

1 Introduction

It is well known [1, 2] that the processes in the gas boundary layer are of great importance in the flow around the bodies and influence on the physical phenomena observed here. A gas deceleration can cause instability of the boundary layer and leads to flow separation [2]. Flow separation increases aerodynamic drag, reduces heat dissipation, and increases the noise in technical systems. Therefore, the ways searching for boundary layer stabilization to cancel flow separation is urgent task.

One of the advanced methods to influence the boundary layers is associated with the surface discharge use [3–7]. According to [3–5], a surface discharge excited directly in the boundary layer is capable of not only generating 3D-disturbances [3, 7] but also forming spatially-oriented jets [4, 5]. It makes it possible to consider the surface discharges both a source of turbulence in the boundary layer and an efficient transporter of turbulence in the space. Therefore, the excitation of a surface discharge

A. V. Ivchenko (✉) · V. G. Shakhov
Samara National Research University, Moskovskoye shosse 34, 443086, Russia
e-mail: fgrt@yandex.ru

V. G. Shakhov
e-mail: shakhov@ssau.ru

changes the mechanisms of dissipation of mechanical energy in the gas and has a significant impact on the near-wall flows [3].

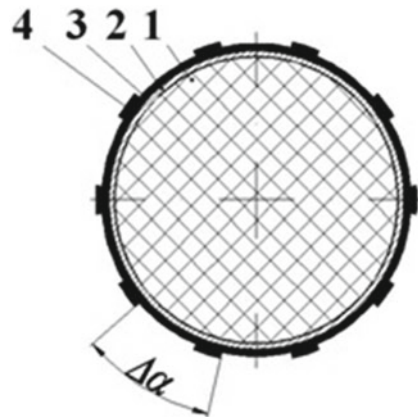
In practices, the turbulent properties of surface discharges are most realized, when gas flows around bluff bodies [6, 7]. In the paper [6], it was experimentally shown possibility of the premature laminar-turbulent transition for circular cylinder. In this case [6], the plasma ignition provides a reduction in the aerodynamic drag of the cylinder by 20–30%. However, for the validation of mathematical models, information about the characteristics of the flows caused by a surface discharge in still atmosphere under the discharge generation mode modification is necessary.

2 Methods and Instruments

Our investigation was performed by using small-size model of the circular cylinder (diameter is 32 mm, length is 150 mm) with the electrode system for surface discharge excitation (Fig. 1). During the experiments the discharge was formed on the surface of the film-type dielectric barrier with thickness $320\ \mu\text{m}$ ($\epsilon = 3.5$ and $\rho_s \approx 10^{14}\ \Omega \times \text{cm}$). For discharge excitation, the alternating voltage ($|U_a| < 4\ \text{kV}$ and $f \cong 8\ \text{kHz}$) was used. The plasma sheets formed around the perimeter of the discharge electrode (Fig. 1. pos. 4), which consisted of ten foil segments with thickness of $40\ \mu\text{m}$ deposited along the generatrix lines of the cylindrical surface. The distance between adjacent segments did not exceed 5 mm at angular step $\Delta\alpha = 36^\circ$. In this case, the discharge electrode couldn't disturb the slow flow ($V < 1\ \text{m/s}$), since its height was less than the shear layer thickness.

At excitation, the inter-electrode gaps on the cylindrical surface were formed by the similarly-charged segments of the discharge electrode that led to the colliding surface discharges generation [8]. For this reason, the surface discharges could serve as source of the jets directed along normal to the dielectric surface [5].

Fig. 1 Aerodynamic model scheme of the cylinder body:
1-cylindrical housing;
2-grounded screen;
3-dielectric barrier;
4-discharge electrode;
 $\Delta\alpha = 36^\circ$ —angular step



Measurement of discharge power consumption was produced by the method of oscilloscopic recording with the help of digital dual-link oscilloscope (PCSU1000) with the acceptance band of 60 MHz, high-voltage divisor (division ration—5000:1) and current shunt $R_{sh} = 26.5 \Omega$. The oscilloscopic data processing was based on the method [9] permitting to identify the voltage-current characteristic of discharge system and to relate the dependency of the discharge power level (Fig. 2) with the observed aerodynamic flows (see Figs. 3 and 4).

For spatial localization of the excited heat flows, optical visualization was produced by the shadow method [10]. For this purpose, the installation based on Maksutov’s optical scheme was used. To obtain the spatial distribution of velocities near cylinder, Particle Image Velocimetry (PIV) system with double-pulsed

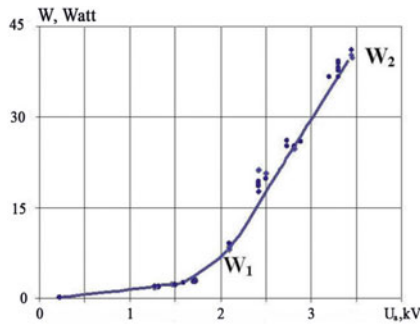


Fig. 2 Dependency of active power W versus voltage level U_a of the surface discharge electrode system on the cylinder body in the quiescent air

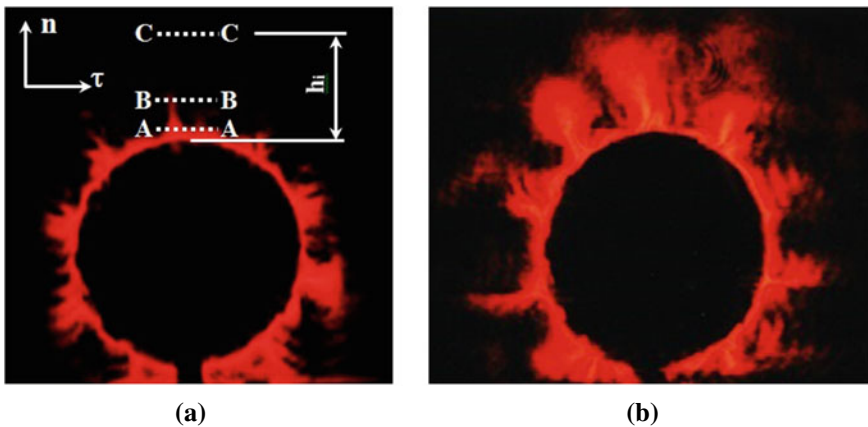
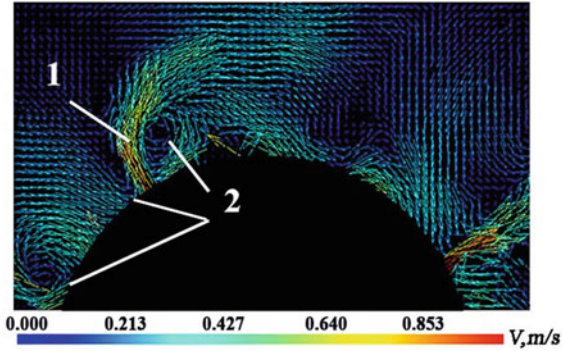


Fig. 3 Flow visualization around the cylinder body by the shadow method at the different power consumption of the surface discharge: $W_1 = 8.2 \text{ W}$ (a) and $W_2 = 39 \text{ W}$ (b). A-A, B-B and C-C lines present cross-sections for LDA-measurements at distances from the cylinder surface: $h_1 = 1 \text{ mm}$, $h_2 = 5 \text{ mm}$, $h_3 = 15 \text{ mm}$ respectively

Fig. 4 Instant PIV data on flow velocity distribution in vicinity of cylinder body under surface discharge action: 1-jet, 2-vortex structure. Registration mode: illumination laser pulse energy is 45 mJ, laser pulses frequency is 8 Hz. Discharge power consumption is $W_2 = 39$ W



frequency laser (Solo-150TX) and camera (Flow Sens-2 M) was applied. While the pulsating flow parameters were determined by Laser Doppler Anemometry (LDA) [11] with help of a laser anemometer (LAD-056C) acting in 2D-mode. Thus, the presented combination of LDA and PIV devices allowed us to determine the average velocity field in the vicinity of the cylinder body as well as parameters of flow pulsations at the predetermined points [11, 12].

3 Results

The flow visualization in the vicinity of the cylinder under surface discharge action showed the presence of a near-wall vortex structure and radially-oriented jets (see Figs. 3 and 4). With an increase in the discharge power consumption, an intensification of the jet process was observed. When the discharge power consumption was reached 39 W, the jets propagated over a distance up to 15–20 mm leaving near-wall area and pushing the gas away from the cylinder.

Quantitative measurements of the averaged and pulsation jet velocity components were performed by the LDA method along three lines located at the different distances (h_i) from cylinder (Fig. 3a). The selected lines were positioned above the central part of the aerodynamic model, where flow had a two-dimensional flow structure.

The velocity registration was carried out by sequential scanning of the selected lines with using the stepper motors of LAD-056. Step between two neighboring spots in each line did not exceeded of 1 mm. For the accumulation of statistical data, in each spots it was recorded no less than 4096 reliable Doppler's flashes caused by passage of oil particles through the measuring volume ($0.05 \times 0.05 \times 1$ mm). For frequent appearance of particles in the measuring volume, the cylinder was placed in a glass box ($700 \times 400 \times 300$ mm) to provide the high-density oil smog.

The data on the averaged flow velocity components are presented in Figs. 5 and 6. The flow velocity profiles qualitatively marched the data given in [5]. In center of the inter-electrode gap we observe the normal-oriented jet while in peripheral areas there are counter flows. Flow properties depended on the discharge power consumption.

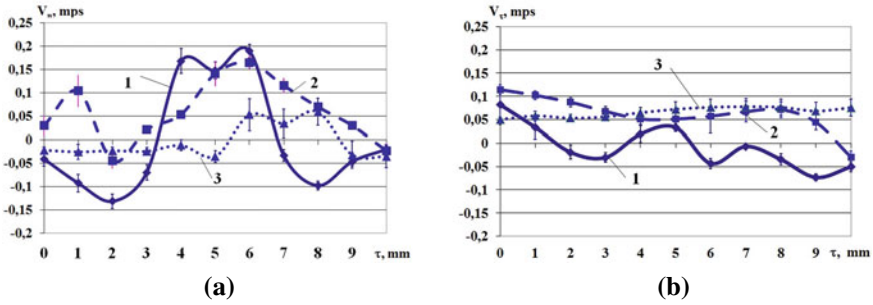


Fig. 5 The tangential (a) and normal (b) components of the averaged flow velocities near cylinder (based on LDA-measurements) at the discharge power consumption $W_1 = 8.2$ W: $1-h_1 = 1$ mm, $2-h_2 = 5$ mm, $3-h_3 = 15$ mm

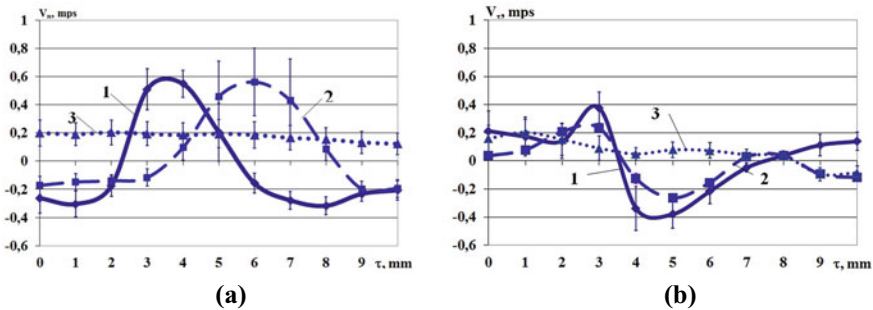


Fig. 6 The tangential (a) and normal (b) components of the averaged flow velocities near cylinder (based on LDA-measurements) at the discharge power consumption $W_2 = 39$ W: $1-h_1 = 1$ mm, $2-h_2 = 5$ mm, $3-h_3 = 15$ mm

At $W_1 = 8.2$ W (Fig. 5) the normal component of flow doesn't exceed of 0.25 m/s while at $W_2 = 39$ W it reaches of 0.8 m/s (Fig. 6). Also these graphs (Figs. 5 and 6) demonstrate that the flow turbulence for W_1 is greater than for W_2 . This is confirmed by the measured values of the velocity dispersion.

The spectral analysis of the velocity pulsation components was carried out by technique described in [13, 14]. Figure 7 shows modification of mean power spectral density (MPSD) of velocities pulsating component in center of the inter- electrode gap under surface discharge action. The obtained spectra demonstrate localization of turbulent pulsations in the range of 0–80 Hz and their intensification with discharge power consumption growth.

By analyzing the spectra in the Fig. 7, we can observe two inertial intervals which indicate a double-stage process of energy dissipation in initial part of the gas jet.

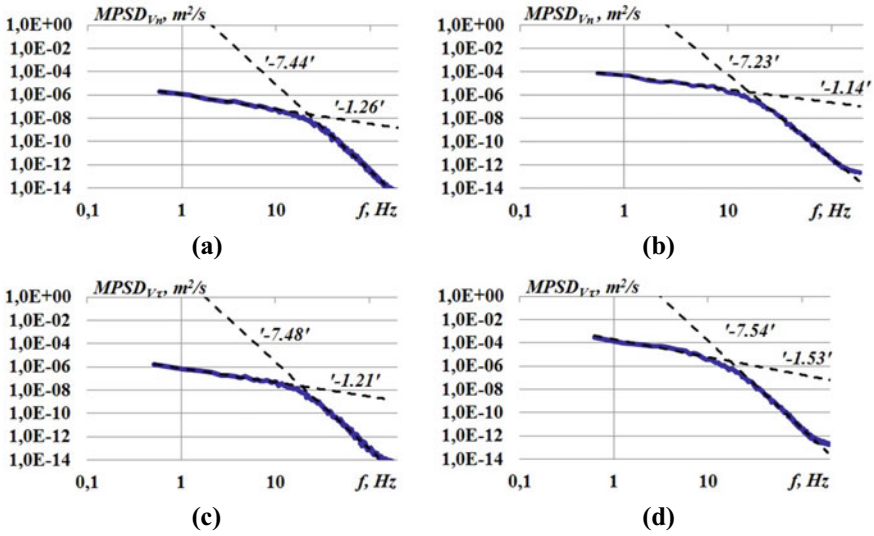


Fig. 7 Mean power spectral density for normal (a), (b) and tangential (c), (d) velocities pulsating components in the center of inter-electrode gap (distance from cylinder is 1 mm) at the different discharge power consumption: a, c $W_1 = 8.2$ W, b, d $W_1 = 39$ W

4 Conclusions

1. To reveal the structure of the flow excited by the surface discharge in the vicinity of a circular cylinder in the quiescent air, the visualization was performed by using the shadow and PIV methods. The obtained pictures demonstrate the vortex structure formation near cylindrical surface under surface discharge action with power consumption around 8 W. While discharge power consumption growth (up to 40 W) provides the generation of radial jets that leave near-wall area around cylinder.
2. The distributions of flow velocity components for near-wall jet under surface discharge action were obtained by using LDA method. The flow velocity profiles near cylindrical surface ($h \cong 1-5$ mm) have analogical structure to flow obtained in case of the flat surface discharge electrode system [5]. Moreover, in both cases, the structure of the jet is similar to the structure of the jets formed in counter flows [15].
3. Based on the spectral analysis data, it was shown that MPSD has two inertial intervals with different values of decrements. The decrements are weakly dependent on the power consumption of the surface discharge and on the orientation of the velocity component. The decrements vary in the range $(-1.14-1.53)$ for the low-frequency interval ($f < 20-30$ Hz) and in the range $(-7.23-7.54)$ for the high-frequency interval ($f > 40$ Hz) of the spectra. According to [16], the obtained values match to well-known theoretical laws. For our conditions, we

believe it is expedient to use the double-cascade turbulence model [16] for flows description excited by surface discharge with Kolmogorov's law (decrement is $'-5/3'$) [17] for low-frequency cascade and with Heisenberg's law (decrement is $'-7'$) [18] for high-frequency cascade.

References

1. H. Schlichting, K. Gersten, *Boundary Layer Theory*, 8th edn. (Springer, Berlin, 2003)
2. P.K. Chang, *Control of Flow Separation* (Hemisphere Publishing Corporation, New York, 1976)
3. S. Grundmann, C. Tropea, Experimental damping of boundary-layer oscillations using DBD plasma actuators. *Int. J. Heat Fluid Flow* **30**, 394–402 (2009)
4. T.C. Corke, M.L. Post, D.M. Orlov, SDBD plasma enhanced aerodynamics: concepts, optimization and applications. *Prog. Aerosp. Sci.* **43**, 193–217 (2007)
5. N. Benard, J. Jolibois, E. Moreau, R. Sosa, G. Artana, G. Touchard, Aerodynamic plasma actuators: a directional micro-jet device. *Thin Solid Films* **516**, 6660–6667 (2008)
6. A.V. Ivchenko, O.A. Zhuravliov, V.G. Shakhov, Comparative studies of cylinder's aerodynamic features depending on propagation direction for the non-arcing surface discharge in subsonic flow, in *Europhysics Conference Abstracts*, vol. **33E** (2009), pp. 1–4
7. H. Akbıyık, Y.E. Akansu, H. Yavuz, Active control of flow around a circular cylinder by using intermittent DBD plasma actuators. *Flow Meas. Instrum.* **53**, 215–220 (2017)
8. A.V. Ivchenko, P.E. Timchenko, V.P. Zakharov, V.L. Marinin, The properties of colliding surface discharges in air, in *Europhysics Conference Abstracts*, vol. **36F** (2012), pp. 1–4
9. V. Samoilovich, V. Gibalov, K. Kozlov, Physical chemistry of the barrier discharge, DVS (1997)
10. G.S. Settles, *Schlieren and Shadowgraph Techniques: Visualizing Phenomena in Transparent Media* (Springer Science & Business Media, Berlin, 2012)
11. Z. Zhang, *LDA Application Methods: Laser Doppler Anemometry for Fluid Dynamics* (Springer Science & Business Media, Berlin, 2010)
12. M. Raffel, C.E. Willert, J. Kompenhans, *Particle Image Velocimetry: A Practical Guide* (Springer Science & Business Media, Berlin, 2001)
13. B. Kysela, J. Konfrest, Z. Chara, LDA measurements and turbulence spectral analysis in an agitated vessel. *EPJ Web Conf.* **45**, 1–7 (2013). Article 01055
14. S. Moreau, G. Plantier, J.-C. Valière, H. Bailliet, L. Simon, Estimation of power spectral density from laser Doppler data via linear interpolation and deconvolution. *Exp. Fluids* **50**, 179–188 (2011)
15. G.N. Abramovich, *Turbulent Jets of Air, Plasma, and Real Gas* (Springer, Berlin, 2013)
16. P.G. Frick, *Turbulence: Approaches and Models* (2nd edn. in Russian) ('R&C Daynamis' Publish House, 2010)
17. U. Frisch, A.N. Kolmogorov, *Turbulence: The Legacy of A. N. Kolmogorov* (Cambridge University Press, Cambridge, 1995)
18. J.O. Hinze, *Turbulence an introduction to its mechanism* (McGraw-Hill Book Company, Inc., New York, 1959)

Numerical and Physical Aspects of Large-Eddy Simulation of Turbulent Mixing in a Helium-Air Supersonic Co-flowing Jet



Alexey Troshin, Sergey Bakhne, and Vladimir Sabelnikov

Abstract This paper addresses a long-standing problem of dissimilar gas mixing prediction within large-eddy simulation approach. A series of simulations was carried out of A.D. Cutler et al. experiment (NASA Langley Research Center) in which a supersonic helium jet issuing into air co-flow was studied. Grid convergence analysis was performed. Variations of turbulent (subgrid-scale) Schmidt number and numerical scheme were done. All these attempts were unsuccessful in approaching the experimental data, including the simulation performed on a grid consisting of 83 million cells. After that, the subgrid length scale was increased, which finally led to agreement with the experimental data in the considered flow region. Physical guesses are given as to why this parameter had a positive effect on the simulation results and what consequences can be derived from this.

1 Introduction

Large-eddy simulation (LES) is a popular high-fidelity tool for studying both canonical and complex flows in many areas. It is of great importance to validate numerical schemes and physical models used in LES. Consequently, there is need for high-quality reference experimental and DNS databases. The data published in [4] is such an example: a careful experimental study of supersonic helium jet in a co-flowing air stream was carried out and a detailed database was created. This database is used in the current study to evaluate LES potential in the area of high-speed variable-density turbulent mixing. To the best of our knowledge, there are no published LES studies of [4] which agree with the experiment, see e.g. [2]. At the iTi Conference 2018, we

A. Troshin (✉) · S. Bakhne · V. Sabelnikov
Central Aerohydrodynamic Institute (TsAGI), Zhukovsky, Russia
e-mail: ai-troshin@yandex.ru

V. Sabelnikov
e-mail: sabelnikov@free.fr

A. Troshin · S. Bakhne
Moscow Institute of Physics and Technology, Dolgoprudny, Russia

presented [11] the first results of our assessment of LES on the database [4] and also received systematic discrepancies with experiment in helium jet mixing intensity. The jet spreading rate was overestimated by a factor of almost 2. In that study, a single computational grid and a single numerical scheme was used. The failure to predict mixing intensity encouraged us to systematically study the possible reasons for the discrepancies, and the results are presented in the current paper.

2 Test Case and Numerical Setting

In the experiment [4], a round cold helium jet issued into a co-flow air stream. The nozzles forming these streams were designed for operating at Mach number 1.8. Due to differences in molecular weights, gas velocities at nozzle exits were significantly different. The flow regime that was used in the simulations is presented in Table 1. These parameters were used at the inlets of the supplying channels.

Characteristic flow time scale was taken to be $t_{char} = D_{out}/U_{out} \approx 1.2 \times 10^{-4}$ s, where $D_{out} = 60.47$ mm is outer nozzle diameter and $U_{out} \approx 485$ m/s is gas velocity at the outer nozzle exit. In LES, statistically steady flow was established during the period of $\Delta t = 20t_{char}$. After that, statistical data was collected during $\Delta T = 100t_{char}$ (fine grid), $200t_{char}$ (medium grid), and $300t_{char}$ (coarse grid).

All the simulations were carried out with the use of in-house computational code *zFlare* which is part of software package EWT-TsAGI [3]. The code is focused on solving unsteady combustion problems within URANS and DES/LES approaches on multiblock structured grids. For the present simulations, hybrid spatial approximation was adopted which blends upwind-biased WENO5 scheme with MP limiter in RANS regions and central difference scheme in LES regions. The blending function was taken from [6]. Base central difference scheme had 4th order (denoted “CD4” hereinafter), but 2nd order scheme (“CD2”) was also considered, as well as a scheme obtained by taking half-sum of WENO5 reconstructions on a cell face, leading to 6th order in smooth flow regions (“symm” scheme). Time integration was done with explicit 2nd order scheme, with time step varying between $1.25 \times 10^{-4}t_{char}$ and $5.0 \times 10^{-4}t_{char}$ depending on the grid. The computational domain and imposed

Table 1 Flow regime specified in the simulations

Flow parameter	Core jet	Co-flow jet	Ambient surroundings
Composition	95% He + 5% O ₂ by volume	Pure air	Pure air
Static temperature T , K	303.45	299.75	294.6
Static pressure p , Pa	615 000	578 300	100 130
Streamwise velocity U , m/s	141.50	22.63	10.0

boundary conditions were the same as in [11]. 3 nested grids were constructed, consisting of 1.3 mln, 10 mln and 83 mln cells. The medium grid was the same as in [11]. The hybrid model was SST-DDES [5] with shear-layer adapted length scale [10]. The model acted in LES mode everywhere except in the turbulent boundary layers inside the nozzle, where small RANS zones were located.

The SST-DDES model uses a hybrid length scale

$$l_{DDES} = l_{RANS} - f_d \max\{0, l_{RANS} - l_{LES}\},$$

from which a dissipation rate $\varepsilon = \bar{\rho} k^{3/2} / l_{DDES}$ entering the turbulent kinetic energy equation is determined. Here, $l_{RANS} = k^{1/2} / (0.09 \omega)$ is a length scale of SST [8] turbulence model, $l_{LES} = C_{DES} \tilde{\Delta}_\omega$ is a subgrid length scale (details of $\tilde{\Delta}_\omega$ definition can be found in [10]), and f_d is a delay function that keeps the model in RANS mode in the boundary layer regardless of the grid spacing. The subgrid length scale contains a coefficient $C_{DES} = F_1 C_{DES1} + (1 - F_1) C_{DES2}$ which varies between its near-wall value C_{DES1} and free-stream value C_{DES2} by means of SST blending function F_1 . The optimal values of C_{DES1} and C_{DES2} depend on the numerical scheme. Based on the simulations of isotropic turbulence in a periodic box, C_{DES2} was taken equal to 1.0. Since C_{DES1} coefficient is of no significance in the current flow, it was set equal to C_{DES2} , making C_{DES} constant.

Most of the simulations were run on HPC cluster with 24 Intel Xeon E5-2680v3 CPUs. Several runs were done on the ‘‘Lomonosov’’ supercomputer [9].

3 Simulation Results

In the present study, we focus on the inner (helium) jet. The instantaneous helium mass fraction fields obtained on three grids are shown in Fig. 1. It is clearly seen how the spatial resolution is increased with that of the grid. Despite a big difference in the grid resolution, one can note that potential core length is nearly the same.

In Fig. 2a, axial distributions of time-averaged helium mass fraction are depicted. On all grids, helium mass fraction falls too rapidly, indicating excessive mixing. Up to $x/D = 15$ from nozzle exit ($D = 10$ mm is inner nozzle diameter), medium grid solution is sufficiently close to the fine grid, in contrast to the coarse one. Even with the fine grid, too rapid mixing is predicted, and it looks like further grid refinement would not help, unless DNS limit is reached. The same mixing overestimation was observed in our previous study [11] and by other authors [2].

Attempts were made to vary different parameters and find out which of them can influence the mixing intensity. Hereinafter, all the results are obtained on medium grid. First, we tried to vary turbulent (subgrid-scale) Schmidt number from 0.5 to 2 and could not find any significant differences between solutions, see Fig. 2b. This may indicate that subgrid model of mass diffusion is not responsible for the incorrect behavior. We tried to vary central difference part of the scheme (which is active in

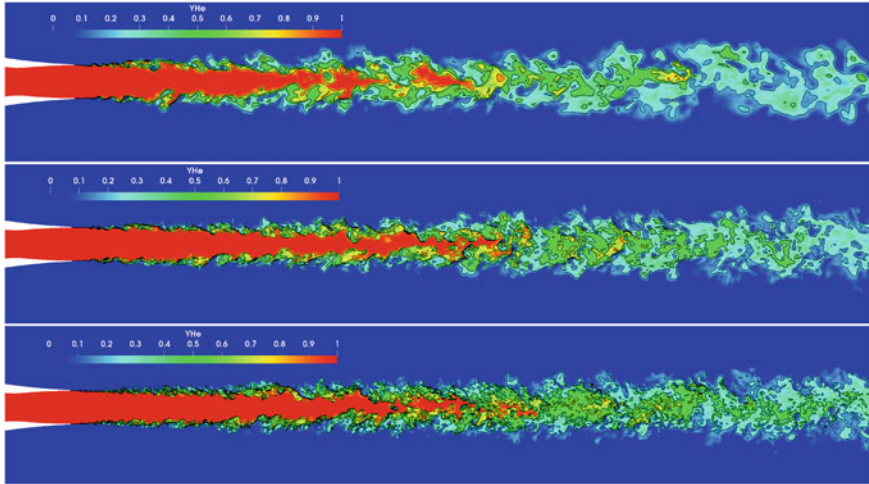


Fig. 1 Helium mass fraction fields on coarse (top), medium (middle) and fine (bottom) grids

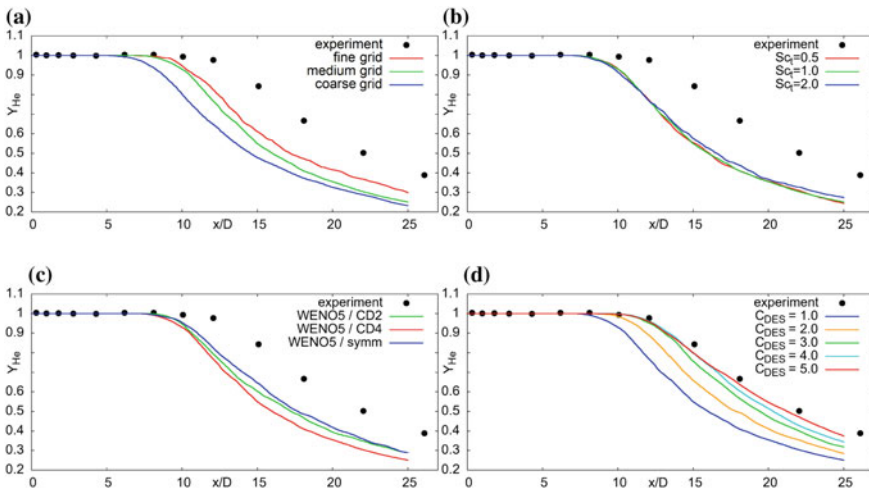


Fig. 2 Influence of simulation parameters on axial distribution of time-averaged helium mass fraction. **a** Grid density. **b** Subgrid-scale Schmidt number. **c** Numerical scheme. **d** Value of C_{DES}

LES region). Indeed, switching to “CD2” and “symm” schemes changed solution a little (see Fig. 2c), but clearly insufficiently to get close to the experiment.

After that, we tried to vary the C_{DES} coefficient entering the subgrid length scale (see Sect. 2). The results are presented in Fig. 2d. Strikingly, we were able to approach experimental data with C_{DES} as high as 5! This is a counter-intuitive result: to reduce the overall diffusion rate, we had to increase the subgrid mixing. As can be seen from Fig. 3, starting from $C_{DES} = 3$, potential core length is captured adequately, and with

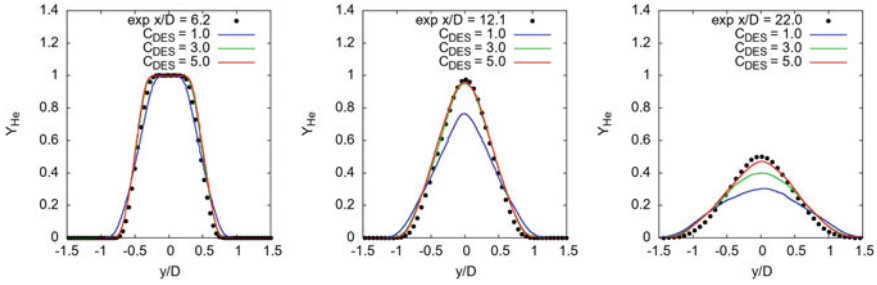


Fig. 3 Time-averaged helium mass fraction in different cross-sections of the jet

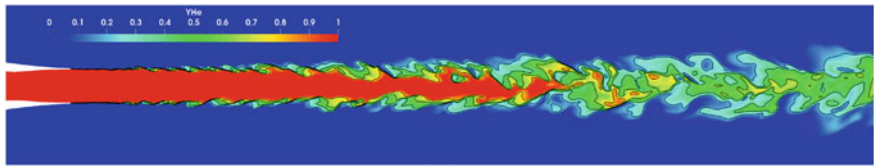


Fig. 4 Instantaneous helium mass fraction fields on medium grid with $C_{DES} = 5$

even higher values of this coefficient, the solution improves further downstream. With C_{DES} equal to 3, the solution follows the experiment up to $x/D = 12$, while $C_{DES} = 5$ allows to fit the data up to at least $x/D = 25$.

An instantaneous helium mass fraction field obtained on the medium grid with $C_{DES} = 5$ is shown in Fig. 4. Compared to Fig. 1, small-scale structures are filtered out. Given the fact that numerical scheme errors are most prominent on the smallest scales, by increasing C_{DES} we somehow change the scheme behavior, probably masking its errors behind the subgrid-scale model.

Why scheme errors lead to excessive diffusion? Some guesses follow from a recent DNS [1] of variable-density temporal mixing layers. In nearly-constant density case, the mixing layer is symmetrical. When the density ratio is high, strong asymmetry arises. Mixing layer tends to develop preferentially towards light fluid, its growth rate being lower than in constant-density case. With a central difference scheme, approximation errors are spatially symmetrical, which is probably unsuitable for taking into account the asymmetrical variable-density effects. On the other hand, subgrid viscosity model explicitly depends on the density field, which may be better suitable for description of dissimilar gas mixing.

4 Conclusions

It is shown that to capture the mixing details adequately, subgrid-scale model should be adjusted to provide an appropriate length scale. On the one hand, the requirement remains that the length scale falls within the inertial range. On the other hand, it

makes no sense to maximize the spatial resolution of the simulation on a given grid: the filter should be sufficiently large to suppress scheme errors, in the present test case 5 times larger than the cell size. It is reasonable to expect that not only SST-DDES, but also other hybrid and subgrid-scale models may require similar adjustments of subgrid length scale in the considered class of flows.

The exact reason for the need to modify the subgrid-scale model has not yet been investigated. The issue is assumed to have numerical nature, but it may turn out to be physical as well [7]. This is an area for further research.

Acknowledgements The research was supported by the Ministry of Education and Science of Russian Federation (“megagrant”, agreement No. 14.G39.31.0001).

References

1. J.R. Baltzer, D. Livescu, Variable-density effects in incompressible non-buoyant shear-driven turbulent mixing layers. *J. Fluid Mech.* **900**, A16 (2020)
2. R.A. Baurle, J.R. Edwards, Hybrid Reynolds-averaged/large-eddy simulations of a coaxial supersonic freejet experiment. *AIAA J* **48**, 551–571 (2010)
3. S. Bosnyakov, I. Kursakov, A. Lysenkov, S. Matyash, S. Mikhailov, V. Vlasenko, J. Quest, Computational tools for supporting the testing of civil aircraft configurations in wind tunnels. *Prog. Aerosp. Sci.* **44**, 67–120 (2008)
4. A.D. Cutler, G.S. Diskin, J.P. Drummond, J.A. White, Supersonic coaxial jet experiment for computational fluid dynamics code validation. *AIAA J* **44**, 585–592 (2006)
5. M.S. Gritskevich, A.V. Garbaruk, J. Schütze, F.R. Menter, Development of DDES and IDDES formulations for the $k-\omega$ shear stress transport model. *Flow Turbul. Combust.* **88**, 431–449 (2012)
6. E.K. Guseva, A.V. Garbaruk, M.K. Strelets, An automatic hybrid numerical scheme for global RANS-LES approaches. *IOP Conf. Ser.: J Phys: Conf Ser.* **929**, 012099 (2017)
7. C.C.K. Lai, J.J. Charonko, K. Prestridge, A Kármán-Howarth-Monin equation for variable-density turbulence. *J. Fluid Mech.* **843**, 382–418 (2018)
8. F.R. Menter, Review of the shear-stress transport turbulence model experience from an industrial perspective. *Int. J. Comput. Fluid Dyn.* **23**(4), 305–316 (2009)
9. V. Sadovnichy, A. Tikhonravov, V. Voevodin, V. Opanasenko, “Lomonosov”: supercomputing at Moscow State University, in *Contemporary High Performance Computing: From Petascale Toward Exascale* (CRC Press, Boca Raton, 2013), pp. 283–307
10. M.L. Shur, P.R. Spalart, M.K. Strelets, A.K. Travin, An enhanced version of DES with rapid transition from RANS to LES in separated flows. *Flow Turbul. Combust.* **95**, 709–737 (2015)
11. A. Troshin, A. Shiryayeva, V. Vlasenko, V. Sabelnikov, Large-eddy simulation of helium and argon supersonic jets in supersonic air co-flow, in *Progress in Turbulence VIII. Proceedings of iTi Conference on Turbulence*, vol. 2018 (2019), pp. 253–258

Turbulent Energy Production in the Boundary Layer of a Gas Flow Near the Free Surface of a Liquid



A. Goltsman and I. Saushin

Abstract Structure of the boundary layer on the air-water interface at the initial tremor-wavelet transition has been experimentally studied. The flow characteristics using the Smoke Image Velocimetry (SIV) optical technique with high temporal and spatial resolution have been measured. The analysis of the obtained results has been showed that the occurrence of an initial tremor-wavelet transition at the interface leads to a local production of turbulence energy into the boundary layer. This phenomenon, by analogy with the theory of flow around rough surfaces, is due to the excess of the wave height over the thickness of the laminar region of the boundary layer. However, due to the exponential growth of the wave height, the extremum of the energy production occurs with a spatial delay depending on the boundary conditions of the problem and the properties of continuous media.

1 Introduction

A gas flow around an interface with a liquid can be called one of the branches of the turbulent boundary layer theory. As for the classical boundary layer on a solid smooth or rough surface, the velocity profiles in gas/liquid interface flow obey the similarity law. However, the mutual influence of the shape of the interphase surface on the velocity profiles significantly complicates the flow process. The wave generation (the length of which can range from 4 to 40 cm [1] at the interface, their frequency, amplitude and velocity of movement are mainly determined by the dynamic pressure of the gas flow and the viscosity of the liquid. This problem, for example, is relevant for the flow of two-phase mixtures in mains, where the revelation of waves at the interface significantly increases the pressure drop [2] and can lead to the appearance

A. Goltsman (✉) · I. Saushin
Institute of Power Engineering and Advanced Technologies, FRC Kazan Scientific Center,
Russian Academy of Sciences, ul. Lobachevskogo, 2/31, Kazan, Tatarstan, Russian Federation
e-mail: an116ya@mail.ru

I. Saushin
e-mail: ilyasaushin@mail.ru

of plugs. A more global example related to the effect of the shape of the interface of the ocean surface on the transfer of heat, momentum and mass with the atmosphere, which determines large-scale weather events, can also be cited. A large number of experimental, analytical and numerical papers on this topic clearly show the non-triviality of the above problem.

The analytical solution of this problem is greatly complicated by the mathematical formulation of the boundary condition at the interface, where necessary assumptions strongly idealize the real picture. Therefore, the results of analytical solutions give only qualitative information, which is difficult to compare with the results of experiments. However, theoretical studies made it possible to formulate the main mechanisms of generation of surface waves, to distinguish the linear and exponential modes of their growth.

Due to the known complexity of numerical simulation of multiphase flows, a solution was obtained for a single-phase statement, that is, the effect of one of the phases on the other was investigated most often. Only a few papers have solved the problem numerically in a two-phase statement [3–6].

In contrast to analytical and numerical statements, experimental studies do not need most of the assumptions, but for this problem they are quite complex in technical terms. For the above reason, in each of the experimental studies, as a rule, one problem was considered: conditions for separation of the boundary layer, mechanisms of wave generation and propagation, and shear stresses at the interface, average or phase dynamics of air flow and its characteristics, the physical processes of the transfer of momentum and heat across the interface.

Numerous experimental works have clearly recorded the effect of a developed wave flow on the boundary layer of the air flow. The classification of waves [7] identifies three wave modes: initial tremor, initial wavelet, and sea wave with transient critical values of $u_\tau H/\nu = 0.3$ and $u_\tau H/\nu = 200$, respectively (where H is the average wave height, ν is the kinematic viscosity of air). In turn, the initial wavelet class at $u_\tau H/\nu = 6$ is divided into two subclasses, earlier stage and later stage. The present paper tries to fill a small scientific gap in the studies of the evolution of a turbulent boundary layer when flowing around an interface with a calm liquid, namely, at the moment of the first appearance of waves—during the initial tremor-wavelet transition. This transition was previously studied exclusively from the point of view of the dynamics of the interface, without considering the effect of the gas flowing around it on the boundary layer. Perhaps the appearance of small waves suggests that they are unable to influence the turbulent boundary layer. However, as the present study has shown, the moment of appearance of the initial wavelet is due to interesting local changes in the boundary layer, the traces of which are lost in the flow direction with the development of wind-wave impact.

2 Experimental Setup and Method

The experiments were carried out in the Hydrodynamics and Heat Transfer Laboratory of the Kazan Scientific Center of the Russian Academy of Sciences. The test section was a rectangular $130 \times 150 \text{ mm}^2$ channel with the length of 2000 mm (Fig. 1). Instead of the lower wall of the channel, at a distance of 40 mm from the inlet section, a rectangular water cavity with a height of 120 mm and a length of 1700 mm was installed. In order to prevent liquid splashing, the back wall of the cavity was increased to 145 mm, and the height of the outlet air channel was accordingly reduced to 105 mm. All walls of the test section were made of 5 mm thick glass. For convenient cleaning of glass surfaces, the upper wall of the channel was removable and was fixed with a sealant during experiments.

To ensure a uniform velocity profile in the test section, in front of the entrance, there was a smooth inlet with 6:1 contraction along the y coordinate (Fig. 2). The walls of the smooth inlet were profiled by a Bernoulli lemniscate and were made of flexible plexiglass. Air entered the smooth inlet section from a 2 m^3 air-aerosol mixture preparation chamber, where clean atmospheric air (20°C , 1.2 kg/m^3) was mixed with aerosol particles by a generator (MT-Gravity fluid with medium fog density and average particle size of $0.1 \dots 5 \mu\text{m}$; Safex aerosol generator). A 1.99 m^3 cylindrical receiver was mounted at the exit from the test section. The air flow rate ($206 \text{ m}^3/\text{h}$) was controlled using a set of critical nozzles with an uncertainty of no more than 0.25%. The required pressure drop for the operation of the nozzles was provided using an air compressor. The flow pattern was recorded by a monochrome high-speed camera Fastec HiSpec with the frame resolution of 1088×140 pixel

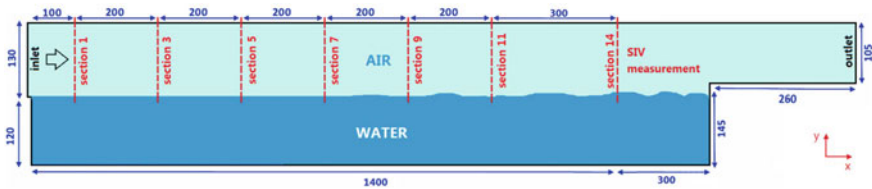


Fig. 1 Test section of experimental setup

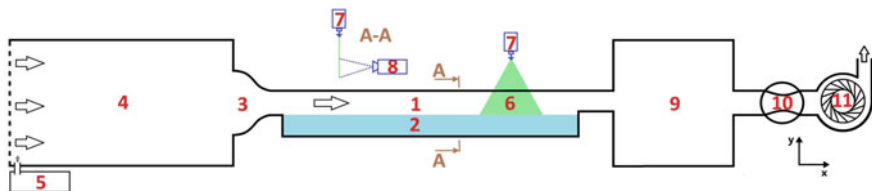


Fig. 2 Experimental setup; 1 test section of air flow, 2 cavity with calm water, 3 smooth inlet, 4 air-aerosol mixture preparation chamber, 5 aerosol generator, 6 measurement area, 7 continuous laser, 8 high-speed camera, 9 receiver tank, 10 set of critical nozzles, 11 air compressor

(scaling factor of 0.03 mm/pixel), frame rate $f = 5692$ 1/s, and recording time of 3.5 s. The camera was equipped with a Navitar 1''F/0.95 lens (focal length 25 mm, manual focus). The measurement area was illuminated by a continuous diode-pumped solid-state laser KLM-532/5000-h. The camera and laser were fixed in the coordinating device and synchronously moved along the test section. The measurements were carried out in seven sections, Fig. 1. The last section was at a distance of 300 mm—12 heights of the forward facing step before the contraction of the channel. This distance was sufficient to suppress the hydraulic effect of the contraction on the velocity profiles in the last section. Therefore, the velocity of the external flow in all measurement sections theoretically should have been constant. Subsequently, this statement was also confirmed by the measurement results. To measure the dynamics of instantaneous velocity fields, the Smoke Image Velocimetry (SIV) method [8] was used.

3 Results

Probably the first and main question concerning the velocity profile in the interface flow was the question of maintaining the logarithmic section of log law. Indeed, for the flow around a smooth plate, the self-similarity of the Reynolds velocity and stress profiles is known (starting with $Re_\theta \approx 450$ and higher). One of the first mentions of the non-fulfillment of the classical 1/7 power-law in the flow around the interface can be found in [7].

Figure 3b shows that the velocity field U^+ can be divided into three areas. In the first section $0.5 < F \leq 1$ m, where an initial tremor-wavelet transition occurs at $F = 0.65$ m, we observe an almost self-similarity of the U^+ profiles along the interface (Fig. 3c) and the identity of the velocity field with the field around a smooth wall (Fig. 3a). Further, on the interval of $1 < F \leq 1.4$ m, the U^+ profiles begin to slowly decrease closer to the boundary layer edge, and a small kink appears in the region of $y^+ \approx 20$. In order to show the further evolution of the U^+ profiles, we added to the graph the results of measurements [9, 10] carried out at similar air velocities at $F = 2.1$ m and $F = 22.7$ m, respectively. In the interval $F > 2$ m, there is already a significant decrease of the U^+ velocity profiles compared to the case of flow around the plate, and further downstream there is a tendency to form a self-similar boundary layer. It is known that in flow around the interface, such a deviation of the U^+ profile is facilitated by two factors: an increase in air velocity and wave slope [9, 11, 12]. Therefore, since the data in Fig. 3 were obtained at a constant air velocity, here we are dealing directly with the second cause.

As is well known, the turbulence production in the boundary layer is mainly due to the spatial gradient of the velocity field. When flowing around an initially smooth interface, there is a critical state of the appearance of an initial wavelet at $F = 0.65$ m. The initial wavelet leads to an increase in the U^+ gradient along the boundary layer thickness in the region of $y^+ \approx 12...30$ only to the $F = 1$ m section (Fig. 3c). From this region the interval of significant growth of $u'u^+$ subsequently affected almost

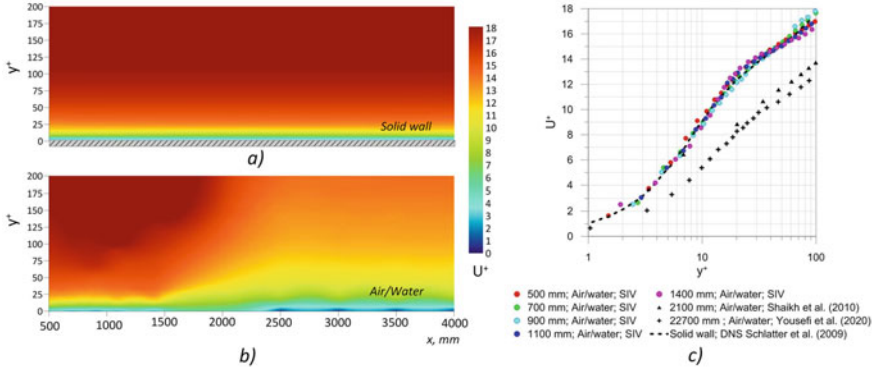


Fig. 3 U^+ velocity component along x coordinate; **a** field in the developed flow around a smooth plate; **b** field in flow around the interface; **c** velocity profiles

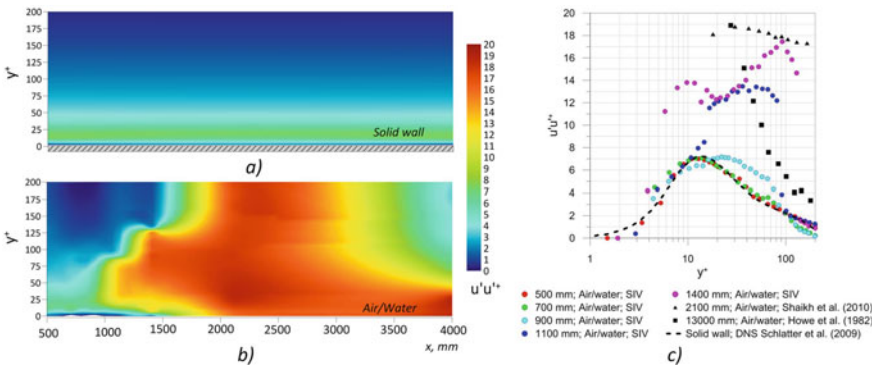


Fig. 4 Turbulent velocity pulsations $\overline{u'_i u'_j}^+$; **a** field in the developed flow around a smooth plate; **b** field in flow around the interface; **c** velocity profiles

the entire thickness of the boundary layer begins, and it continues until a new self-similarity of the U^+ profiles is revealed (Fig. 4). When the flow regime is established, the $\overline{u'_i u'_j}^+$ profiles in comparison with the case of flow around a smooth plate differ by an almost threefold increase in values in the region of the extremum (buffer sublayer). The $\overline{v'_i v'_j}^+$ and $\overline{u'_i v'_j}^+$ fields are very similar to each other and, in general, retain the same tendency as $\overline{u'_i u'_j}^+$.

4 Conclusion

The boundary layer along an initial tremor is essentially no different from the case of a smooth wall. This is mainly due to the fact that the initial tremor wave height is significantly lower than the laminar sublayer thickness. From the theory of the

boundary layer along a rough surface, the interface is hydraulically smooth. If the air flow velocity is higher than the critical one (2–4 m/s), the wave height will gradually increase to 0.05 mm and the transition from the initial tremor to the initial wavelet will take place (where the wave height grows exponentially). As long as the wave height does not exceed the thickness of the laminar sublayer, there will be no significant changes in the boundary layer. Therefore, the effect of the transition from the initial tremor to the initial wavelet on the boundary layer occurs with a small spatial delay. Obviously, the delay depends on the properties of continuous media and the air flow velocity.

When the wave height exceeds the thickness of the laminar sublayer in the buffer region, the kink in the velocity profile increases, which promotes the production of turbulence energy. From this section, the appearance of a zone of increased turbulence affecting almost the entire thickness of the boundary layer is observed, which apparently continues up to a certain critical wavelength. After this region, a well-studied flow pattern around the interface appears which has many of its own features.

Acknowledgements The study was supported by the President of Russian Federation grant for the support of young Russian scientists (Project No. MK-1256.2019.1). Computational resources for numerical simulation of the present study were carried out with financial support from the government assignment for FRC Kazan Scientific Center of RAS FMEG-2021-0001.

References

1. S.R. Massel, *Ocean Surface Waves: Their Physics and Prediction*, vol. 45 (World Scientific, Singapore, 2017), p. 667
2. N. Andritsos, T.J. Hanratty, Influence of interfacial waves in stratified gas-liquid flows. *AIChE J.* **33**(3), 444–454 (1987)
3. P. Lombardi, V. De Angelis, S. Banerjee, Direct numerical simulation of near- interface turbulence in coupled gas-liquid flow. *Phys. Fluids* **8**(6), 1643–1665 (1996)
4. V. De Angelis, Numerical investigation and modeling of mass transfer processes at sheared gas-liquid interfaces. PhD Dissertation, University of California (2000)
5. M. Fulgosi, D. Lakehal, S. Banerjee, V. De Angelis, Direct numerical simulation of turbulence in a sheared air-water flow with a deformable interface. *J. Fluid Mech.* **482**, 319–345 (2003)
6. M.Y. Lin, C.H. Moeng, W.T. Tsai, P.P. Sullivan, S.E. Belcher, Direct numerical simulation of wind-wave generation processes. *J. Fluid Mech.* **616**, 1–30 (2008)
7. H. Kunishi, An experimental study on the generation and growth of wind waves. *J. Bull.-Disaster Prev. Res. Inst.* **61**, 1–41 (1963)
8. N.I. Mikheev, A.E. Goltsman, I.I. Saushin, O.A. Dushina, Estimation of turbulent energy dissipation in the boundary layer using smoke image velocimetry. *Exp. Fluids* **58**(8), 97 (2017)
9. K. Yousefi, F. Veron, M.P. Buckley, Momentum flux measurements in the airflow over wind-generated surface waves. *J. Fluid Mech.* **650** (2020)
10. N. Shaikh, K. Siddiqui, An experimental investigation of the near surface flow over air-water and air-solid interfaces. *J. Phys. Fluids* **22**(2), (2010)
11. C.T. Hsu, E.Y. Hsu, On the structure of turbulent flow over a progressive water wave: theory and experiment in a transformed wave-following coordinate system. Part 2. *J. Fluid Mech.* **131**, 123–153 (1983)
12. P.P. Sullivan, J.C. McWilliams, C.H. Moeng, Simulation of turbulent flow over idealized water waves. *J. Fluid Mech.* **404**, 47–85 (2000)

Phase Distribution of the Developed Three-Component Pipe Flows



I. Saushin and A. Goltsman

Abstract In contrast to single-component pipe flows, where the developed velocity profile depending on the Reynolds number plays a defining role in the flow measurement, the addition of other phases leads to the wide range of flow regimes and to an obvious increase in the number of dimensionless parameters of the problem. In the case of developed pipe flow of a three-component mixture, such as oil-gas-water three-phase flow in the oil well production and oil-gas transportation, the number of regimes depending on the classification can reach 10 or more. Based on numerical simulation, the present paper shows the studied ten regimes of the developed flow of a gas-oil-water mixture in a horizontal pipe. Depending on the developed all ten flow regimes, the resulting phase distribution of the mixture components was used to estimate the uncertainty of isokinetic sampling by known types of tube-type probes without and with prior mixing. The results of the study are relevant for further research on the preparation of the mixture using mixing devices in order to correctly determine the phase composition by the isokinetic sampling method.

1 Introduction

One of the main problems of multicomponent developed pipe flows is the measurement of the flow rate of one or more of the phases. In contrast to single-component pipe flows, where the developed velocity profile depending on the Reynolds number plays a defining role in the flow measurement, the addition of other phases leads to the wide range of flow regimes and to an obvious increase in the number of dimensionless parameters of the problem. In the case of developed pipe flow of a three-component

I. Saushin (✉) · A. Goltsman
Institute of Power Engineering and Advanced Technologies, FRC Kazan Scientific Center,
Russian Academy of Sciences, ul. Lobachevskogo, 2/31, Kazan, Tatarstan, Russian Federation
e-mail: ilyasaushin@mail.ru

A. Goltsman
e-mail: an116ya@mail.ru

mixture, such as oil-gas-water three-phase flow in the oil well production and oil-gas transportation, the number of regimes depending on the classification can reach 10 or more.

Measurement and analysis of multicomponent flows became possible only through some compromise on the accuracy of some parameters and the development of unique and very expensive sensors. However, even with such trade-offs, the use of expensive sensors does not guarantee sufficient accuracy in estimating the flow rates of each phase. Moreover, the use of methods of identifying flow regimes based on gamma radiation [1] or electro-tomography [2] for periodic or permanent analysis of the composition of the produced mixture from each well is obviously impossible for many cases.

The early detection of water is an important measurement for subsea gas condensate wells where inhibitors may be added to prevent the formation of scale and hydrates in the pipeline downstream of the well head. To manage the use of the inhibitors, the detection and quantification of the water can result in significant cost savings. Unfortunately, the metrological methods for diagnosing such flows are scientifically and technically extremely complex and unprofitable.

Therefore, the simplest way to determine the phase composition of a mixture is to artificially bring it into a homogeneous state in the local section of the pipeline, where sampling is performed, as a rule, by the isokinetic method. For two-phase like fluid-fluid flows, it is recommended to sampling after pumps or dispersers in the relevant standards [3–5]; however, when a third component (compressible) of the mixture appears, the use of such devices can be severely limited. Moreover, sampling from flows of gas-fluid-fluid mixtures [3–5] is completely unregulated. An alternative way to prepare a three-component mixture in front of the sampling region is to mechanically mix it under the effect of the energy of the flow itself. This raises the question of the correlation of existing mixing devices for pipe flows with a wide spectrum of the mixture regime map.

2 Problem Statement and Method

2.1 Three-Phase Flow Regimes and Isokinetic Probe Design

Classification of the flow regimes of a gas/liquid/liquid mixture is a separate scientific problem. In view of the motion of continuous media, the specific velocity of each component plays a decisive role here. To date, there are two approaches to representing the gas/liquid/liquid flow: considering it as a two-component flow of liquids with gas [6–9], or as a three-component mixture flow [10–13]. In present work, the second

point of view was adopted, and the classification of regimes itself was taken from work [12]. According to this classification, the flow of a gas/liquid/liquid mixture can be described by 10 regimes depending on the specific velocities of each phase, Fig. 1. Red markers show the investigated flow regimes, which are formed at different specific velocities of the j_i phases (Fig. 2, regime map): 1. Oil-based dispersed plug flow; 2. Oil-based dispersed slug flow; 3. Oil-based dispersed stratified/wavy flow; 4. Oil-based separated stratified/wavy flow; 5. Oil-based separated wavy stratifying-annular flow; 6. Oil-based separated/dispersed stratifying-annular flow; 7. Water-based dispersed slug flow; 8. Water-based dispersed stratified/wavy flow; 9. Water-based separated/dispersed incipient stratifying annular Flow; 10. Water-based dispersed stratifying-annular flow.

At this stage of the research, the well-known and proven designs proposed in [4, 5] for two-component liquid/liquid flows as the isokinetic probes were taken. 4 designs were considered—A, B, C, D types, which differ in the number and location of probes in the pipeline section, Fig. 1.

Designs of sampling devices A [5], B [4, 5], C [4, 5] have the same inlet cross-sectional area of the probes and differ only in their number. The D-type probe, which was proposed in [5], has a feature that is expressed in an increase in the diameter of the inlet cross-sections of the probes close to the pipe wall.

2.2 Simulation Method

The CFD solver ANSYS Fluent R19.2 is used to perform numerical simulations of Gas-Liquid-Liquid flow in a tube. The three-fluid Eulerian-Eulerian transient Volume of Fluid (VOF) model in explicit formulation is employed to represent each incompressible phase as interpenetrating continua and the conservation equations for mass and momentum for each phase are ensemble-averaged. These conservation equations are closed with the Re-Normalisation Group (RNG) $k-\epsilon$ turbulence model using standard wall functions. A second-order upwind discretization scheme was used for the momentum equations while a first-order upwind discretization was used for volume fraction, turbulent kinetic and turbulent dissipation energy. These schemes ensured, in general, satisfactory accuracy, stability and convergence. The convergence criterion is based on the residual value of the calculated variables, i.e., mass, velocity components, turbulent kinetic energies, turbulent dissipation energies and volume fraction. In the present calculations, the threshold values were set to a thousandth of the initial residual value of each variable. The pressure staggering option (PRESTO) and Pressure-Implicit with Splitting of Operators (PISO) algorithms) are used to resolve the coupling between velocity and pressure.

The boundary conditions fully reproduced the experiment procedure [10], in which the flow of an air/water/oil mixture in a 19 mm diameter and 3000 mm length pipe was investigated. A homogeneous mixture was supplied into the inlet section with a fraction of each of the three components given through mass flow rate: incompressible air ($\mu = 1.7894 \cdot 10^{-5}$ Pa·s, $\rho = 1.225$ kg/m³), oil ($\mu = 0.1164$ Pa·s, $\rho = 864$ kg/m³) and water ($\mu = 0.001003$ Pa·s, $\rho = 998.2$ kg/m³). Specific oil rate of 18.98 kg/h was constant, air and water flow rate varied in the ranges of 0.07–29.34 and 1.45–63.14 kg/h, respectively. Maintaining the desired range of y^+ in multiphase unsteady flows is complicated by the variability of the mixture properties in the local computational domain of a fixed volume over time, which in turn causes the spatial inhomogeneity of the magnitude of this characteristic. For this reason the scalable wall functions were used in the calculations. The maximum of y^+ for the selected turbulence model should not go beyond the fully turbulent portion or log-law region (corresponds to the region where turbulent shear predominates), that is the values of the order of 300. For the remaining eight flow regimes, the y^+ was within this interval.

3 Results

The results of numerical simulation on the flow pattern with the results of experiments [12] are in good agreement. We reproduced the features of all ten regimes. To estimate the sampling uncertainty for each of the four device designs, the Δ parameter was chosen; it describes the percentage difference between the oil phase content in the liquid mixture that flows through the pipe in 10s and the liquid mixture that was captured by the probes. For convenience, the regime maps are painted in four colors according to the deviation Δ of the CFD estimates of the oil volume fraction in the water/oil mixture from the true value of N : green— $\Delta \leq 10\%$, yellow— $\Delta \leq 20\%$, orange— $\Delta \leq 30\%$, red— $\Delta > 30\%$, Fig. 1. A sampling device with a single probe (Type A) located in the center of the pipe should not be used in mixture flows of liquid and gases. Since for regimes with a tunneling gas flow in the center or in the upper part of the pipe, this probe is useless. Installing a mixing device will probably not help here either. The increase in the number of such probes (Type B and C) expanded the list of regimes where the uncertainty in measuring the phase oil content below 10 % was achieved. But the smallest uncertainty for all regimes was obtained by the Type D sampling device. This, apparently, was due to the increased diameter of the inlet section of the probe near the wall, where the flow of the heaviest liquid, water, takes place in most regimes. If the mixing device is located in front of the sampling area, using the B, C and D probes are likely to be equivalent, but this needs to be verified.

Fig. 1 Uncertainty Δ of estimating the phase oil content for each air/oil/water flow regime with an isokinetic sampling device [2, 3]. Green— $\Delta \leq 10\%$, yellow— $\Delta \leq 20\%$, orange— $\Delta \leq 30\%$, red— $\Delta > 30\%$. Blue color shows water, brown shows oil, and gray indicates the air phase. In the upper right corner of the figure, the inlet cross-sections of the samplers for the considered types of devices are shown

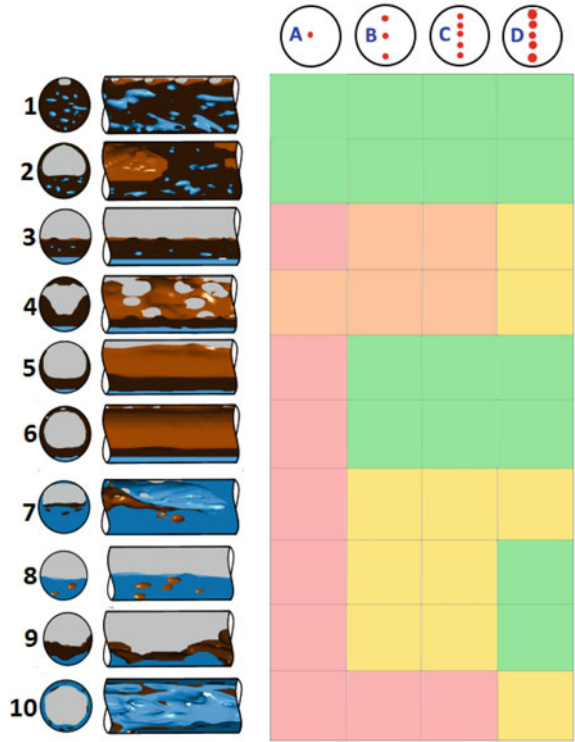
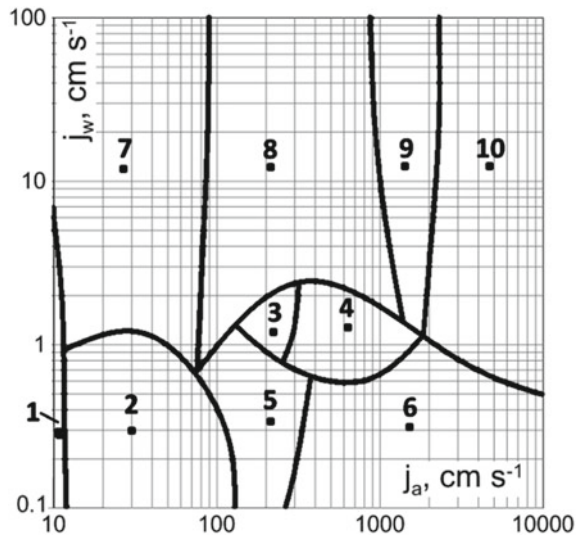


Fig. 2 Three-phase flow regime map ($j_o = 4.3 \text{ cm/s}$). Markers indicate the present investigated regimes



4 Conclusion

The present paper shows that the phase content of a mixture can be estimated with a fairly good uncertainty and simple isokinetic probes used for two-component liquid mixture flows. It was obtained that this uncertainty can be reduced by pre-mixing the flow before the mixture sampling section. Therefore, we plan to use these results further to choose the optimal mixing device for the air/oil/water flow. Obviously, this approach is inferior in accuracy to modern multiphase flowmeters and can only serve as a rough estimate. Nevertheless, given the technical complexity of maintenance and the cost of multiphase flowmeters, the classical method of isokinetic sampling may be the only available in many cases and sometimes quite sufficient method for estimating the phase composition of a gas/liquid/liquid mixture.

Acknowledgements This study was supported by the Russian Science Foundation (Project no. 19-79-00160). Computational resources for numerical simulation of the present study were carried out with financial support from the government assignment for Federal Research Center “Kazan Scientific Center of Russian Academy of Sciences” FMEG-2021-0001.

References

1. B.K. Arvoh, R. Hoffmann, M. Halstensen, Estimation of volume fractions and flow regime identification in multiphase flow based on gamma measurements and multivariate calibration. *Flow Meas. Instrum.* **23**(1), 56–65 (2012)
2. A. Zhao, Y.Y. Ren, L. Zhu, X. Yang, Multi-scale long-range magnitude and sign correlations in vertical upward oil-gas-water three-phase flow. *Z. Naturforsch.* **71**(1), 33–43 (2016)
3. ISO 3170, Petroleum liquids - manual sampling. International Organization for Standardization (2004)
4. ISO 3171, Petroleum liquids - automatic pipeline sampling. International Organization for Standardization (1988)
5. GOST 2517-2012, Petroleum and petroleum products. Methods of sampling. Interstate Council for Standardization, Metrology and Certification (2018)
6. M.S. Malinowsky, Petroleum and petroleum products. An experimental study of oil-water and oil-water-gas flowing mixtures in horizontal pipes. MSc. thesis, University of Tulsa, USA (1975)
7. G.C. Laffin, An experimental study on the effects of flowrate, water fraction and gas-liquid ratio on air-oil-water flow in horizontal pipes. BSc. thesis, University of Tulsa, USA (1976)
8. H.H. Stapelberg, D. Mewes, The flow of two immiscible liquids and air in a horizontal pipe, in *Advances in Gas-Liquid Flows FED* (1990), pp. 89–96
9. H.H. Stapelberg, D. Mewes, The flow of two immiscible liquids in horizontal pipes - pressure drop and flow regimes, in *European Two-Phase Flow Group Meeting*, Varese (1990)
10. D.P. Sobocinsk, Horizontal co-current flow of water, gas-oil and air. Master thesis, University of Oklahoma (1955)

11. A. Pleshko, M.P. Sharma, An experimental study of vertical three-phase (oilwater-air) upward flows, advances in gas-liquid flows, in *Winter Annual Meeting of the American Society of Mechanical Engineers*, Dallas, Texas (1990)
12. M. Acikgoz, F. Franca, R.T. Lahey Jr., An experimental study of three-phase flow regimes. *Int. J. Multiph. Flow* **18**(3), 327–336 (1990)
13. L. Pan, High pressure three-phase (gas/liquid/liquid) flow. Ph.D. thesis, Imperial College, University of London, UK (1996)